STATISTICAL MODELING AND MARKOV CHAIN MONTE CARLO INFERENCE OF MAJORANA DEMONSTRATOR BACKGROUND DATA

Thomas F. Gilliss

A dissertation submitted to the faculty of the University of North Carolina at Chapel Hill in partial fulfillment of the requirements for the degree of Doctor of Philosophy in the Department of Physics & Astronomy.

Chapel Hill
2019

Approved by:

Steven R. Elliott

Jonathan Engel

Matthew P. Green

Reyco Henning

John F. Wilkerson

ABSTRACT

THOMAS F. GILLISS: Statistical Modeling and Markov Chain Monte Carlo Inference of the Majorana Demonstrator Background Data
(Under the direction of John F. Wilkerson)

Observation of neutrinoless double-beta decay ($0\nu\beta\beta$) would establish lepton number violation, constrain the absolute neutrino mass scale, and imply the Majorana nature of neutrinos. Germanium-based $0\nu\beta\beta$ experiments are entering the tonne-scale era with discovery potential for half lives approaching 10^{28} years, covering the region of effective Majorana neutrino masses indicative of the inverted ordering scenario for the three neutrino mass eigenstates. Sensitivity to such protracted decay rates requires < 0.1 background counts in the signal region per tonne-year of an experiment's exposure, an order of magnitude improvement from current experiments observing tens of kilograms of ^{76}Ge. Toward this goal, this work describes the simulation and analysis of 26.0 kilogram-years of background data from the Majorana Demonstrator, a $0\nu\beta\beta$ experiment operating an array of high-purity germanium detectors in a low-background environment at the Sanford Underground Research Facility. A latest analysis of this data yields a half life sensitivity of 4.8×10^{25} years. Detailed simulation of the Demonstrator design and constraints on the radiopurity of its components facilitate Bayesian statistical modeling of the background data and Markov chain Monte Carlo sampling for inference of background sources, essential inputs for the next-generation tonne-scale experiment LEGEND.

ACKNOWLEDGEMENTS

This material is based upon work supported by the U.S. Department of Energy, Office of Science, Office of Nuclear Physics, the Particle Astrophysics and Nuclear Physics Programs of the National Science Foundation, and the Sanford Underground Research Facility.

TABLE OF CONTENTS

LIST OF TABLES ix

LIST OF FIGURES xii

1 Neutrinos and $0\nu\beta\beta$ 1

1.1 Neutrino Interactions 1

1.2 Massive Neutrino Oscillations 3

1.3 Neutrino Mass 4

1.4 Neutrino Dirac or Majorana Nature 5

1.5 Neutrinoless Double-Beta Decay 8

1.6 Implications of $0\nu\beta\beta$ 10

2 Experimental Requirements 12

2.1 Sensitivity 12

2.2 Discovery-Level Sensitivity 13

2.3 Improving Sensitivity 14

2.4 Reducing Backgrounds 16

2.4.1 Cosmic Rays and Neutrons 17

2.4.2 Radioimpurities in the Detector and Shielding 17

2.4.3 Anthropogenic Contamination and Radon 19

2.4.4 Energy Resolution 19

2.4.5 Target Isotope and Quantity 20

3 The Majorana Demonstrator 22

3.1 Overview of Experimental Design 23

3.1.1 Modules 23
3.1.2 Shielding 24
3.1.3 Data Acquisition 25
3.1.4 Calibration 26
3.1.5 Ge PPC Detectors 26
3.1.6 Materials and Assembly 27
3.2 Backgrounds 28
3.3 Background Signatures 31
3.4 Event Discrimination 35
4 Majorana Demonstrator Background Data 37
4.1 Data Sets 37
4.2 Data Selection 40
4.3 Spectral Analysis 42
4.4 Current Status 47
5 Majorana Demonstrator Simulations 51
5.1 Simulated Components 52
5.2 Simulations Processing 52
5.3 Simulations Post-Processing 55
5.4 Handling of Enriched and Natural Detectors 58
5.5 Calculating Specific Activity for Cosmogenic Products 58
5.6 Summary 59
6 Background Model 60
6.1 Assay Sample Selection 60
6.2 Expected Background Index 63
6.3 Comparison of Preliminary and As-Built Models 64
6.4 Comparison of As-Built Model and Data 69
7 Toward Background Model Inference 73

7.1 Comparison of Simulations to Peaks in Data 73
7.2 Comparison of Simulations to Calibration Data 78
7.3 Effects of Modeling the Lithiated Layer and Cuts 79
8 Inference Methods 83
8.1 Markov Chain Monte Carlo 84
8.2 Hamiltonian Monte Carlo 85
8.3 Statistical Model 87
8.4 Probabilistic Programming 88
8.5 Summary 89
9 Background Model Inference 92
9.1 Model Components and Parameters 92
9.2 Evaluating DS0 for ^{210}Pb Activity 93
9.3 Systematic Errors in Fits 94
9.3.1 Energy Range 94
9.3.2 Binning 96
9.3.3 Cut and Data Selection 98
9.4 Full Regression to DS1-6a 98
9.4.1 $2\nu\beta\beta$ Results 99
9.4.2 Results from other Components 101
9.4.3 Summary of Major Components 104
10 Conclusions 106
10.1 Future Work 107
APPENDIX A: DETECTOR SELECTION 109
APPENDIX B: ASSAY SAMPLE SELECTION 111
APPENDIX C: COMPARISON OF SIMULATIONS TO CALIBRATION DATA 114
C-1 M1 Calibration Source 114

C-2 M2 Calibration Source 122

APPENDIX D: DETAILED EXPECTED CONTRIBUTIONS 129

APPENDIX E: DETAILED REGRESSION RESULTS 132

BIBLIOGRAPHY 144

LIST OF TABLES

4.1 Exposure information for each data set. Symbols are exposure $\mathcal{E}$, average livetime t, and active mass m_{act}. 39

4.2 Peak rates calculated via sideband subtraction, from the DS1-6a energy spectrum. Both open and blind data are included and data cleaning, LN fill, and muon veto cuts are applied. The peak rates that reject a background-only hypothesis at $> 90\%$CL are presented with a 68% Gaussian standard error. A 90% upper limit is reported for peak rates consistent with background. I_γ is the intra-isotope intensity. 44

4.3 Peak rates calculated via Bayesian inference, from the DS1-6a energy spectrum. Both open and blind data are included and data cleaning, LN fill, and muon veto cuts are applied. The peak rates that reject a background-only hypothesis at $> 90\%$CL are presented with a 68% credible interval. A 90% upper limit is reported for peak rates consistent with background. I_γ is the intra-isotope intensity. 45

6.1 Estimates for the mass and specific activity of ^{232}Th and ^{238}U contaminants in MAJORANA DEMONSTRATOR materials. Materials are listed roughly in order of distance from the detectors. Connectors are not included in calculations for the vespel row. 61

6.2 Expected contributions to the background index from the sources listed in the first column. The second column represents the as-built background model assuming the DS5 configuration. The third column also uses the as-built background model but assumes all detectors are operational. The fourth column presents the analogous results of the preliminary background model published in Ref [41]. The row labeled "Plastics, Other" includes the contributions of stainless steel from the modules' service bodies, the glass break from the cryogenics system, and the phosphor bronze spring washers assisting HV connections at the detectors. 65

6.3 Percent differences in background index for components in the as-built model, with all detectors operational, and the preliminary model of Ref [41]. Column labeled "% Difference" is calculated as $100 \times$ (As-Built $-$ Preliminary)/Preliminary. .. 66

6.4 A comparison of mass, efficiency, and background rate for a selection of components from the preliminary and as-built models. Columns labeled "% Difference" are calculated as $100 \times$ (As-Built $-$ Preliminary)/Preliminary. 68

6.5 A comparison of cut survival fractions for a selection of components from the preliminary and as-built models. Columns labeled "% Difference" are calculated as $100 \times$ (As-Built $-$ Preliminary)/Preliminary. 69

7.1 Comparison of simulated peaks to those observed in DS1-6a data. For ^{232}Th and ^{238}U, the listed individual simulated components were scaled to match the 238.6 keV ^{212}Pb or 351.9 keV ^{214}Pb peak, respectively. Components best matching the data are included here, along with the best-matched component of the opposing decay chain for comparison. As the scaled simulation spectra are binned, peak rates in this table were calculated via binned integration for both simulations and data. 75

9.1 Statistical and systematic uncertainties on the $2\nu\beta\beta$ half life in $^{\text{enr}}$Ge. 102

9.2 The ten largest components resulting from the fit to DS1-6a data. The second and third columns present the counts attributed to each component and the percentage of the total fitted counts. The third and fourth columns summarize each component's marginal posterior distribution. 102

9.3 Expected contributions to the background index from the sources listed in the first column. The second column represents the as-built background model assuming the DS5 configuration. The third column also uses values inferred from regression of the as-built model to data. The fourth column presents the analogous results of the preliminary background model published in Ref [41]. The row labeled "Plastics, Other" includes the contributions of stainless steel from the modules' service bodies, the glass break from the cryogenics system, and the phosphor bronze spring washers assisting HV connections at the detectors. 103

A.1 Detector information for channel selection in data and simulations. A value of 0 indicates an inoperable detector, 1 indicates an operating detector included in analysis, and 2 indicates that a detector was not present in the given experimental configuration. 110

B.1 Bulk Natural Radioactivity: Estimates for the specific activity of contaminants in MAJORANA DEMONSTRATOR materials' bulk. 112

B.2 Surface Natural Radioactivity: Estimates for the specific activity of contaminants from the surface of MAJORANA DEMONSTRATOR materials. 112

B.3 Contaminants Out-of-Equilibrium with Natural Radioactivity: Estimates for the specific activity of contaminants in MAJORANA DEMONSTRATOR materials. .. 113

B.4 Cosmogenic Activation Products: Estimates for the specific activity of contaminants in MAJORANA DEMONSTRATOR materials. 113

D.1 The second and third columns present the counts attributed to each component and the percentage of the total fitted counts. The subsequent columns summarize each component's prior distribution. 130

D.2 The second and third columns present the counts attributed to each component and the percentage of the total fitted counts. The subsequent columns summarize each component's prior distribution. 131

E.1 The second and third columns present the counts attributed to each component and the percentage of the total fitted counts. The subsequent columns summarize each component's prior distribution and marginal posterior distribution. 133

E.2 The second and third columns present the counts attributed to each component and the percentage of the total fitted counts. The subsequent columns summarize each component's prior distribution and marginal posterior distribution. 134

LIST OF FIGURES

1.1 A charged current interaction in which a negatively charged lepton l^- transforms into a neutrino of the corresponding flavor ν_l with a W^- boson carrying away the difference in mass and charge. 2

1.2 A charged current interaction in which the emission of a W^- boson transforms one species of quark into another. 2

1.3 The four states of a Dirac neutrino, connected by transformations of helicity and particle-antiparticle. These four states are limited to two in the case of a Majorana neutrino. Figure from [7]. 7

1.4 Masses of nuclei along an even-A isobar illustrate the staggering effect of $n-n$ and $p-p$ spin-pairing on binding energy. A generic level diagram is shown for cases in which double-beta decay is possible. Figures adapted from [17, 18]. 9

1.5 The $0\nu\beta\beta$ diagram assuming the light neutrino exchange mechanism. Figure from [7]. 10

2.1 A hypothesis test for confirming H_0, or rejecting H_0 in favor of H_1, in an experiment with observable X. The decision making boundaries of the test depend on predetermined values of α and β. 14

2.2 $n_{\min}$ calculated as a function of μ_B for 95%, 3σ, and 5σ significance levels of α (top). $S_{\min}$ calculated as a function of μ_B for $(1-\alpha, 1-\beta)$ pairs $(95\%, 95\%)$, $(3\sigma, 95\%)$, and $(5\sigma, 90\%)$ (bottom). Figures from [25]. 15

2.3 An illustration of overlap between the $2\nu\beta\beta$ continuum and $0\nu\beta\beta$ peak at $Q_{\beta\beta}$ for an experiment with 5% energy resolution. Figure from [23]. 20

3.1 A cross sectional rendering of one MJD cryostat containing an array of detectors (teal and grayish-teal). The detectors are stacked vertically into strings prior to installation in a cryostat. Enriched detectors occupy the bottom two rows of each string in this rendering, with natural detectors occupying the top two rows. 23

3.2 A cross sectional rendering of the MAJORANA DEMONSTRATOR. The two cryostats connect via crossarm tubes to their respective vacuum equipment, cryogenics, and electronics. Layers of passive and active shielding surround the cryostats. 24

3.3 A cartoon cross section of a PPC detector shown alongside a photograph of such a detector. Note that the p+ contact— labeled in the cartoon— is shown facing out of the page in the photograph. HPGe detectors of PPC design offer many advantages to a $0\nu\beta\beta$ experiment. 27

3.4 A Ge crystal placed in a detector mount. As labeled in the image, the mount includes UGEFCu structural and electrical components as well as insulating components made of PTFE. 29

3.5 A low-mass front end electronic board for connection to the point contact of a detector. A field-effect transistor is the central component responding to induced current from drifting charges in the detector, or from an external pulser line placed nearby. 30

3.6 A string of natural germanium detectors shown beside a rendering of the assembly. Signal cables extending from each detector's LMFE can be seen hanging on the left side of the image. 31

3.7 Event topologies of typical gamma ray interactions with a detector of intermediate volume. Figures are from [50]. 33

3.8 Event topologies of typical gamma ray interactions considering the effects of materials surrounding a detector. Figures are from [50]. 34

4.1 Differences in experimental configuration are evident between DS0 and DS1-6a. These spectra include hits from both ^{nat}Ge and ^{enr}Ge, include both open and blind data, and are presented with data cleaning, LN fill, muon veto, and multiplicity cuts applied. 40

4.2 Data sets beyond DS0 are generally consistent in rate. Data sets of shorter exposure display larger relative uncertainty. These spectra include hits from both ^{nat}Ge and ^{enr}Ge, include both open and blind data, and are presented with data cleaning, LN fill, muon veto, and multiplicity cuts applied. 41

4.3 A comparison of the ^{nat}Ge, ^{enr}Ge, and total energy spectra for DS1-6a. These spectra include both open and blind data, and are presented with data cleaning, LN fill, muon veto, and multiplicity cuts applied. 42

4.4 The DS1-6a spectrum with prominent γ peaks labeled by decay chain. Note overlap between the 510.8 (^{208}Tl, ^{232}Th) and 511.0 keV (e^+e^- annihilation) peaks. This spectrum is comprised of individual detector hits from both ^{nat}Ge and ^{enr}Ge, includes both open and blind data, and is presented with data cleaning, LN fill, muon veto, and multiplicity cuts applied. PSA and DCR cuts are not applied. 43

4.5 Rate as a function of time and enrichment, for a selection of the strongest peaks. Rates are calculated for each data set and plotted at the data set's midpoint in days. Open and blind DS0-6a are included with the multiplicity cut applied. The start of DS0 lies at zero days, and DS3 and DS4 overlap in time. Horizontal lines indicate a data set's duration, and the ^{nat}Ge and ^{enr}Ge data points have been staggered about data set midpoints for clarity. 48

4.6 Rate as a function of detector, for a selection of the strongest peaks in DS1-6a. C2P6D1 (^{enr}Ge) is excluded due to low statistics, having operated solely in DS4. Rates were calculated with the multiplicity cut applied. 49

4.7 DS0-6a ^{enr}Ge data before (black) and after (red) the application of DCR, AvsE, and multiplicity cuts. The inset figure displays the integration window for the $0\nu\beta\beta$ background index, with the regions surrounding $Q_{\beta\beta}$ and known ^{232}Th and ^{238}U lines highlighted. The inset blue curve represents the calculated flat background index and the 90% CL upper limit on the number of counts in the $0\nu\beta\beta$ peak region. 50

5.1 Renderings of a detector unit (top), detector array (middle), and cryostat vessel (bottom), as modeled in MaGe. 53

5.2 The four simulated segments of the ^{232}Th decay chain. 54

5.3 The ten simulated segments of the ^{238}U decay chain. 55

6.1 The expected individual and summed background contributions based on as-built simulations, masses, and assay selection. The simulations shown here assume all detectors are operational with the multiplicity and PSA cuts applied, and contributions from both ^{nat}Ge and ^{enr}Ge are included. 70

6.2 The individual and summed background contributions expected for the DS5 configuration based on as-built simulations, masses, and assay selection. Both ^{nat}Ge and ^{enr}Ge are included with the multiplicity cut applied. The analogous DS5 data is overlaid for comparison and normalized residuals are calculated. 71

6.3 The individual and summed background contributions expected for the DS0 configuration based on as-built simulations, masses, and assay selection. Both ^{nat}Ge and ^{enr}Ge are included with no cuts applied. The analogous DS0 data is overlaid for comparison and normalized residuals are calculated. 72

7.1 ^{232}Th from the inner Cu shield reasonably approximates high and low energy peaks when scaled to the 238.6 keV peak from ^{212}Pb. 76

7.2 ^{232}Th from the LMFEs under-predicts high energy peaks when scaled to the 238.6 keV peak from ^{212}Pb. 76

7.3 ^{238}U from the LMFEs reasonably approximates peaks when scaled to the 351.9 keV peak from ^{214}Pb. 77

7.4 ^{238}U from the inner Cu shield over-predicts higher energy peaks when scaled to the 351.9 keV peak from ^{214}Pb. 77

7.5 PTFE tubing wraps helically around each cryostat forming a track for a calibration line source. 78

7.6 Data from DS5b M1 calibration source runs compared with analogous simulations. Data cleaning and DCR cuts are applied, and both ^{nat}Ge and ^{enr}Ge are included. 79

7.7 Data from DS5b M2 calibration source runs compared with analogous simulations. Data cleaning and DCR cuts are applied, and both ^{nat}Ge and ^{enr}Ge are included. 80

7.8 Data from DS5b M1 calibration source runs compared with analogous simulations. Data cleaning, multiplicity, and DCR cuts are applied, and both ^{nat}Ge and ^{enr}Ge are included. 81

7.9 Data from DS5b M1 calibration source runs compared with analogous simulations. Data cleaning, multiplicity, multisite, and DCR cuts are applied, and both ^{nat}Ge and ^{enr}Ge are included. 82

8.1 In each HMC transition, a momentum is proposed and a phase space trajectory is calculated. After traversing the trajectory, the explored parameters are recovered by projecting away the auxiliary momenta. Figure from Ref [78]. 87

8.2 A probabilistic graphical model for unpooled parameters w_j in which no two mixture components share the same parameter. Open nodes represent random variables w_j and shaded nodes represent observed variables c_i. 89

8.3 A probabilistic graphical model for pooled parameters w_j. In this diagram, mixture components $j-1$ and j share the same parameter. Open nodes represent random variables and shaded nodes represent observed variables. 90

8.4 A probabilistic graphical model for parameters w_j related by a common hyperparameter. In this hierarchical diagram, parameters w_{j-1} and w_j are drawn from the same underlying distribution h. Open nodes represent random variables and shaded nodes represent observed variables. 91

9.1 Marginal posterior for the specific activity of ^{210}Pb in the Pb shield inferred from regression of DS0 simulations to data. The posterior (solid black) indicates a value roughly four times less than the expected value encoded in the prior distribution (dashed purple). 94

9.2 The spectral contributions of each decay chain resulting from regression of simulations to open DS0 data under two sets of cuts: data cleaning and DCR; and data cleaning, multiplicity, and DCR. 95

9.3 The spectral contributions of each decay chain resulting from regression of simulations to open DS1-6a data under data cleaning and DCR cuts, with the likelihood evaluated between 100-2617 keV..... 97

9.4 The spectral contributions of each decay chain resulting from regression of simulations to open and blind DS1-6a data under two sets of cuts: data cleaning and DCR; and data cleaning, multiplicity, and DCR. Since the open data is used under two cuts, it contributes twice to the total exposure listed in the legend. 100

9.5 Marginal posterior for the specific activity of $2\nu\beta\beta$ in the $^{\text{enr}}$Ge inferred from regression of simulations to DS1-6a data. The posterior (solid black) indicates a best-fit value roughly 10% below the expected value encoded in the prior distribution (dashed purple). Solid grey lines indicate a 68% credible interval. A diffuse prior distribution was set for the parameter, indicated by the black dashed line seemingly parallel to the horizontal axis. 101

E.1 $2\nu\beta\beta$ 135

E.2 ^{57}Co 136

E.3 ^{60}Co 137

E.4 ^{68}Ge 138

E.5 ^{40}K 139

E.6 ^{210}Pb 140

E.7 ^{222}Rn 141

E.8 ^{232}Th 142

E.9 ^{238}U 143

CHAPTER 1
Neutrinos and $0\nu\beta\beta$

The existence of the neutrino was postulated in 1930 in the context of β-decay [1]. Assuming a two-body model of this nuclear transformation, the quantities energy, momentum, and angular momentum could not be conserved by an outgoing electron and recoiling nucleus alone. Allowing for a low-mass, charge-neutral, spin-1/2 neutrino to exit the nucleus alongside the electron, the resulting three-body model recovered the expected symmetries.

Though unknown at the time, the postulated neutrino was the electron antineutrino as it participates in the weak force transformation of a neutron into a proton,

$$n \rightarrow p + e^{-} + \bar{\nu}_e.$$

By rearranging these components of β-decay, the existence of the neutrino was first confirmed in 1956 [2]. An electron antineutrino was captured on a proton, thereby transforming the proton into a neutron and the electron antineutrino into a positron.

$$\bar{\nu}_e + p \rightarrow n + e^{+}.$$

The nature of the weak force and its role in the transformation of leptons and quarks was uncovered during the twentieth century, along with the neutrino's relation to the other leptons. The small mass, neutral charge, oscillatory behavior, and handedness of the neutrino set it apart from the charged leptons and implied new physics beyond the Standard Model.

1.1 Neutrino Interactions

Neutrinos are light mass, electrically neutral fermions known only to interact via the weak nuclear and gravitational forces. Neutrinos are detected and categorized by their weak interactions

and the charged leptons that accompany them. The charged current interactions involve the vertex of Fig 1.1 with a W boson carrying mass and charge. In this way, and through Fig 1.2, the W bosons connect the two states of each $SU(2)$ doublet in the three generations of leptons and quarks.

$$\begin{pmatrix} \nu_e \\ e \end{pmatrix} \quad \begin{pmatrix} \nu_\mu \\ \mu \end{pmatrix} \quad \begin{pmatrix} \nu_\tau \\ \tau \end{pmatrix}$$
$$\begin{pmatrix} u \\ d \end{pmatrix} \quad \begin{pmatrix} c \\ s \end{pmatrix} \quad \begin{pmatrix} t \\ b \end{pmatrix} \tag{1.1}$$

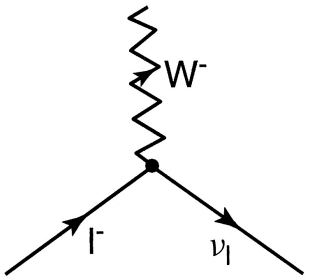

Figure 1.1: A charged current interaction in which a negatively charged lepton l^- transforms into a neutrino of the corresponding flavor ν_l with a W^- boson carrying away the difference in mass and charge.

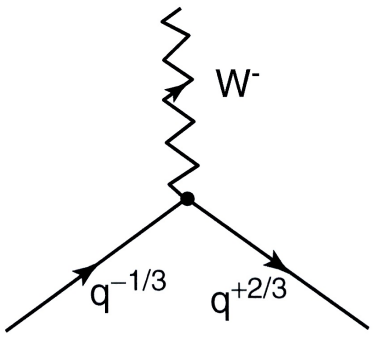

Figure 1.2: A charged current interaction in which the emission of a W^- boson transforms one species of quark into another.

1.2 Massive Neutrino Oscillations

The three generations of neutrinos depicted in Eqn 1.1 are known as the three neutrino flavors. The discovery of oscillations between these flavors established each flavor eigenstate as a superposition of mass eigenstates [3, 4]. That is, the flavor states ν_f are mixtures of the mass states ν_m as

$$\nu_f = \sum_m U_{fm}\nu_m \tag{1.2}$$

where U_{fm} is an element of the 3×3 unitary leptonic mixing matrix [5, 6].

For a beam of neutrinos with momentum p, all created in flavor state f, the wave function for each neutrino will be

$$\psi(x,t) = \sum_m U_{fm}\nu_m e^{ipx} e^{-iE_m t} \tag{1.3}$$

as a function of position x and time t [7]. The neutrinos are of low mass and so are highly relativistic with position $x \approx t$ and free particle energies E_m

$$\begin{aligned} E_m^2 &= p^2 + M_m^2 \\ M_m &\ll p \\ E_m &\approx p + \frac{M_m^2}{2p} \end{aligned} \tag{1.4}$$

where M_m is the mass eigenvalue. With these approximations, Eqn 1.3 is rewritten

$$\psi(t,t) = \sum_m U_{fm}\nu_m e^{-i\frac{M_m^2}{2p}t}. \tag{1.5}$$

A substitution for ν_m by the inverse of Eqn 1.2 makes apparent that the wave function $\psi(t,t)$ is actually a superposition of all flavors

$$\psi(t,t) = \sum_{f'} \left[\sum_m U_{fm} U^*_{f'm} e^{-i\frac{M_m^2}{2p}t} \right] \nu_{f'} \tag{1.6}$$

such that the probability of finding a neutrino in flavor f' is then given by $|\psi(t,t)|^2$

$$\begin{aligned} p(f \to f'; x \approx t) &= \sum_{m'} \sum_{m} U^*_{fm'} U_{f'm'} U_{fm} U^*_{f'm} e^{i\frac{(M^2_{m'} - M^2_m)}{2p}t} \\ &= \sum_m \left|U_{fm} U_{f'm}\right|^2 + \sum_{m'} \sum_{m \neq m'} U^*_{fm'} U_{f'm'} U_{fm} U^*_{f'm} e^{i\frac{(M^2_{m'} - M^2_m)}{2p}t} \\ &= \sum_m U^2_{fm} U^2_{f'm} + 2 \sum_{m' \neq m} U_{fm'} U_{f'm'} U_{fm} U_{f'm} \cos\left(\frac{\Delta M^2}{2p} x\right) \end{aligned} \tag{1.7}$$

where the third line assumes the elements of U are real, and $\Delta M^2 \equiv |M^2_{m'} - M^2_m|$ [7].

Eqn 1.7 shows that the probability of flavor oscillation varies as a function of distance, with the frequency of those oscillations dependent on the mass splittings and momentum, and the amplitude of those oscillations dependent on the couplings between the relevant flavor and mass states. Observed oscillation between each flavor implies that the three mass states are non-degenerate.

1.3 Neutrino Mass

As discussed in Section 1.2, neutrino oscillations reveal the mass splittings ΔM^2, but not the absolute masses M_m themselves. Separate experiments are able to probe this physics.

For example, kinematic studies of β-decay in ^{3}H place the effective mass of the electron antineutrino at < 2.3 eV [8, 9]. Kinematic β-decay experiments analyze the endpoint of the β-decay spectrum to determine the rest mass of the neutrino. With the masses being so small, such experiments do not resolve the particular mass eigenstate in which each electron antineutrino was created, but rather measure the effective mass: the sum of each mass state's coupling to the electron flavor

$$M^2_\beta = \sum_m |U_{em}|^2 M^2_m. \tag{1.8}$$

Independently, measurements from cosmological observations probe the sum of the mass eigenstates

$$M_{\text{tot}} = \sum_m M_m \tag{1.9}$$

and set an upper limit of about $M_{\text{tot}} < (0.12 - 0.54)$ eV [10].

Without knowledge of the individual mass eigenvalues, the ordering of the mass eigenstates—which by convention have been labeled ν_1, ν_2, ν_3— is uncertain. Observations of matter-enhanced oscillations have determined the mass of ν_2 to be greater than that of ν_1, but the ordering of ν_3 relative to this pair remains unknown [11].

1.4 Neutrino Dirac or Majorana Nature

Previous sections have discussed the small masses and neutral electric charge of the neutrinos. These properties set neutrinos apart from the other fermions which do carry charge and possess masses greater than those of the neutrinos by at least a factor of 10^6 [12]. Additionally, the opposite handedness of neutrinos and antineutrinos appears intrinsic to the particles [13, 14]. Altogether, the nature of the neutrino may differ from that of the other fermions.

The Dirac equation for relativistic spin-1/2 particles is satisfied by a set of 4×4 γ^μ matrices obeying the Clifford algebra, and a four-component spinor ψ comprised of two two-component Weyl spinors

$$(i\gamma^\mu \partial_\mu - m)\,\psi = 0. \tag{1.10}$$

In the Majorana representation of the γ^μ matrices, all elements of those matrices are imaginary and the Lorentz transformations are consequently real. If ψ were to then satisfy a reality condition $\psi = \psi^*$, it would remain real in any reference frame.

The reality condition in the Majorana representation suggests an analogous condition in other representations. In general, this condition is invariance under charge conjugation with the so-called Majorana condition taking the form $\psi = \psi^{(c)}$. In the chiral representation, charge conjugation is carried out as

$$\psi^{(c)} = C\left(\bar{\psi}\right)^{\mathrm{T}} = -i\gamma^2\psi^* \tag{1.11}$$

with the definitions

$$\begin{aligned} \bar{\psi} &= \psi^{\dagger}\gamma^{0} \\ C &= \begin{pmatrix} -i\sigma_y & 0 \\ 0 & i\sigma_y \end{pmatrix} \\ \sigma_y &= \begin{pmatrix} 0 & -i \\ i & 0 \end{pmatrix}. \end{aligned} \tag{1.12}$$

To illustrate charge conjugation in greater detail, consider two independent left handed Weyl spinors λ and ρ. A four-component spinor can be constructed with the left handed λ comprising the top two elements, and right handed $i\sigma_y\rho^*$ comprising the bottom two.

$$\psi = \begin{pmatrix} \lambda \\ i\sigma_y\rho^* \end{pmatrix}. \tag{1.13}$$

Applying charge conjugation yields

$$\psi^{(c)} = \begin{pmatrix} \rho \\ i\sigma_y\lambda^* \end{pmatrix} \tag{1.14}$$

which is of the same form as Eqn 1.13, with a left handed object on top and a right handed object on bottom. The Majorana condition is then

$$\begin{pmatrix} \lambda \\ i\sigma_y\rho^* \end{pmatrix} = \psi = \psi^{(c)} = \begin{pmatrix} \rho \\ i\sigma_y\lambda^* \end{pmatrix} \tag{1.15}$$

which requires that λ and ρ are not independent, but are instead equal, and that ψ is constructed from a single Weyl spinor as opposed to two [15]. If the neutrino satisfies the Majorana condition of Eqn 1.15 it would be referred to as a Majorana fermion, having properties distinct from those of a Dirac fermion.

A Majorana fermion can carry no charge as a consequence of its invariance under charge conjugation. Electric and magnetic dipole moments must also vanish due to the requirement of invariant interaction energy under CPT. Third, for a Majorana fermion, a Lorentz boost to a frame

in which the particle's momentum is reversed is indistinguishable from a CPT transformation which simply reverses the particle's spin [7]. In this sense, a Majorana fermion would be its own antiparticle. These conditions are summarized in Fig 1.3.

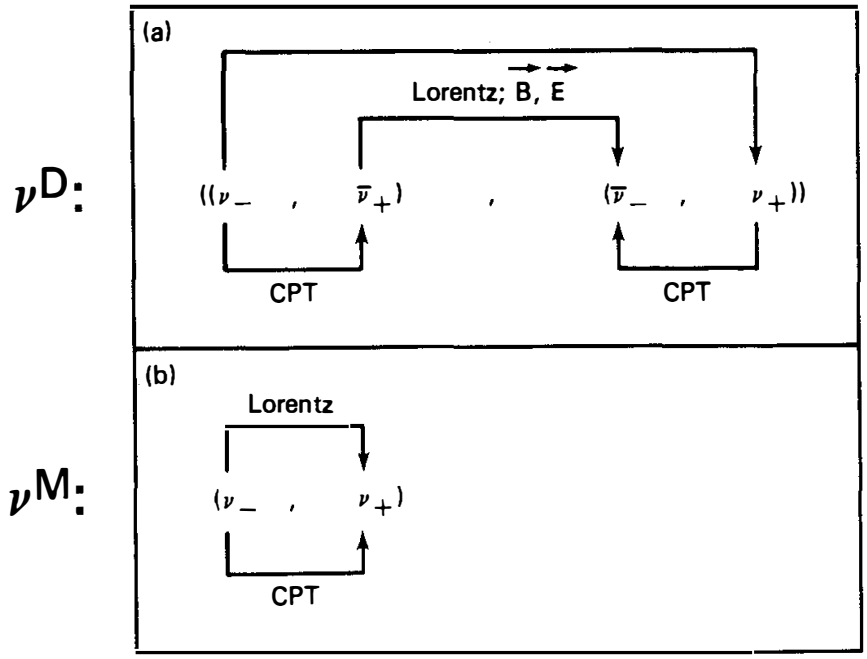

Figure 1.3: The four states of a Dirac neutrino, connected by transformations of helicity and particle-antiparticle. These four states are limited to two in the case of a Majorana neutrino. Figure from [7].

Additionally, comparing the action of Dirac and Majorana fermions, differences appear in the mass terms [15]. In the Dirac Lagrangian, the mass term appears as

$$m\left(\psi_R^\dagger \psi_L + \psi_L^\dagger \psi_R\right) \tag{1.16}$$

with left and right handed Weyl spinors ψ_L and ψ_R. In the Majorana Lagrangian, for which only one Weyl spinor is needed— say, $\lambda = \psi_L$ and $i\sigma_y\lambda^* = \psi_R$—

$$m\left((i\sigma_y\lambda^*)^\dagger\lambda + \lambda^\dagger(i\sigma_y\lambda^*)\right). \tag{1.17}$$

A Majorana neutrino would allow for a possible "see-saw" mechanism explaining the small left handed neutrino masses through effects of much heavier right handed Majorana mass terms [16].

With reference to Fig 1.3 and the preceding discussion, it is evident that as the neutrino mass approaches zero, so diminishes the possibility of exploring alternate helicity states of the particle via Lorentz transformations and electromagnetic rotations. For the Dirac neutrino, two accessible states remain: the neutrino and its antiparticle. In this limit, any observable distinction between the two remaining states of the Dirac neutrino and the two spin states of the Majorana neutrino gradually disappears.

1.5 Neutrinoless Double-Beta Decay

Due to the exceedingly small mass states of the neutrino, it is difficult in practice to distinguish between the particle's Dirac or Majorana nature. Neutrinoless double-beta decay ($0\nu\beta\beta$) presents a promising experimental avenue by which to probe this physics.

$0\nu\beta\beta$ is a second-order weak process involving the conversion of two neutrons into protons, with the emission of two electrons.

$$(Z-2, A) \rightarrow (Z, A) + 2e^{-}. \tag{1.18}$$

Though yet unobserved, such a nuclear transformation may occur among even-even nuclei within an isobar, where single β-decay is energetically forbidden. Fig 1.4 illustrates this scenario in which nuclear pairing forces lead to staggered binding energies of neighboring even-even and odd-odd nuclei.

One simple model is to assume $0\nu\beta\beta$ proceeds through light Majorana neutrino exchange, with the Feynman diagram of Fig 1.5. From this diagram, it appears that an antineutrino of predominantly positive helicity is emitted at the first leptonic vertex while a neutrino of predominantly negative helicity is absorbed at the second. For this exchange to occur, either there must be right handed weak currents or the exchanged neutrino must be in a left handed state. The amplitude for the antineutrino to be found in the left handed state of its helicity admixture is proportional to the particular mass M_m in which it was created [7, 19]. Furthermore, the amplitude depends on the coupling of each mass state to the electron neutrino flavor at the two leptonic vertices. Measurement of this process is thus sensitive to an effective neutrino mass

$$M_{\beta\beta} = \left| \sum_m U_{em}^2 M_m \right|. \tag{1.19}$$

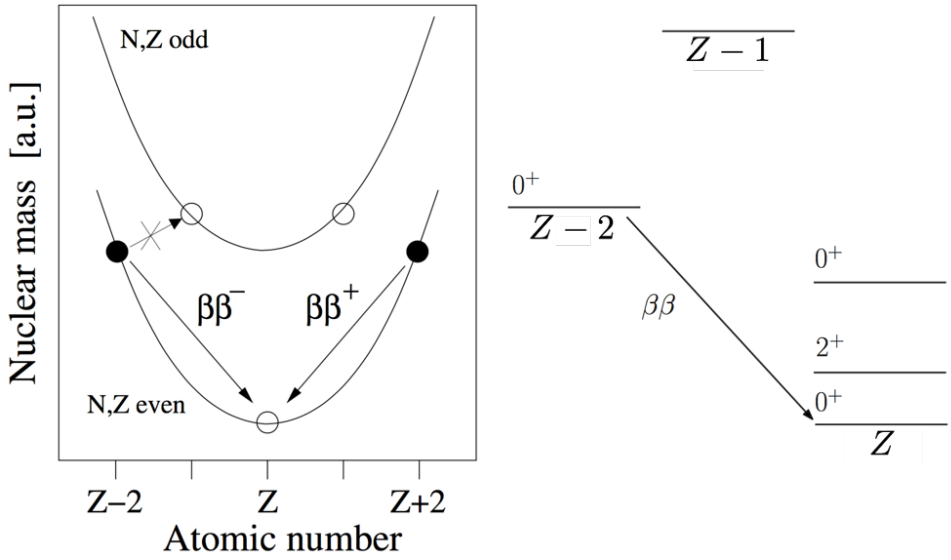

Figure 1.4: Masses of nuclei along an even-A isobar illustrate the staggering effect of $n-n$ and $p-p$ spin-pairing on binding energy. A generic level diagram is shown for cases in which double-beta decay is possible. Figures adapted from [17, 18].

With these dependencies in mind, the $0\nu\beta\beta$ half life is expressed as

$$\left(T_{1/2}^{0\nu}\right)^{-1} = G^{0\nu} \left|\mathcal{M}^{0\nu}\right|^2 M_{\beta\beta}^2. \tag{1.20}$$

The factor $G^{0\nu}$ describes the phase space for the outgoing leptons. $\mathcal{M}^{0\nu}$ is the nuclear matrix element, describing the amplitude for transition between initial and final nuclear states, and containing the weak coupling constants g_A.

As discussed, the rate of $0\nu\beta\beta$ is suppressed by the small neutrino masses and by the second-order nature of the transition. $0\nu\beta\beta$ is favored, however by the relatively large phase space for two outgoing leptons. Compared to two-neutrino double-beta decay ($2\nu\beta\beta$)

$$(Z-2, A) \rightarrow (Z, A) + 2e^- + 2\bar{\nu}_e, \tag{1.21}$$

which involves emission of four leptons, $0\nu\beta\beta$ phase space is favored by six orders of magnitude [7].

As a point of comparison, $2\nu\beta\beta$ has been observed in 11 isotopes with measured half lives between 10^{18} and 10^{21} years. Present research limits the $0\nu\beta\beta$ half life in a few isotopes of interest to no less than 10^{25} years [12, 20]. An observation of $0\nu\beta\beta$ would establish the decay rate, but

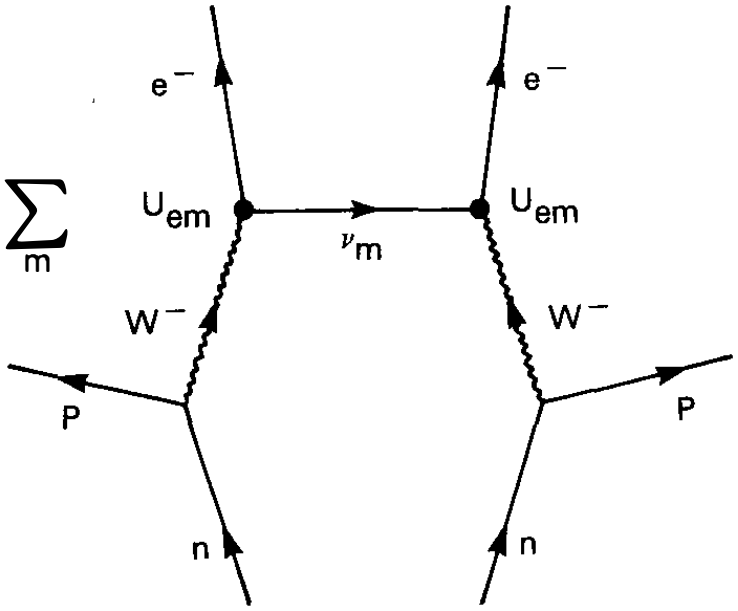

Figure 1.5: The $0\nu\beta\beta$ diagram assuming the light neutrino exchange mechanism. Figure from [7].

inference of the effective neutrino mass requires calculation of the nuclear matrix element, itself an active area of research [21]. An observation would also require further tests in order to establish the lepton number violating mechanism of $0\nu\beta\beta$.

1.6 Implications of $0\nu\beta\beta$

The observation of $0\nu\beta\beta$ would have several implications for nuclear and particle physics. Primarily, neutrinos would be established as Majorana particles differing from the other leptons [22]. Next, as evinced by Eqn 1.18, the decay would demonstrate that lepton number L is not a conserved quantity; the Standard Model does not require an underlying symmetry for the conservation of L or baryon number B. Finally, coupled with knowledge of the nuclear matrix element, the effective neutrino mass of Eqn 1.19 would provide the scale of the neutrino masses, potentially indicating the ordering of the mass states discussed in Section 1.2.

With neutrinos established as Majorana particles, pathways emerge for the origin of the small neutrino masses. Namely, the see-saw mechanism describes a scenario in which the usual Dirac mass of Eqn 1.16 exists alongside the left handed Majorana mass of Eqn 1.17 and an analogous right

handed Majorana mass. In this case the familiar light neutrino mass would be driven down by the ratio of the Dirac mass and a large right handed Majorana mass [23].

With implications for cosmology, heavy right handed neutrinos with mass of the correct order to yield the light neutrino mass could also have generated the observed matter-antimatter asymmetry. These heavy neutrinos would have decayed at a rate out of equilibrium with expansion in the early universe, accumulating a lepton-antilepton asymmetry. In a process known as baryogenesis via leptogenesis, the lepton asymmetry would then have been converted to baryon asymmetry by $B + L$-violating Standard Model effects [11, 19].

All in all, the observation of $0\nu\beta\beta$ would lend credence to a set of reasonably self-consistent theories, connecting Majorana neutrinos and their exceptionally small mass to the origin of the baryon asymmetry.

CHAPTER 2
Experimental Requirements

As discussed in Chapter 1, the $0\nu\beta\beta$ rate is suppressed by the small neutrino masses. Unless an experiment is background free, detection of the diminutive $0\nu\beta\beta$ signal requires observation of excess counts above a statistically fluctuating background. Capability of achieving this task is typically reported via metrics known as $0\nu\beta\beta$ half life sensitivity and $0\nu\beta\beta$ discovery potential. These figures of merit can be optimized through experimental design.

2.1 Sensitivity

A simple counting experiment observes the value $n = B+S$ where B is the number of background counts and S is the number of counts from the potential signal. This observed quantity is related to the mean values μ_B and μ_S of B and S via the Poisson distribution

$$p(n|\mu_B, \mu_S) = \frac{(\mu_B + \mu_S)^n}{n!} e^{-(\mu_B+\mu_S)}. \tag{2.1}$$

With the value μ_B known, a value $n_{\min}$ then represents the minimum number of counts needed to refute the hypothesis that no signal is present. At a predetermined significance level α, $n_{\min}$ is the value that solves

$$\int_0^{n_{\min}} p(n|\mu_B)\mathrm{d}n = 1 - \alpha. \tag{2.2}$$

With no signal present, $\mu_S < n_{\min} - \mu_B$ with significance α; this is an upper limit on μ_S denoted $\mathrm{UL}(\mu_S)$. When there are appreciable background statistics, such that $\mu_B \gg 5 - 10$ counts, the Poisson distribution is of Gaussian form and $\mathrm{UL}(\mu_S)$ is proportional to the standard deviation $\sqrt{\mu_B}$. This approximation is not valid when $\mu_B < 5 - 10$ counts, in which case the Poisson distribution tails deviate from Gaussian behavior. The confidence band method of Neymann, with acceptance regions built from $p(n|\mu_B, \mu_S)$ following the ordering principle of Ref [24], yields consistent frequentist

inference of confidence intervals on μ_S for known μ_B and any value of n. UL(μ_S), assuming no signal is present, determines the experiment's sensitivity to half lives below

$$S_{1/2}^{0\nu} = \ln(2)\frac{N_{\beta\beta}}{\mathrm{UL}(\mu_s)}t. \tag{2.3}$$

In this expression, $N_{\beta\beta}$ is the initial number of $0\nu\beta\beta$ nuclei in the observed target mass, and t is the observation time such that $\mu_B = bt$ for expected background rate b.

From a Bayesian perspective, the posterior probability of μ_B and μ_S is

$$p(\mu_B, \mu_S|n) = \frac{p(n|\mu_B, \mu_S)p(\mu_B)p(\mu_S)}{p(n)} \tag{2.4}$$

with marginal posterior probability of μ_S

$$p(\mu_S|n) = \int p(\mu_B, \mu_S|n)\mathrm{d}\mu_B. \tag{2.5}$$

UL(μ_S) is then the value that solves the following integral with significance α

$$\int_0^{\mathrm{UL}(\mu_S)} p(\mu_S|n)\mathrm{d}\mu_S = 1 - \alpha. \tag{2.6}$$

2.2 Discovery-Level Sensitivity

The discovery-level sensitivity denotes the μ_S for which a desired fraction $1 - \beta$ of an ensemble of experiments would refute the zero-signal null hypothesis of Eqn 2.2 [25, 26]. In this case, the required magnitude of μ_S, denoted S_{min}, is a function of the mean background μ_B, the predetermined significance α, and the aforementioned fraction $1 - \beta$. Specifically, S_{min} is the value that satisfies

$$\int_0^{n_{\mathrm{min}}} p(n|\mu_B + S_{\mathrm{min}})\mathrm{d}n = \beta, \tag{2.7}$$

where n_{min} depends on μ_B and α as discussed in Section 2.1. Fig 2.1 illustrates the calculations of Eqn 2.2 and Eqn 2.7.

To claim discovery of a phenomenon like $0\nu\beta\beta$, stringent thresholds would be set with α typically at the 5σ level and $1 - \beta$ at the 90% CL level. Calculations for n_{min} and S_{min} as a function of these

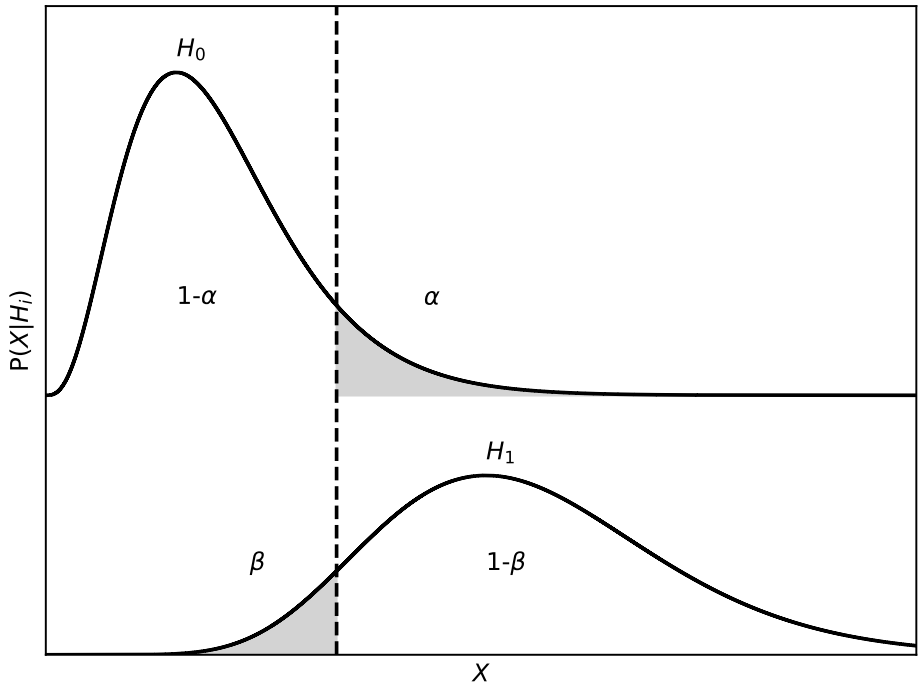

Figure 2.1: A hypothesis test for confirming H_0, or rejecting H_0 in favor of H_1, in an experiment with observable X. The decision making boundaries of the test depend on predetermined values of α and β.

parameters and μ_B are presented in Fig 2.2. With $S_{\min}$ in hand, an experiment's discovery-level sensitivity to half life is given by

$$S^{0\nu}_{1/2} = \ln(2)\frac{N_{\beta\beta}}{S_{\min}}t. \tag{2.8}$$

2.3 Improving Sensitivity

In a spectroscopic experiment where event energies are recorded, energy resolution can serve to define a region of interest (ROI) and exclude background events outside its boundaries. The background rate b is then defined as the expected number of counts collected in t per unit of energy E, and $\mu_B = bt\delta_E$ where δ_E is the energy resolution. The number of background counts is thus reduced as energy resolution improves.

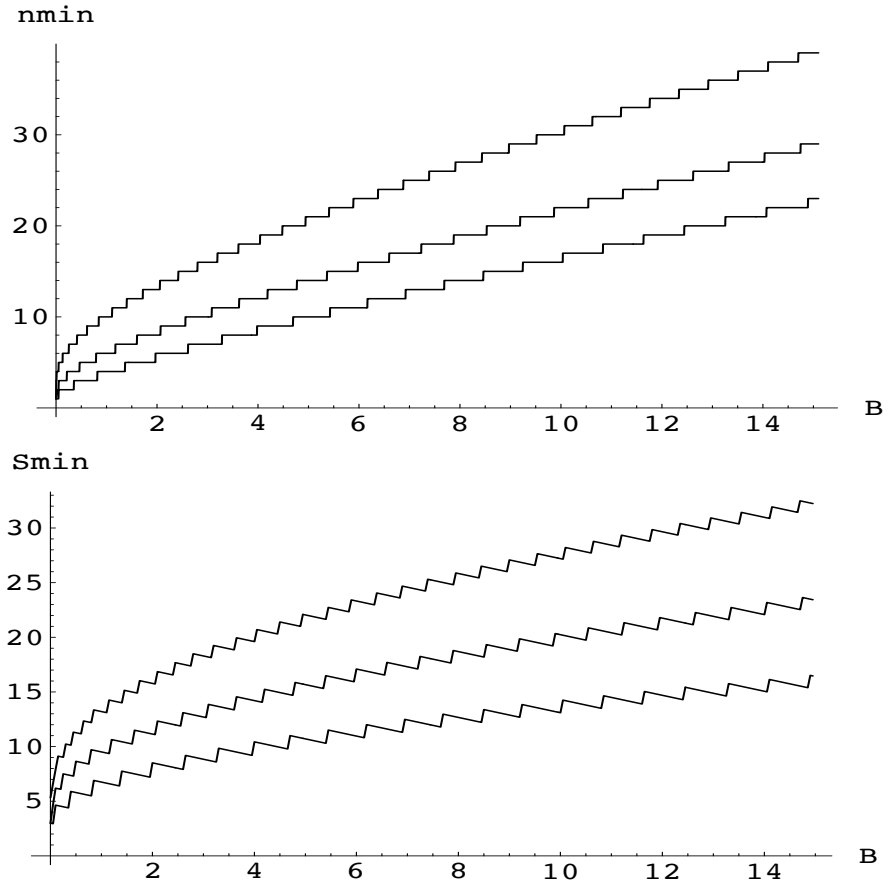

Figure 2.2: $n_{\min}$ calculated as a function of μ_B for 95%, 3σ, and 5σ significance levels of α (top). $S_{\min}$ calculated as a function of μ_B for $(1-\alpha, 1-\beta)$ pairs $(95\%, 95\%)$, $(3\sigma, 95\%)$, and $(5\sigma, 90\%)$ (bottom). Figures from [25].

In addition to reductions in μ_B via resolution, Eqn 2.3 indicates that sensitivity can be extended to longer half lives by increasing t and $N_{\beta\beta}$. While an increase in t constitutes a longer run time of the experiment, an increase in $N_{\beta\beta}$ requires an increase in the target mass M which for a pure atomic species goes as

$$M = \frac{N_{\beta\beta}}{\eta N_A} m_A, \tag{2.9}$$

where N_A is Avogadro's number, m_A is the mass per mole of $0\nu\beta\beta$ candidate atoms, and η is the fraction of atoms in M that are $0\nu\beta\beta$ candidates.

A real experiment also detects events with some efficiency ϵ such that the number of actual events B_0 is related to those detected B by $B_0 = B/\epsilon$.

With these extensions in place, b gains dependence on mass such that

$$\mu_B = bM\delta_E t, \tag{2.10}$$

and Eqn 2.3 for half life sensitivity becomes

$$S_{1/2}^{0\nu} = \ln(2)\frac{M\eta N_A}{m_A}\frac{\epsilon}{\mathrm{UL}(\mu_S)}t. \tag{2.11}$$

As discussed in Section 2.1, $\mathrm{UL}(\mu_S)$ depends on μ_B, and in the regime of high background statistics, Eqn 2.11 becomes

$$\begin{aligned} S_{1/2}^{0\nu} &> \ln(2)\frac{M\eta N_A}{m_A}\frac{\epsilon}{n_\sigma\sqrt{bM\delta_E t}}t \\ &= \ln(2)\frac{\eta N_A}{m_A}\frac{\epsilon}{n_\sigma}\sqrt{\frac{Mt}{b\delta_E}}, \end{aligned} \tag{2.12}$$

where n_σ is a multiple relating the Poisson standard deviation to the desired significance level.

2.4 Reducing Backgrounds

For the sensitivity to scale linearly with exposure, the background rate must be low such that $\mu_B = bM\delta_E t \ll 1$. This requires avoidance or removal of several background sources that have been well-documented by the community of rare event experiments [27, 28].

2.4.1 Cosmic Rays and Neutrons

A detector operated at sea level will record high rates of interactions from cosmic ray secondaries like muons and nucleons. Cosmic ray particles intersect the atmosphere with an approximate flux of 1000 m^{-2} s^{-1}. These hadronic particles interact with the atmosphere producing showers of secondary particles, most of which are absorbed before reaching the surface. At the surface, the remaining shower is comprised mostly of neutrons and muons, with approximate fluxes of 64 and 190 m^{-2} s^{-1}, respectively [27]. By moving detector operation below ground, the nucleonic component can be removed by absorption in the first few tens of meters water equivalent (m.w.e.) shielding from earth's surface. Greater depth is needed to appreciably reduce the muon flux, culling the lowest energy muons.

At depth, the remaining muons contribute to the background rate via direct interaction with the detector or via production of tertiary neutrons which themselves interact in the detector. Operation of an active veto system to detect passing muons and reject coincident data avoids the background contributions of these muons and tertiary neutrons. The veto time should be long enough to capture tertiary particles caused by the muon spallation, including radioactive isotopes, photons, and neutrons. Most tertiary neutrons produced outside of the detector apparatus can be removed by shielding such as borated polyethylene; polyethylene is comprised of low-Z isotopes that thermalize neutrons via efficient energy transfer in inelastic scattering, and the boron dopant provides a high neutron absorption cross section.

At a few hundreds of m.w.e. the expected rate of cosmic ray muons and tertiary neutron events is superseded by neutrons from natural fission and (α, n) reactions. The rates of these processes are independent of depth due to their origin in radioimpurities within the rock walls of the underground experimental cavern. These neutrons can likewise be removed by polyethylene shielding.

2.4.2 Radioimpurities in the Detector and Shielding

Radioimpurities in detector and shielding materials also contribute to the background rate independent of depth. These impurities are introduced in detector and shielding materials through natural concentrations of long-lived radionuclides in ore and raw material, and via cosmic ray spallation. Of particular concern are the decay chains of the primordial radioisotopes ^{40}K, ^{232}Th,

and ^{238}U whose half lives exceed 10^9 yr. Of additional concern are any long lived cosmogenically induced isotopes, like ^{68}Ge or ^{60}Co with 270.93 and 1925.28 dy half lives. Radiation from the decay of these isotopes and their progeny can deposit energy at the $0\nu\beta\beta$ Q-value. Despite their long half lives, these radioimpurities constitute a large potential background in $0\nu\beta\beta$ experiments since their decays appear short lived relative to experimental sensitivities beyond 10^{25} yr.

If the decays of radioimpurities take place far from the detector, their contribution to the background rate can be reduced with shielding. γ radiation is best absorbed with high-Z materials like Pb, which provide large cross sections for scattering and absorption. α's and β's are not very penetrating and will be stopped by a thin layer of material.

Decays in close proximity to the detector, within the inner layers of shielding, bring up special considerations. α's and β's at or within the detector can deposit energy, and γ's of sufficient energy— including bremsstrahlung from β's— can reach the detector from a range of distances. Active veto techniques can be applied to backgrounds in or near the detector, at the expense of complexity in design or analysis.

Backgrounds near the detector can also be reduced by controlling materials production and selection. The concentration of primordial impurities in raw materials can be reduced through techniques like zone refining and electroforming, and materials screening can be required so that only the most radiopure materials are used. ^{40}K, ^{232}Th, and ^{238}U exist in typical concentrations of 850, 44, and 36 Bq kg^{-1} in the earth's upper crust [27]. Concentrations in particular raw materials vary by orders of magnitude depending on chemical composition of ore and the material's chemical and geological histories. The sensitivity goals of $0\nu\beta\beta$ experiments typically require concentrations at or below the μBq kg^{-1} level.

Concentrations of long-lived radioimpurities are also produced by interactions with the hadronic component of cosmic ray events of Section 2.4.1. Cosmogenic activation can be reduced by limiting above-ground exposure of parts and materials. The activation rate is dependent on both material and flux of incident particles, and thus can be reduced by selecting materials with low interaction cross sections or by storing materials at depth. Activity that has already been accrued can be mitigated by allowing time for those isotopes to decay prior to operation of an experiment.

2.4.3 Anthropogenic Contamination and Radon

Anthropogenically introduced radioimpurities become a concern for parts closest to the detector. Contaminants can be introduced on the surfaces of parts via machining and handling, or via diffusion and plate out of radionuclides. Complicated parts production involving many reagents affords many opportunities for contamination [27].

Contamination can also arise from exposure of parts to air by which airborne radionuclides can deposit on surfaces. The isotopes ^{220}Rn and ^{222}Rn, present in the ^{232}Th and ^{238}U chains, are of particular concern with their daughters typically being positively charged and able to plate out on surfaces. Rn in the bulk of materials can also appear at parts surfaces via diffusion. The mobility of Rn can lead to disequilibrium within the ^{232}Th and ^{238}U chains and localized concentrations of long-lived Rn daughters. In particular the decay of ^{222}Rn feeds ^{210}Pb of 22 yr half life [27, 28, 23].

With typical levels of 40 Bq m^{-3} for airborne ^{222}Rn in underground laboratory settings, low background experiments operate in cleanroom environments with controlled air flow and avoid exposure of parts to laboratory air when possible [28]. Furthermore, a volume surrounding the detector is typically purged with a slight over-pressure of evaporated nitrogen to reduce the concentration of airborne impurities. Prior to installation of detectors in a purge enclosure, surface contamination can be mitigated by simplifying parts production procedures, implementing cleaning procedures like acid leaching, and by minimizing handling. Reducing the surface area of components via design, or by polishing, can also minimize risks of plate-out [27].

2.4.4 Energy Resolution

As detailed in Section 2.3, energy resolution acts to distinguish the ROI from neighboring regions of the energy spectrum that may be populated by background counts. The power of resolution is nicely illustrated in the case of the background posed to $0\nu\beta\beta$ by $2\nu\beta\beta$.

As an alternate decay mode of the target nuclei, $2\nu\beta\beta$ poses an irreducible background for $0\nu\beta\beta$ experiments. The endpoint of the $2\nu\beta\beta$ continuum abuts the $0\nu\beta\beta$ ROI at the double-beta decay Q-value ($Q_{\beta\beta}$). Though the $2\nu\beta\beta$ decays cannot be avoided, their contribution to the ROI can be reduced by improving resolution. The signal to background ratio of $0\nu\beta\beta$ to $2\nu\beta\beta$ in the ROI is

approximately

$$\frac{S}{B} \approx \left(\frac{Q_{\beta\beta}}{\delta_E}\right)^6 \frac{T^{2\nu}_{1/2}}{T^{0\nu}_{1/2}}, \tag{2.13}$$

with overlap in the case of 5% energy resolution shown in Fig 2.3 [23].

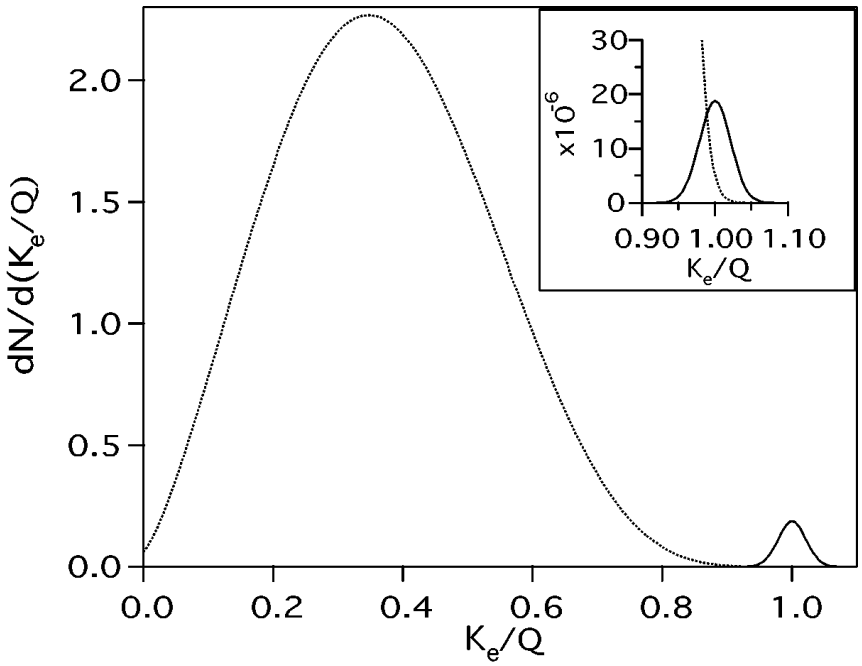

Figure 2.3: An illustration of overlap between the $2\nu\beta\beta$ continuum and $0\nu\beta\beta$ peak at $Q_{\beta\beta}$ for an experiment with 5% energy resolution. Figure from [23].

Aside from narrowing an experiment's region of interest, resolution aids in identifying the backgrounds that are present. Poor resolution acts to smear spectral features across a range of energies such that they become indistinguishable from a continuum background [29]. Conversely, good resolution preserves idiosyncratic features of individual background sources and helps to break any degeneracy in their spectral shapes.

2.4.5 Target Isotope and Quantity

An experiment's choice of target isotope will affect Eqn 2.13 via $Q_{\beta\beta}$ and the $\beta\beta$ half lives. The choice of isotope also affects δ_E if a source-equals-detector approach is taken, as is often done for its advantages in detection efficiency. The chosen isotope's $Q_{\beta\beta}$ will also determine where the $0\nu\beta\beta$

region of interest lies with respect to background sources. A large $Q_{\beta\beta}$ is generally desirable in order to set the region of interest above the transition energies of most natural radioactive isotopes.

In a source-equals-detector approach, increasing the detector mass will improve the signal-to-noise ratio of $0\nu\beta\beta$ to backgrounds originating outside the detector. Increasing detector mass would be useful, for instance, in experiments for which the irreducible rate of neutrino-electron elastic scattering in the detector represents a significant portion of the background budget [30].

CHAPTER 3
The Majorana Demonstrator

The Majorana Demonstrator (MJD) is a research and development project searching for the $0\nu\beta\beta$ of ^{76}Ge. The experiment takes a calorimetric approach to $0\nu\beta\beta$ measurement, employing a collection of Ge diode detectors within which a certain percentage of nuclei are of the $0\nu\beta\beta$ candidate isotope ^{76}Ge (source = detector). In accordance with the high-sensitivity requirements of rare event searches, the Demonstrator leverages the superior energy resolution of its detectors along with numerous techniques for background mitigatation and rejection. The experiment is currently operating on the 4850' level of the Sanford Underground Research Facility in Lead, SD.

In fielding a $0\nu\beta\beta$ search, the stated goals of the Majorana Demonstrator are as follows [31].

1. Achieve a background level of < 2 c/(FWHM tonne yr) in the 2.5 keV FWHM (full-width half-maximum) surrounding the 2039 keV Q-value for ^{76}Ge $0\nu\beta\beta$.

2. Demonstrate feasibility of scaling the technology to a tonne-scale experiment.

3. Perform searches for physics beyond the Standard Model.

The first item above was based on the sensitivity requirements of a tonne-scale $0\nu\beta\beta$ experiment. A background level < 2 c/(FWHM tonne yr) would scale to < 1 c/(FWHM tonne yr) in a tonne-scale experiment with sensitivity to a $0\nu\beta\beta$ half life greater than 10^{27} yr as well as an effective Majorana mass of the electron neutrino indicative of an inverted hierarchy scenario.

In addition to sufficient reduction of backgrounds, the second item requires scalability of techniques employed by the Demonstrator. The calorimetric approach of the experiment provides an advantage in this aspect, since detection efficiency for any double-beta decay events is high and does not diminish with increased numbers of detectors or reasonable increases in size of detectors. Along these lines, the Demonstrator employs compact arrays of many detectors in a modular design that can be feasibly repeated in a scaled-up scenario.

The last item notes that, in addition to $0\nu\beta\beta$, the high-resolution, low-noise Ge detectors deployed in such a low-background environment allow for other physics campaigns sensitive to processes not described by the Standard Model. These include studies of light WIMP dark matter electric couplings, solar axion electric couplings, Pauli exclusion violating electronic transitions, unbound fractionally charged particles, and trinucleon decays of Ge isotopes [32, 33, 34].

3.1 Overview of Experimental Design

3.1.1 Modules

The Majorana Demonstrator is comprised of 58 P-type point contact high-purity Ge detectors. Of these detectors, 34 are enriched to 88% in ^{76}Ge and total 29.7 kg in mass, and 24 are of natural Ge (7.8% ^{76}Ge) totaling to 14.4 kg. The Ge crystals are each assembled into a detector unit equipped with front-end electronics, and up to five detector units are stacked atop one another in a formation known as a string. Up to seven strings are then placed together in a cryostat forming a compact array of detectors. A cross section of this general configuration is displayed in Fig. 3.1.

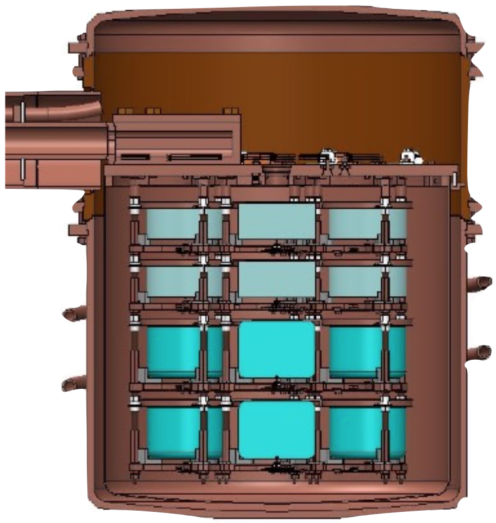

Figure 3.1: A cross sectional rendering of one MJD cryostat containing an array of detectors (teal and grayish-teal). The detectors are stacked vertically into strings prior to installation in a cryostat. Enriched detectors occupy the bottom two rows of each string in this rendering, with natural detectors occupying the top two rows.

The sealed cryostat is evacuated to pressures below 10^{-6} Torr, and detectors are cooled to liquid nitrogen (LN) temperatures and biased to several kilovolts. The supporting systems necessary to maintain these operating conditions are accessed via the crossarm tube seen extending horizontally from the side of the cryostat in Fig. 3.2. The crossarm tube connects the cryostat volume to a

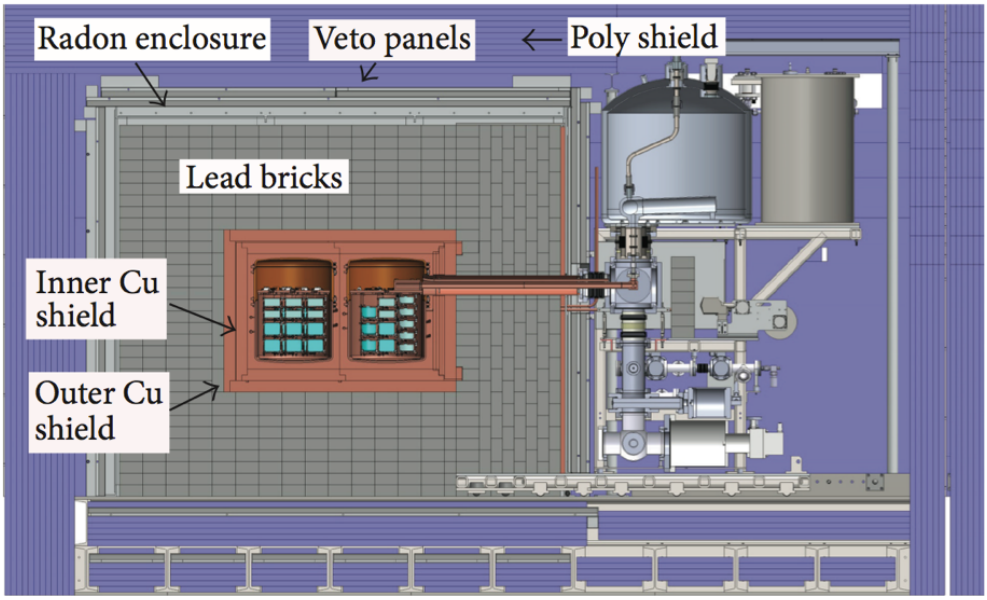

Figure 3.2: A cross sectional rendering of the MAJORANA DEMONSTRATOR. The two cryostats connect via crossarm tubes to their respective vacuum equipment, cryogenics, and electronics. Layers of passive and active shielding surround the cryostats.

multi-stage vacuum system, and a thermosyphon which passes through the tube thermally couples the detectors to a LN reservoir. Electrical connections to the detectors and front-end electronics are also fed through the crossarm tube and connect to the requisite HV and data acquisition equipment.

A cryostat and its supporting systems are collectively referred to as a module and two such modules are deployed in the DEMONSTRATOR. The two independent modules are inserted together within a layered system of passive and active shielding, and the entire setup is operated in a cleanroom maintained at hundreds of 0.5 μm particles per ft^3.

3.1.2 Shielding

Shielding is intended to attenuate and absorb radiation from external sources, reducing the number of undesired events incident upon the detectors. The layers of shielding, visible in Fig. 3.2,

include a 5 cm thick inner Cu shield made of underground electroformed Cu (UGEFCu), a 5 cm thick outer Cu shield made of commercial oxygen-free high thermal conductivity (OFHC) Cu, a 45 cm thick layer of stacked high-purity Pb bricks, a surrounding LN-purged enclosure to exclude Rn, two layers of plastic scintillators forming a 4π active muon veto system, and 30 cm of polyethylene, the inner 5 cm of which are borated high density polyethylene. As previously mentioned, the experiment is operated in a clean room with 1477 m of rock overburden providing approximately 4260 m.w.e. shielding [35].

Additional components of note include an infrared (IR) shield placed within the cryostat, but around the detectors, to absorb IR shine from the cryostat and reduce the amount of IR-induced leakage current through the detectors. Also of note, the p-type Ge crystals themselves are manufactured such that their n-type outer surfaces provide an approximately 1 mm dead layer. This layer absorbs low-energy radiation as well as α's and β's from contaminants in nearby components or detector surfaces.

3.1.3 Data Acquisition

Pulses from MJD detectors are readout by front-end electronics stationed immediately beneath the point contact electrode of each detector. Following the front-end electronics, signals are driven along 2 m of cable to preamplifiers assigned to each detector. This first stage of amplification acts as a resistive feedback (RC) circuit leading to pulse shapes that rise quickly from the baseline and then return exponentially. In a second stage of amplification, signals are split into high- and low-gain channels which are individually digitized.

Digitization is performed by GRETINA digitizer boards which trigger when an on-board trapezoidal filter exceeds a given threshold [36]. The digitizer operates at 100MHz and records triggered pulses as a time series of 2020 samples (10 ns/sample). This 20 μs trace length is able to store several microseconds of baseline, a typical ~ 1 μs rising edge, and several microseconds of the falling edge of a pulse. An optional pre-summing mode allows for an extended trace length by downsampling certain portions of a pulse.

The digitizer is VME-based and digitizer records are readout using a VME-based dedicated computer. This data is in turn readout by a Macintosh computer running the Object-oriented Real-time Control and Acquisition application (ORCA) [37]. Veto data is also readout by ORCA

via VME-based CAEN digitizers. Data files are then copied and passed through various phases of processing in preparation for analysis.

3.1.4 Calibration

To validate livetime of detector channels and measure gain and resolution stability, a calibration system is implemented for each module [38]. The calibration systems each consist of a ^{228}Th line source that is stored outside the shield and is automatically fed along a track through the shield toward its associated cryostat. The track wraps in a helix about the cryostat and thus the calibration source subtends an appreciable solid angle with respect to the detector array. Calibration runs of 1 hr duration are regularly taken to ensure stable detector performance.

To determine the trigger efficiency, gain stability, and livetime of each detector, detectors are pulsed via their front ends periodically. A 16-bit DAC is dedicated to each detector and a square pulse is generated once every eight seconds.

3.1.5 Ge PPC Detectors

MAJORANA employs p-type point contact (PPC) high-purity Ge (HPGe) detectors in its two modules. These detectors are similar in shape to coaxial Ge detectors except that the long central contact is replaced by a shallow point contact [39]. As pictured in Fig. 3.3, the detectors are p-type Ge in their bulk with a small p+ electrode at one end. The lithiated outer surface of the detectors forms the opposing n+ electrode and is held at positive voltage (typically 3-5 kV) when operating the detectors under reverse bias. A passivated region acts as an electrical insulator separating the cathode and anode regions.

The operating principle of these detectors is similar to other semiconductor drift detectors. Under reverse bias, free charge carriers are removed from a central depleted region. Incident radiation of sufficient energy to ionize charges in this region creates electron-hole pairs which are drifted under the applied electric field toward their respective electrodes; incident radiation of approximately 3 eV is required to promote an electron from the valence to conduction band in Ge. As charges move through the detector's electric potential, a current is induced at the electrodes and an electrical pulse can be recorded and studied [40]. Energy resolution of these detectors then depends on a

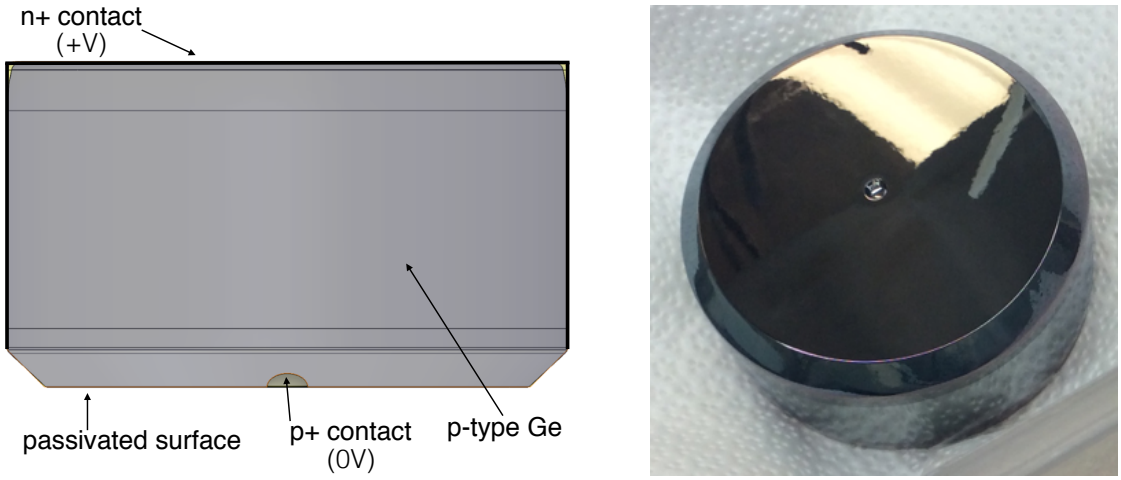

Figure 3.3: A cartoon cross section of a PPC detector shown alongside a photograph of such a detector. Note that the p+ contact— labeled in the cartoon— is shown facing out of the page in the photograph. HPGe detectors of PPC design offer many advantages to a $0\nu\beta\beta$ experiment.

pulse's accurate reconstruction of the incident energy. In addition to deposited energy, pulse shape can also be leveraged to deduce position and timing information for a given event.

The use of HPGe PPC technology offers several advantages in performing a $0\nu\beta\beta$ search. First, HPGe detectors have excellent energy resolution which allows for discrimination between species of events that deposit similar energies. Next, the simple PPC design enables manufacturing of large volume crystals offering improved detection efficiencies. As compared to a segmented detector, the simple design also reduces needed connections which constitute potential background sources. Additionally, the point contact configuration creates an unequal weighting potential at the p+ versus n+ contacts and the resulting electric fields provide drift times and paths that depend highly on an event's location within the detector. The detailed information of drift path and timing is encoded in pulse shapes. Event topologies can then be identified using pulse shape analysis (PSA) techniques. Lastly, the PPC design is of low capacitance yielding low-noise performance and low-energy thresholds during analysis.

3.1.6 Materials and Assembly

Given the stringent sensitivity requirements needed to observe double-beta decay, any materials used for the assembly of detector arrays, cryostats, and inner shielding must be low-background in nature. Concerning the cryostats and detector arrays, this requirement for radiopure materials has

led most notably to the use of UGEFCu for structural and conducting components, polytetrafluoroethylene (PTFE) for electrically and thermally insulating components, and Vespel for structural and electrically insulating components. Cleanliness is also considered and measured for assembly materials with lesser potential impact on detectors.

These cleanliness concerns motivated an extensive assay program through which potential materials have been vetted. Activities for prospective materials have been determined, in some cases, to sub-μBq levels and impurities to sub-parts per trillion with techniques including γ-ray counting, neutron activation analysis (NAA), and inductively coupled plasma mass spectrometry (ICPMS) [41, 42]. Along with the assay program, MJD has developed materials cleaning procedures and a parts tracking database in which the histories of thousands of custom parts can be monitored [43].

Parts were sourced from low-background stock, underwent cleaning processes, and passed quality assurance checks, before being used for assembly of the experiment. In particular, detector arrays were assembled from such parts with the work taking place in glove boxes purged with LN boil-off to limit Rn exposure. Fig. 3.4 provides an image of the first step in this process in which a Ge crystal is placed in a detector mount. A low-mass front end (LMFE) pictured in Fig 3.5 is affixed to the bottom of the detector unit, contacting the p+ electrode and providing cabling to connect the detector unit to its amplification and an external pulser. Multiple completed detector units are then stacked into a string as shown in Fig. 3.6.

3.2 Backgrounds

Several classes of background are expected in the MAJORANA DEMONSTRATOR given the experimental design, including choice of $\beta\beta$-decay isotope, primary assembly materials, and underground location. Building from the discussion of Section 2.4, a selection of additional detail relevant to MAJORANA is included here.

As described in Section 3.1.2, Pb is a primary shielding material in MAJORANA. In addition to typical concentrations of the naturally occurring long-lived radionuclides, Pb bricks can contain an elevated concentration of ^{210}Pb. The ^{210}Pb concentration exceeds that expected of the ^{238}U decay chain due to the Pb manufacturing process which chemically purifies Pb, but does not isotopically remove ^{210}Pb.

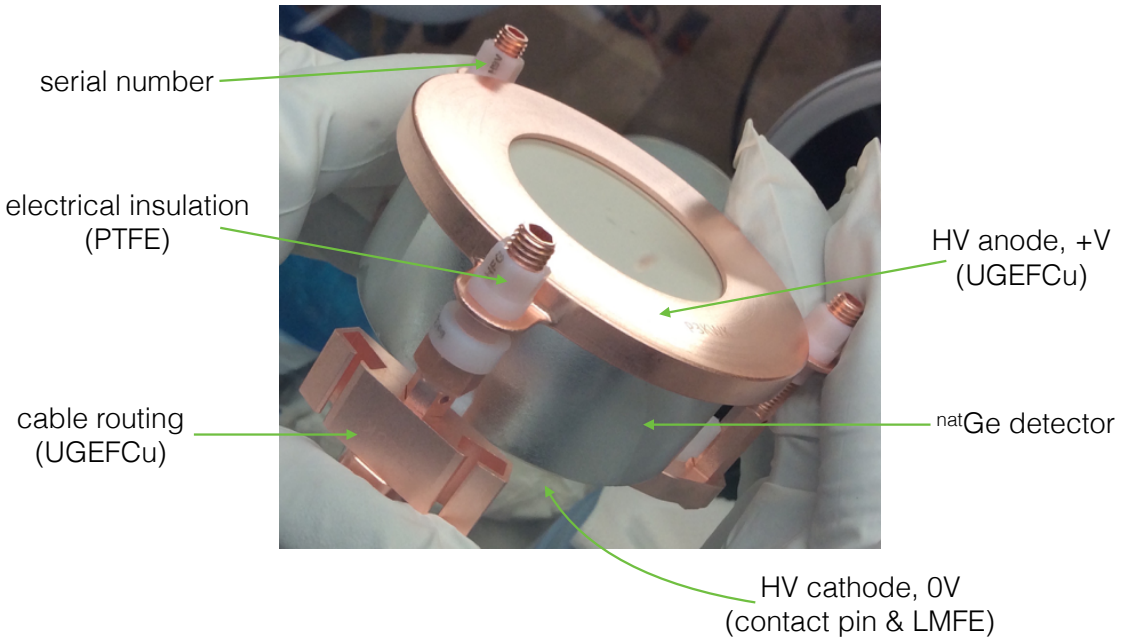

Figure 3.4: A Ge crystal placed in a detector mount. As labeled in the image, the mount includes UGEFCu structural and electrical components as well as insulating components made of PTFE.

The $2\nu\beta\beta$ of ^{76}Ge is an additional source of background discussed in Section 2.4.4. The summed energies of the electrons emitted in $2\nu\beta\beta$ fall along a spectrum ending at $Q_{\beta\beta}$ and subsequently contribute events in the ROI. The relative ROI contribution of $2\nu\beta\beta$ will, however, be small since the $2\nu\beta\beta$ endpoint is of little strength and the detector resolution is narrow. The signal-to-background ratio of counts due to $0\nu\beta\beta$ and $2\nu\beta\beta$ is approximated by Eqn 2.13. Considering the case of MAJORANA, with $\delta_E = 2.53$ keV, $Q = 2039$ keV, $T^{2\nu}_{1/2} \approx 10^{21}$ yr, and assuming $T^{0\nu}_{1/2} \approx 10^{28}$ yr, this ratio is on the order of 10^{10}, indicating that $2\nu\beta\beta$ contributes negligible background within the ROI.

Cosmogenically produced radioisotopes were introduced in Section 2.4.2. ^{68}Ge, for instance, is produced in Ge through reactions, like ^{70}Ge(n,3n)^{68}Ge, which take place while HPGe detectors are manufactured in and shipped between surface facilities. The isotopes ^{57}Co, ^{54}Mn, ^{65}Zn, ^{60}Co, ^{55}Fe, and ^{3}H, are also produced in Ge [44, 45, 46]. For $^{\text{enr}}$Ge the concentration of these impurities is reduced by limiting cosmogenic exposure, and the concentrations of non-Ge impurities are reduced by zone refining. The manufacturing and storage of $^{\text{nat}}$Ge detectors was not as tightly constrained [47]. In any case, all detectors were brought underground ahead of data taking to allow for the decay of cosmogenic impurities.

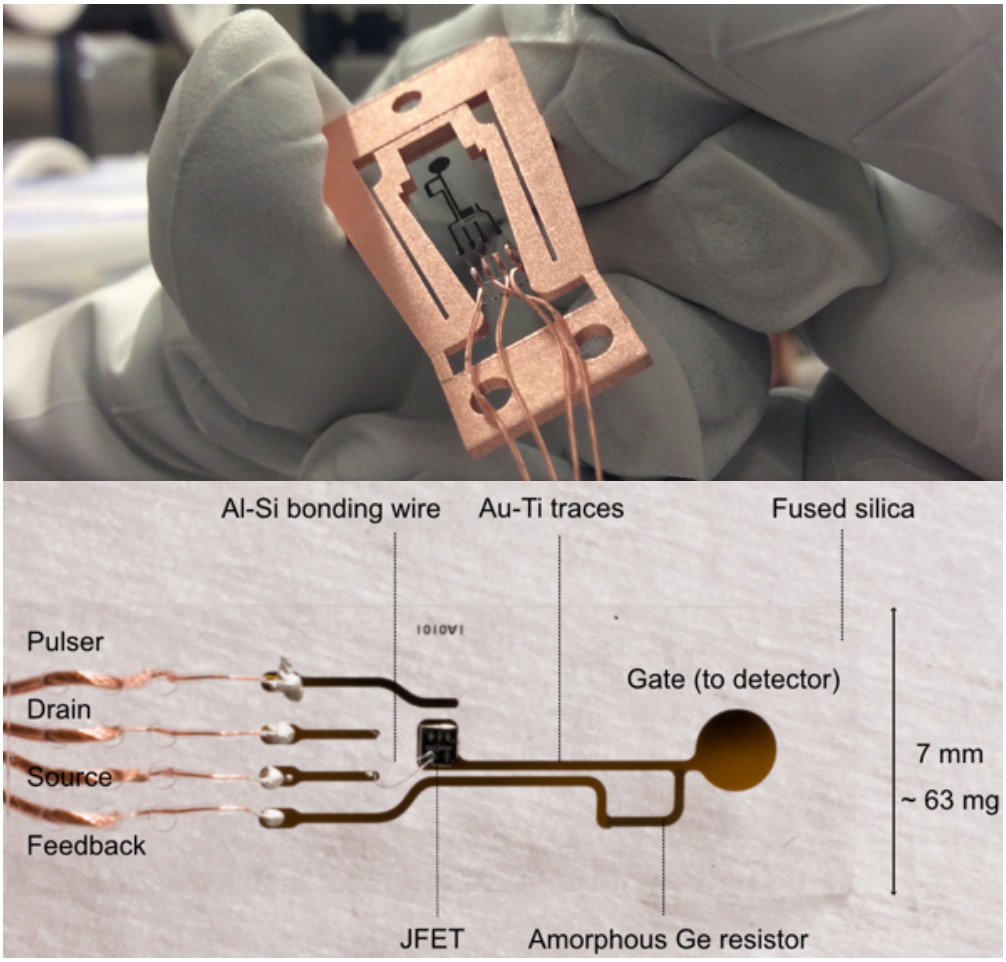

Figure 3.5: A low-mass front end electronic board for connection to the point contact of a detector. A field-effect transistor is the central component responding to induced current from drifting charges in the detector, or from an external pulser line placed nearby.

In addition to cosmogenic production in the detectors, ^{60}Co is produced in Cu [48, 49]. Most UGEFCu parts remained underground at all times, but certain small parts were brought above ground for a brief parylene coating procedure. The UGEFCu spring clips depicted previously in Fig 3.5 also spent time above ground due to occasional LMFE repair work. Finally, UGEFCu elements of the cryostat vessel and thermosyphon were brought above ground for welding. OFHC Cu was procured commercially and consequently accrued greater cosmogenic exposure.

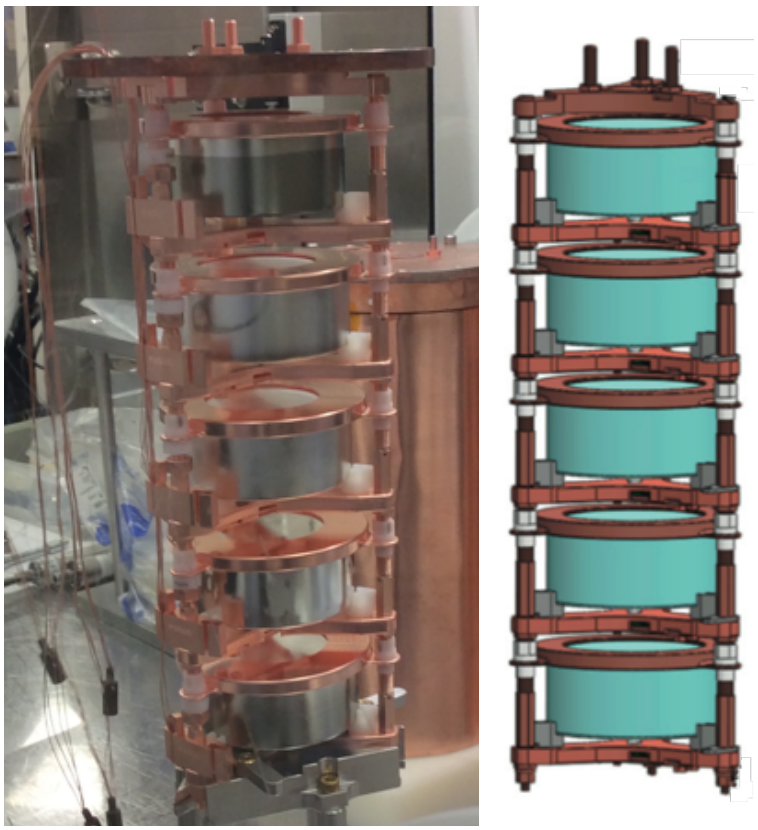

Figure 3.6: A string of natural germanium detectors shown beside a rendering of the assembly. Signal cables extending from each detector's LMFE can be seen hanging on the left side of the image.

3.3 Background Signatures

The ultimate concern with backgrounds in MAJORANA is their effect on the observed energy spectrum. Particularly troubling backgrounds are those with potential to contribute to the count rate within the ROI, or to obscure information needed to reject counts in the ROI.

There are numerous physical processes and event topologies through which backgrounds can deposit energy, but we mention just a few here which leave notable signatures in the measured energy spectrum. These are continua from beta decay, continua from Compton scattering of γ-rays, and characteristic peaks from absorption of monoenergetic events. Events are also observed from α particles incident on the passivated surfaces of detectors. Full energy is not collected from such surface events and hence the characteristic α energies appear along a continuum in the spectrum. It is also common for coincident events to sum in energy and appear at higher energies in the spectrum than would be deposited by the events individually.

Observed β's are likely to originate from more central locations in the experiment. The mean free path of electrons and positrons is on the order of mm in the Ge and shielding, so any registered β events likely originate close to or within a detector. These energy depositions take on a range of values according to familiar β-decay spectral shapes. Distant β's can, however, lead to energy depositions across a range of energies via bremsstrahlung: decelerated electrons undergo electromagnetic radiative losses as they traverse the shielding. This energy loss is greatest for high energy electrons in high-Z materials and thus β-emitters in the Pb shielding are a concern.

Compton scattering is an electromagnetic process dominant for γ-rays between 1 and 5 MeV. Photons scatter from electrons, imparting energy to the electrons as a function of the scattering angle. Scattered photons can then be of a continuum of lesser energies, and the electrons of a continuum of increased energies. If close to or within the detector, scattered electrons go on to deposit energy along the Compton continuum according to

$$E_e = h\nu - h\nu' = h\nu \left(\frac{(h\nu/m_e c^2)(1-\cos\theta)}{1+(h\nu/m_e c^2)(1-\cos\theta)} \right) \tag{3.1}$$

where θ is the angle between the incoming direction of the photon and the outgoing direction of the photon. Note the $\theta = \pi$ condition for maximum imparted electron energy. This maximum energy for the Compton continuum, due to an original photon energy $h\nu$, is known as the Compton edge and occurs at an energy $E_C = h\nu - E_e|_{\theta=\pi}$ less than the original photon energy. Scattered photons, also referred to as down-scattered, may go on to additional scatterings or to be photoelectrically absorbed once they are of sufficiently low energy ($h\nu \lesssim 1$ MeV).

Monoenergetic energy depositions occur when the entire energy of incident radiation is absorbed. A peak will form if the value of energy deposited is characteristic of some physical process of sufficient activity to rise above background. For instance, repeated instances of a characteristic low energy X-ray could undergo photoelectric absorption and form a peak at lower energies in the spectrum. Higher energy γ-rays could also have their full characteristic energy absorbed if the detector is of large enough volume to contain all scatterings and the final low-energy absorption.

At still higher energies ($h\nu > 2m_e c^2$), pair production is common for γ-rays and characteristic peaks can once more form. Following absorption of the electron and recombination of the positron, one, both, or neither of the annihilation photons could be absorbed within the detector. For a

given incident γ energy, these three cases lead to characteristic peaks in the spectrum known as the single-escape peak (SEP), the full-energy peak (FEP), and the double-escape peak (DEP) illustrated in Fig 3.7.

Fig. 3.7 also illustrates event topologies for Compton scattering, photoelectric absorption, and pair production in an intermediate sized detector. Complexity is added to the spectrum if the material surrounding a detector is considered, as shown in Fig. 3.8. In this case, backscattered events deposit a fraction of their initial energy in the detector, and a host of other physical interactions deposit both diffuse and characteristic energies.

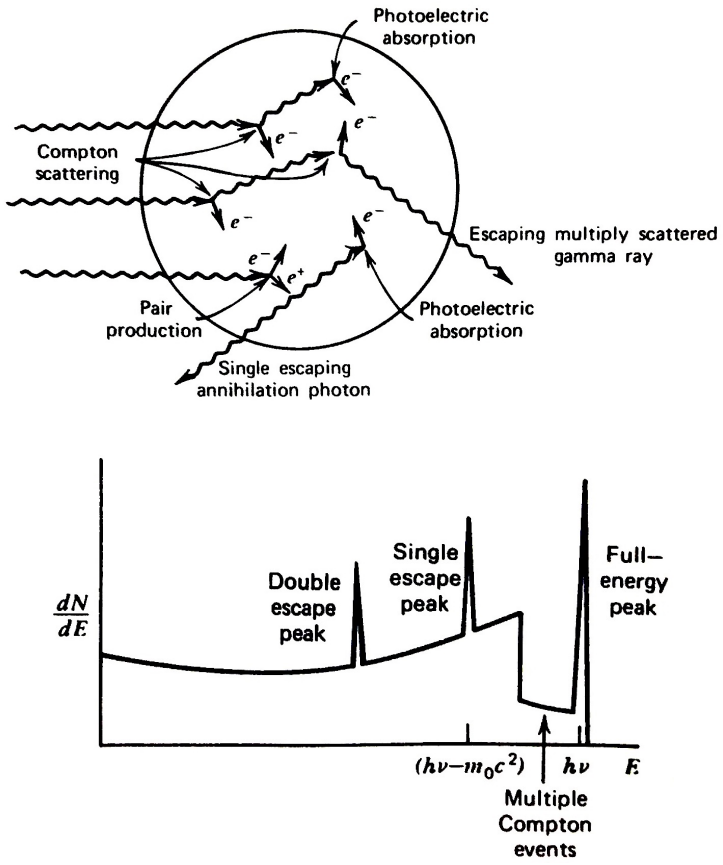

Figure 3.7: Event topologies of typical gamma ray interactions with a detector of intermediate volume. Figures are from [50].

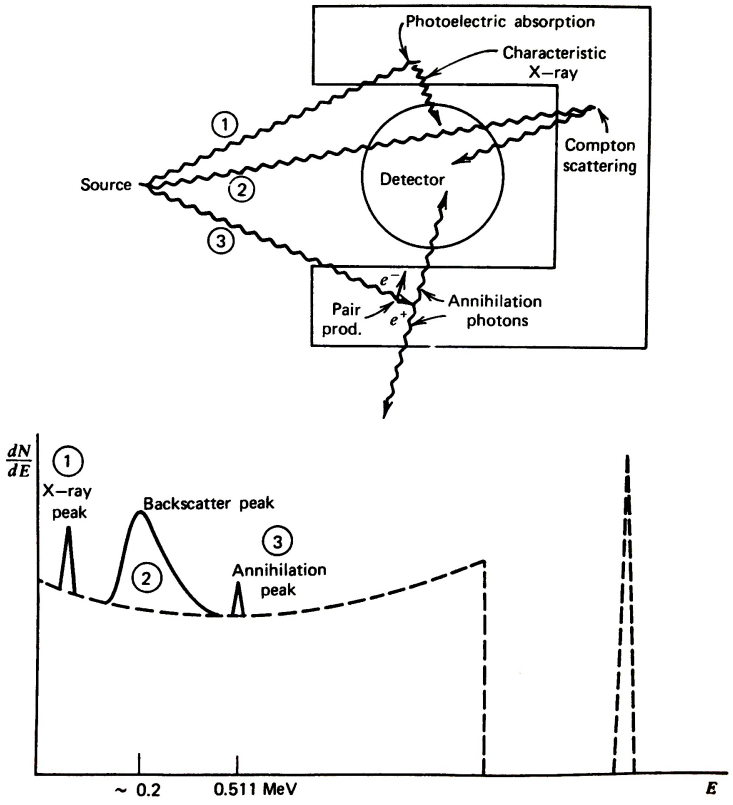

Figure 3.8: Event topologies of typical gamma ray interactions considering the effects of materials surrounding a detector. Figures are from [50].

As the backscatter peak is a notable feature in the observed MJD spectrum, it is worth noting its origin. Analogous to Eq. 3.1, we can express the Compton scattered photon's energy as

$$E_\gamma = h\nu' = \frac{h\nu}{1 + (h\nu/m_e c^2)(1 - \cos\theta)}. \tag{3.2}$$

At large angles,

$$h\nu'|_{\theta=\pi} = \frac{h\nu}{1 + (2h\nu/m_e c^2)} \tag{3.3}$$

which reduces to $m_e c^2/2 \approx 0.25 MeV$, in the limit $h\nu \gg m_e c^2/2$.

3.4 Event Discrimination

Given the short path length of electrons in Ge, the energy of a $0\nu\beta\beta$ decay would be contained within ~ 1 mm^3 and would appear as a single site event (SSE) in a detector. Multisite events (MSE) and events coincident between detectors are thus labeled as background and rejected from data. Along these same lines, detector coincidences and muon veto periods are rejected from data. Furthermore, α events and other recorded hits with pulse shapes dissimilar from $0\nu\beta\beta$ are rejected. Parameters on which data is rejected are collectively referred to as "cuts".

Multisite events are removed from data on the basis of pulse shape. Multiple energy depositions within a detector lead to multiple peaks in the recorded current pulse. Comparison of the maximum current A to the energy E of a pulse yields an "AvsE" parameter that distinguishes MSEs from SSEs. Monte Carlo simulations indicate that 90% of $0\nu\beta\beta$ events are single site. Consequently, the AvsE parameter is tuned to accept 90% of SSEs, with the 2614 keV SEP from calibration data used as the source of SSEs for tuning [51].

Events coincident between detectors in time are also rejected as background. During processing of recorded data, coincident detector hits are grouped into an event and the number of coincident detectors is recorded as the event multiplicity. As $0\nu\beta\beta$ events are expected to be SSE, any events of multiplicity greater than one are rejected. This multiplicity cut is often referred to as "granularity" due to its leveraging of the granular design of the detector array. Additional rejection of data occurs when detectors record hits in coincidence with a muon veto event, or in coincidence with a transfer of LN to the modules.

Pulse shape analysis is also used to reject unphysical events or events that are dissimilar from a $0\nu\beta\beta$ pulse shape. Microphonics, microdischarges, and other noise events can lead to detector triggers and recorded waveforms of distinct unphysical morphology. These events are removed by data cleaning cuts.

Finally, α events are also removed from data on the basis of pulse shape. These α's, originating from sources near the point contact, ionize charges on the passivated surface. The charges slowly drift to the point contact yielding a delayed charge signal which manifests as a characteristic rise of the tail of a pulse. A cut on this morphology rejects these delayed charge recovery (DCR) events.

The DCR cut is tuned to retain 99% of SSE events in the 1-2.38 MeV Compton shoulder of the 2614 keV peak from calibration data [52, 53].

CHAPTER 4
Majorana Demonstrator Background Data

The fundamental task in studying background data is to identify the sources, weighted by their activities, whose summation yields the observed energy spectrum. A sense for the major classes of background facing the Majorana Demonstrator can be gleaned from the experiment's accumulated data. Characteristic features in the energy spectrum can reveal the activity, location, and species of background sources. Additional arguments based on the data under PSA and multiplicity cuts can help to resolve the image captured by the energy spectrum.

Monte Carlo simulation of the experiment is another aid in identifying background sources, though reliability depends on model accuracy. Radiation transport simulations yield the expected energy spectra from background sources with their complicated dependencies on experimental geometry, materials, and particle species. Regression of the simulated backgrounds to the data deconstructs the observed spectrum into a summation of the underlying background components.

Both analysis of the data and comparison with simulations are limited when the data is of low statistics. The relative uncertainty of a low statistics energy spectrum diminishes the ability to identify and distinguish background sources, an issue endemic to a low-background, rare-event search like $0\nu\beta\beta$.

4.1 Data Sets

The Majorana Demonstrator collected data throughout its construction and commissioning. Accordingly, the data is partitioned into data sets, with each data set representing a particular experimental configuration.

Data taking began in June 2015 with Data Set 0 (DS0). During this time, there was no inner Cu shielding in place and only Module 1 (M1) was installed in the south shield position; a blank monolith of shielding was in place in the east position. DS1 began in December 2015, following

rework of the M1 strings and installation of the inner Cu shield. Following DS1, a change to the digitizer configurations was made to test multi-sampling or pre-summing which offered downsampled, extended views of waveform baselines and tails. This configuration change was reflected in DS2 which began in May 2016. Pre-summing was disabled after the DS2 period.

Construction of the second module M2 took place alongside DS1 and DS2. In July 2016, M2 was inserted in the east shield position, in place of the blank monolith. M1 and M2 were then operated simultaneously, but with independent DAQ systems. These two data sets began in August 2016, with the M1 and M2 data labeled as DS3 and DS4 respectively. The independent DAQ systems were merged in October 2016 and DS5 began. During the initial three months of DS5 livetime, the polyethylene shield installation was completed and the grounding configuration of the modules and shield was adjusted. This period also saw an increased level of electronics noise, and altogether this portion of data was grouped as a subset of DS5, known as DS5a. The remainder of DS5 was partitioned into DS5b and DS5c, both taken with the final experimental configuration in place, but distinguished by the blindness scheme implemented in DS5c. The blindness scheme is discussed below.

Pre-summing was once again enabled and DS6 began in May 2017. Aside from digitizer pre-summing, the configurations of DS5c and DS6 are the same. Data from the first five months of DS6 livetime was labeled as DS6a for analysis, ending in April 2018. DS6 has since continued, with DS6b running until November 2018, and DS6c extending to the present day.

Data sets 0 through 6a are relevant to the work in this document and the details of their exposures are summarized in Table 4.1. Further comments on this table are provided in Section 4.2.

The aforementioned blindness scheme conceals certain portions of the data to avoid biasing physics analyses. The scheme operates on a 124 hour cycle, collecting 31 hours of open data followed by 93 hours of blind data. The energy region below 100 keV is concealed in blind data to prevent biasing of low-energy searches for new physics. Additionally, events of multiplicity > 1 are concealed in blind data to prevent bias in searches for $0\nu\beta\beta$ decays to excited states.

Table 4.1: Exposure information for each data set. Symbols are exposure $\mathcal{E}$, average livetime t, and active mass m_{act}.

Data Set	t (dy)	$^{\text{nat}}$Ge m_{act} (kg)	$^{\text{enr}}$Ge m_{act} (kg)	$^{\text{nat}}$Ge $\mathcal{E}$ (kg dy)	$^{\text{enr}}$Ge $\mathcal{E}$ (kg dy)	Total $\mathcal{E}$ (kg dy)
DS0 open	43.2	3.9	10.7	171.0	460.1	631.1
DS1 blind	15.5	1.1	11.9	16.8	184.9	201.7
DS1 open	55.4	1.1	11.9	63.3	661.8	725.1
DS2 blind	29.9	1.1	11.3	33.2	338.6	371.8
DS2 open	9.4	1.1	11.3	10.7	106.3	117.0
DS3 open	29.2	2.8	12.6	81.7	368.5	450.3
DS4 open	18.8	3.9	5.5	73.8	102.9	176.7
DS5a open	71.4	9.0	17.5	627.6	1260.6	1888.2
DS5b open	37.2	9.0	18.4	336.2	674.4	1010.6
DS5c blind	33.1	7.9	17.0	266.4	545.7	812.1
DS5c open	10.7	7.9	17.0	86.3	174.8	261.1
DS6a blind	172.5	7.9	17.4	1172.4	3260.5	4432.9
DS6a open	73.3	7.9	17.4	511.9	1366.0	1877.9

Data Set	$^{\text{nat}}$Ge $\mathcal{E}$ (kg yr)	$^{\text{enr}}$Ge $\mathcal{E}$ (kg yr)	Total $\mathcal{E}$ (kg yr)
DS0-6a	9.4	26.0	35.5
DS1-6a	9.0	24.8	33.7

4.2 Data Selection

Data from each experimental configuration is useful for the task of identifying backgrounds present in the MAJORANA DEMONSTRATOR. Though $0\nu\beta\beta$ results are based on the lowest background configurations, data sets for which the full shielding configuration was not in place open a window to sources that are diminished, yet still present, in later data sets. For instance, DS0, which was collected with no inner Cu shield in place displays a low-energy count rate approximately ten times that of the latter data sets. As displayed in Fig 4.1, this low-energy feature peaks between 100 and 200 keV and, with knowledge of the DS0 and DS1-6a configurations, its origin can be inferred to lie in the outer Cu shield or beyond; Fig 4.1 combines the counts recorded in all operating $^{\text{nat}}$Ge and $^{\text{enr}}$Ge detectors and normalizes by their combined exposure, with cuts as described in Section 3.4. Monoenergetic peaks at 1173 and 1332 keV from ^{60}Co, and at 1460 keV from ^{40}K, also appear in the DS0 spectrum and with diminished rates in the DS1-6a spectrum.

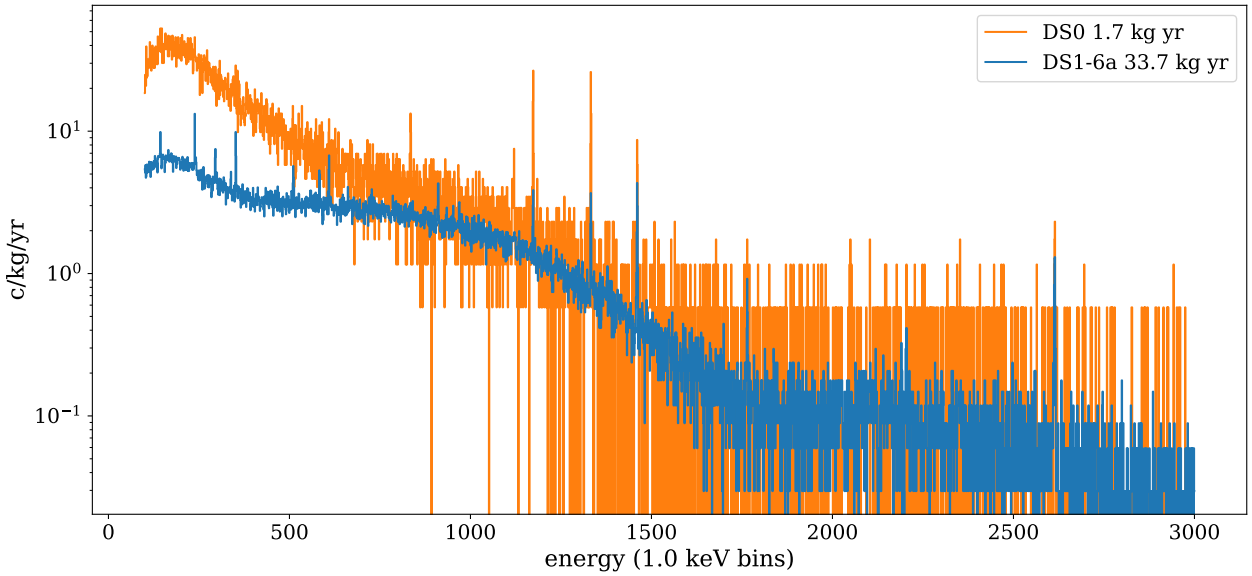

Figure 4.1: Differences in experimental configuration are evident between DS0 and DS1-6a. These spectra include hits from both $^{\text{nat}}$Ge and $^{\text{enr}}$Ge, include both open and blind data, and are presented with data cleaning, LN fill, muon veto, and multiplicity cuts applied.

Data sets beyond DS0 differ less dramatically in configuration and this is reflected in the consistency of their energy spectra, as shown in Fig 4.2. A two-sample χ^2 test between each distribution of Fig 4.2 confirms that data sets 5a-6a are consistent with the assumption of being

drawn from the same underlying distribution [54]. Data sets 1-4 vary more, as is expected from their differing configurations; with a 90% CL threshold, the DS4 distribution matches no other data set. This is likely due to the low exposure and large relative statistical uncertainty of DS4 evident in Table 4.1.

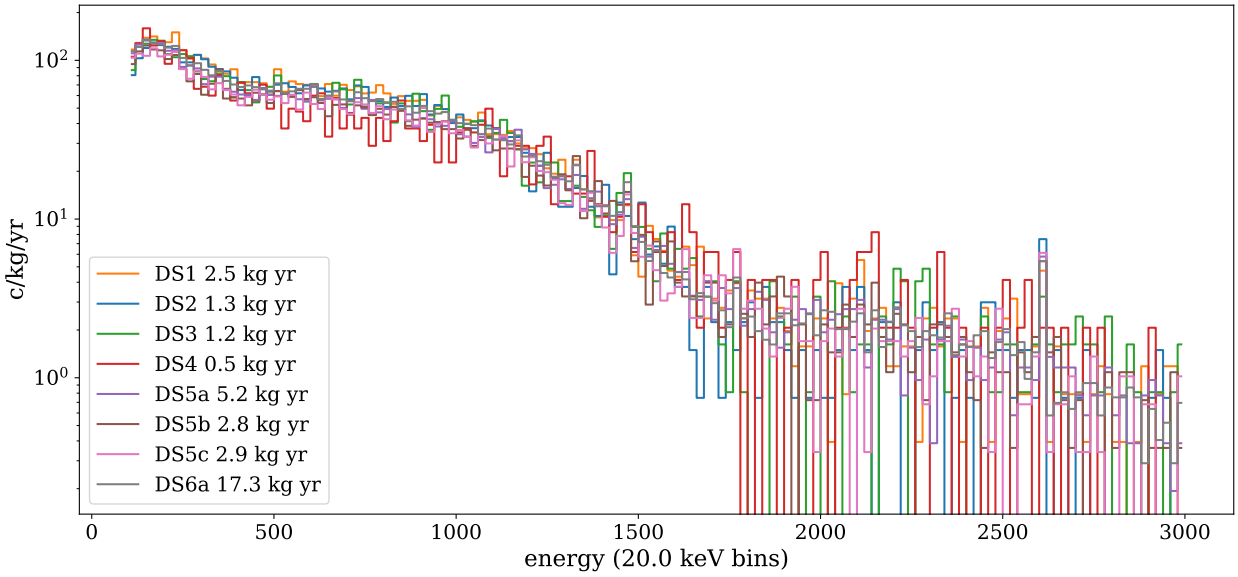

Figure 4.2: Data sets beyond DS0 are generally consistent in rate. Data sets of shorter exposure display larger relative uncertainty. These spectra include hits from both $^{\text{nat}}$Ge and $^{\text{enr}}$Ge, include both open and blind data, and are presented with data cleaning, LN fill, muon veto, and multiplicity cuts applied.

When analyzing the MAJORANA exposure, the combination of DS1-6a is often considered. These data sets all include inner Cu shielding and collectively represent a 33.74 ± 0.04 kg yr exposure with over 35×10^6 counts. Exposure information for the combined DS1-6a, is included in Table 4.1.

Each data set is comprised of data from the set of detectors operating during its livetime. Detectors can vary in relative contribution to a data set due to their active mass, livetime, and enrichment. As illustrated in Fig 4.3, detector enrichment leads to differing spectral shapes from $^{\text{nat}}$Ge and $^{\text{enr}}$Ge detectors. $^{\text{enr}}$Ge detectors exhibit a more prominent $2\nu\beta\beta$ spectral component due to greater concentrations of ^{76}Ge, while $^{\text{nat}}$Ge detectors include greater cosmogenic activities due to higher cross sections for cosmogenic production and longer surface exposure during manufacturing and storage. Also visible in Fig 4.3 is the roughly three times greater data-taking exposure of $^{\text{enr}}$Ge over $^{\text{nat}}$Ge. Though only $^{\text{enr}}$Ge are used in a $0\nu\beta\beta$ physics analysis, incorporation of $^{\text{nat}}$Ge provides

additional information for the identification of background sources. The relative contributions of ^{nat}Ge and ^{enr}Ge for each data set are compiled in Table 4.1.

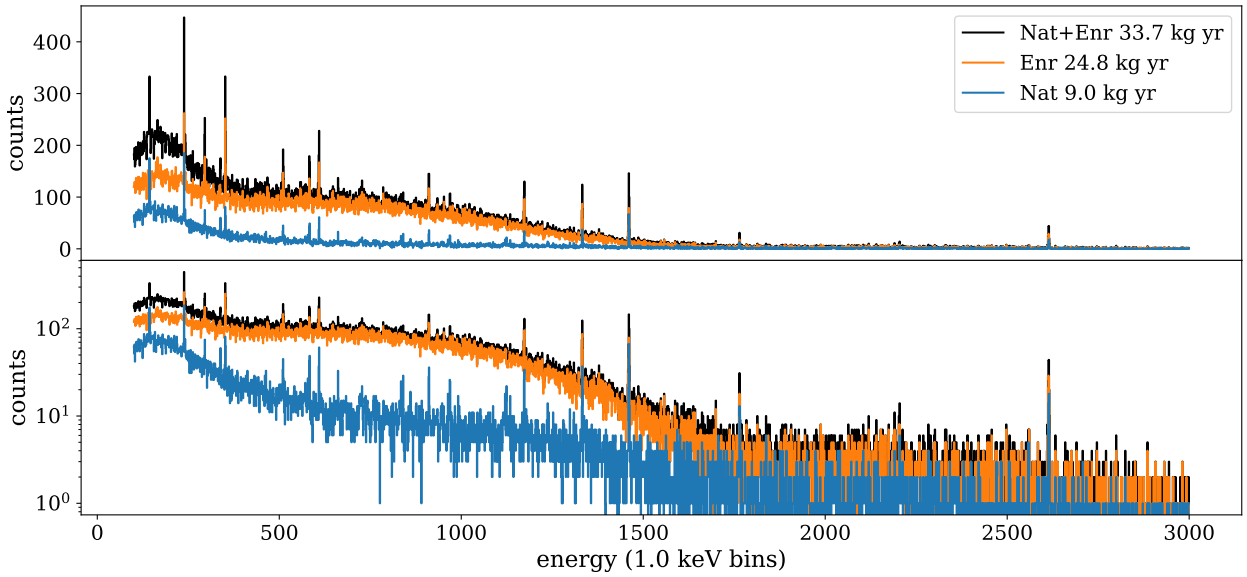

Figure 4.3: A comparison of the ^{nat}Ge, ^{enr}Ge, and total energy spectra for DS1-6a. These spectra include both open and blind data, and are presented with data cleaning, LN fill, muon veto, and multiplicity cuts applied.

Additionally, only high-quality runs and detector channels are selected for use in the data set. Runs can be rejected for high noise and count rate, DAQ errors, veto and slow controls errors, or software and data production errors. Individual detector channels can be removed from the data if those crystals are not biased, or if they yield unreliable PSA performance. Detectors exhibiting reliable performance are considered “good" and are included in analysis. These data selection criteria are evaluated for all runs and detectors via automated data processing routines, and any data flagged for insufficient quality is removed prior to running physics analyses. Further details are summarized in Appendix A.

4.3 Spectral Analysis

The full data set incorporates sufficient statistics for monoenergetic peaks to emerge above continuum backgrounds. Fig 4.4 labels the origins of these peaks, most being affiliated with the ^{232}Th, ^{238}U, and ^{40}K primordial isotopes and their decay chains. Appreciable peaks from the cosmogenic

products ^{60}Co and ^{57}Co also appear. The strengths of these peaks depend on a number of factors, including the concentrations of radioimpurities in the source of the decays, the solid angle subtended by the source with respect to detectors, interaction of radiation with intervening material, and the half lives and branching ratios of the primordial isotopes and their decay chains.

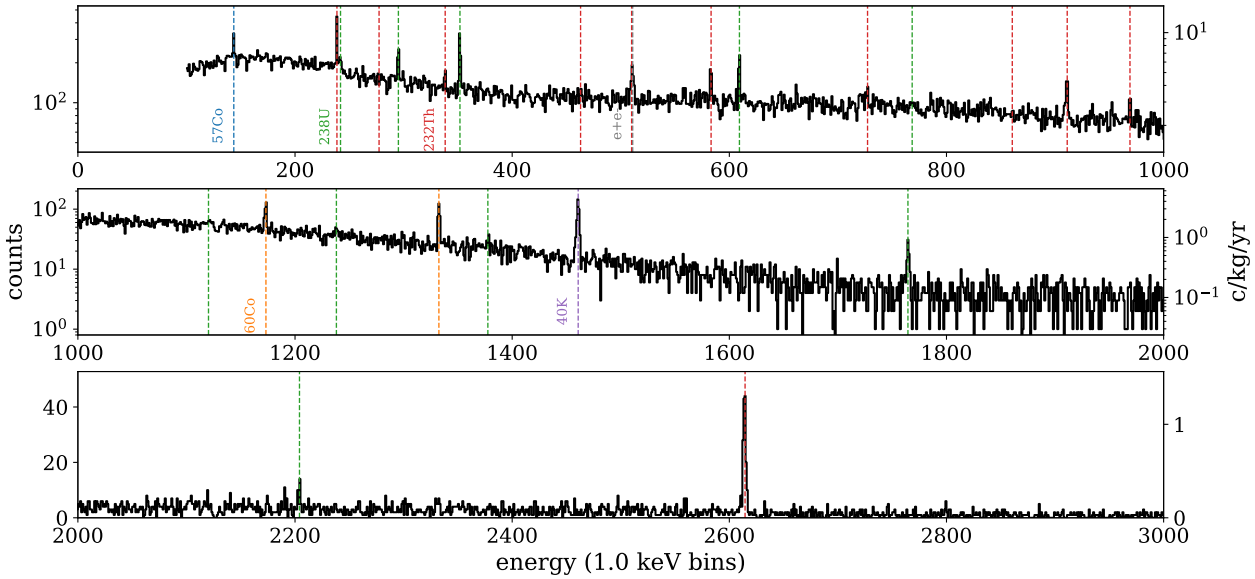

Figure 4.4: The DS1-6a spectrum with prominent γ peaks labeled by decay chain. Note overlap between the 510.8 (^{208}Tl, ^{232}Th) and 511.0 keV (e^+e^- annihilation) peaks. This spectrum is comprised of individual detector hits from both ^{nat}Ge and ^{enr}Ge, includes both open and blind data, and is presented with data cleaning, LN fill, muon veto, and multiplicity cuts applied. PSA and DCR cuts are not applied.

Peak rates in c/(kg yr) were calculated for the most prominent peaks in the DS1-6a spectrum and are presented in Tables 4.2 and 4.3. The 351.9 keV gamma peak of ^{214}Pb, from the ^{238}U chain, appears with greatest strength in the total spectrum— 9.3 c/(kg yr) with 68% credible interval of same units (8.5, 10.1). This is followed by 1460.8 keV (^{40}K), 238.6 keV (^{214}Pb, ^{232}Th), and 1332.5 and 1173.2 keV (^{60}Co).

From separate analysis of the ^{nat}Ge and ^{enr}Ge spectra, it appears that these background sources generally appear with higher rate in the ^{nat}Ge. This is most notable in 1460.8 keV (^{40}K), 609.3 keV (^{214}Bi, ^{238}U), and 238.6 keV (^{214}Pb, ^{232}Th), which appear at roughly twice the ^{enr}Ge rate in ^{nat}Ge. These differences in rate could result from the installation of ^{nat}Ge as top detectors in strings,

Table 4.2: Peak rates calculated via sideband subtraction, from the DS1-6a energy spectrum. Both open and blind data are included and data cleaning, LN fill, and muon veto cuts are applied. The peak rates that reject a background-only hypothesis at $> 90\%$CL are presented with a 68% Gaussian standard error. A 90% upper limit is reported for peak rates consistent with background. I_γ is the intra-isotope intensity.

Decay Chain	Isotope	E_γ (keV)	I_γ (%)	^{nat}Ge Rate c/(kg yr) *8.98 kg yr*	^{enr}Ge Rate c/(kg yr) *24.76 kg yr*	Total Rate c/(kg yr) *33.74 kg yr*
^{232}Th	^{228}Ac	338.3	11.2	4.6 ± 1.3	1.7 ± 0.8	2.5 ± 0.7
^{232}Th	^{228}Ac	911.2	26.6	5.9 ± 1.1	3.8 ± 0.9	4.3 ± 0.7
^{232}Th	^{228}Ac	969.0	16.2	3.4 ± 1.1	1.2 ± 0.8	1.8 ± 0.6
^{232}Th	^{212}Pb	238.6	43.6	13.0 ± 2.0	5.3 ± 0.9	7.4 ± 0.9
^{232}Th	^{212}Bi	727.3	6.7	2.2 ± 1.0	1.3 ± 0.8	1.5 ± 0.7
^{232}Th	^{208}Tl	583.2	84.5	7.4 ± 1.3	4.0 ± 0.9	4.9 ± 0.7
^{232}Th	^{208}Tl	2614.5	99.2	5.4 ± 0.8	3.6 ± 0.4	4.1 ± 0.4
^{238}U	^{214}Pb	241.9	7.5	3.1 ± 1.6	1.4 ± 0.9	1.9 ± 0.8
^{238}U	^{214}Pb	295.2	19.2	6.0 ± 1.5	4.6 ± 0.9	4.9 ± 0.8
^{238}U	^{214}Pb	351.9	37.1	9.8 ± 1.5	9.2 ± 1.0	9.4 ± 0.8
^{238}U	^{214}Bi	609.3	46.1	9.1 ± 1.3	4.9 ± 0.9	6.0 ± 0.8
^{238}U	^{214}Bi	1120.3	15.0	< 1.2	0.9 ± 0.7	< 1.4
^{238}U	^{214}Bi	1764.5	15.9	2.3 ± 0.7	1.4 ± 0.3	1.7 ± 0.3
^{238}U	^{214}Bi	2204.1	5.0	0.7 ± 0.5	0.6 ± 0.2	0.6 ± 0.2
^{60}Co	^{60}Co	1173.2	99.8	7.5 ± 1.2	6.0 ± 0.8	6.4 ± 0.7
^{60}Co	^{60}Co	1332.5	100.0	7.5 ± 1.2	7.5 ± 0.7	7.5 ± 0.6
^{40}K	^{40}K	1460.8	10.7	14.3 ± 1.4	6.8 ± 0.6	8.8 ± 0.6
^{57}Co	^{57}Co	143.6	100.0	9.3 ± 2.0	< 1.2	2.6 ± 0.8

Table 4.3: Peak rates calculated via Bayesian inference, from the DS1-6a energy spectrum. Both open and blind data are included and data cleaning, LN fill, and muon veto cuts are applied. The peak rates that reject a background-only hypothesis at $> 90\%$CL are presented with a 68% credible interval. A 90% upper limit is reported for peak rates consistent with background. I_γ is the intra-isotope intensity.

Decay Chain	Isotope	E_γ (keV)	I_γ (%)	^{nat}Ge Rate c/(kg yr) *8.98 kg yr*	^{enr}Ge Rate c/(kg yr) *24.76 kg yr*	Total Rate c/(kg yr) *33.74 kg yr*
^{232}Th	^{228}Ac	338.3	11.2	4.5 (3.3, 5.9)	1.7 (1.0, 2.5)	2.5 (1.8, 3.1)
^{232}Th	^{228}Ac	911.2	26.6	5.9 (4.8, 7.0)	3.8 (2.9, 4.6)	4.3 (3.6, 5.0)
^{232}Th	^{228}Ac	969.0	16.2	3.4 (2.4, 4.5)	1.2 (0.5, 1.9)	1.8 (1.2, 2.4)
^{232}Th	^{212}Pb	238.6	43.6	13.0 (11.1, 15.0)	5.3 (4.4, 6.2)	7.4 (6.5, 8.2)
^{232}Th	^{212}Bi	727.3	6.7	2.2 (1.3, 3.2)	1.3 (0.5, 2.0)	1.5 (0.9, 2.2)
^{232}Th	^{208}Tl	583.2	84.5	7.3 (6.1, 8.6)	4.0 (3.1, 4.8)	4.9 (4.2, 5.6)
^{232}Th	^{208}Tl	2614.5	99.2	5.4 (4.6, 6.2)	3.5 (3.1, 3.9)	4.0 (3.7, 4.4)
^{238}U	^{214}Pb	241.9	7.5	3.1 (1.6, 4.6)	1.4 (0.6, 2.2)	1.9 (1.2, 2.6)
^{238}U	^{214}Pb	295.2	19.2	5.9 (4.5, 7.4)	4.6 (3.7, 5.4)	4.9 (4.2, 5.7)
^{238}U	^{214}Pb	351.9	37.1	9.7 (8.3, 11.3)	9.2 (8.2, 10.1)	9.3 (8.5, 10.1)
^{238}U	^{214}Bi	609.3	46.1	9.0 (7.7, 10.3)	4.9 (4.0, 5.8)	6.0 (5.3, 6.8)
^{238}U	^{214}Bi	1120.3	15.0	< 1.6	0.9 (0.3, 1.5)	0.6 (0.2, 1.1)
^{238}U	^{214}Bi	1764.5	15.9	2.3 (1.6, 2.9)	1.4 (1.1, 1.7)	1.7 (1.4, 1.9)
^{238}U	^{214}Bi	2204.1	5.0	0.7 (0.3, 1.1)	0.5 (0.4, 0.8)	0.6 (0.4, 0.8)
^{60}Co	^{60}Co	1173.2	99.8	7.5 (6.3, 8.7)	6.0 (5.3, 6.8)	6.4 (5.8, 7.1)
^{60}Co	^{60}Co	1332.5	100.0	7.4 (6.3, 8.6)	7.4 (6.7, 8.1)	7.4 (6.8, 8.0)
^{40}K	^{40}K	1460.8	10.7	14.2 (12.9, 15.6)	6.8 (6.2, 7.4)	8.8 (8.2, 9.3)
^{57}Co	^{57}Co	143.6	100.0	9.3 (7.3, 11.2)	< 1.5	2.6 (1.8, 3.3)

detector positions with line-of-sight exposure to potential backgrounds from the module crossarms. The 143.6 keV (^{57}Co) line appears almost exclusively in the $^{\mathrm{nat}}$Ge due to cosmogenic production.

Peak rates were calculated by defining a central region of interest about a known peak energy, and two regions of assumed flat background on either side of the central region. The width of the central region was set to contain 99% of a Gaussian peak whose width is known from calibrations in each data set. The two sidebands were each set to roughly half the width of the central region. For Table 4.2, the peak rate was calculated by sideband subtraction: integrating counts in the peak and sideband regions and subtracting the sideband region's counts— normalized for differences in integration window— from those of the peak region as described in Ref [55]. The critical limit assumed Gaussian background fluctuations.

Table 4.3 takes a Bayesian approach, integrating the counts in the central and sideband regions, but inferring the signal rate through marginalization rather than sideband subtraction. The procedure models the counts in the background and peak regions as Poisson distributed

$$\begin{aligned} p(C_{\mathrm{pk}}|\mu_{\mathrm{S}}+\mu_{\mathrm{B}}/\tau) &= \frac{(\mu_{\mathrm{S}}+\mu_{\mathrm{B}}/\tau)^{C_{\mathrm{pk}}}}{C_{\mathrm{pk}}!}e^{-(\mu_{\mathrm{S}}+\mu_{\mathrm{B}}/\tau)} \\ p(C_{\mathrm{sb}}|\mu_{\mathrm{B}}) &= \frac{(\mu_{\mathrm{B}})^{C_{\mathrm{sb}}}}{C_{\mathrm{sb}}!}e^{-(\mu_{\mathrm{B}})} \end{aligned} \tag{4.1}$$

where C_{pk} and C_{sb} are the counts in the peak region and two sideband regions, respectively. μ_{B} represents the expected background counts in the sideband regions. The factor τ is the ratio of the total sideband width to the peak region width so that μ_{B}/τ is then the expected background counts in the peak region. μ_{S} represents the expected signal counts in the peak region.

With these likelihoods for the observed counts in the peak and sideband regions, the posterior for the expected counts can be constructed from Bayes' theorem as

$$\begin{aligned} p(\mu_{\mathrm{S}},\mu_{\mathrm{B}}|C_{\mathrm{pk}},C_{\mathrm{sb}}) &= \frac{p(C_{\mathrm{pk}},C_{\mathrm{sb}}|\mu_{\mathrm{S}},\mu_{\mathrm{B}})p(\mu_{\mathrm{S}},\mu_{\mathrm{B}})}{p(C_{\mathrm{pk}},C_{\mathrm{sb}})} \\ &\propto p(C_{\mathrm{pk}}|\mu_{\mathrm{S}},\mu_{\mathrm{B}})p(C_{\mathrm{sb}}|\mu_{\mathrm{B}})p(\mu_{\mathrm{S}})p(\mu_{\mathrm{B}}) \\ &\propto p(C_{\mathrm{pk}}|\mu_{\mathrm{S}},\mu_{\mathrm{B}})p(C_{\mathrm{sb}}|\mu_{\mathrm{B}}) \end{aligned} \tag{4.2}$$

noting the conditional independencies of C_{pk} and C_{sb}, and of μ_{S} and μ_{B}, and treating the prior distributions $p(\mu_{\mathrm{S}})$ and $p(\mu_{\mathrm{B}})$ as uniform. The quantity of interest μ_S is then obtained by marginal-

ization,

$$p(\mu_{\mathrm{S}}|C_{\mathrm{pk}}, C_{\mathrm{sb}}) = \int p(\mu_{\mathrm{S}}, \mu_{\mathrm{B}}|C_{\mathrm{pk}}, C_{\mathrm{sb}})\mathrm{d}\mu_{\mathrm{B}}. \tag{4.3}$$

For long-lived isotopes, half lives will exceed the runtime of MAJORANA and count rates due to that isotope will appear constant across data sets. Assuming secular equilibrium within decay chains, count rates due to the progeny of long-lived primordial radionuclides will also appear constant across data sets. Studies of event rate versus time are thus tests of decay chain equilibria and can indicate if background sources should be considered constant or as variable over time.

Fig 4.5 displays count rates as a function of time and detector type for the most prominent peaks of Table 4.3. The plotted peak rates from the ^{238}U and ^{232}Th chains, as well as those from ^{40}K and ^{60}Co, appear constant within errors across data sets 1-6a. These peak rates appear highest in DS0 due to the lack of inner Cu shielding in that configuration. The last panel of Fig 4.5 shows that the ^{57}Co rate in $^{\mathrm{nat}}$Ge decreases across data sets. This is a result of ^{57}Co's 271.74 dy half life which is visible on the scale of the experiment's runtime.

The count rates in the preceding figures are normalized to the total exposure of active detectors in a data set. Though these figures are useful for visualizing trends in the data, a more detailed analysis considers the effect of which detectors are operating in each data set (cf. Appendix A). Individual detectors can vary in count rate due to differences in their associated electronics, their positions within the arrays, their operational status and exposure, and the detector units themselves.

Along these lines, Fig 4.6 displays count rates of individual good detectors for a selection of the strongest peaks in DS1-6a. The scatter in this figure reflects the potential for detector dependence, though uncertainties are large given the low statistics of individual detectors. As in the preceding discussion, it can be seen that count rates are generally higher in $^{\mathrm{nat}}$Ge than $^{\mathrm{enr}}$Ge.

4.4 Current Status

As of April 2019, the DEMONSTRATOR has accrued approximately 40 kg yr of $^{\mathrm{enr}}$Ge exposure. Data from the 26.02 ± 0.53 kg yr $^{\mathrm{enr}}$Ge exposure of DS0-6a is presented in Fig 4.7. The $2\nu\beta\beta$ continuum is evident between 0.4 and 2 MeV, along with a low-energy population dominated by ^{210}Pb bremsstrahlung from the Pb shield. Monoenergetic γ peaks are also visible, with the peak of highest energy at 2614 keV. The 2-3 MeV region is dominated by a continuum of surface α events

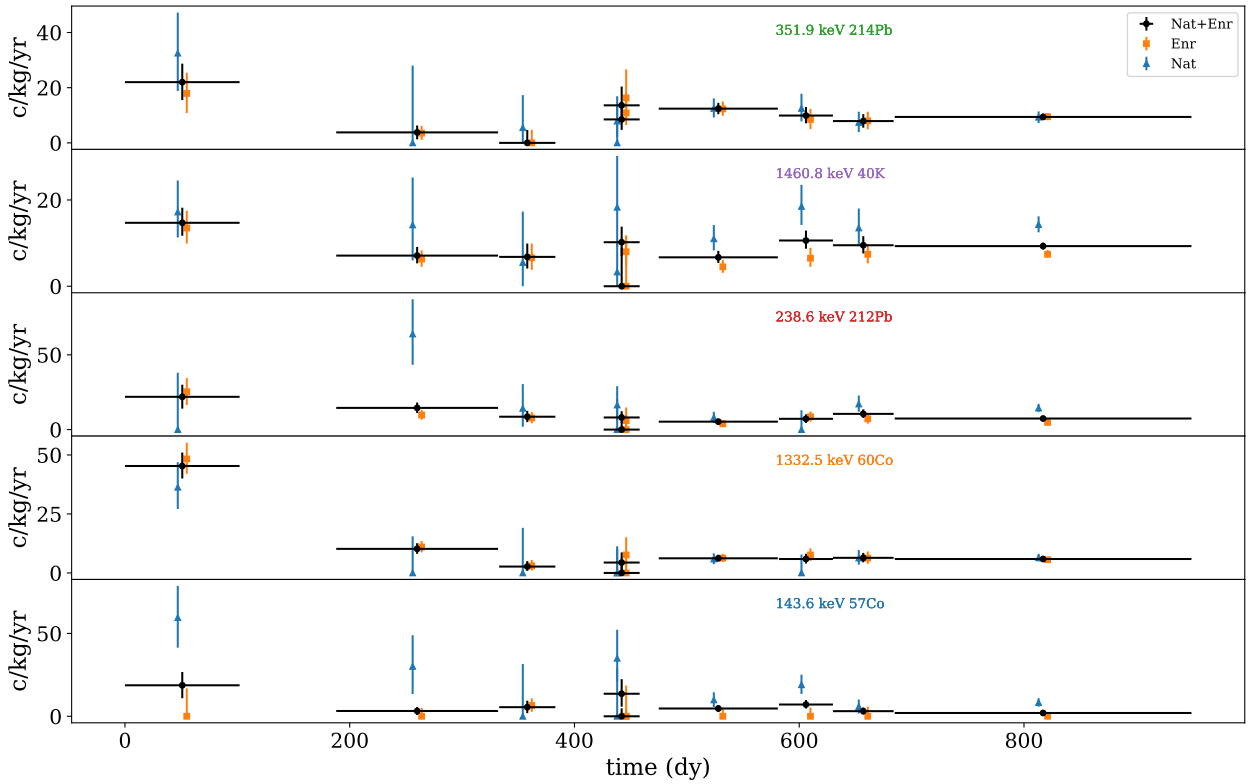

Figure 4.5: Rate as a function of time and enrichment, for a selection of the strongest peaks. Rates are calculated for each data set and plotted at the data set's midpoint in days. Open and blind DS0-6a are included with the multiplicity cut applied. The start of DS0 lies at zero days, and DS3 and DS4 overlap in time. Horizontal lines indicate a data set's duration, and the $^{\text{nat}}$Ge and $^{\text{enr}}$Ge data points have been staggered about data set midpoints for clarity.

described in Chapter 3. The application of the DCR, AvsE, and multiplicity cuts described in Section 3.4 drastically reduces the rate between 1950-2350 keV by removing α events and MSEs, and by accepting only events of multiplicity one.

The most recent $0\nu\beta\beta$ analysis considers the $^{\text{enr}}$Ge data from the lowest background data DS1-4,5b-6a comprising 21.31 ± 0.41 kg yr of exposure [56]. The exposure-weighted average FWHM resolution for this data set is 2.53 ± 0.08 keV at 2039 keV. Assuming a flat background rate near $Q_{\beta\beta}$ as indicated by simulations, counts are integrated from 1950-2350 keV excluding 10 keV regions at 2039, 2103, 2118, and 2204 keV. Respectively, these four regions cover the $0\nu\beta\beta$ ROI and known gamma peaks due to the ^{208}Tl (^{232}Th) SEP and two ^{214}Bi (^{238}U) emissions. 36 counts appear in this 350 keV integration window yielding a background index of $4.7 \pm 0.8 \times 10^{-3}$ c/(keV kg yr) or a

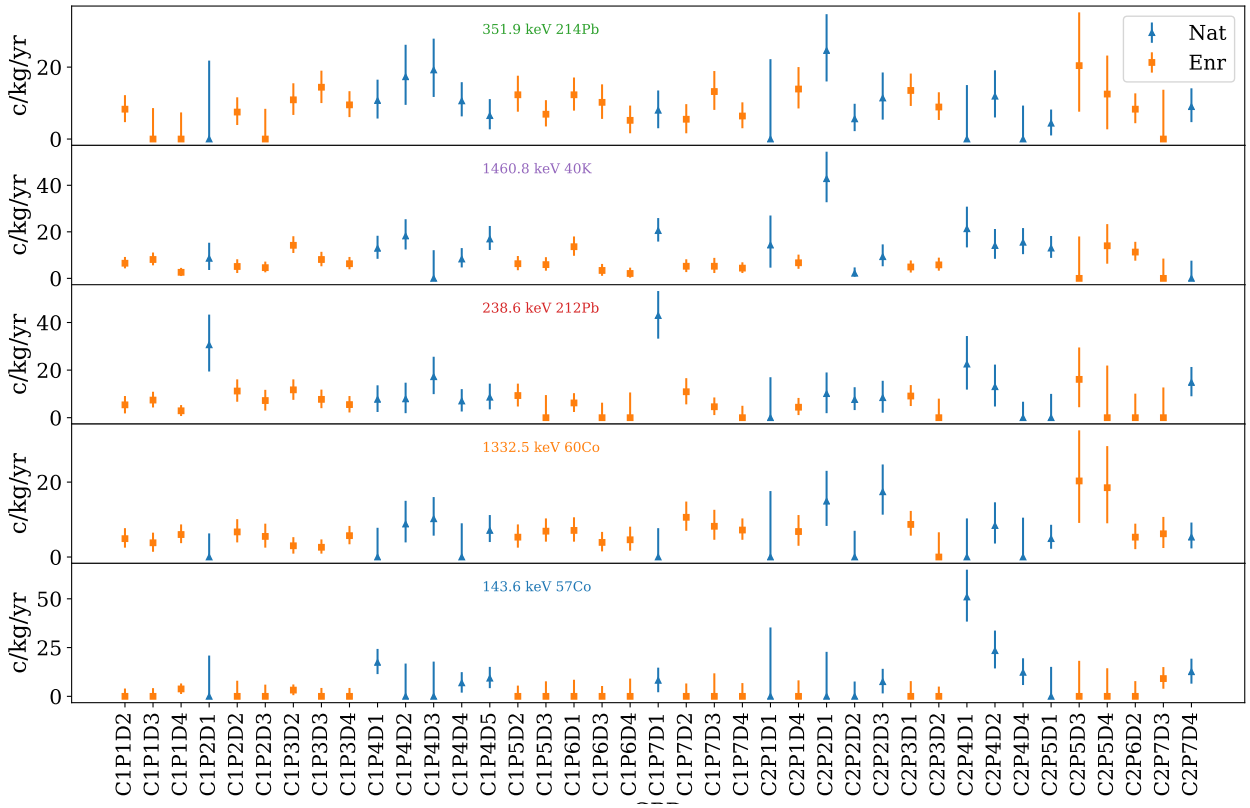

Figure 4.6: Rate as a function of detector, for a selection of the strongest peaks in DS1-6a. C2P6D1 ($^{\text{enr}}$Ge) is excluded due to low statistics, having operated solely in DS4. Rates were calculated with the multiplicity cut applied.

rate in the $0\nu\beta\beta$ peak region of

$$11.9 \pm 2.0 \text{ c/(FWHM tonne yr)}.$$

With the resolution and background index determined, an optimal ROI width of 4.14 keV is set [57]. This in turn can be used for a counting analysis based on the counts observed in the ROI and the expected background rate in the ROI. Alternatively, the limit on $T_{1/2}^{0\nu}$ can be determined through a profile likelihood procedure [58, 59]. This procedure yields the limit

$$T_{1/2}^{0\nu} > 2.7 \times 10^{25} \text{ yr (90\% CL)},$$

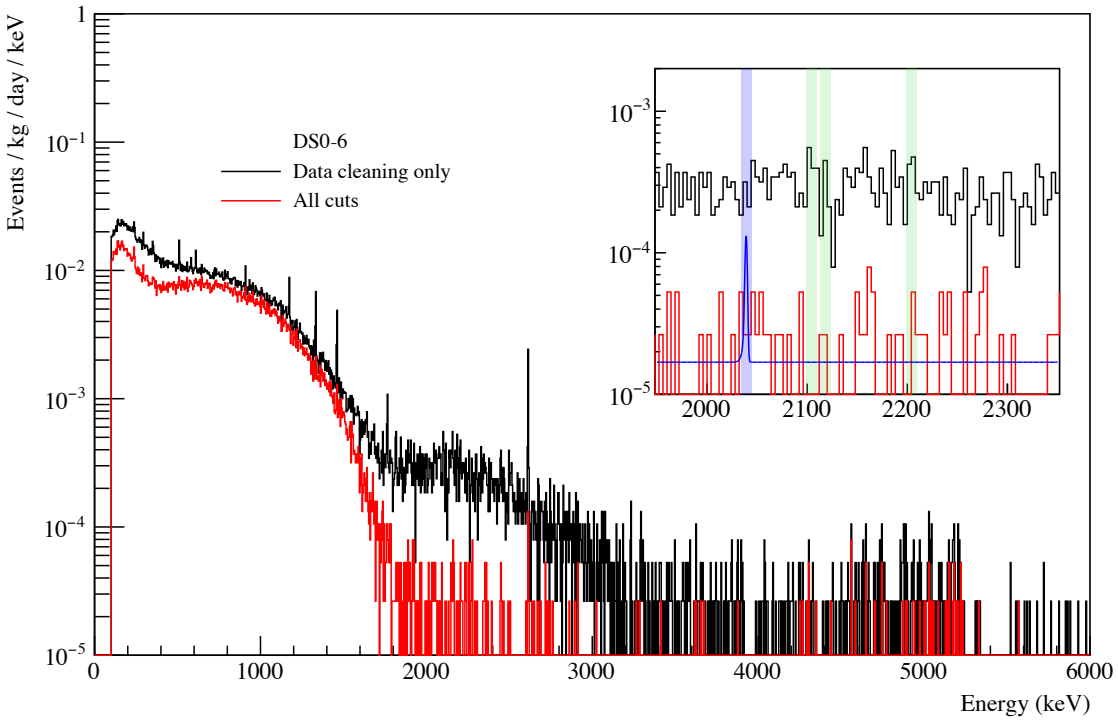

Figure 4.7: DS0-6a $^{\text{enr}}$Ge data before (black) and after (red) the application of DCR, AvsE, and multiplicity cuts. The inset figure displays the integration window for the $0\nu\beta\beta$ background index, with the regions surrounding $Q_{\beta\beta}$ and known ^{232}Th and ^{238}U lines highlighted. The inset blue curve represents the calculated flat background index and the 90% CL upper limit on the number of counts in the $0\nu\beta\beta$ peak region.

and the sensitivity— analogous to discussions of Sections 2.1 and 2.2— to half lives less than

$$4.8 \times 10^{25} \text{ yr (90\% CL)}.$$

CHAPTER 5

Majorana Demonstrator Simulations

A detector's absolute detection efficiency is given by the product of its intrinsic detection efficiency, geometry-dependent efficiency, and any data acquisition or analysis efficiencies. The intrinsic detection efficiency describes the efficiency with which a particle incident on the detector will be registered. A geometry-dependent efficiency expresses the fact that the source will be located at some distance relative to the detector, and thus the detector subtends some fraction of solid angle with respect to the source. Beyond these quantities, a further reduction in registered events may occur due to selective processes like triggering thresholds for digitization, or pulse shape analysis cuts.

For a point source at some distance from a detector, for which N identical decays have occurred, a simple absolute efficiency (ignoring any data acquisition or analysis efficiencies) is expressed as

$$\epsilon = \frac{N}{S} = \epsilon_{\text{int}}\epsilon_{\text{geo}} = \epsilon_{\text{int}}\frac{\Omega}{4\pi}.$$

Here, N is the number of events registered, S is the true number of decay events, ϵ_{int} and ϵ_{geo} are the intrinsic and geometric efficiencies, and Ω is the aforementioned solid angle. Ω is determined by integrating over the detector surface facing the source. A second integration over the source volume is required if the source volume is not negligible [50].

The integrations involved in efficiency calculations quickly graduate beyond analytic solution for realistic source-detector configurations, and numerical techniques become necessary; Monte Carlo techniques are well suited. In particular, Monte Carlo radiation transport simulation allows for approximations of detection efficiency that account for realistic dependencies on radiation species and energy, the scattering or absorption of radiation by intervening material, and the resulting probabilistic paths of generated particles. In a detailed simulation, data acquisition and analysis efficiencies can also be included.

5.1 Simulated Components

The MAJORANA DEMONSTRATOR simulates a full model of its experimental geometry using the MaGe framework, based on Geant4 [60, 61]. In this model, there are 67 unique component designs used for 3779 individual parts. Related parts are consolidated into component groups, of which there are 38 in total. Renderings of the MaGe model's detailed cryostat geometry are displayed in Fig 5.1.

The PTFE parts of a detector unit (DU) serve as an example of how parts are grouped in the simulations. The DU PTFE parts are treated as a single component group named "DUPTFE", a reasonable grouping since these components originate from the same stock material, share similar histories regarding processing and handling, and occupy the same locations with respect to each crystal in the array. As labeled in Fig 5.1, DUPTFE includes the following parts for each DU. First, three crystal insulators act to support the Ge crystal and provide electrical isolation from the hollow hex rods and crystal mounting plate. Second, three HV nuts maintain contact between the HV ring and crystal, and provide electrical isolation between the HV ring and hollow hex rods. Third, one HV fork nut clamps the HV fork against the HV ring. Finally, one center bushing supports and electrically isolates the contact pin which connects a crystal to its front end electronics.

Separate simulations are executed for each component group, and, in each simulation job, decays are generated only from within the members of the given component group. Furthermore, simulations are executed for each expected radioactive contaminant, with an individual job for each segment of the contaminant's decay chain. For instance, the long-lived ^{232}Th and ^{238}U contaminants discussed in Section 2.4 are each followed by a series of radioactive nuclides ending in a stable isotope of Pb. These chains are simulated in segments as displayed in Fig 5.2 and Fig 5.3, with each segment representing a series of decays assumed to be in secular equilibrium.

5.2 Simulations Processing

Once the MaGe simulations have finished, the raw output is processed for the purposes of event building, application of dead layer effects, energy calculation, imposition of PSA and granularity cuts, and data reduction. By looping through the raw step-level output, energy depositions within a

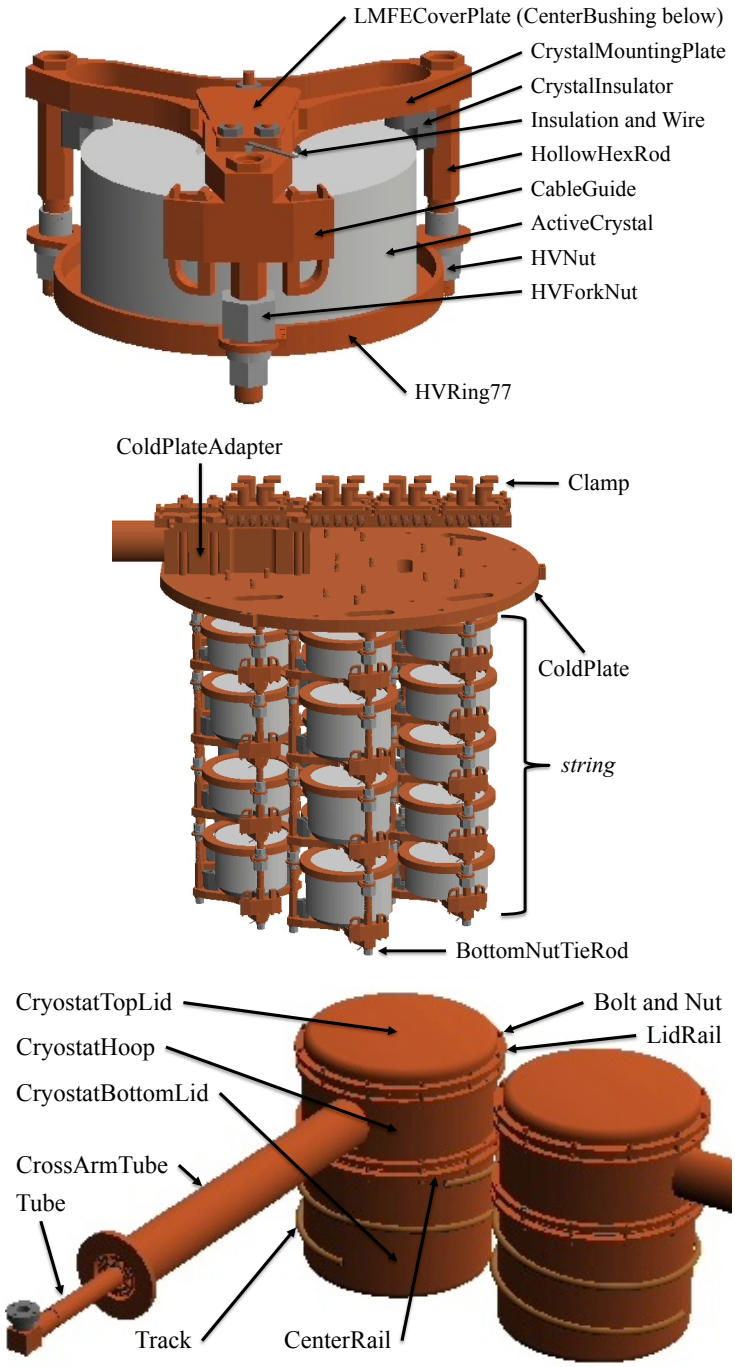

Figure 5.1: Renderings of a detector unit (top), detector array (middle), and cryostat vessel (bottom), as modeled in MaGe.

crystal can be summed for each simulated decay. Energy at each step is reduced according to the deadness of the deposition's location within a crystal [62, 63].

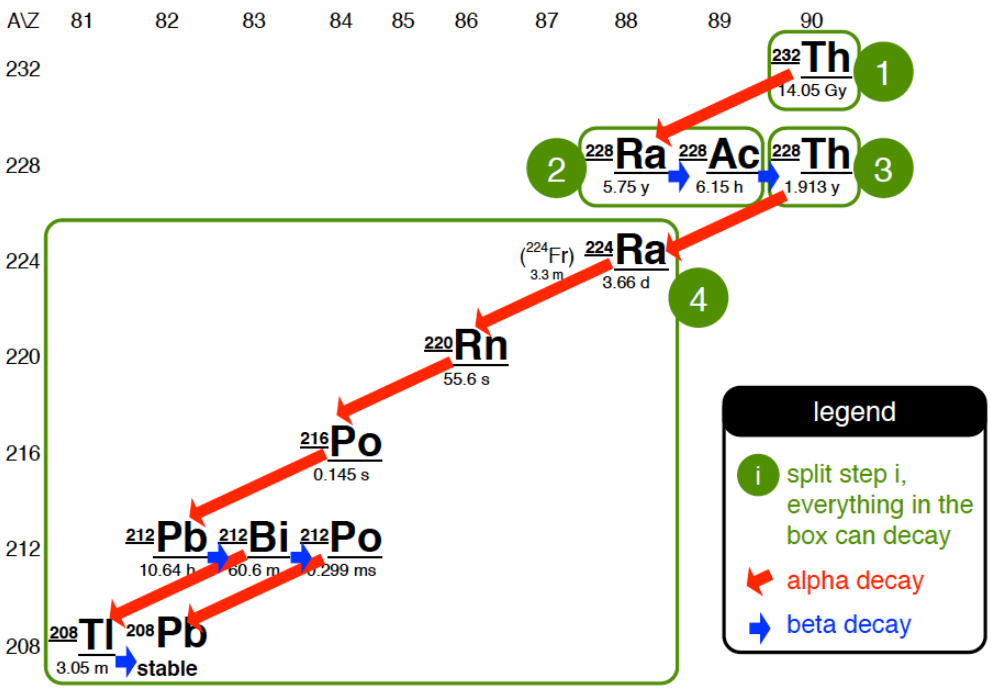

Figure 5.2: The four simulated segments of the ^{232}Th decay chain.

The position of each energy deposition is also assigned a charge collection time (hole drift time) according to crystal-dependent electric field simulations [64]. For MSEs within a crystal, a drift time difference Δt is calculated between energy depositions. An event is tagged as multisite if its largest Δt exceeds a tuned energy-dependent threshold of minimum detectable time difference.

Finally, the multiplicity cut is prepared for the experimental configuration being simulated, accounting for the operational detectors of the corresponding data set. For each simulated decay, the number of operational detectors hit in coincidence is recorded as the event multiplicity.

As discussed in Section 4.1, the DEMONSTRATOR data is divided into data sets representing developments in the experimental configuration. The changes in shielding are reflected in separate simulation jobs for DS0— with no inner Cu shield—, DS1 and DS2— with no second module inserted—, and the later data sets. As mentioned, changes in operational detector lists between data sets are reflected in the processing of multiplicity and individual detector hits. The simulations are executed with all detectors treated as sensitive volumes, but processing ignores hits in those detectors marked as inoperable in the given configuration.

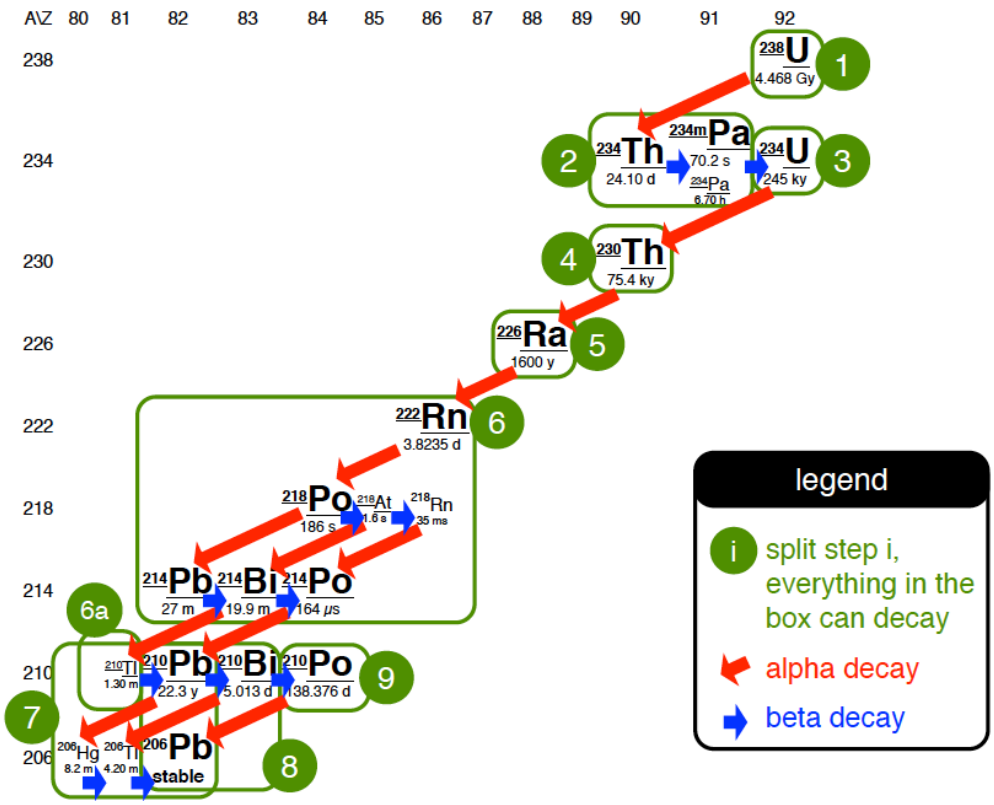

Figure 5.3: The ten simulated segments of the ^{238}U decay chain.

Altogether, data set dependence of shielding and operational detectors in the simulations and processing, along with calculations of energy, PSA, and multiplicity, facilitates comparison with the observed data.

5.3 Simulations Post-Processing

With energy and cut parameters calculated for each hit, the simulations can be compared with experimental data. This is primarily done through analysis of one-dimensional energy spectra.

Each simulation job represents a series of decays from a segment of a decay chain, with the radiated particles generated from within a hardware component. For each of these simulations, a histogram is built for each detector populated by the energy of events incident within that detector's volume. Starting from these histograms, various scalings and combinations can be applied to determine the spectral contributions of hardware components and decay chains. By scaling the simulations to units of counts or counts per exposure, comparisons can be made with the data.

In general a simulated spectrum is made into a form comparable to data through the multiplication of three terms,

$$\text{Efficiency} \times \text{Specific Activity} \times \text{Mass} = \text{Count Rate}.$$

The first term derives from the simulations which yield the energy-dependent efficiency with which detectors observe contaminant decays originating from a component. The second term describes the concentration of a contaminant within a component— that is, the activity per mass of a contaminant present within a component. The final term scales the activity per mass into a total activity for a given component. The product of these terms is an energy-dependent count rate which can be compared with the observed rate from data.

The five steps in the typical procedure for building spectra from the processed simulations— referred to as post-processing— are described below. To indicate the contents of a spectrum at each step, relevant descriptors are concatenated: decay chain segments, full decay chains, hardware components, and detectors are respectively abbreviated as `sg`, `dc`, `hw`, and `dt`. The dimensions at

each step are also provided.

$$
\begin{aligned}
&\textbf{0.}\ \texttt{dt\_hw\_sg}\ (\text{counts/decay/keV}) \\
&\textbf{1.}\ \texttt{dt\_hw\_dc} = \sum_{\texttt{sg}} \texttt{dt\_hw\_sg} \times \text{branchingRatio}_{\texttt{sg}} \\
&\quad \texttt{dt\_hw\_dc}\ (\text{counts/decay/keV}) \\
&\textbf{2.}\ \texttt{hw\_dc} = \frac{1}{M_{\texttt{dt}}} \sum_{\texttt{dt}} \texttt{dt\_hw\_dc} \\
&\quad \texttt{hw\_dc}\ (\text{counts/decay/kg}_{\texttt{dt}}\text{/keV}) \\
&\textbf{3.}\ \text{activity}_{\texttt{hw\_dc}} \left(\left(\frac{\mu\text{Bq}}{\text{kg}} \right)_{\texttt{hw}} \times \frac{\text{Bq}}{\mu\text{Bq}} \times \text{kg}_{\texttt{hw}} \times \frac{\text{s}}{\text{yr}} \right) = \left(\frac{\text{decay}}{\text{yr}} \right) \\
&\quad \texttt{dt\_dc} = \sum_{\texttt{hw}} \texttt{dt\_hw\_dc} \times \frac{\text{activity}_{\texttt{hw\_dc}}}{m_{\texttt{dt}}} \\
&\quad \texttt{dt\_dc}\ (\text{counts/kg}_{\texttt{dt}}\text{/yr/keV}) \\
&\textbf{4.}\ \texttt{dc} = \sum_{\texttt{dt}} \texttt{dt\_dc} \times \frac{m_{\texttt{dt}}}{M_{\texttt{dt}}} \\
&\quad \texttt{dc}\ (\text{counts/kg}_{\texttt{dt}}\text{/yr/keV}) \\
&\textbf{5.}\ \text{fullBackgroundModel} = \sum_{\texttt{dc}} \texttt{dc} \\
&\quad \text{fullBackgroundModel}\ (\text{counts/kg}_{\texttt{dt}}\text{/yr/keV})
\end{aligned}
\tag{5.1}
$$

It is important to note the distinction between mass terms: some masses represent the mass of a component from which decays are generated, while others represent the mass of the operating detectors. Physical masses are used for the mass of a component, with units $\text{kg}_{\texttt{hw}}$, and simulated masses are used for detectors, with units $\text{kg}_{\texttt{dt}}$. $M_{\texttt{dt}}$ is used to denote the total mass of a given set of operating detectors, while $m_{\texttt{dt}}$ denotes an individual detector mass from that set. Summations over detectors include only operational detectors.

Aside from the `dt_hw_sg` simulated efficiency distributions, the inputs to the procedure in Eqn 5.1 are obtained from the as-built details of the MAJORANA DEMONSTRATOR. These details include detector masses, each detector's operational status and ^{76}Ge enrichment fraction, each hardware component's physical mass and material, and estimates of specific activity for those materials and hardware components.

The specific activity estimates in units $(\mu\text{Bq/kg})_{\texttt{hw}}$ are obtained from the MAJORANA DEMONSTRATOR assay campaign [41], records of parts histories tracked in a dedicated database [43], and values from the low-background literature. These values are compiled in Appendix B and discussed further in Chapter 6.

At the end of the post-processing procedure— step 5 above—, the resulting spectrum gives the total expected background model and is used for comparison with the observed data. The full expected background model spectrum is useful for broad comparisons, but spectra at more granular levels of specificity— steps 1 and 2— are of greater use. Comparison of these hardware and decay chain component spectra to the data allows for inference of radioactive contaminant locations and activities.

5.4 Handling of Enriched and Natural Detectors

Contaminants internal to the crystals are handled identically to contaminants external to the crystals. The mass of the contaminant source is set to the total physical mass of the hardware component ($\text{kg}_{\texttt{hw}}$), which in this case is the $^{\text{nat}}$Ge or $^{\text{enr}}$Ge crystals. The detector masses ($\text{kg}_{\texttt{dt}}$), represented by $m_{\texttt{dt}}$ and $M_{\texttt{dt}}$ in Eqn 5.1, are based on the simulated masses of the operational detectors. If an analysis wishes to only examine $^{\text{enr}}$Ge crystals, then only $^{\text{enr}}$Ge crystals are included in the set of analyzed detectors, and the summations over operational detectors and the values of $M_{\texttt{dt}}$ are adjusted accordingly.

5.5 Calculating Specific Activity for Cosmogenic Products

For parts expected to have accrued appreciable concentrations of cosmogenic contaminants, specific activity is estimated from surface exposure and cosmogenic production rate. For such parts, the calculation of $(\mu\text{Bq/kg})_{\texttt{hw}}$ generally proceeds as $t \times r \times \tau^{-1}$, where t (dy) is the effective sea-level exposure of the part, r (atoms dy^{-1} $\text{kg}_{\texttt{hw}}$) is the production rate of the cosmogenic isotope at sea level, and τ (dy) is the lifetime of the cosmogenic isotope. This simple calculation assumes the lifetime τ of the isotope is much greater than the exposure t.

5.6 Summary

The calculations described in this chapter prepare the simulations for comparison to data. When coupled with as-built details of the MAJORANA DEMONSTRATOR, the weighted and combined simulations provide an expected background spectrum, and deviations from the observed spectrum point to inaccuracies in components and parameters of the model. Further inference of model components and parameters is possible via regression of simulations to data.

CHAPTER 6
Background Model

As discussed in Chapter 5, the simulations produce energy spectra representing the efficiency with which contaminants are detected. Given knowledge of parts masses and specific activities, those efficiencies are weighted and combined into units comparable to observed data. This procedure yields an expected background budget for the MAJORANA DEMONSTRATOR.

6.1 Assay Sample Selection

Estimates for the specific activities of parts are obtained from the MAJORANA DEMONSTRATOR assay campaign which has compiled hundreds of samples regarding the intrinsic radioactivity of stock materials and processed parts [41]. Several techniques are used for measurement, including γ-ray counting, mass spectrometry, and neutron activation analysis. For materials not addressed by the assay campaign, values from the low-background literature are considered. For parts with appreciable cosmogenic exposure, effective sea-level exposures are estimated from DEMONSTRATOR records [43], and cosmogenic production rates from literature are adopted.

From these assay measurements and calculations, which generally represent small sample sizes of materials, values are selected which are deemed most representative of the as-built DEMONSTRATOR. Table 6.1 summarizes the assay values selected for ^{232}Th, ^{238}U, and ^{40}K present in MAJORANA DEMONSTRATOR materials' bulk, and a few items with greatest impact are discussed below. Full details are included in Appendix B

The specific activity of the electroformed copper (EFCu) was estimated from four bulk samples produced by MAJORANA. These samples underwent a heavy etch before ^{232}Th and ^{238}U levels were measured via inductively coupled plasma mass spectrometry (ICPMS). Additional small EFCu parts were assayed after having gone through the typical machining and handling of MAJORANA parts. While these additional sampled parts underwent more realistic handling, their large surface

Table 6.1: Estimates for the mass and specific activity of ^{232}Th and ^{238}U contaminants in MAJORANA DEMONSTRATOR materials. Materials are listed roughly in order of distance from the detectors. Connectors are not included in calculations for the vespel row.

Material	kg	Decay Chain	μBq kg^{-1}	Reference
^{enr}Ge	2.97E1	^{232}Th	< 0.01	[65]
		^{238}U	< 0.01	[65]
LMFE	4.6E-3	^{232}Th	7566.31 ± 136.08	[41]
		^{238}U	10571.45 ± 263.83	[41]
PTFE	4.0E-1	^{232}Th	0.10 ± 0.01	[41]
		^{238}U	< 4.97	[41]
EFCu	1.2E3	^{232}Th	< 0.12	[41]
		^{238}U	< 0.11	[41]
Parylene	1.7e-3	^{232}Th	2150.21 ± 121.71	[41]
		^{238}U	3109.25 ± 746.22	[41]
Cable	5.9E-1	^{232}Th	585.97 ± 356.95	[66]
		^{238}U	1405.38 ± 800.36	[66]
Vespel	7.0E-2	^{232}Th	< 11.77	[41]
		^{238}U	< 1049.68	[41]
Connector	7.1E-2	^{232}Th	390.28 ± 361.48	[41]
		^{238}U	539.77 ± 409.12	[41]
OFHC Cu	1.4E3	^{232}Th	1.10 ± 0.20	[41]
		^{238}U	1.49 ± 0.25	[41]
Stainless Steel	9.8E1	^{232}Th	< 12000	[67]
		^{238}U	< 3000	[67]
Pb	4.9E4	^{232}Th	5.27 ± 5.27	[41]
		^{238}U	36.07 ± 24.87	[41]

area to volume ratio suggests the results are more indicative of surface activity than bulk activity; their estimated surface activities are adopted as 1.8 ± 0.4 and 2.8 ± 0.6 μBq m^{-2} in ^{232}Th and ^{238}U. Nevertheless, the assay values of these small parts can be used to reasonably loosen the upper limit on EFCu activity, allowing consideration of a wider range of possible activities in a regression procedure for background inference.

The samples selected for oxygen free high conductivity copper (OFHC Cu) represent the surface of rolled stock material used for the outer copper shield. Several sources of OFHC Cu were used in the experiment, and though some sources yielded lower assay values, the outer copper shield sample— sourced from Aurubis— was chosen for its more conservative value, and for the material's proximity to detectors as installed in the DEMONSTRATOR.

The assay values for Pb were selected as an average of ICPMS measurements made on the bricks used in the DEMONSTRATOR shield. The Pb shield bricks were sourced from both a decommissioned counting facility at the University of Washington and from Sullivan Metals Inc. The Sullivan bricks were formed from virgin Doe Run Mine Pb. The concentration of ^{210}Pb in the lead shield was estimated at < 2.5 Bq kg^{-1} based on a γ-counting measurement of bricks from Sullivan.

The MAJORANA DEMONSTRATOR tested several batches of signal and HV cables produced by Axon'. Improvements in clean manufacturing lead to accepted cables with assayed activities 2.19±0.20 and 145.51 ± 14.92 μBq kg^{-1} for ^{232}Th and ^{238}U in HV cables, < 3448.45 and < 6218.5 μBq kg^{-1} for ^{232}Th and ^{238}U in signal cables. Most recent, more sensitive assay of signal cables used in the DEMONSTRATOR suggests 585.97 ± 356 and 1405.38 ± 800.36 μBq kg^{-1} for ^{232}Th and ^{238}U. The uncertainty on these latest assay values is quoted here as the difference between assay of the full cable and the sum of the assay of its parts. The latest estimate for signal cable activities is adopted for the HV cables as well.

Previous studies from Ref [68] estimated surface contributions from ^{222}Rn daughters to be as large as 0.2 c/(ROI tonne yr), with negligible contributions from the bulk of the nitrogen purge volume. This estimated background index corresponds in the present DEMONSTRATOR simulations to a specific activity of 89.20 ± 44.60 μBq m^{-2} from surfaces. Comparison of present simulations to collected data has in turn indicated a 82:18 ratio of surface to bulk activity, yielding a specific activity of 1165 ± 223 μBq kg^{-1} from the purge volume bulk [69]. The specific activity from the purge gas bulk is reported in units μBq kg^{-1} assuming 1.251 mg cm^{-3}.

Cosmogenic activation for some components was estimated based on knowledge of the components' histories and activation rates in their respective materials. $^{\text{enr}}$Ge crystals were taken on average to have accrued approximately 29 dy of effective sea-level exposure prior to being brought underground; they arrived underground in January 2014, and underwent 1.5 yr of cool-down prior to the start of DS0. An activation rate of 2.12 atoms/(kg dy) was used for ^{68}Ge in $^{\text{enr}}$Ge, and a rate of 2.55 atoms/(kg dy) was likewise used for ^{60}Co [46].

^{60}Co activation was also considered in copper parts, with an activation rate of 86.4 atoms/(kg dy) [48]. Welded copper parts from the vessel and thermosyphon assemblies spent on average 12 dy on the surface, and were held permanently underground from December 2014 onward. Copper parts that received parylene coating spent at most five days on the surface, with the last batch of parylene coating returning underground in December 2014. ^{60}Co activation was assumed in the copper spring clips at the saturation level of 2100 μBq kg^{-1}, given the frequent shipments of these parts between laboratories [49]. Spring clips were assumed to have no cool-down time prior to DS0. Lastly, the outer copper shield was assumed to have accrued 180 dy of surface exposure prior to arrival underground in October 2012.

6.2 Expected Background Index

Using the selected assay samples and known masses of hardware components, as-built simulations were scaled to estimate the MAJORANA DEMONSTRATOR background index, an indication of the background rate in the $0\nu\beta\beta$ region of interest. The background index was calculated for two experimental configurations: first, under the assumption of the DS5 configuration, and second under the assumption that all detectors are operational. Furthermore, the background indices were calculated from analysis of the $^{\text{enr}}$Ge detectors only. $^{\text{nat}}$Ge detectors contribute to the multiplicity cut, but only energy spectra of the $^{\text{enr}}$Ge detectors are integrated. Multiplicity and PSA cuts were applied to simulate a real $^{\text{enr}}$Ge analysis.

For the calculations, a 350 keV background integration window covering the $0\nu\beta\beta$ Q-value was used. The window covers 1950-2350 keV with four 10-keV regions removed from the integration. These four regions surround the 2103.5 keV ^{208}Tl (^{232}Th) single escape peak, the 2118.6 keV ^{214}Bi (^{238}U) peak, the 2039.06 keV Q-value, and the 2204.1 keV ^{214}Bi (^{238}U) peak [70].

The expected background index for the DS5 configuration is presented in Table 6.2, along with analogous results assuming all detectors are operational, and assuming the preliminary background model to be described in Section 6.3. For the DS5 configuration, the sum of the individual contributions is 6.81 c/(ROI tonne yr), mostly attributable to the Pb shield, cables, and connectors. Assuming all detectors are operational, the sum of the individual contributions is 5.98 c/(ROI tonne yr), with largest contributions from the Pb shield, cables, and connectors.

The background indices of these calculations both exceed the < 3.5 c/(ROI tonne yr) of the preliminary background model published in Ref [41]. These discrepancies can be studied in greater detail from the items in Table 6.2, for which further detail is presented in Table 6.3. Differences between the models arise from changes in assay, mass, or efficiency, which can be associated with particular decay chains, hardware components, or cuts. Further detail based on a systematic comparison of the preliminary and as-built models is presented in the next section. The details of the preliminary model are recorded in Refs [41, 68, 71].

For several components in Table 6.2, the same prediction is used for the preliminary and as-built models. For instance, γ's and neutrons originating external to the DEMONSTRATOR shield are predicted at 0.1 c/(ROI tonne yr) based on radioactivity of the rock walls and laboratory shotcrete, and on the shield thickness [68]. The depth-dependent background contributions from direct muons and muon induced neutron events are also held the same between models [72, 73].

6.3 Comparison of Preliminary and As-Built Models

The preliminary background model detailed in Ref [41] is based on assay samples and simulations executed prior to 2016. As described in Section 4.1, the final configuration of the DEMONSTRATOR was realized in 2017. With knowledge of the final configuration, simulations were updated to reflect the as-built DEMONSTRATOR. Additional assay samples were also gathered since publication of Ref [41] and, together with the updated simulations, were referenced for an updated, as-built background model.

Differences arise between the preliminary and as-built models for several reasons. First, design elements of the experiment changed such that some hardware components placed in the simulated geometry of the preliminary model do not exist— or exist in different form— in the geometry

Table 6.2: Expected contributions to the background index from the sources listed in the first column. The second column represents the as-built background model assuming the DS5 configuration. The third column also uses the as-built background model but assumes all detectors are operational. The fourth column presents the analogous results of the preliminary background model published in Ref [41]. The row labeled "Plastics, Other" includes the contributions of stainless steel from the modules' service bodies, the glass break from the cryogenics system, and the phosphor bronze spring washers assisting HV connections at the detectors.

Background Contribution	As-Built DS5 c/(ROI tonne yr)	As-Built All c/(ROI tonne yr)	Rate Preliminary c/(ROI tonne yr)
EFCu	5.47E-01	4.62E-01	2.30E-01
OFHC Cu Shielding	2.80E-01	2.54E-01	2.90E-01
Pb Shielding	1.60E+00	1.45E+00	6.30E-01
Cables and Internal Connectors	1.77E+00	1.60E+00	3.80E-01
Front Ends	1.03E+00	8.09E-01	6.00E-01
^{232}Th, ^{238}U within the Ge	4.97E-01	3.95E-01	7.00E-02
Plastics, Other	9.76E-02	8.75E-02	3.90E-01
^{68}Ge, ^{60}Co within the ^{enr}Ge	7.66E-03	6.12E-03	7.00E-02
^{60}Co within the Cu	7.21E-02	4.86E-02	9.00E-02
External γ-rays, (α,n) reactions	1.00E-01	1.00E-01	1.00E-01
Rn and surface α emission	2.54E-01	2.22E-01	5.00E-02
Ge, Cu, Pb (n,n'γ) reactions	2.10E-01	2.10E-01	2.10E-01
Ge(n,n') reactions	1.70E-01	1.70E-01	1.70E-01
Ge(n,gamma)	1.30E-01	1.30E-01	1.30E-01
Direct muon passage	3.00E-02	3.00E-02	3.00E-02
ν induced background	<1.00E-02	<1.00E-02	<1.00E-02
Total c/(ROI tonne yr)	6.81E+00	5.98E+00	3.50E+00
Total c/(keV kg yr)	1.70E-03	1.50E-03	8.75E-04

Table 6.3: Percent differences in background index for components in the as-built model, with all detectors operational, and the preliminary model of Ref [41]. Column labeled "% Difference" is calculated as $100 \times$ (As-Built − Preliminary)/Preliminary.

Background Contribution	% Difference	Note
EFCu:	100.89	^{232}Th assay increase
OFHC Cu Shielding:	-12.47	Efficiency decrease from cut tuning
Pb Shielding:	129.42	Efficiency increase from geometry, generator, or fluctuation
Cables and Internal Connectors:	320.83	Assay increase from ^{232}Th and ^{238}U
Front Ends:	34.83	Efficiency increase from geometry, generator, or fluctuation
^{232}Th, ^{238}U within the Ge:	464.67	Efficiency increase from cut tuning
Plastics, Other:	-77.55	Mass decrease from Vespel and Parylene
^{68}Ge, ^{60}Co within the $^{\text{enr}}$Ge:	-91.26	Efficiency changes and updated assay assumptions
^{60}Co within the Cu:	-46.02	Assay decrease from ^{60}Co
Rn and surface α emission:	344.89	Assay increase from surface ^{222}Rn

of the as-built model. As a result of differences in geometry, differences in simulated detection efficiencies arise. Second, for parts that are similar between the two models, masses can also vary since measurements of installed parts were not always available for use in the preliminary model. Finally, expected activities of parts can vary between the two models, since additional assay samples and knowledge of the histories of installed parts are incorporated in the as-built model.

For a systematic check with the preliminary model, a set of parts was selected which exist in similar form in both the preliminary and as-built model. For this comparison, the as-built model was analyzed under the assumption that all detectors are active, since that same assumption was made in the preliminary model. Additionally, for comparisons between simulations without multiplicity applied, summed event energies are used to populate the efficiency spectra since this was done in the preliminary model. Finally, for an even comparison, event rates were calculated by integrating over the same regions as were integrated over in the preliminary model. Those integration windows are listed below.

^{208}Tl: 1989 - 2089 keV

^{214}Bi: 2025 - 2050 keV

^{60}Co: 2029 - 2049 keV in crystals, else 2025 - 2050 keV

^{68}Ge: 2029 - 2049 keV

To begin, a comparison was made between the preliminary and as-built masses, efficiencies, and ROI rates. To facilitate comparison, the assay values of the preliminary model were applied to both models when calculating ROI rate.

The results of these comparisons are compiled in Table 6.4 with notable differences existing in a few instances. The masses of the Seals components differ by roughly a factor of ten, due to the as-built model's use of PTFE seals which are more dense than the parylene seals of the preliminary model. Next, the masses of the TopCables differ by roughly a factor of three. This arises from the models' assumed cable lengths and multiplicities atop the coldplate. The as-built model includes more slack of the cables atop the coldplate and also includes the mass of spare cables. Next, the detection efficiencies for decays in the Pb differ by factors of four and two for ^{232}Th and ^{238}U. This is in part due to differences in cut efficiencies, but could also arise from differences in the geometry of the models or statistics of the simulation campaigns. Finally, large differences exist between the

Table 6.4: A comparison of mass, efficiency, and background rate for a selection of components from the preliminary and as-built models. Columns labeled "% Difference" are calculated as $100 \times (\text{As-Built} - \text{Preliminary})/\text{Preliminary}$.

HW Group	Chain	% Difference Mass kg	% Difference Efficiency c/(decay tonne keV yr)	% Difference Rate c/(ROI tonne yr)
Ge	^{232}Th	-1.15	2408.68	2379.91
	^{238}U	-1.15	372.35	366.94
EFCu	^{232}Th	1.25	-14.24	-13.17
	^{238}U	1.25	-35.14	-34.34
CommCu	^{232}Th	0.59	-18.76	-18.28
	^{238}U	0.59	-28.37	-27.95
Pb	^{232}Th	-4.38	306.46	288.66
	^{238}U	-4.38	102.57	93.70
FrontEndBoards	^{232}Th	-7.50	51.59	40.22
	^{238}U	-7.50	-5.40	-12.49
Connectors	^{232}Th	-1.37	-60.95	-61.48
	^{238}U	-1.37	-72.18	-72.56
TopCables	^{232}Th	179.10	-55.14	25.22
	^{238}U	179.10	-77.16	-36.26
BottomCables	^{232}Th	-19.97	-1.62	-21.27
	^{238}U	-19.97	-4.08	-23.24
CrossarmCables	^{232}Th	15.45	-72.51	-68.26
	^{238}U	15.45	-87.90	-86.04
Cables	^{232}Th	57.04	-38.00	-2.64
	^{238}U	57.04	-59.11	-35.79
Vespel	^{232}Th	-91.24	11.72	-90.21
	^{238}U	-91.24	-20.36	-93.02
PTFE	^{232}Th	-9.08	32.20	20.20
	^{238}U	-9.08	-7.53	-15.93
Seals	^{232}Th	959.22	-35.02	588.23
	^{238}U	959.22	-27.09	672.23
ParyleneCoating	^{232}Th	-79.07	-19.29	-83.11
	^{238}U	-79.07	-34.73	-86.34

Table 6.5: A comparison of cut survival fractions for a selection of components from the preliminary and as-built models. Columns labeled "% Difference" are calculated as 100 × (As-Built − Preliminary)/Preliminary.

HW Group	Chain	% Difference Multiplicity	% Difference Multiplicity & PSA	% Difference PSA
EFCu	^{232}Th	-27.43	-46.04	-25.65
	^{238}U	-16.91	-69.10	-62.82
CommCu	^{232}Th	-22.86	-44.40	-27.93
	^{238}U	-14.81	-48.03	-38.99
Pb	^{232}Th	-25.36	-49.78	-32.72
	^{238}U	-25.31	-42.56	-23.09
FrontEndBoards	^{232}Th	-11.06	-21.52	-11.76
	^{238}U	23.68	9.10	-11.79
Ge	^{232}Th	122.14	1309.71	534.61
	^{238}U	83.20	286.93	111.20

detection efficiencies for contaminants within the Ge crystals. These differences arise largely from differences in cut efficiencies.

The cut efficiencies vary between the two models due to geometry of the crystals, arrangement of the detectors in the arrays, and tuning of the Δt PSA parameter as described in Section 5.2. The difference in cut efficiencies is explored in Table 6.5. The values in this table represent cut survival fractions, calculated as the ratio of events in the background integration window after and before the application of cuts. From this table, the large variation between the Ge efficiencies of Table 6.4 is seen as a result of heightened dependence on PSA cut tuning between the two models.

6.4 Comparison of As-Built Model and Data

A true test of the as-built model is its ability to approximate the observed data based solely on the prior expectations. By combining all simulated contaminants, and scaling their contributions by their expected activities in each hardware component, a comparison can be made between the expected as-built background model and the data. Fig 6.1 shows the expected contributions of each decay chain, along with the total of all contributions, assuming all detectors are active.

Fig 6.2 compares the expected model for the DS5 configuration to the DS5 data. ^{60}Co and ^{40}K peaks are reasonably predicted, along with the continuum. ^{232}Th and ^{238}U peaks are, however, underpredicted. This suggests that the ^{232}Th and ^{238}U activities are underestimated by the chosen assay samples. The 2614 keV ^{208}Tl (^{232}Th) peak, for instance, would need to increase by roughly a factor

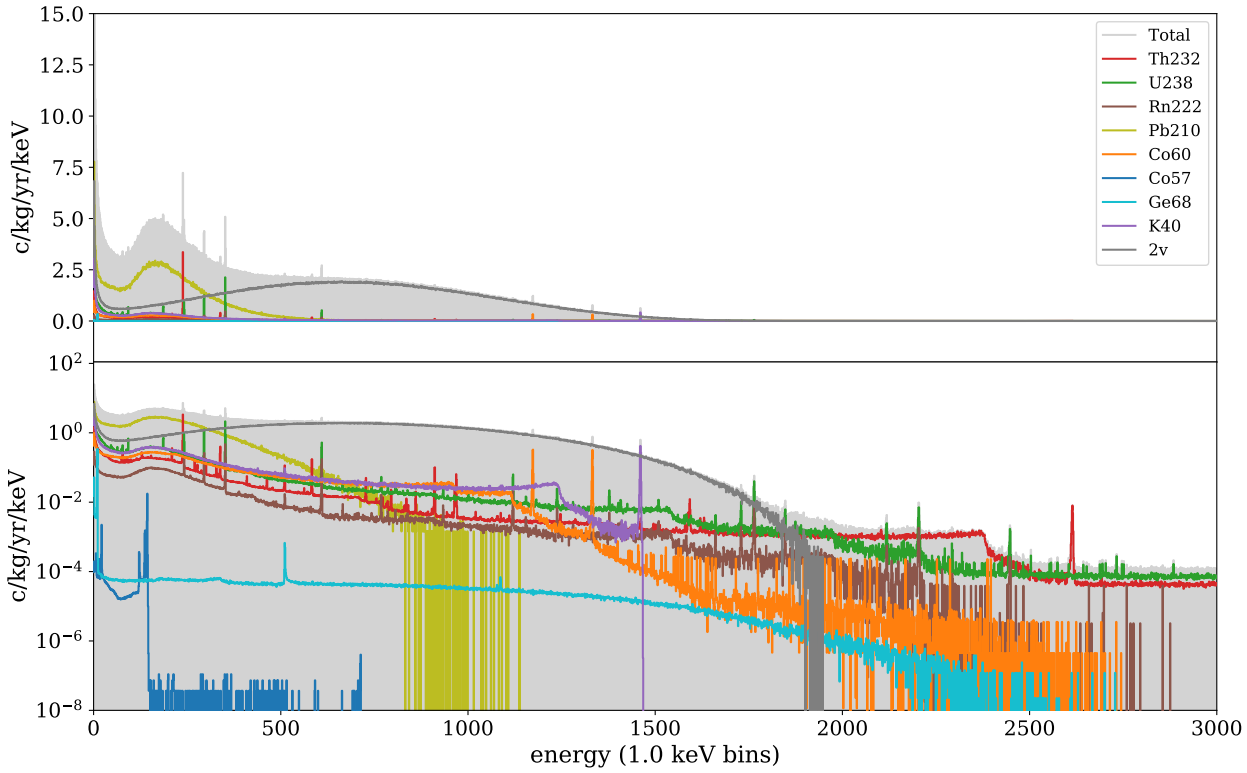

Figure 6.1: The expected individual and summed background contributions based on as-built simulations, masses, and assay selection. The simulations shown here assume all detectors are operational with the multiplicity and PSA cuts applied, and contributions from both $^{\text{nat}}$Ge and $^{\text{enr}}$Ge are included.

of five to match the data. An increase to these activities would also lead to a rise in their backscatter peaks near 200 keV— this in turn suggests that the activity of the ^{210}Pb component should be lowered, an offset needed in order to maintain agreement at those lower energies. Furthermore the better prediction of the lower energy ^{238}U and ^{232}Th peaks as compared to, say, their 1764 and 2614 keV peaks suggests the additional unaccounted for activity is from distant components from which lower energy gammas would be attenuated to a greater degree.

A comparison of the expected model and data for DS0, for which the lack of inner copper shield leads to greater sensitivity to ^{210}Pb from the Pb shield, is consistent with suggestions from the DS5 comparison. Namely, the ^{210}Pb contribution is over-predicted and the 2614 keV peak is once again under-predicted. Fig 6.3 displays this DS0 comparison.

The comparison of Fig 6.2, along with the expected background index of 1.59×10^{-3} c/(keV kg yr) from Section 6.2, highlights the under-prediction of the observed background

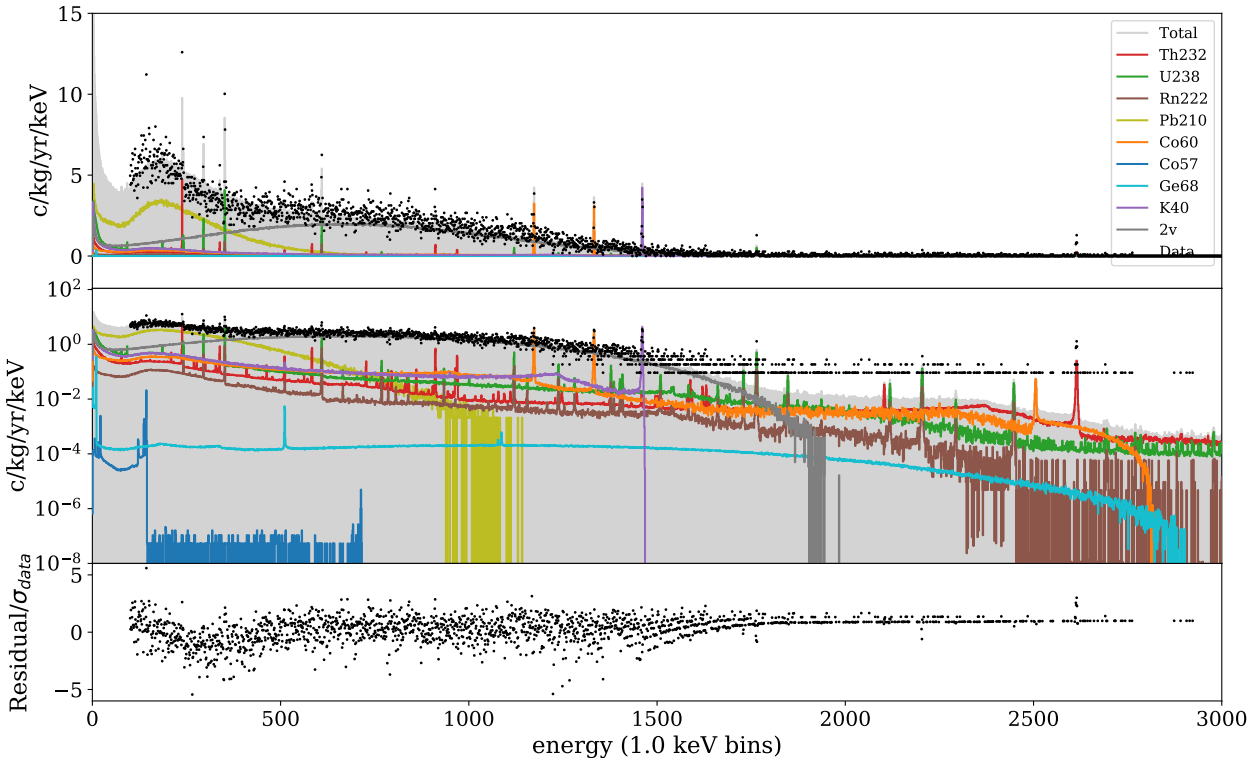

Figure 6.2: The individual and summed background contributions expected for the DS5 configuration based on as-built simulations, masses, and assay selection. Both $^{\text{nat}}$Ge and $^{\text{enr}}$Ge are included with the multiplicity cut applied. The analogous DS5 data is overlaid for comparison and normalized residuals are calculated.

index of Section 4.4, $4.7 \pm 0.8 \times 10^{-3}$ c/(keV kg yr). Based on the qualitative assessments of this section, the under-prediction likely stems from low predictions of ^{232}Th activity in distant components. A more detailed approach to the inference of under-predicted background sources will require the regression techniques discussed in later chapters.

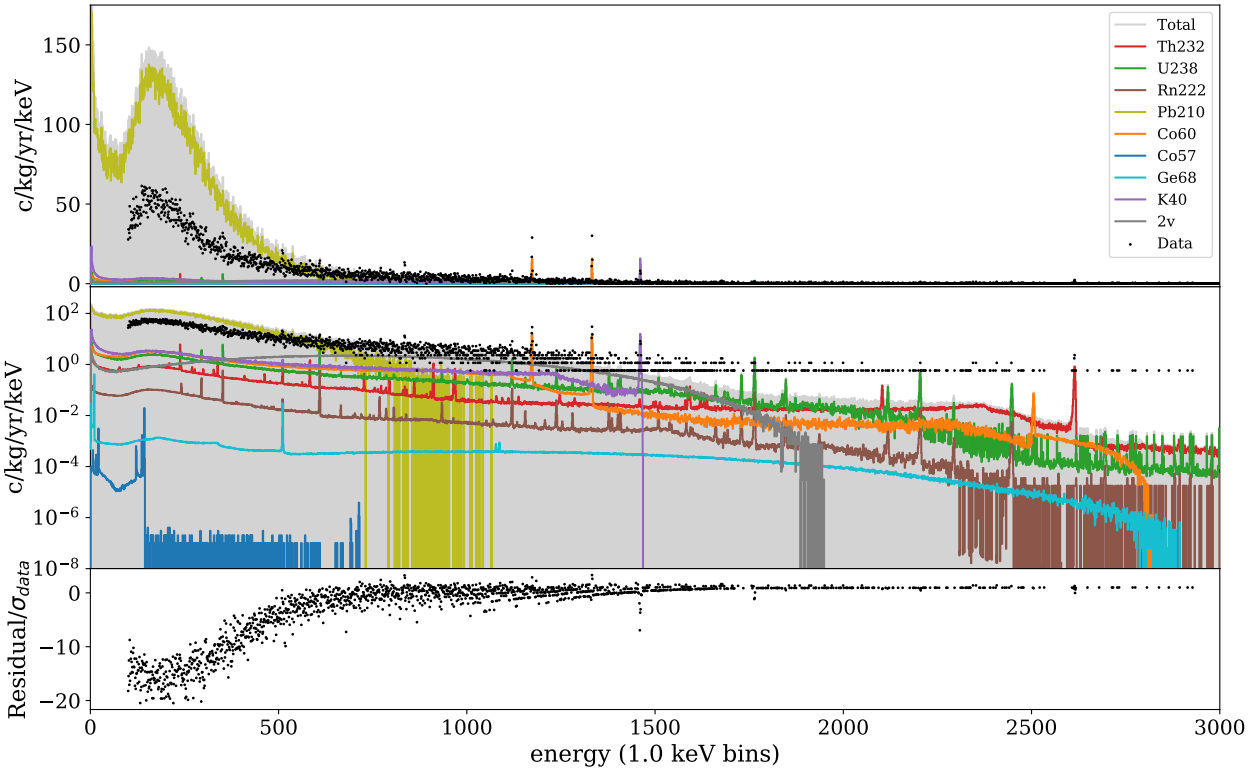

Figure 6.3: The individual and summed background contributions expected for the DS0 configuration based on as-built simulations, masses, and assay selection. Both ^{nat}Ge and ^{enr}Ge are included with no cuts applied. The analogous DS0 data is overlaid for comparison and normalized residuals are calculated.

CHAPTER 7
Toward Background Model Inference

With the expected background model in place, further inference is possible via regression of simulations to data. Regression faces numerous challenges, among them high-dimensionality of the model, degenerate model components, limited data, and limited simulation statistics. To counteract these challenges, an understanding of the physics can guide the grouping of components, and model selection procedures can be put in place to incorporate only those components which are most explanatory. Prior knowledge on component activities from assay can break degeneracies and constrain the total parameter space within the assay uncertainties.

In the following, Section 7.1 builds knowledge for which model components may be most significant by comparing MAJORANA data to the many individually simulated components. Chapter 8 then describes methods for incorporating those many components into a single statistical model, along with computational methods for inferring the most significant components.

Section 7.2 provides further comparison of simulations and data, this time examining the ^{228}Th calibration data described in Chapter 3. Comparison of individual detector spectra tests the simulations' ability to reproduce the source's location with the effects of intervening material, and tests the background model's ability to predict the activity of the calibration source.

7.1 Comparison of Simulations to Peaks in Data

The strength of observed peaks in the data depends on a number of factors including the concentration and lifetime of radionuclides, the branching among decay modes, attenuation of emitted radiation, and solid angle subtended by the source with respect to detectors. Though some of these effects can be constrained by analysis of data alone, comparison with simulations simultaneously accounts for all of these effects.

To gain intuition for which components best match the observed background data, a comparison was made between the ^{232}Th or ^{238}U spectrum of each simulated component and the observed γ peaks in the data. For each ^{232}Th or ^{238}U component spectrum, that particular spectrum was isolated, and the remaining contaminant spectra from all other components were combined and held fixed to their assay values. Then the isolated ^{232}Th or ^{238}U spectrum was incorporated and scaled so that the total model matched the data at the most active peak in the given decay chain. Based on Table 4.3, the peaks chosen for scaling were 238.6 keV from ^{212}Pb (^{232}Th) and 351.9 keV from ^{214}Pb (^{238}U).

With the total model now matching the strongest observed peak in a given decay chain, count rates were calculated at the energies of other notable peaks in the decay chain. The count rates calculated from the full simulated spectrum were compared to those from the observed data and a χ^2 statistic was calculated.

For the ^{232}Th chain, the simulated components yielding the lowest χ^2 value were the inner Cu shield, thermosyphon and shield Vespel, cables along the crossarm tube, connectors atop the coldplate, and cables atop the coldplate. Likewise, for ^{238}U, the components best matching the peaks were the LMFEs, parylene coated DU copper, the germanium crystals, and DU copper surfaces. These lists indicate components whose spectral shapes best match the data, and while they do not necessarily align with the components expected to have highest activity based on assay, they do suggest a trend: The ^{232}Th components that best match the observed ^{232}Th peaks all lie above the cold plate and beyond— distant from the detectors—, while the best-matched ^{238}U components lie below the coldplate close to the detectors. It is interesting to note that, though the inner Cu shield matches well with the observed ^{232}Th peaks, the outer Cu shield provides a poor match. These results, calculated for the combination of DS1-6a, are compiled in Table 7.1.

Fig 7.1 and 7.2 display the scaled inner Cu shield and LMFE ^{232}Th spectra. The ^{232}Th peaks at high and low energies are reasonably approximated by the distant inner Cu shield, though such scaling would require a factor of 10^2 increase from the expected activity of that component and an over-prediction of ^{232}Th backscatter. In contrast, the ^{232}Th spectrum of nearby LMFEs under-predicts peak strengths at higher energies. Fig 7.3 and 7.4 offer the analogous comparison for the ^{238}U chain. These simulations do not account for the 143.6 keV ^{57}Co line discussed, for instance, in Section 4.3.

Table 7.1: Comparison of simulated peaks to those observed in DS1-6a data. For ^{232}Th and ^{238}U, the listed individual simulated components were scaled to match the 238.6 keV ^{212}Pb or 351.9 keV ^{214}Pb peak, respectively. Components best matching the data are included here, along with the best-matched component of the opposing decay chain for comparison. As the scaled simulation spectra are binned, peak rates in this table were calculated via binned integration for both simulations and data.

^{232}Th Isotope	^{228}Ac	^{228}Ac	^{228}Ac	^{212}Bi	^{208}Tl	^{208}Tl
E_γ (keV)	338.3	911.2	969.0	727.3	583.2	2614.5
I_γ (%)	11.2	26.6	16.2	6.7	84.5	99.2
Data Rate (c/(kg yr))	2.4 (1.7, 3.1)	5.7 (5.0, 6.5)	1.3 (0.6, 2.1)	1.3 (0.6, 2.1)	4.7 (3.9, 5.5)	4.1 (3.7, 4.4)
RadShieldCuInner	2.1 (1.4, 2.9)	3.7 (3.0, 4.4)	1.9 (1.2, 2.6)	1.1 (0.4, 1.7)	4.4 (3.6, 5.1)	3.9 (3.6, 4.2)
ThermosyphonAndShieldVespel	2.1 (1.4, 2.9)	3.3 (2.6, 4.0)	1.7 (1.1, 2.5)	1.0 (0.3, 1.6)	4.1 (3.4, 4.9)	3.0 (2.7, 3.3)
CrossarmCables	2.1 (1.3, 2.8)	3.1 (2.4, 3.7)	1.6 (0.9, 2.3)	1.0 (0.3, 1.6)	4.1 (3.4, 4.9)	3.1 (2.8, 3.4)
Connectors	2.1 (1.4, 2.9)	3.0 (2.4, 3.7)	1.6 (0.9, 2.3)	0.9 (0.3, 1.5)	3.9 (3.2, 4.6)	2.5 (2.3, 2.8)
ColdplateCables	2.2 (1.4, 2.9)	3.1 (2.4, 3.7)	1.5 (0.8, 2.2)	0.9 (0.3, 1.5)	3.7 (3.1, 4.5)	2.4 (2.2, 2.7)
—						
LMFEs	1.9 (1.1, 2.6)	2.0 (1.4, 2.7)	1.0 (0.4, 1.6)	< 1.7	2.7 (2.0, 3.4)	1.3 (1.2, 1.6)
^{238}U Isotope	^{214}Pb	^{214}Pb	^{214}Bi	^{214}Bi	^{214}Bi	^{214}Bi
E_γ (keV)	241.9	295.2	609.3	1120.3	1764.5	2204.1
I_γ (%)	7.5	19.2	46.1	15.0	15.9	5.0
Data Rate (c/(kg yr))	< 1.3	4.5 (3.7, 5.4)	6.0 (5.2, 6.8)	1.2 (0.7, 1.8)	1.7 (1.5, 2.0)	0.4 (0.3, 0.6)
LMFEs	< 1.9	5.0 (4.2, 5.9)	7.3 (6.6, 8.1)	1.7 (1.2, 2.2)	1.8 (1.6, 2.0)	0.5 (0.4, 0.6)
DUCoatedCu	< 1.9	5.0 (4.2, 5.9)	7.4 (6.7, 8.2)	1.7 (1.2, 2.2)	1.8 (1.6, 2.0)	0.5 (0.4, 0.6)
Ge	< 1.8	4.7 (3.8, 5.5)	7.3 (6.5, 8.1)	1.8 (1.2, 2.3)	1.8 (1.5, 2.0)	0.5 (0.4, 0.7)
DUCu Surface	< 1.9	5.0 (4.2, 5.9)	7.4 (6.7, 8.2)	1.8 (1.3, 2.3)	1.7 (1.6, 2.0)	0.5 (0.4, 0.6)
StringCables	< 1.9	5.0 (4.2, 5.9)	7.5 (6.8, 8.3)	1.8 (1.3, 2.3)	1.8 (1.6, 2.0)	0.5 (0.4, 0.6)
—						
RadShieldCuInner	< 1.8	4.6 (3.8, 5.5)	8.5 (7.7, 9.3)	2.3 (1.8, 2.9)	2.4 (2.2, 2.7)	0.7 (0.6, 0.9)

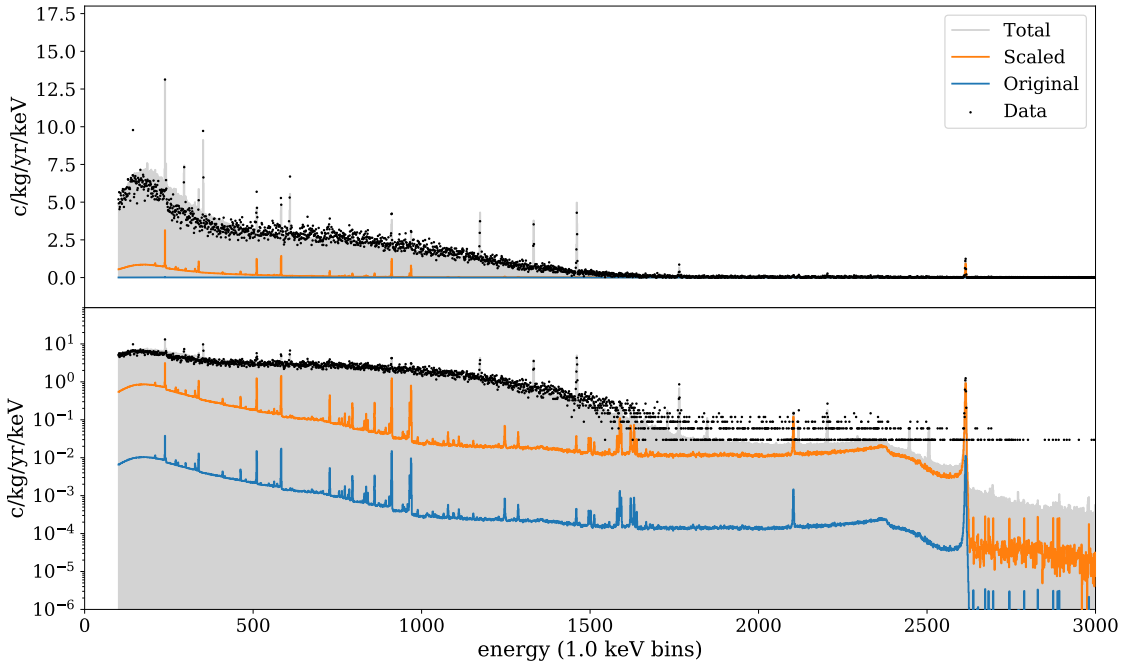

Figure 7.1: ^{232}Th from the inner Cu shield reasonably approximates high and low energy peaks when scaled to the 238.6 keV peak from ^{212}Pb.

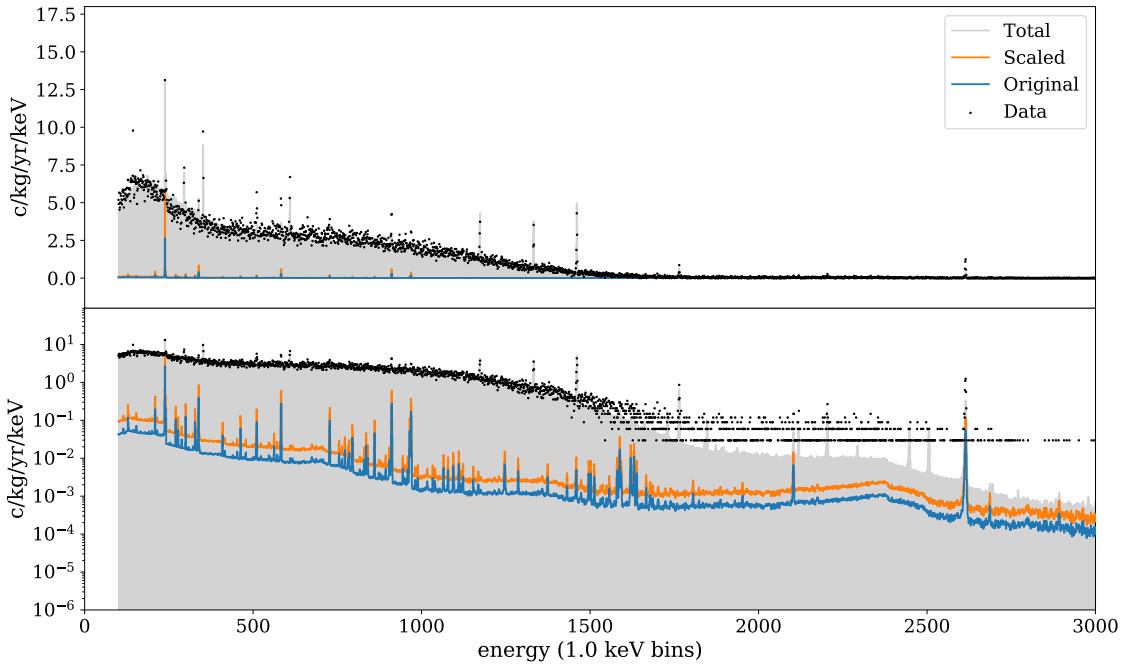

Figure 7.2: ^{232}Th from the LMFEs under-predicts high energy peaks when scaled to the 238.6 keV peak from ^{212}Pb.

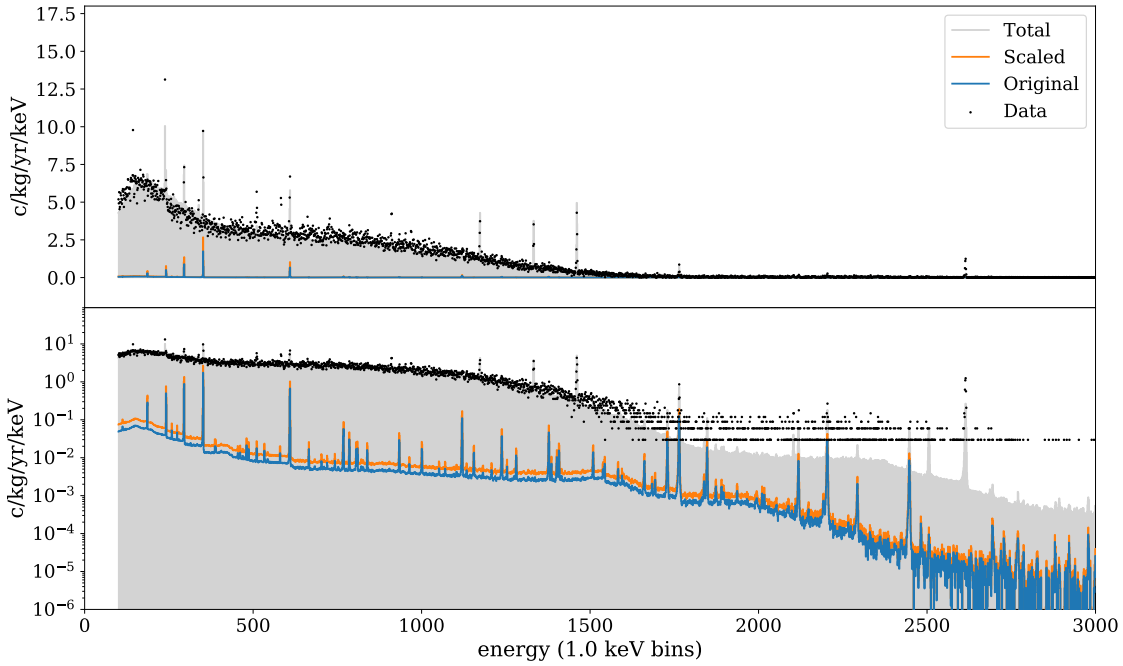

Figure 7.3: ^{238}U from the LMFEs reasonably approximates peaks when scaled to the 351.9 keV peak from ^{214}Pb.

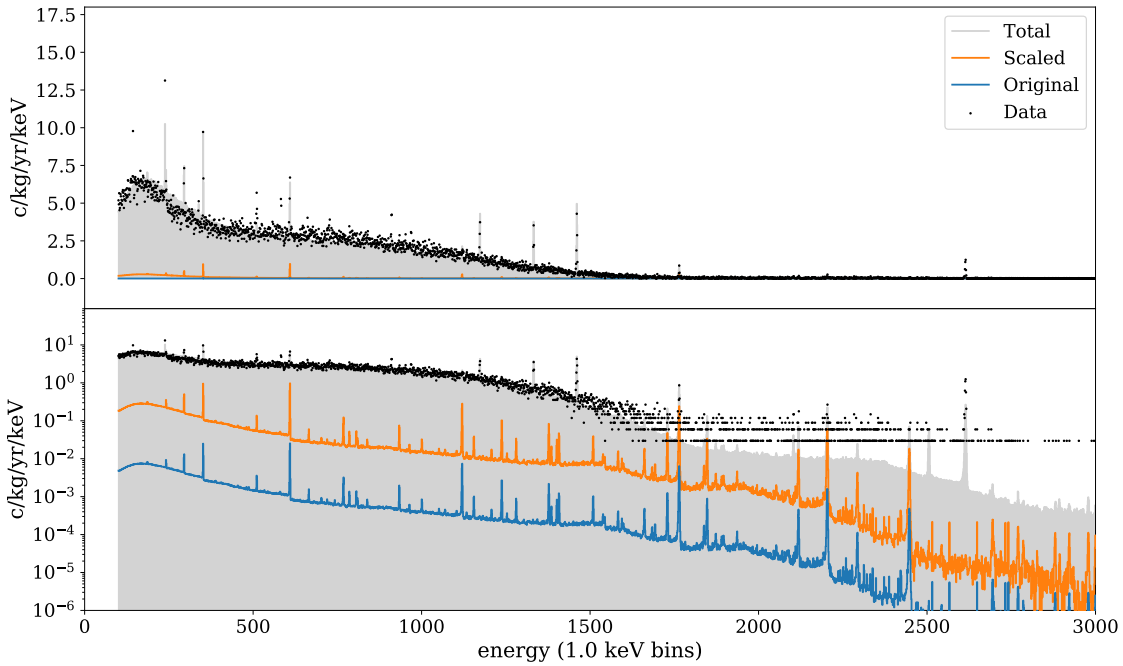

Figure 7.4: ^{238}U from the inner Cu shield over-predicts higher energy peaks when scaled to the 351.9 keV peak from ^{214}Pb.

7.2 Comparison of Simulations to Calibration Data

As discussed in Chapter 3, each MAJORANA cryostat is equipped with a calibration system. During calibration runs, either the M1 or M2 ^{228}Th calibration source is deployed, being inserted into its helical track surrounding a cryostat. The calibration track is shown in Fig 7.5. The calibration sources are 2 m long, each with integrated activities of 10360.0 $\pm$ 210.0 Bq measured on May 1, 2013. Deviations in activity along the length of the sources are within 3% [38].

Figure 7.5: PTFE tubing wraps helically around each cryostat forming a track for a calibration line source.

The positioning of the calibration track is reflected in the event rates of detectors in various locations of the array. Comparison of simulations to subsets of M1 and M2 DS5b calibration runs reveals that the simulations reasonably reconstruct the data; a subset of 11 contiguous calibration runs was selected for each module. Figures 7.6 and 7.7 compare simulations to M1 and M2 calibration source runs under the data cleaning and DCR cuts, with all operational detectors included. In these figures, the residuals are multipolar at peaks due to slight mismatch in energy resolution between the simulations and aggregated data. The systematically larger residuals below 500 keV are discussed in the following section.

DS5b was collected 1392 dy after the initial source activity measurement. The expected source activities during DS5b are thereby reduced to 2603.1 $\pm$ 52.8 Bq according to the 1.9125 yr half life of ^{228}Th.

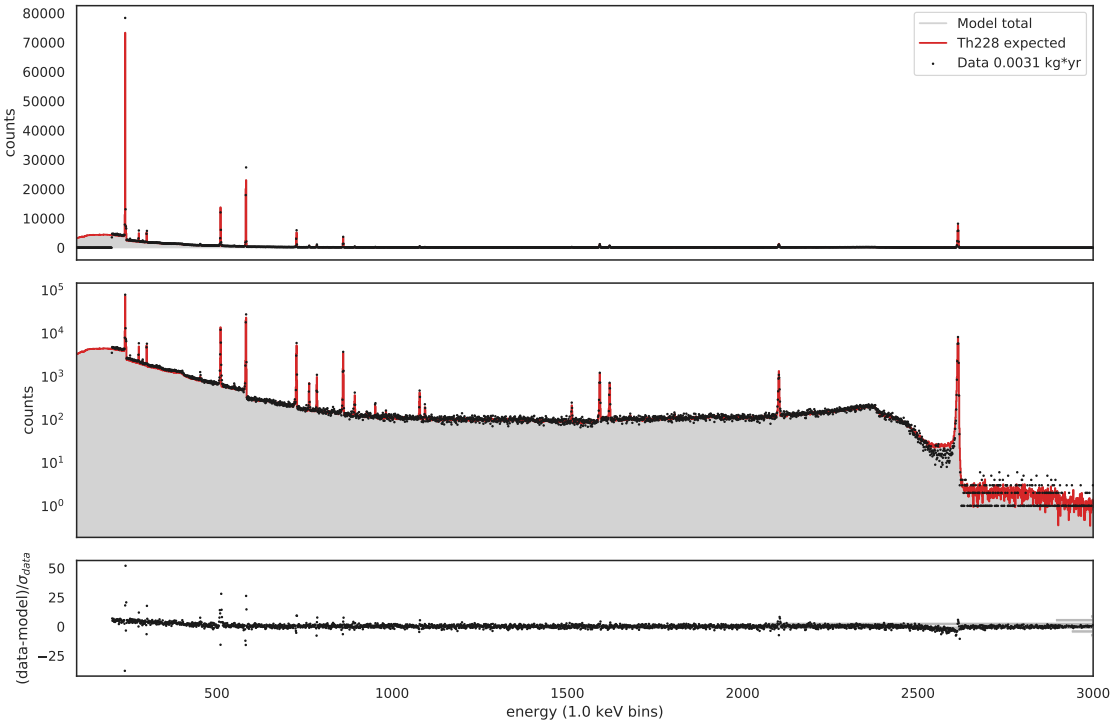

Figure 7.6: Data from DS5b M1 calibration source runs compared with analogous simulations. Data cleaning and DCR cuts are applied, and both $^{\text{nat}}$Ge and $^{\text{enr}}$Ge are included.

Agreement between data and simulations is also seen on an individual detector basis, indicating the simulations' faithful reconstruction of the experimental configuration during calibration runs. Comparisons for all operational detectors during M1 and M2 calibration source runs are included in Appendix C. Data from detector C2P6D2 appears with fewer counts than expected based on the calibration simulations and source activities.

7.3 Effects of Modeling the Lithiated Layer and Cuts

As introduced in Sections 3.1 and 5.2, incomplete charge collection occurs for events interacting in the lithiated outer layer of detectors. The effect leads to degraded energy events, shifting events into low-energy tails of spectral peaks and populating a continuum of events at energies below 500 keV. For each $^{\text{enr}}$Ge detector, the properties of the lithiated layer are determined through comparison of calibration data and analogous simulations. $^{\text{nat}}$Ge detectors are similar in geometry and each is treated with the same lithiated layer model. The result of modeling the lithiated layers is evident in

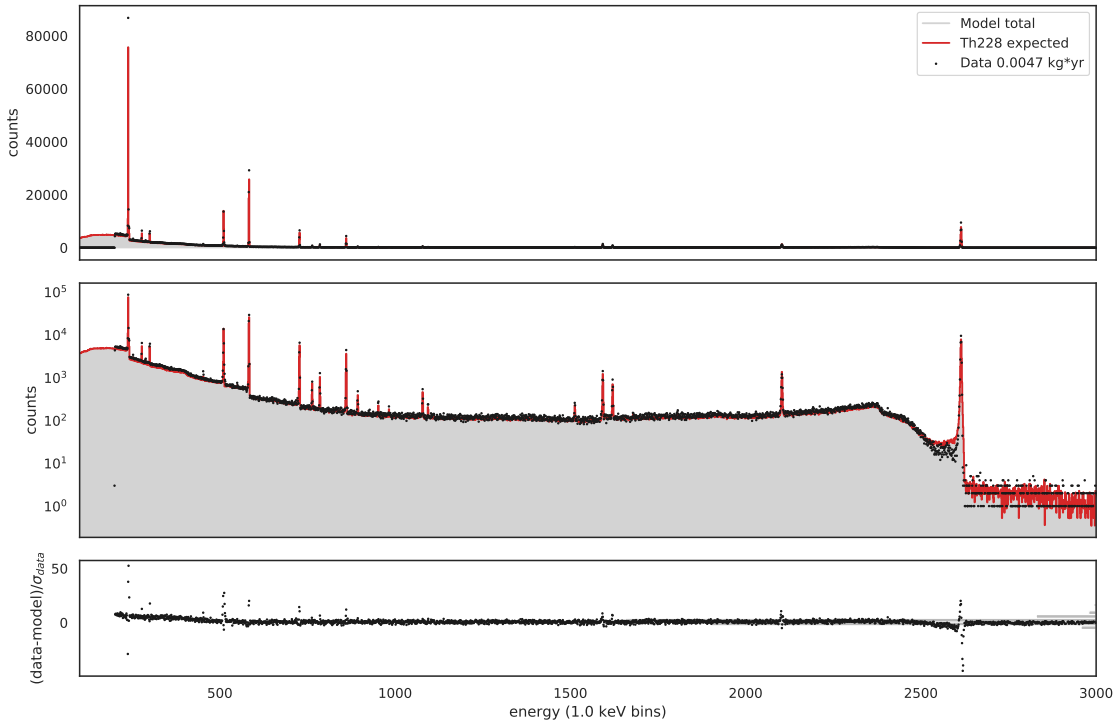

Figure 7.7: Data from DS5b M2 calibration source runs compared with analogous simulations. Data cleaning and DCR cuts are applied, and both $^{\text{nat}}$Ge and $^{\text{enr}}$Ge are included.

Figures 7.6 and 7.7 for which the agreement between simulation and data is generally strong. As indicated by the residuals, however, the modeling assumes too many events in the low-energy tail of the 2615 keV peak— typically populated by multiple Compton scatters within a detector— and too few events in the continuum below 500 keV.

The modeling of cuts can also be evaluated through comparison of calibration data and simulations. Fig 7.8 displays multiplicity-one calibration data alongside the expectation based on knowledge of the DS5b configuration and initial ^{228}Th source activities. The agreement is reasonable, while retaining the same under- and over-estimates noted in Fig 7.6 due to modeling of the lithiated layer. A comparison for M2 shows similar results.

Fig 7.9 adds the effect of the PSA cut. Agreement is reasonable at low energies, but too few events are expected to survive at energies above 1500 keV. A comparison for M2 shows similar results. With the PSA cut in place, under-prediction by the simulations would instill a bias toward greater component radioactivities in regression results.

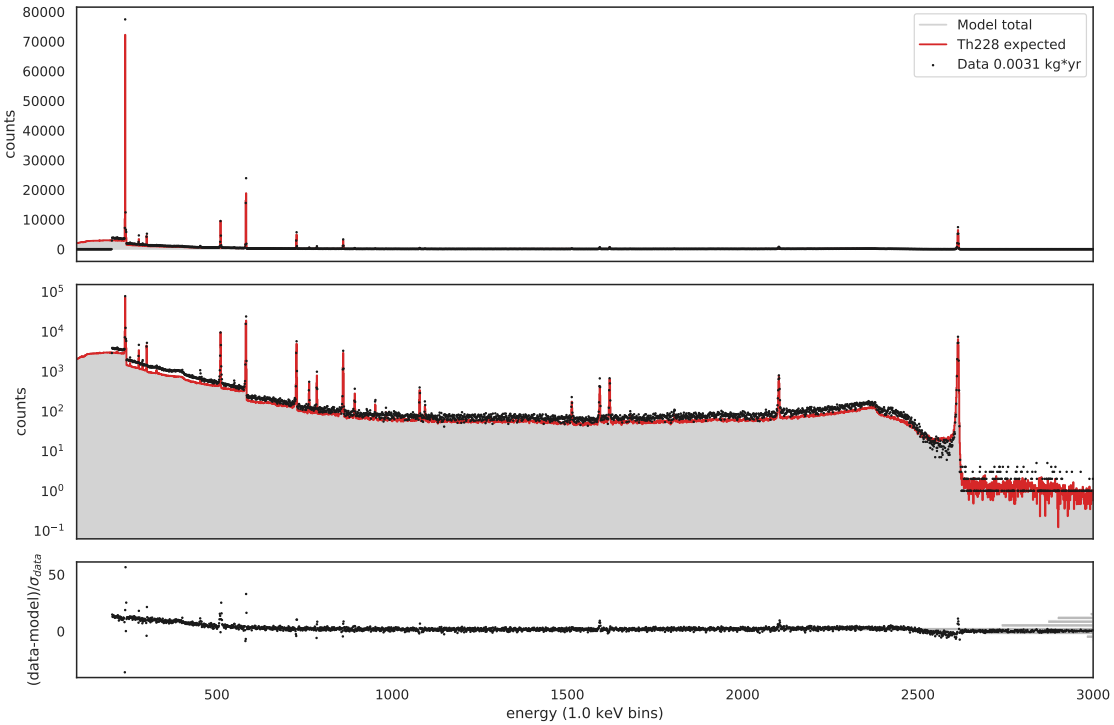

Figure 7.8: Data from DS5b M1 calibration source runs compared with analogous simulations. Data cleaning, multiplicity, and DCR cuts are applied, and both $^{\text{nat}}$Ge and $^{\text{enr}}$Ge are included.

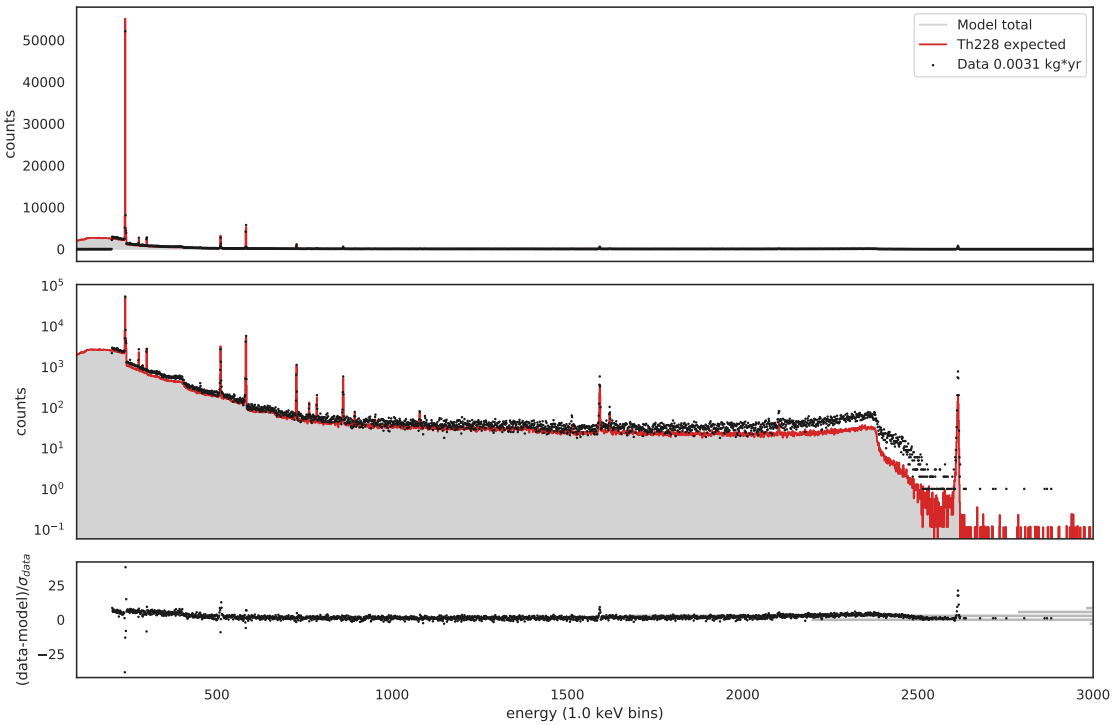

Figure 7.9: Data from DS5b M1 calibration source runs compared with analogous simulations. Data cleaning, multiplicity, multisite, and DCR cuts are applied, and both $^{\text{nat}}$Ge and $^{\text{enr}}$Ge are included.

CHAPTER 8
Inference Methods

Statistical inference involves the calculation of expectation values of a function $f(\theta)$ with respect to a target distribution $\pi(\theta)$ over the space of the parameters θ

$$\mathrm{E}_\pi[f(\theta)] = \int f(\theta)\pi(\theta)\mathrm{d}\theta. \tag{8.1}$$

In a Bayesian context, the target distribution is taken as the posterior distribution of the parameters conditioned on observed data X

$$\pi(\theta|X) = \frac{p(X|\theta)p(\theta)}{p(X)} \tag{8.2}$$

where terms on the right hand side represent the likelihood of the data conditioned on parameters $p(X|\theta)$, the prior distribution on the parameters $p(\theta)$, and the marginalized likelihood for observing the data $p(X)$.

With access to a target posterior distribution, subsequent calculations of expectation values can yield mean values, moments, credible intervals, and so forth. In general, however, analytic evaluation of the target distribution needed for Eqn 8.1 is not possible. Approximation techniques become necessary and Monte Carlo (MC) integration is one such technique with wide applicability, approximating integration via the discrete sum of samples from a target function. That is,

$$\int \pi(\theta)\mathrm{d}\theta \approx \frac{V}{N}\sum_{i=1}^{N}\pi(\theta^{(i)}) \tag{8.3}$$

with N samples $\{\theta^{(1)}, ..., \theta^{(N)}\}$ drawn from $\pi(\theta)$ within some volume V of parameter space.

Approximate expectation values follow from the same set of MC samples as

$$\mathrm{E}_\pi[f(\theta)] \approx \frac{1}{N}\sum_{i=1}^{N} f(\theta^{(i)}). \tag{8.4}$$

By the Central Limit Theorem, these expectation values will be normally distributed with standard error proportional to $1/\sqrt{N}$. The value of N is controlled by the analyst and can be adjusted to yield desired accuracy [74, 75].

8.1 Markov Chain Monte Carlo

The aforementioned MC approximations rely on samples being drawn in correct proportions from the target distribution $\pi(\theta)$. In general, the form of $\pi(\theta)$ will be non-standard such that it is difficult to directly draw independent samples. In this case, a Markov chain can be employed by which a series of draws— conditional only on their immediate predecessor— eventually converges to a stationary distribution which has been set to $\pi(\theta)$ by design. This approach is known as Markov chain Monte Carlo (MCMC).

In the familiar Metropolis-Hastings MCMC algorithm, a Markov chain proceeds from a current value $\theta^{(i)}$ to a next value $\theta^{(i+1)}$ with a probability given by the transition kernel

$$\begin{aligned} p(\theta^{(i+1)}|\theta^{(i)}) = q(\theta^{(i+1)}|\theta^{(i)})\alpha(\theta^{(i)},\theta^{(i+1)}) \\ + I(\theta^{(i+1)} = \theta^{(i)}) \left[1 - \int q(Y|\theta^{(i)})\alpha(\theta^{(i)},Y)\mathrm{d}Y\right]. \end{aligned} \tag{8.5}$$

Before a transition is made, a new value for the Markov chain is proposed and either accepted or rejected. The two terms of the transition kernel encode the probabilities for either accepting this proposed value or rejecting it, and their sum represents the total probability for making a given transition via either path.

The first term in the transition kernel describes the probability that the Markov chain moves to $\theta^{(i+1)}$ via proposal and acceptance of that value, where $q(\theta^{(i+1)}|\theta^{(i)})$ is the conditional probability of proposing $\theta^{(i+1)}$ and $\alpha(\theta^{(i)},\theta^{(i+1)})$ is the probability of accepting that proposal. The second term describes the probability that the Markov chain moves to $\theta^{(i+1)}$ via rejection of any proposed value Y. In this case, the chain remains at its current value by rule, setting $\theta^{(i+1)}$ to the value of $\theta^{(i)}$. The indicator function I is equal to one if its argument is true, and zero otherwise. The acceptance probability is computed from the proposal and target distributions by taking the minimum of [74]

$$\alpha(\theta^{(i)},\theta^{(i+1)}) = \min\left\{1,\ \frac{\pi(\theta^{(i+1)})q(\theta^{(i)}|\theta^{(i+1)})}{\pi(\theta^{(i)})q(\theta^{(i+1)}|\theta^{(i)})}\right\}. \tag{8.6}$$

With the above in place, the Metropolis-Hastings MCMC algorithm proceeds in pseudo-code as follows.

```
Initialize N to total number of steps in chain
Initialize X to any starting value for chain
Initialize i to 0
While i < N:
        Sample Y from q(Y|X)
        Sample U from Uniform(0,1)
        If U <= alpha(X,Y): Set X to Y
        Increment i
```

8.2 Hamiltonian Monte Carlo

The greatest contribution to expectation values comes from the target distribution's region of greatest probability mass, known as the typical set. To efficiently approximate expectations, a Markov chain should then quickly converge to and explore the typical set, avoiding low-impact exploration of the volume of parameter space for which the target is of low density. For distributions of increasing dimension, the parameter space volume grows rapidly and regions of high density occupy a diminishing fraction of the total volume. As a result, the typical set narrows and becomes more singular in an effect known as concentration of measure.

Simple implementations of the Metropolis-Algorithm will scale poorly with increasing dimension of the target distribution. In such cases, the proposal distribution comes to favor exploration over volumes much larger than the narrow crevices into which the typical set concentrates. The typical set then goes unexplored and the Markov chain stagnates, sampling only points of low density on the boundary of the typical set. The scale of the proposal distribution can be reduced to access the typical set, but the resulting small step sizes lead to slow exploration of the full typical set.

The effects of increasing dimension, and the need of the MCMC algorithm to adapt to the geometry of the typical set motivate Hamiltonian Monte Carlo (HMC) as an advancement beyond Metropolis-Hastings. HMC treats the target distribution as a physical potential and introduces auxiliary momenta to construct trajectories that explore the typical set [76, 77, 78].

In the Hamiltonian formalism, we reinterpret the parameters θ as spatial coordinates q. The target distribution is then expanded with momenta p, one for each spatial coordinate,

$$\pi(q) \to \pi(q, p), \tag{8.7}$$

and the joint distribution $\pi(q, p)$ describes phase space. Factoring this joint distribution as $\pi(p|q)\pi(q)$ separates the terms into familiar kinetic and potential energy terms, with respective dependencies on both p and q, and q alone. Furthermore, this factoring correctly forms the Hamiltonian H as the total energy, or sum of the kinetic and potential energies $K(p, q)$ and $V(q)$

$$\begin{aligned} \pi(q, p) &= e^{-H(q,p)} \\ H(q, p) &= -\ln\left[\pi(q, p)\right] \\ &= -\ln\left[\pi(p|q)\pi(q)\right] \\ &= -\ln\left[\pi(p|q)\right] - \ln\left[\pi(q)\right] \\ &= K(p, q) + V(q). \end{aligned} \tag{8.8}$$

With H in place, each HMC transition proceeds first by sampling a momentum p from the conditional distribution $\pi(p|q)$. With p and q designated in phase space, Hamilton's equations are integrated to construct a trajectory through the typical set

$$\begin{aligned} \frac{\mathrm{d}q}{\mathrm{d}t} &= +\frac{\partial H}{\partial p} = \frac{\partial K}{\partial p} \\ \frac{\mathrm{d}p}{\mathrm{d}t} &= -\frac{\partial H}{\partial q} = -\frac{\partial K}{\partial q} - \frac{\partial V}{\partial q}. \end{aligned} \tag{8.9}$$

Note that $\partial V/\partial q$ represents the gradient of the target distribution. This incorporates the geometry of the distribution and leads to efficient exploration of the typical set; the exploration is coherent, contrasting the diffusive random walk of the Metropolis-Hastings algorithm. After integration, the parameter values are recovered by projecting away the momenta from $\pi(q, p)$ to $\pi(q)$. Several transitions are illustrated in the cartoon of Fig 8.1.

The techniques of HMC are extended, and sampling efficiency improved, in the No-U-Turn Sampler (NUTS) algorithm [79]. NUTS integrates a phase space trajectory both forward and backward in time stopping once the exploration begins to retrace its steps.

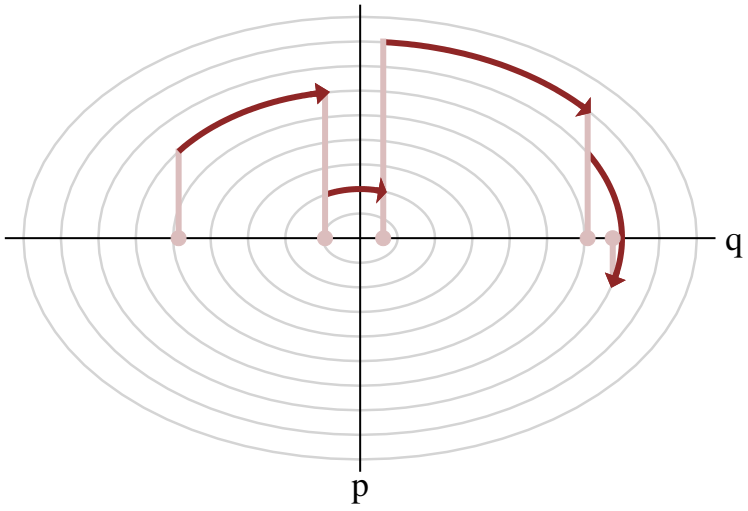

Figure 8.1: In each HMC transition, a momentum is proposed and a phase space trajectory is calculated. After traversing the trajectory, the explored parameters are recovered by projecting away the auxiliary momenta. Figure from Ref [78].

8.3 Statistical Model

The spectroscopic data collected by the MAJORANA DEMONSTRATOR arises from decay transitions that are Poisson distributed in time. Detectors record incident radiation from these transitions and events are binned according to their energy. As a measurement's exposure increases, an energy spectrum is populated with each bin accruing counts c_i in a Poisson time-distributed fashion according to an expected mean value of counts λ_i

$$p(c_i|\lambda_i) = \frac{\lambda_i^{c_i} e^{-\lambda_i}}{c_i!} \tag{8.10}$$

where the subscript i denotes values for the ith bin. In this way, Eqn 8.10 represents the likelihood for observing the counts c_i given an underlying mean value λ_i.

λ_i can be expanded as the product of exposure $\mathcal{E}$ and expected rate r_i, $\lambda_i = r_i\mathcal{E}$. With known $\mathcal{E}$, Eqn 8.10 then represents the likelihood of observing c_i counts in the ith bin for a given r_i. A regression procedure to infer r_i is complicated by the presence of multiple sources of counts. To account for this, r_i must be modeled as a mixture of sources each contributing with some weight,

$$r_i = \sum_j w_j s_{ji}. \tag{8.11}$$

Here, s_{ji} is the rate of source j in bin i assuming unit activity per mass, and w_j represents the activity per mass. For MAJORANA, the s_{ji} are obtained through radiation transport simulations, and Eqn 8.10 can be used to infer the most likely values of the w_j.

The simultaneous likelihood of all bins in the spectrum is obtained by taking the product over the individual likelihoods for each bin

$$\mathcal{L} = \prod_i p(c_i|\lambda_i). \tag{8.12}$$

Previous studies, including measurements from the MAJORANA assay campaign, provide constraints on the activity per mass of experimental hardware. These results correspond to the w_j and are reported as central values with standard error. For each of the w_j for which inference is sought, assay measurements are gathered, averaged, and encoded in a prior distribution. A truncated normal distribution is adopted for the priors, with a central assay value set as mean, its standard error set as the standard deviation, and the truncation set to exclude unphysical values below zero.

Together with the likelihood, the priors induce the posterior distribution according to Eqn 8.2. Credible intervals for the posterior probability of individual w_j are obtained by marginalization over the full posterior.

8.4 Probabilistic Programming

A Bayesian statistical model can be specified in code using a probabilistic programming (PP) framework. Such frameworks include tools for creating and sampling from random variables in a network of conditional dependencies known as a probabilistic graphical model [80]. Deterministic variables are also handled and their operations can be included in the model. PyMC3 is a PP framework that additionally includes tools for MCMC sampling from a Bayesian graphical model and tools for performing posterior analysis based on those MCMC samples [81].

The joint prior of Eqn 8.2 can be factored in a number of ways depending on assumptions of conditional independence among the free parameters of a model. With reference to the previous section, one such factorization might consider an independent w_j for each source s_{ji}, factoring $p(\theta)$

as

$$p(\theta) = p(\vec{w}) = \prod_j p(w_j). \tag{8.13}$$

This results in the graphical model of Fig 8.2, an arrangement referred to here as an unpooled model. In the graphical model of Fig 8.2, a separate random variable w_j— denoted by open nodes— is declared for each mixture component j. Edges connect those nodes to the observed variables c_i shown as shaded nodes. Along the edges between nodes, the w_j are multiplied by the corresponding s_{ji} in preparation for comparison with c_i. This follows the procedure of Section 8.3.

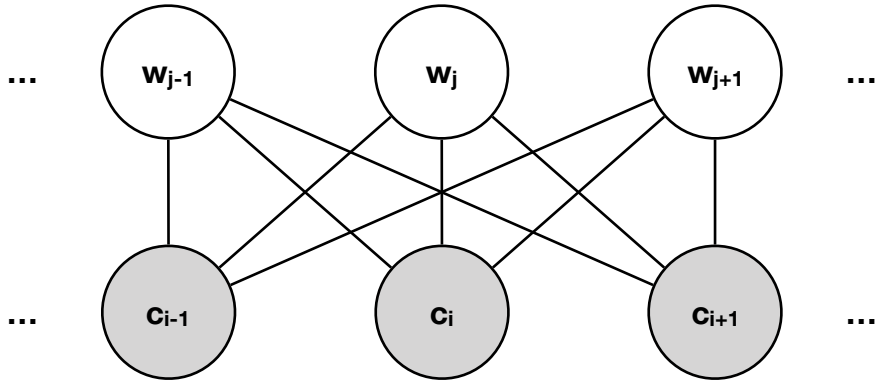

Figure 8.2: A probabilistic graphical model for unpooled parameters w_j in which no two mixture components share the same parameter. Open nodes represent random variables w_j and shaded nodes represent observed variables c_i.

An alternative construction of the model, typically used in this work, considers some of the w_j parameters to be shared between sources, pooling those parameters together as displayed in Fig 8.3. Still another specification, known as a hierarchical model, could consider some of the w_j as independent samples from a shared underlying random variable or hyperparameter h. The graph for such a model is included in Fig 8.4. A hierarchical approach can provide a compromise between the simplification of pooled models, which tends to underfit the data, and the full independence of parameters in unpooled models, which tends to overfit the data [82].

8.5 Summary

Several sources of background are expected in the MAJORANA DEMONSTRATOR and thus the observed energy spectrum is modeled as a mixture of those sources. With prior information available

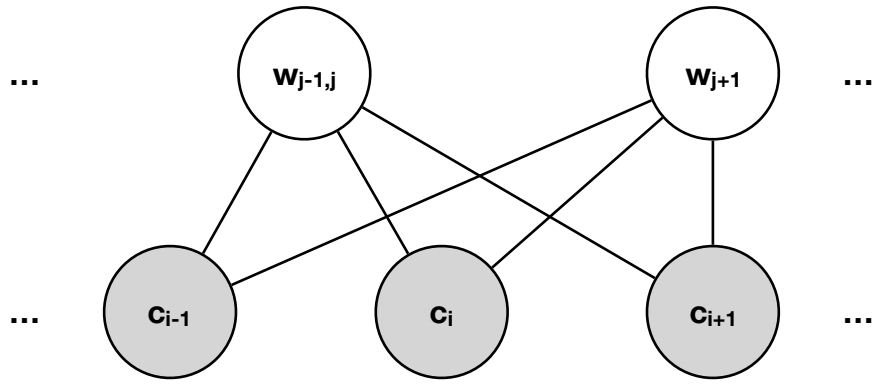

Figure 8.3: A probabilistic graphical model for pooled parameters w_j. In this diagram, mixture components $j-1$ and j share the same parameter. Open nodes represent random variables and shaded nodes represent observed variables.

from the assay of material radioactivities, it is natural to incorporate those measurements and express the background model in the Bayesian domain. In the resulting statistical model, an extensive list of simulated DEMONSTRATOR components are each assigned a free parameter representing the weight of that component in the mixture. The structure of conditional dependencies between parameters and observations is then encoded in the PyMC3 probabilistic programming framework.

With a model in place, optimization techniques can determine point values for each parameter that yield a best fit of the model to data. Alternatively, MCMC sampling techniques approximate the entire posterior and enable calculation of expectation values relative to those samples. From these samples, best fit parameters can be inferred along with estimates of uncertainty. Efficient sampling of the posterior is enabled by the gradient-based Hamiltonian Monte Carlo and No-U-Turn Sampler algorithms.

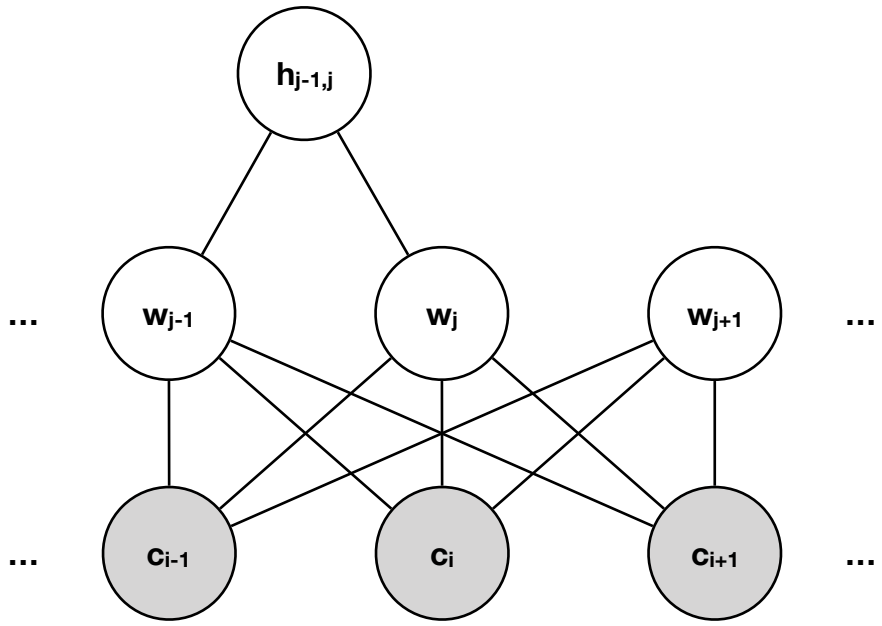

Figure 8.4: A probabilistic graphical model for parameters w_j related by a common hyperparameter. In this hierarchical diagram, parameters w_{j-1} and w_j are drawn from the same underlying distribution h. Open nodes represent random variables and shaded nodes represent observed variables.

CHAPTER 9
Background Model Inference

The MAJORANA DEMONSTRATOR data were characterized in Chapter 4. This initial work led to the simulation of background components in Chapter 5, and the scaling of those simulations according to assay in Chapter 6. Using the intuition built from studies in Chapter 7 and the methods of Chapter 8, the following sections describe regression of simulations to data to infer the relative strengths of components in the MAJORANA DEMONSTRATOR background model.

9.1 Model Components and Parameters

The full model used for inference incorporates the contribution of each contaminant present within each hardware component. As such, each component in the model is gathered from step 2 of the simulations processing described in Eqn 5.1. In total there are 148 unique combinations of contaminant decay chain and hardware component, including for instance

`2v_bulk_EnrGe`:	$2\nu\beta\beta$ within the $^{\text{enr}}$Ge bulk
`Th232_bulk_M2DUCopper`:	^{232}Th within the M2 DU EFCu bulk
`U238_bulk_M2CPSigCables`:	^{238}U within the M2 coldplate signal cable bulk
`Pb210_pbbrem_RadShieldPb`:	^{210}Pb within the Pb shield bulk
`Rn222_surf_N2`:	^{222}Rn from surfaces of the nitrogen purge volume

The first and third items in each component name indicate the simulated decay chain and hardware component. The second item indicates the generator used to produce decays in the MaGe simulations.

The model is further expanded according to the experimental configurations being considered. The full exposure of the DEMONSTRATOR considered in this work includes data sets 0-6a and a set of simulated components is produced for each distinct configuration. Additionally, the data can be viewed under several cuts and a set of simulated components is produced for each.

In full specificity, the simulated component names would be of the form

`decayChain_generator_hardwareComponent_configuration_cut`.

In the unpooled model of Fig 8.2, each component would be assigned its own free parameter for specific activity as described in Eqn 8.11 and Eqn 8.13. Certain hardware components and contaminants, however, persist between experimental configurations and cuts making it reasonable to associate the same specific activity with multiple simulated components. Sharing such parameters between components aligns with the pooled model of Fig 8.3 and reduces the total parameter space.

9.2 Evaluating DS0 for ^{210}Pb Activity

The DS0 configuration, which includes neither the inner Cu shield nor M2, differs most from the other data sets. Without the inner Cu shield, the contribution of ^{210}Pb from the Pb shield dominates in DS0. With this in mind, initial regressions of simulated components to DS0 data were executed, with the goal of refining the constraint on ^{210}Pb activity.

Three separate models were evaluated via the MCMC regression procedure of Chapter 8. The first model compared DS0 data under data cleaning and DCR cuts to the analogous simulations. The second model compared DS0 data under data cleaning, multiplicity, and DCR cuts to the analogous simulations. The third model considered the DS0 data under both of these sets of cuts simultaneously. In this third model, the parameters for specific activity were pooled among simulated components that differed only in cut.

The third model yielded the smallest percent statistical uncertainty on the fitted parameter for the specific activity of ^{210}Pb in the Pb shield, with the result of $(5.55 \pm 0.09) \times 10^5$ μBq kg^{-1} displayed in the marginal posterior distribution of Fig 9.1. The fitted spectral contributions of each decay chain are displayed in Fig 9.2.

The first and second models respectively yielded 5.48×10^5 and 5.73×10^5 μBq kg^{-1}. The 0.25×10^5 μBq kg^{-1} difference between these values was adopted as the estimated error on the activity, and the final result $(5.55 \pm 0.25) \times 10^5$ μBq kg^{-1} was used to update the corresponding prior distribution for later fits to DS1-6a.

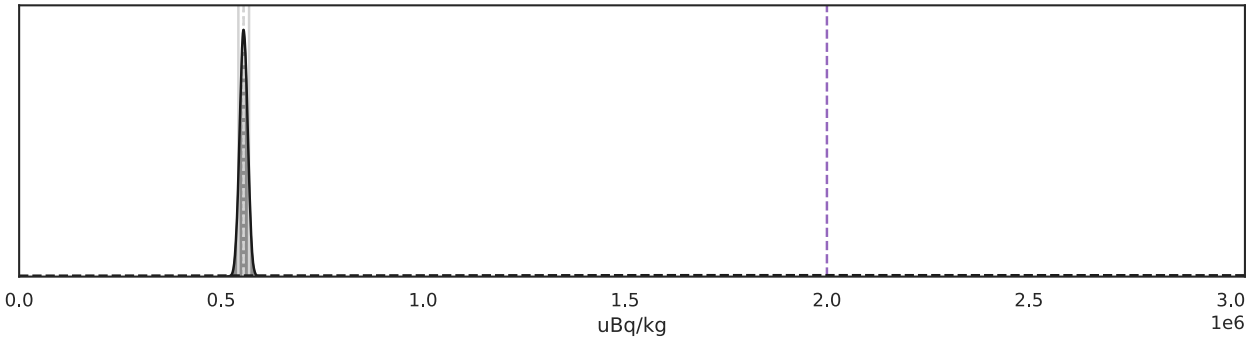

Figure 9.1: Marginal posterior for the specific activity of ^{210}Pb in the Pb shield inferred from regression of DS0 simulations to data. The posterior (solid black) indicates a value roughly four times less than the expected value encoded in the prior distribution (dashed purple).

9.3 Systematic Errors in Fits

The regression procedure for spectral fits requires a number of settings such as the bin width for simulated and observed spectra, and the energy range over which the likelihood function is evaluated. The choice of values for these settings can bias results, and the following discussion seeks to characterize the magnitude of the error.

9.3.1 Energy Range

The energy range over which the likelihood is evaluated can affect results by inclusion or omission of key spectral features. Exclusion of the 2614 keV ^{232}Th peak, for instance, may induce systematic under-estimation of ^{232}Th activity in hardware components. Likewise, truncation of low-energy continua could lead to under-emphasis of components that involve effects of Compton backscatter, bremsstrahlung, or energy degradation in the lithiated layer of detectors. As such, several models were constructed and executed to gauge the effect of energy range on fits.

Using open DS1-6a data under data cleaning and DCR cuts, the ranges 50-3000, 50-2617, 100-2617, and 100-3000 keV were evaluated. Additional models were tested for 0-3000 keV and 0-2617 keV, but both regression procedures stalled due to the mismatch between simulations and data at the lowest energies, likely due to noise events in some data sets. Of the four tested ranges, the lower limits were chosen to explore the potential of data below the 100 keV threshold of blind

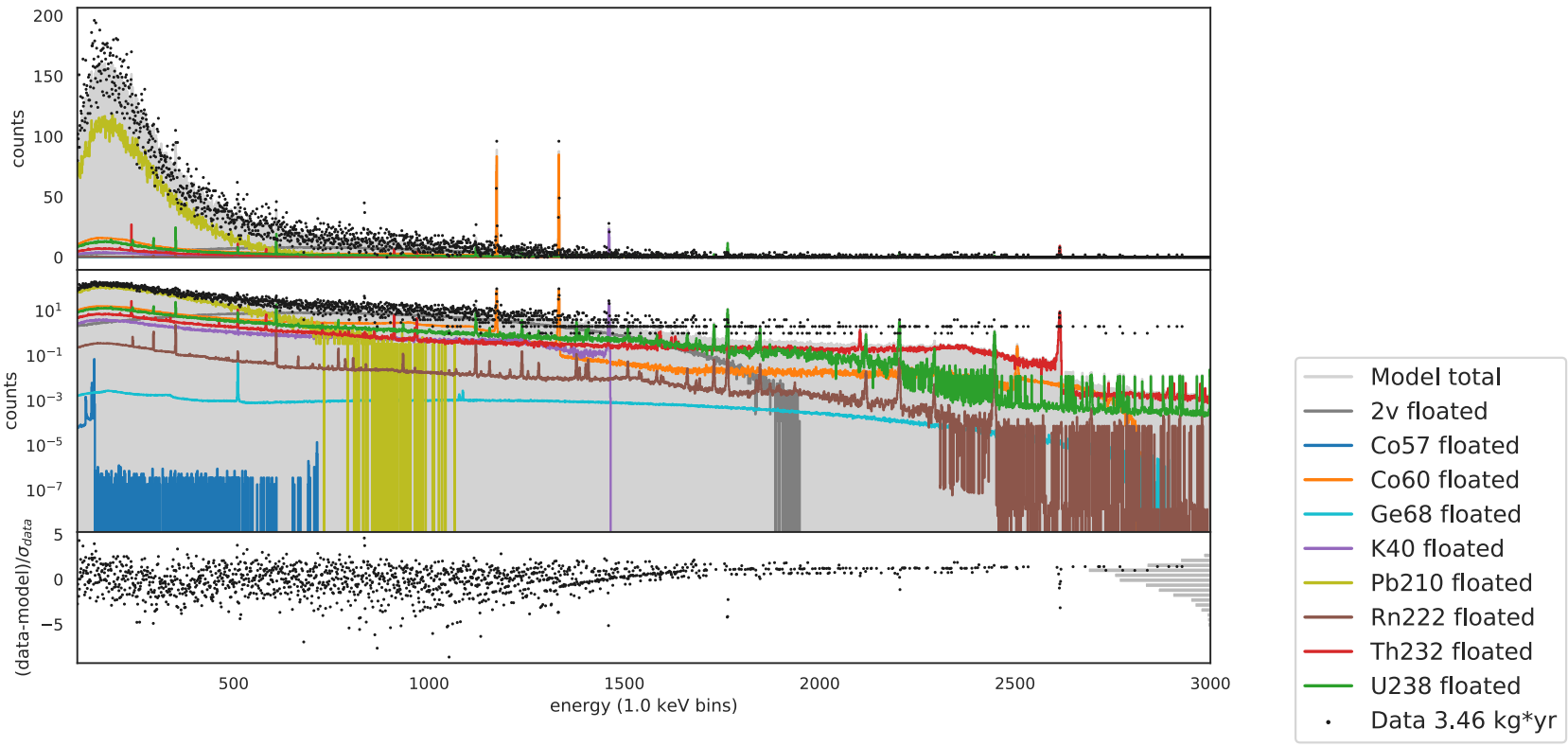

Figure 9.2: The spectral contributions of each decay chain resulting from regression of simulations to open DS0 data under two sets of cuts: data cleaning and DCR; and data cleaning, multiplicity, and DCR.

data, but above the impact of low energy noise. The upper limits were chosen to explore the effect of data above the 2614 keV ^{232}Th peak which may be populated by events surviving the DCR cut.

From the four tested ranges, results indicated that error was highly dependent on individual simulated components. This is to be expected since components vary in spectral shape, with idiosyncratic features being included or excluded based on the choice of range. Focusing on $2\nu\beta\beta$ in the $^{\text{enr}}$Ge, the maximum variation in estimated specific activity between any of the tested ranges was 0.99%. Ranges with a 3000 keV upper limit systematically yielded higher values for $2\nu\beta\beta$ $^{\text{enr}}$Ge specific activity, and ranges with a 50 keV lower limit systematically yielded lower specific activities. For comparison, $2\nu\beta\beta$ in the $^{\text{nat}}$Ge showed a maximum 6.85% variation among the tested ranges. For ^{210}Pb in the Pb shield, a dominant component below 500 keV with sufficient inclusion in all tested ranges, the maximum deviation was only 0.07%.

^{60}Co in the $^{\text{nat}}$Ge provides an interesting case study, with a maximum deviation of 19.36% in estimated specific activity among the tested ranges. This large deviation indicates the inclusion and exclusion by the tested energy ranges of a prominent spectral feature for ^{60}Co in the $^{\text{nat}}$Ge. The deviation also illustrates the relative freedom of components of lesser strength and greater susceptibility to correlations. The key feature for ^{60}Co in the $^{\text{nat}}$Ge can be seen in Fig 9.3 above the ^{60}Co 2505 keV sum peak where ^{60}Co in the $^{\text{nat}}$Ge is one of the only components free to float upward and improve the agreement between model and data. The estimated specific activity of ^{60}Co in the $^{\text{nat}}$Ge is systematically less for energy ranges ending at 2617 keV. Conversely, inclusion of energies up to 3000 keV increases the estimated specific activity.

9.3.2 Binning

The choice of bin width can also induce bias in results. Wider binning can smooth over spectral features that would otherwise break degeneracies between components of similar shape. Conversely, narrow binning lowers the statistics in each bin and underpopulates key spectral features. Several bin widths were explored, including 1, 2, 4, 5, and 10 keV. Open DS1-6a data under data cleaning and DCR cuts were used and the evaluated energy range was held between the 100 keV blind data threshold and the 2614 keV ^{232}Th peak.

Relative to energy range, binning was of lesser effect. For $2\nu\beta\beta$ in the $^{\text{enr}}$Ge the maximum deviation in specific activity among the tested binnings was 0.64%. For $2\nu\beta\beta$ in the $^{\text{nat}}$Ge, the

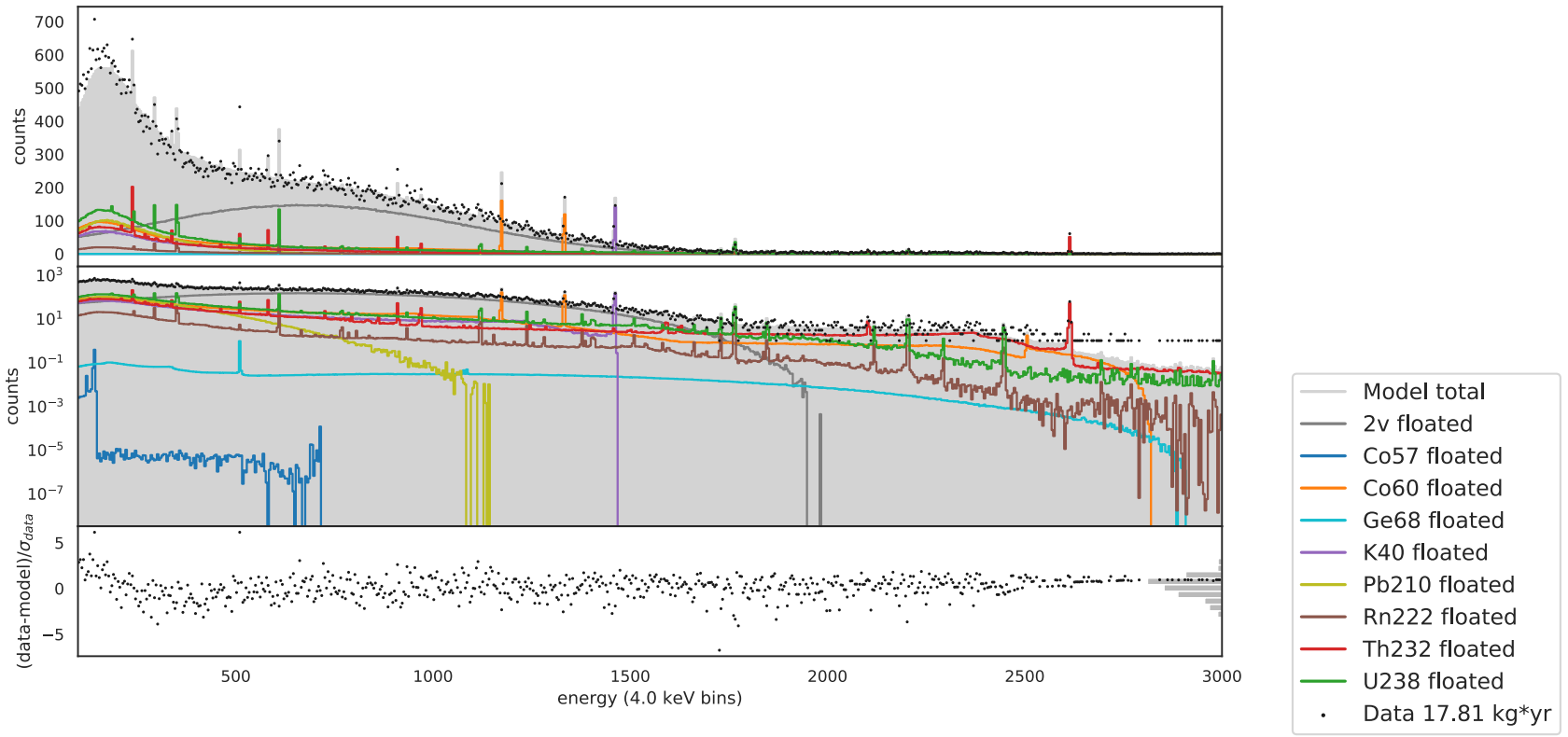

Figure 9.3: The spectral contributions of each decay chain resulting from regression of simulations to open DS1-6a data under data cleaning and DCR cuts, with the likelihood evaluated between 100-2617 keV.

maximum deviation was 2.7%. For further comparison, the maximum deviations for ^{210}Pb in the Pb and ^{60}Co in the $^{\text{nat}}$Ge were 1.32% and 2.59%.

These tests suggest that the error due to binning, like that of energy range, is also dependent on individual simulated components. Furthermore these tests demonstrated the greater computational cost brought on by finer binning and the subsequent increase in function calls for each evaluation of the likelihood. Drawing 3×10^4 MCMC samples in each test, the regression procedures with 1, 2, 4, 5, and 10 keV binnings respectively ran for 12, 8, 3, 2, and 1 hr.

9.3.3 Cut and Data Selection

To characterize error dependent on the cuts employed in a regression analysis, two tests were executed that differed only in the cut applied to the data set. Open DS1-6a data were used, the evaluated energy range was held between the 100 keV blind data threshold and the 2614 keV ^{232}Th peak, and the binning was set to 10 keV. The first test used data under data cleaning and DCR cuts, and the second test additionally imposed the multiplicity cut.

Errors were once again dependent on the individual simulated components. For $2\nu\beta\beta$ in $^{\text{enr}}$Ge the resulting specific activity between the two procedures differed by 0.91% with the first procedure yielding the greater value. The results for $2\nu\beta\beta$ in $^{\text{nat}}$Ge differed by 8.61%. The deviations among results for ^{210}Pb in the Pb and ^{60}Co in the $^{\text{nat}}$Ge were 0.10% and 20.63%.

An additional third test was run using both open and blind data from DS1-6a under data cleaning, multiplicity, and DCR cuts. With the additional statistics of the blind data, the result for $2\nu\beta\beta$ in $^{\text{enr}}$Ge deviated from that of the first procedure by 4.03%.

The multisite PSA cut was not considered for regression procedures due to poor agreement with data at high energies, as demonstrated in Section 7.3.

9.4 Full Regression to DS1-6a

A final regression procedure was executed using the available open and blind data from DS1-6a. Open and blind data were combined and viewed under data cleaning, multiplicity, and DCR cuts. The open data were additionally viewed under just data cleaning and DCR cuts. The regression procedure evaluated the energy range between the 100 keV blind data threshold and the 2614 keV

^{232}Th peak, and the binning was set to 10 keV. A total of 3×10^4 MCMC samples were drawn, an amount sufficient to keep MC error below 1% on each fitted parameter. As in the analyses of the previous sections of this chapter, data from both $^{\text{nat}}$Ge and $^{\text{enr}}$Ge were included.

Between the six distinct configurations involved, and two cuts, there were 1,640 simulated components. Parameters were pooled among components that differed only in configuration and cut, as discussed in Section 9.1, so that the regression was reduced to 148 free parameters, one for each unique combination of decay chain and hardware component. The results of the regression procedure are displayed in Fig 9.4.

9.4.1 $2\nu\beta\beta$ Results

The total fitted model accounts for 94.45% of the 204,483 counts in the observed spectrum. $2\nu\beta\beta$ within the $^{\text{enr}}$Ge is the dominant model component, comprising 40.69% of the fitted counts. The marginal posterior distribution for this component is displayed in Fig 9.5 with mean 71.93 μBq kg^{-1}, standard deviation 1.02 μBq kg^{-1}, and MC error 0.01 μBq kg^{-1}. The prior distribution displayed in this figure is centered on the measurement reported in Ref [83].

The specific activity is converted into a $2\nu\beta\beta$ half life in units of years via

$$T_{1/2}^{2\nu} = \frac{\ln 2 \; N_A}{m_A} \frac{\eta}{w_{2\nu}} \tag{9.1}$$

where N_A is Avogadro's number, η represents the 0.88 ^{76}Ge enrichment fraction of MAJORANA $^{\text{enr}}$Ge, m_A is the 75.6×10^{-3} kg molar mass of ^{76}Ge, and $w_{2\nu}$ is the specific activity of $2\nu\beta\beta$ in the $^{\text{enr}}$Ge in units decay/(kg yr). Along with the errors summarized in Table 9.1, this analysis yields a $2\nu\beta\beta$ half life of $(2.141 \pm 0.092) \times 10^{21}$ yr.

In this analysis, only open data were available under the minimal data cleaning and DCR cuts; the blind data were restricted to include the multiplicity cut. A future analysis with access to the full unblinded DEMONSTRATOR exposure may provide a more accurate measurement of the $2\nu\beta\beta$ half life. Additionally, an analysis involving only the $^{\text{enr}}$Ge exposure may be beneficial.

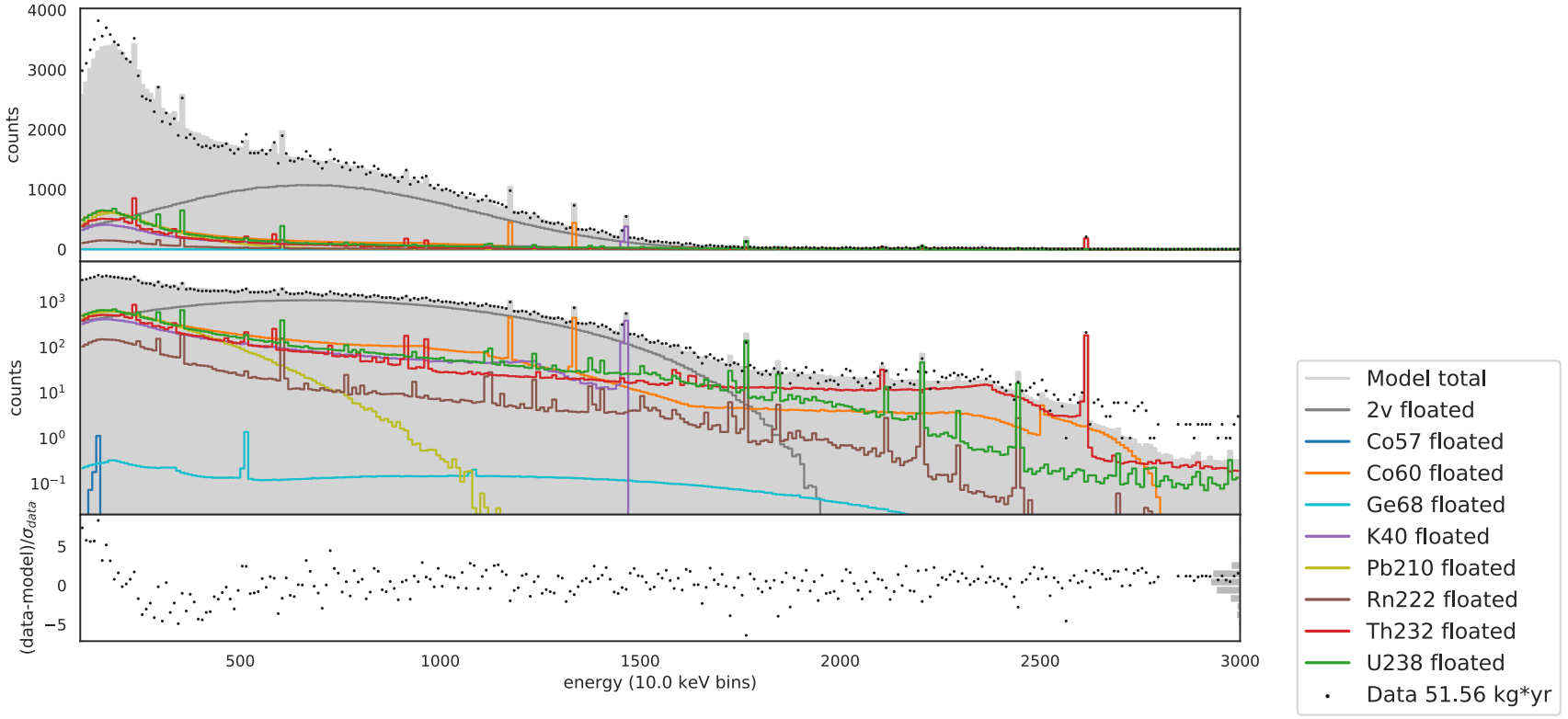

Figure 9.4: The spectral contributions of each decay chain resulting from regression of simulations to open and blind DS1-6a data under two sets of cuts: data cleaning and DCR; and data cleaning, multiplicity, and DCR. Since the open data is used under two cuts, it contributes twice to the total exposure listed in the legend.

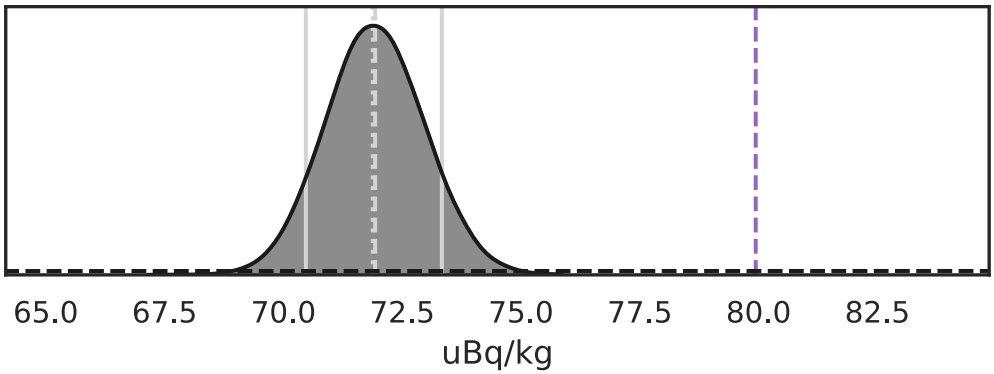

Figure 9.5: Marginal posterior for the specific activity of $2\nu\beta\beta$ in the $^{\text{enr}}$Ge inferred from regression of simulations to DS1-6a data. The posterior (solid black) indicates a best-fit value roughly 10% below the expected value encoded in the prior distribution (dashed purple). Solid grey lines indicate a 68% credible interval. A diffuse prior distribution was set for the parameter, indicated by the black dashed line seemingly parallel to the horizontal axis.

9.4.2 Results from other Components

Following $2\nu\beta\beta$ in the $^{\text{enr}}$Ge, the next largest contributors to events each comprise <10% of the fitted counts. The top ten components by fitted counts are listed in Table 9.2 and a full ordered list of fitted components is included in Appendix E. The posteriors for each decay chain and hardware component are also summarized in Appendix E; from these results, any deviations from assay measurements can be assessed. For further comparison, a full ordered list of the expected values of components— prior to regression— is included in Appendix D.

Focusing on EFCu components, the specific activities inferred for the detector units and strings do not stray appreciably from their expected ^{232}Th and ^{238}U assay values. A factor of four increase beyond the ^{232}Th assay value is seen, however, for the inner Cu shield. Likewise, a factor of three increase is seen for ^{232}Th in vessel Cu. As summarized in Table 9.3, these fit results contribute to a factor of two increase in the ^{232}Th and ^{238}U EFCu background index contribution relative to the assay-based as-built background model. As in Table 6.2, Table 9.3 aggregates the ROI contributions of major component groups to form a background budget and estimate a background index for the Demonstrator.

Cables were modeled separately, with free parameters assigned to HV cables and signal cables in three locations: along the crossarms, atop the coldplates, and below the coldplates along strings. The crossarm cables did not stray significantly from their ^{232}Th and ^{238}U assay values. String cables

Table 9.1: Statistical and systematic uncertainties on the $2\nu\beta\beta$ half life in $^{\text{enr}}$Ge.

Item	Uncertainty on $T_{1/2}^{2\nu}$ (%)
Posterior	1.41
MC Error	0.01
Energy Range	0.99
Bin Width	0.64
Cut and Data Selection	4.03
Active $^{\text{enr}}$Ge Exposure	0.02
Total	4.43

Table 9.2: The ten largest components resulting from the fit to DS1-6a data. The second and third columns present the counts attributed to each component and the percentage of the total fitted counts. The third and fourth columns summarize each component's marginal posterior distribution.

Parameter	Counts	%	Mean μBq kg^{-1}	Std. Dev. μBq kg^{-1}
$2\nu\beta\beta$ $^{\text{enr}}$Ge, Bulk	78,581.26	40.69	71.93	1.02
^{60}Co Outer Cu Shield, Bulk	18,377.60	9.52	83.12	6.50
^{210}Pb Pb Shield, Bulk	14,407.69	7.46	583917.52	21744.97
^{238}U Pb Shield, Bulk	14,248.53	7.38	166.22	15.51
$2\nu\beta\beta$ $^{\text{nat}}$Ge, Bulk	14,199.52	7.35	30.44	2.29
^{40}K Pb Shield, Bulk	11,103.21	5.75	1053.51	136.33
^{232}Th Pb Shield, Bulk	8,453.90	4.38	61.37	3.64
^{60}Co $^{\text{nat}}$Ge, Bulk	4,663.25	2.41	11.18	0.94
^{222}Rn Purge Volume, Surface	4,133.76	2.14	213.97	36.68
^{232}Th M1 Coldplate HV Cables, Bulk	3,186.00	1.65	2743.26	322.49

Table 9.3: Expected contributions to the background index from the sources listed in the first column. The second column represents the as-built background model assuming the DS5 configuration. The third column also uses values inferred from regression of the as-built model to data. The fourth column presents the analogous results of the preliminary background model published in Ref [41]. The row labeled "Plastics, Other" includes the contributions of stainless steel from the modules' service bodies, the glass break from the cryogenics system, and the phosphor bronze spring washers assisting HV connections at the detectors.

Background Contribution	As-Built DS5 c/(ROI tonne yr)	As-Built DS5 Activities from Fit c/(ROI tonne yr)	Rate Preliminary c/(ROI tonne yr)
EFCu	5.47E-01	1.31E+00	2.30E-01
OFHC Cu Shielding	2.80E-01	3.03E-01	2.90E-01
Pb Shielding	1.60E+00	1.51E+01	6.30E-01
Cables and Internal Connectors	1.77E+00	4.92E+00	3.80E-01
Front Ends	1.03E+00	1.04E+00	6.00E-01
^{232}Th, ^{238}U within the Ge	4.97E-01	8.07E-01	7.00E-02
Plastics, Other	9.76E-02	1.04E-01	3.90E-01
^{68}Ge, ^{60}Co within the ^{enr}Ge	7.66E-03	1.06E-02	7.00E-02
^{60}Co within the Cu	7.21E-02	1.86E-02	9.00E-02
External γ-rays, (α,n) reactions	1.00E-01	1.00E-01	1.00E-01
Rn and surface α emission	2.54E-01	5.52E-01	5.00E-02
Ge, Cu, Pb (n,n'γ) reactions	2.10E-01	2.10E-01	2.10E-01
Ge(n,n') reactions	1.70E-01	1.70E-01	1.70E-01
Ge(n,gamma)	1.30E-01	1.30E-01	1.30E-01
Direct muon passage	3.00E-02	3.00E-02	3.00E-02
ν induced background	<1.00E-02	<1.00E-02	<1.00E-02
Total c/(ROI tonne yr)	6.81E+00	2.48E+01	3.50E+00
Total c/(keV kg yr)	1.70E-03	6.19E-03	8.75E-04

did, however, show a roughly factor of two increase in both ^{232}Th and ^{238}U activity. Coldplate cables exhibited a larger variation, with their HV cables surpassing the prior expectation for ^{232}Th activity by roughly a factor of four. For the ^{238}U activity in coldplate cables, an asymmetry arose between M1 and M2, with the M2 HV coldplate cables roughly doubling in activity while M1 cables remained close to prior expectations. All in all, the coldplate cables contributed more counts than the string and crossarm groupings.

Connectors showed a factor of three increase in ^{232}Th activity but remained close to their ^{238}U prior. This change, together with the increase in coldplate cables activity, contributed to a factor of three increase in the ^{232}Th and ^{238}U background index contribution relative to the assay-based as-built background model. This is summarized in the "Cables and Internal Connectors" row of Table 9.3.

Pb shielding constituted the largest increase over assay-based expectations. The inferred activities for ^{238}U and ^{232}Th increased by factors of roughly five and twelve relative to their priors. These changes led to a factor of ten increase in the ^{232}Th and ^{238}U background index contribution relative to the assay-based as-built background model. This is summarized in the "Pb Shielding" row of Table 9.3. Regarding ^{210}Pb activity, the fitted activity remained close to its prior expectation based on the regression to DS0 of Section 9.2.

Though contaminants internal to Ge crystals contribute little to the total background index, their inferred activities exhibited increases worth noting. ^{232}Th activities within all crystals doubled. ^{238}U activities doubled within $^{\text{nat}}$Ge and tripled within $^{\text{enr}}$Ge. Additionally, despite limiting the energy range evaluated in the regression, ^{60}Co in $^{\text{nat}}$Ge increased by roughly a factor of five over its prior expectation.

As a final note, the inferred activities of low-mass front ends did not deviate significantly from prior expectations.

9.4.3 Summary of Major Components

The groups of components contributing most to the background index used for $0\nu\beta\beta$ analyses are Pb shielding, cables and connectors, EFCu, and front ends. The percentage contributions of each of these major components to the total background index inferred from the regression to DS1-6a are as follows.

Pb shielding:	60.89%
Cables and Internal Connectors:	19.84%
EFCu:	5.28%
Front Ends:	4.19%

The total background index, as summarized in Table 9.3, is 6.19 $\times$ 10^{-3} c/(keV kg yr). This value is 31.7% greater than the observed background index of 4.7 $\times$ 10^{-3} c/(keV kg yr).

Considering the experimental geometry detailed in Chapters 3 and 5, a statement can be made based on the distance of inferred background sources from the detectors within the MAJORANA modules. The components contributing most to the fitted counts, and which exhibited the largest deviations in activity from assay-based expectations, are distant from the detectors. The detailed results of Appendix E show that most top-contributing components lie above the coldplate or beyond. The largest contributors from within the cryostats, below the coldplates are contaminants internal to the Ge, front ends, and string cables. These internal components comprise $< 10\%$ of the fitted counts. Activity of contaminants internal to the Ge can be constrained through analysis of alpha peaks in data, but such constraints were not applied in this regression.

CHAPTER 10
Conclusions

This work analyzes 35.5 kg yr of exposure from $^{\text{enr}}$Ge and $^{\text{nat}}$Ge detectors with the goal of determining the components underlying the MAJORANA DEMONSTRATOR background spectrum. Spectral analyses like those of Chapter 4 constrain the possible activities of contaminants, but are limited in their power to locate sources. Monte Carlo radiation transport simulations, described in Chapter 5, help in this matter by offering access to constituent spectra underlying the observed data, though the relative strengths of those constituents are unknown.

Each simulated constituent refers to a contaminant in an individual hardware component of the experiment, aligning naturally with the output of the DEMONSTRATOR's assay campaign. Assay measurements provide estimates of the relative strengths of the background spectrum constituents and are used to predict the total background index of the DEMONSTRATOR. This procedure was carried out in a preliminary background model summarized in Table 6.2, predicting 8.75×10^{-4} c/(keV kg yr).

Following assembly of the DEMONSTRATOR, as-built knowledge of the experiment was incorporated in updated simulations and assay campaigns. This work produced an as-built background model predicting 1.70×10^{-3} c/(keV kg yr), also summarized in Table 6.2. Despite the improved fidelity of the as-built background model, its prediction fell short of the observed background index of 4.7×10^{-3} c/(keV kg yr) described in Section 4.4. The deficit in the predicted background index may lie in underestimate of hardware contamination, inaccuracies in the modeling of background components, or in background components that have not been modeled.

Comparison of simulations to data via regression can assist in pinpointing sources of backgrounds that have been underestimated or inadequately modeled. Along these lines, the many detailed components of the as-built simulations were gathered and assigned prior distributions for their radioactivity. The activities were treated as random variables able to weight the simulations such that a total simulated model could be constructed and compared with observed data. Markov chain

Monte Carlo techniques were used to explore the posterior of this Bayesian statistical model and infer most probable values for each component's activity.

Access to the posterior distribution of this model yields a measurement of each hardware component's activity. These can be compared with initial measurements from the assay campaign, or with literature values. One such measurement, for the activity of $2\nu\beta\beta$ in $^{\mathrm{enr}}$Ge, implied a $2\nu\beta\beta$ half life of $(2.141 \pm 0.092) \times 10^{21}$ yr.

In general, the MCMC procedure found that simulated components increased in activity, counteracting the assay-based underestimates of activity in order to better match the observed data. Particularly, components farther from the detectors showed the greatest increase. These include distant EFCu parts, Pb shields, and coldplate cables. Small parts close to detectors, integral to the low-background experiment, did not account for the assay-based underestimates of background index. Such small parts saw more modest increases in their estimated activities or remained the same.

When measured activities obtained from the MCMC procedure are used to scale the simulations, an increased background index is predicted. This predicted value of 6.19×10^{-3} c/(keV kg yr) is broken down in Table 9.3 alongside the predictions of the preliminary and as-built background models discussed above.

10.1 Future Work

Continuation of this work can progress through several avenues. Primarily, treating the simulations in greater detail provides more degrees of freedom and yields a better fit to the data. Hardware components, some of which represent groups of parts, can be divided into smaller collections. Decay chains can be subdivided as well into their various branches.

Errors on measurements can also be improved. In particular, systematic error in the simulations can be assessed via independent validation simulations and subsequent comparison with literature values [61]. Statistical error in simulated components can also be characterized and accounted for in the regression procedure through the techniques of Ref [84]. The full unblinded DEMONSTRATOR exposure can be employed in future analyses to obtain more accurate estimates of the $2\nu\beta\beta$ half life and component activities. The impacts of $^{\mathrm{nat}}$Ge versus $^{\mathrm{enr}}$Ge data selection can also be explored.

Simulations processing in which the multiplicity and PSA cuts, and lithiated layer effects are modeled can be tuned to improve agreement with calibration data. In particular, agreement between data and simulations under the PSA cut could benefit $2\nu\beta\beta$ measurements by removing multisite events not indicative of double-beta decay.

Improvements to the regression procedure can go on to include ideas from model selection. A most probable model may exclude certain components, or perhaps impose conditional dependence between components; model selection procedures will aid in proposing, testing, and comparing those models. Model selection routines will benefit from improvements to the efficiency of the regression procedure. Potential avenues for optimization of code include alternate specification of the graphical model in the given probabilistic programming language, and parallelization of simultaneously sampled Markov chains.

APPENDIX A
DETECTOR SELECTION

Time periods and detector channels of poor quality are removed from the full set of data collected by the MAJORANA DEMONSTRATOR. Runs can be rejected for high noise and detector rate, DAQ errors, veto and slow controls errors, or software and data production errors. Individual detector channels can be removed from the data if they are not biased, or if they are biased but yield unreliable pulse shape analysis performance. Details of detectors included in each data set are summarized in Table A.1.

Table A.1: Detector information for channel selection in data and simulations. A value of 0 indicates an inoperable detector, 1 indicates an operating detector included in analysis, and 2 indicates that a detector was not present in the given experimental configuration.

Serial Number	Position	Active Mass (kg)	Modeled Mass (kg)	DS0	DS1	DS2	DS3	DS4	DS5a	DS5b	DS5c	DS6a
B8482	C1P7D1	0.561	0.638128	1	1	1	1	2	1	1	1	1
P42574B	C1P7D2	0.71	0.778219	1	1	1	1	2	1	1	1	1
P42662B	C1P7D3	0.591	0.625347	1	1	0	1	2	1	1	1	1
P42537A	C1P7D4	0.964	1.034	0	1	1	1	2	0	1	1	1
P42574C	C1P6D1	0.732	0.804621	0	1	1	1	2	1	1	1	1
P42661B	C1P6D2	0.675	0.753518	1	0	0	0	2	0	0	0	0
P42574A	C1P6D3	0.701	0.767722	1	1	1	1	2	1	1	1	1
P42662A	C1P6D4	0.572	0.633498	0	1	1	1	2	1	1	1	1
B8474	C1P2D1	0.56	0.637903	0	1	1	1	2	1	1	0	0
P42664A	C1P2D2	0.723	0.823932	1	1	1	1	2	1	1	1	1
P42665A	C1P2D3	0.659	0.715755	1	1	1	1	2	1	1	1	1
P42662C	C1P2D4	0.689	0.738831	0	0	0	0	2	0	0	0	0
P42698B	C1P1D1	0.51	0.552389	1	0	0	0	2	0	0	0	0
P42575A	C1P1D2	0.979	1.03926	1	1	1	1	2	1	1	1	1
P42661C	C1P1D3	0.811	0.902409	1	1	1	1	2	1	1	1	1
P42538A	C1P1D4	0.968	1.03263	1	1	1	1	2	1	1	1	1
B8480	C1P3D1	0.551	0.637857	0	0	0	0	2	0	0	0	0
P42698A	C1P3D2	0.886	0.990778	0	1	1	1	2	1	1	1	1
P42538B	C1P3D3	0.949	0.989629	0	1	1	1	2	1	1	1	1
P42573A	C1P3D4	1.024	1.05382	1	1	1	1	2	1	1	1	1
B8477	C1P5D1	0.553	0.637746	1	0	0	0	2	0	0	0	0
P42575B	C1P5D2	0.73	0.814487	1	0	0	1	2	1	1	1	1
P42661A	C1P5D3	0.632	0.705699	1	1	1	1	2	1	1	1	1
P42573B	C1P5D4	0.982	1.05365	1	0	0	0	2	0	0	0	0
B8455	C1P4D1	0.558	0.638121	1	0	0	1	2	1	1	1	1
B8470	C1P4D2	0.564	0.638381	1	0	0	0	2	1	1	1	1
B8463	C1P4D3	0.567	0.638	1	0	0	0	2	1	1	1	1
B8465	C1P4D4	0.545	0.638431	1	0	0	1	2	1	1	1	1
B8469	C1P4D5	0.557	0.638603	1	0	0	1	2	1	1	1	1
B8461	C2P2D5	0.577	0.63878	2	2	2	2	0	0	0	0	0
B8595	C2P2D4	0.558	0.63804	2	2	2	2	0	0	0	0	0
B8594	C2P2D3	0.559	0.638027	2	2	2	2	1	1	1	1	1
B8576	C2P2D2	0.562	0.637948	2	2	2	2	1	1	1	1	1
P42748A	C2P1D4	0.917	1.02625	2	2	2	2	1	1	1	0	1
P42748B	C2P1D3	0.903	0.970365	2	2	2	2	0	0	0	0	0
P42664B	C2P1D2	0.576	0.684834	2	2	2	2	0	0	0	0	0
B8459	C2P1D1	0.556	0.637666	2	2	2	2	0	1	1	1	0
P42853A	C2P3D3	0.996	1.03539	2	2	2	2	0	0	0	0	0
B8607	C2P4D1	0.558	0.638345	2	2	2	2	1	1	1	1	1
P42749B	C2P3D2	0.852	0.922068	2	2	2	2	1	1	1	1	1
B8481	C2P2D1	0.581	0.638145	2	2	2	2	1	1	1	1	1
P42749A	C2P3D1	0.872	0.935734	2	2	2	2	1	1	1	1	1
B8473	C2P4D5	0.562	0.639193	2	2	2	2	0	0	0	0	0
B8466	C2P4D4	0.566	0.638667	2	2	2	2	1	1	1	1	1
B8621	C2P4D3	0.565	0.638331	2	2	2	2	0	0	0	0	0
B8456	C2P4D2	0.579	0.638232	2	2	2	2	0	1	1	1	1
B8717	C2P7D4	0.567	0.638586	2	2	2	2	1	1	1	0	1
P42909A	C2P7D3	0.562	0.603793	2	2	2	2	1	1	1	0	1
P42712B	C2P7D2	0.968	1.04548	2	2	2	2	0	0	0	0	0
P42665C	C2P6D4	0.778	0.853455	2	2	2	2	0	0	0	0	0
P42909C	C2P6D3	0.821	0.850061	2	2	2	2	0	0	0	0	0
P42909B	C2P6D2	0.775	0.828354	2	2	2	2	1	1	1	1	1
P23517A	C2P6D1	0.462	0.551892	2	2	2	2	1	0	0	0	0
P42712A	C2P5D4	0.802	0.867683	2	2	2	2	0	1	1	1	1
P42853B	C2P5D3	1.031	1.11407	2	2	2	2	1	1	1	1	0
B8619	C2P7D1	0.566	0.638104	2	2	2	2	0	0	0	0	0
P42665B	C2P5D2	0.591	0.643725	2	2	2	2	0	0	0	0	0
B8487	C2P5D1	0.557	0.637958	2	2	2	2	1	1	1	1	1

APPENDIX B
ASSAY SAMPLE SELECTION

Full details of the selected assay values for materials and contaminants are summarized in Tables B.1, B.2, B.3, and B.4.

Table B.1: Bulk Natural Radioactivity: Estimates for the specific activity of contaminants in Majorana Demonstrator materials' bulk.

Material	Decay Chain	μBq kg^{-1}	Reference
^{nat}Ge	^{232}Th	< 0.01	[65]
	^{238}U	< 0.01	[65]
	^{40}K	-	-
^{enr}Ge	^{232}Th	< 0.01	[65]
	^{238}U	< 0.01	[65]
	^{40}K	-	-
Stainless Steel	^{232}Th	< 12000	[67]
	^{238}U	< 3000	[67]
	^{40}K	< 4000	[85]
EFCu	^{232}Th	< 0.12	[41]
	^{238}U	< 0.11	[41]
	^{40}K	12.41 ± 2.48	[86]
OFHC Cu	^{232}Th	1.10 ± 0.20	[41]
	^{238}U	1.49 ± 0.25	[41]
	^{40}K	12.41 ± 2.48	[86]
Pb	^{232}Th	5.27 ± 5.27	[41]
	^{238}U	36.07 ± 24.87	[41]
	^{40}K	418.88 ± 173.45	[41]
Phosphor Bronze	^{232}Th	24.67 ± 2.76	[87]
	^{238}U	134.32 ± 3.73	[87]
	^{40}K	< 2047.87	[86]
Glass Break	^{232}Th	48684 ± 8114	[88]
	^{238}U	161681 ± 74622	[88]
	^{40}K	5523055.2 ± 248227.2	[88]
LMFE	^{232}Th	7566.31 ± 136.08	[41]
	^{238}U	10571.45 ± 263.83	[41]
	^{40}K	< 4717.18	[41]
Connector	^{232}Th	390.28 ± 361.48	[41]
	^{238}U	539.77 ± 409.12	[41]
	^{40}K	< 29011.55	[41]
HV Cable	^{232}Th	585.97 ± 356.95	[66]
	^{238}U	1405.38 ± 800.36	[66]
	^{40}K	< 12411.36	[41]
Signal Cable	^{232}Th	585.97 ± 356.95	[66]
	^{238}U	1405.38 ± 800.36	[66]
	^{40}K	< 12411.36	[41]
Vespel	^{232}Th	< 11.77	[41]
	^{238}U	< 1049.68	[41]
	^{40}K	10859.94 ± 9308.52	[41]
Parylene	^{232}Th	2150.21 ± 121.71	[41]
	^{238}U	3109.25 ± 746.22	[41]
	^{40}K	28547.00 ± 2661.73	[41]
PTFE	^{232}Th	0.10 ± 0.01	[41]
	^{238}U	< 4.97	[41]
	^{40}K	4.65 ± 0.62	[41]
PTFE Gasket	^{232}Th	< 20.69	[41]
	^{238}U	< 94.52	[41]
	^{40}K	4.65 ± 0.62	[41]
PTFE O-ring	^{232}Th	65.32 ± 10.52	[89]
	^{238}U	< 116.91	[89]
	^{40}K	< 93.09	[89]

Table B.2: Surface Natural Radioactivity: Estimates for the specific activity of contaminants from the surface of Majorana Demonstrator materials.

Material	Decay Chain	μBq m^{-2}	Reference
EFCu	^{232}Th	1.8 ± 0.4	[41]
	^{238}U	2.8 ± 0.6	[41]

Table B.3: Contaminants Out-of-Equilibrium with Natural Radioactivity: Estimates for the specific activity of contaminants in MAJORANA DEMONSTRATOR materials.

Material	Decay Chain	μBq kg^{-1}	Reference
Pb	^{210}Pb	< 2500000	[90]
Nitrogen	^{222}Rn	1165 ± 233	[68, 69]

Material	Decay Chain	μBq m^{-2}	Reference
Nitrogen	^{222}Rn	89.20 ± 44.60	[68, 69]

Table B.4: Cosmogenic Activation Products: Estimates for the specific activity of contaminants in MAJORANA DEMONSTRATOR materials.

Material	Decay Chain	atoms/(kg dy)	Reference
^{nat}Ge	^{68}Ge	30	[46]
	^{60}Co	3.98	[46]
	^{57}Co	6.84	[46]
^{enr}Ge	^{68}Ge	2.12	[46]
	^{60}Co	2.55	[46]
	^{57}Co	0.7	[46]
EFCu	^{60}Co	86.4	[48]
OFHC Cu	^{60}Co	86.4	[48]

Material	Decay Chain	Surface dy	UG Date	μBq kg^{-1}
^{nat}Ge	^{68}Ge	Saturated	2010-11-11	8.09E-03
	^{60}Co	Saturated	2010-11-11	2.39E+00
	^{57}Co	Saturated	2010-11-11	3.46E-03
^{enr}Ge	^{68}Ge	29.05	2014-01-21	2.09E-02
	^{60}Co	29.05	2014-01-21	1.46E-01
Welded Cu (EFCu)	^{60}Co	12	2014-12-09	2.53
Spring Clip Cu (EFCu)	^{60}Co	Saturated	2015-06-26	7.04E+02
Outer Cu Shield (OFHC Cu)	^{60}Co	180	2012-10-25	2.18E+01

APPENDIX C
COMPARISON OF SIMULATIONS TO CALIBRATION DATA

The positioning of the calibration track is reflected in the event rates of detectors in various locations of the array. The following plots compare DS5b calibration data, under data cleaning and DCR cuts, to the analogous simulations for each operational detector.

C-1 M1 Calibration Source

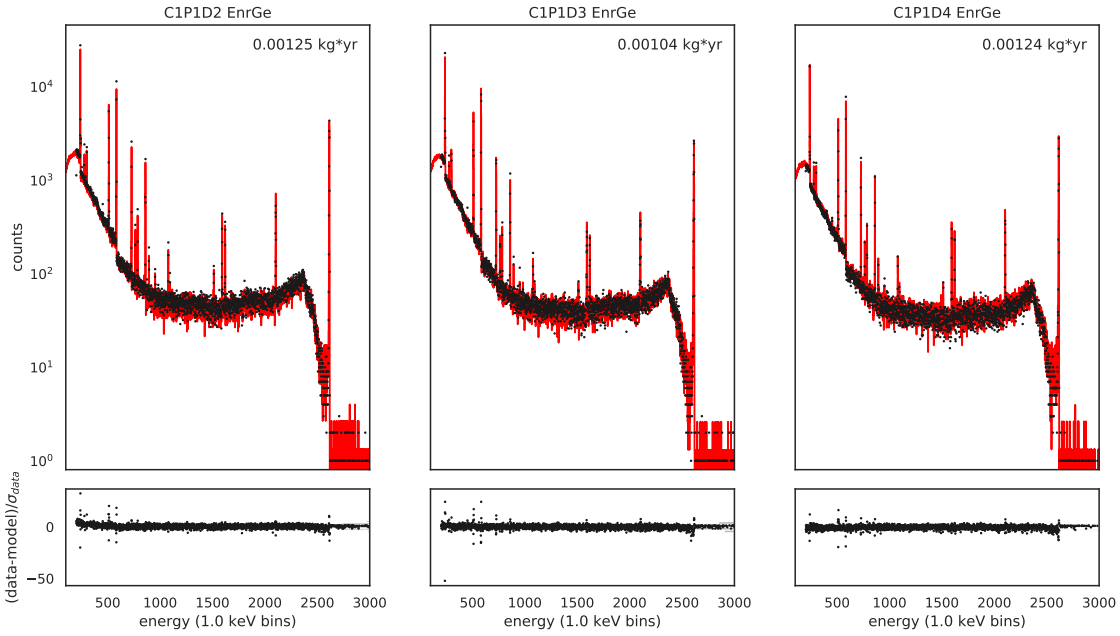

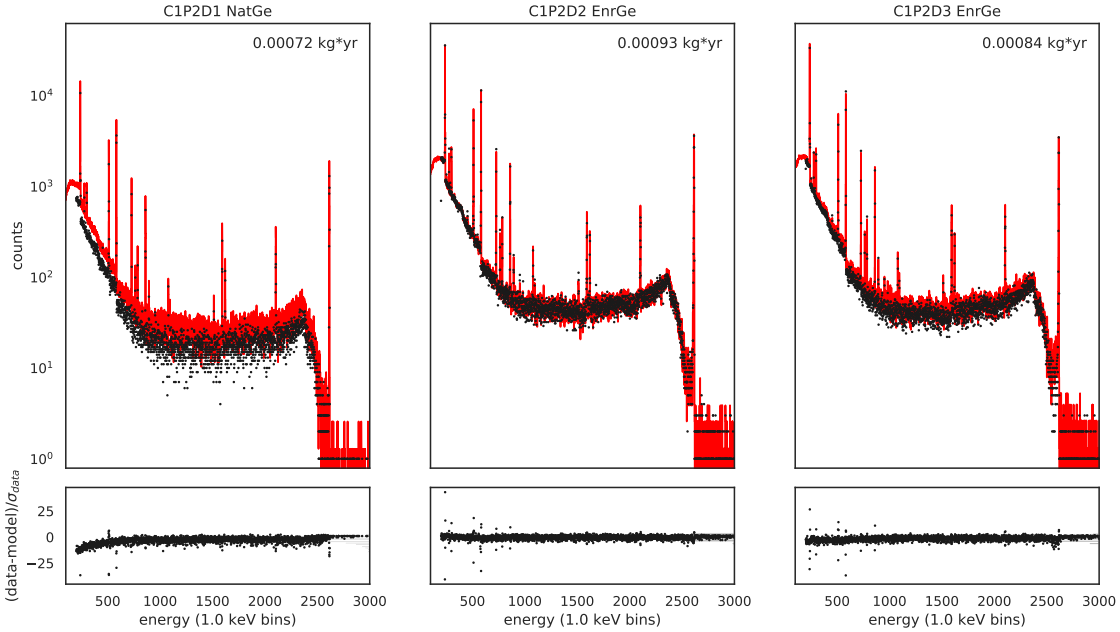
C1P2D1 NatGe
0.00072 kg*yr
C1P2D2 EnrGe
0.00093 kg*yr
C1P2D3 EnrGe
0.00084 kg*yr
counts
(data-model)/σ_{data}
energy (1.0 keV bins)

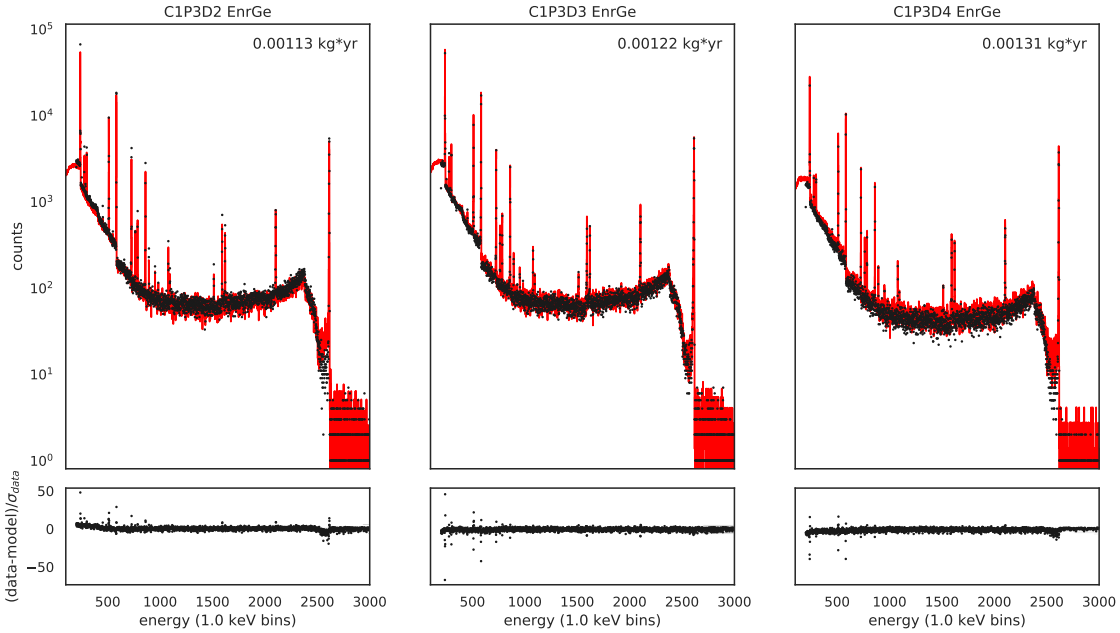
C1P3D2 EnrGe
0.00113 kg*yr
C1P3D3 EnrGe
0.00122 kg*yr
C1P3D4 EnrGe
0.00131 kg*yr
counts
(data-model)/σ_{data}
energy (1.0 keV bins)

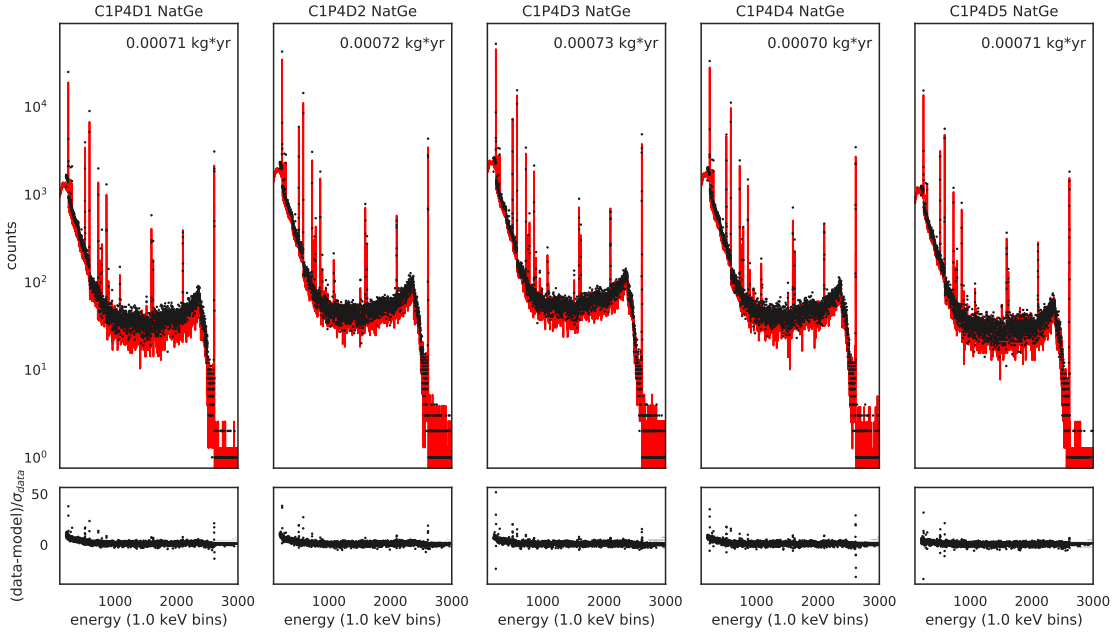
C1P4D1 NatGe
0.00071 kg*yr
C1P4D2 NatGe
0.00072 kg*yr
C1P4D3 NatGe
0.00073 kg*yr
C1P4D4 NatGe
0.00070 kg*yr
C1P4D5 NatGe
0.00071 kg*yr
counts
(data-model)/σ_{data}
energy (1.0 keV bins)

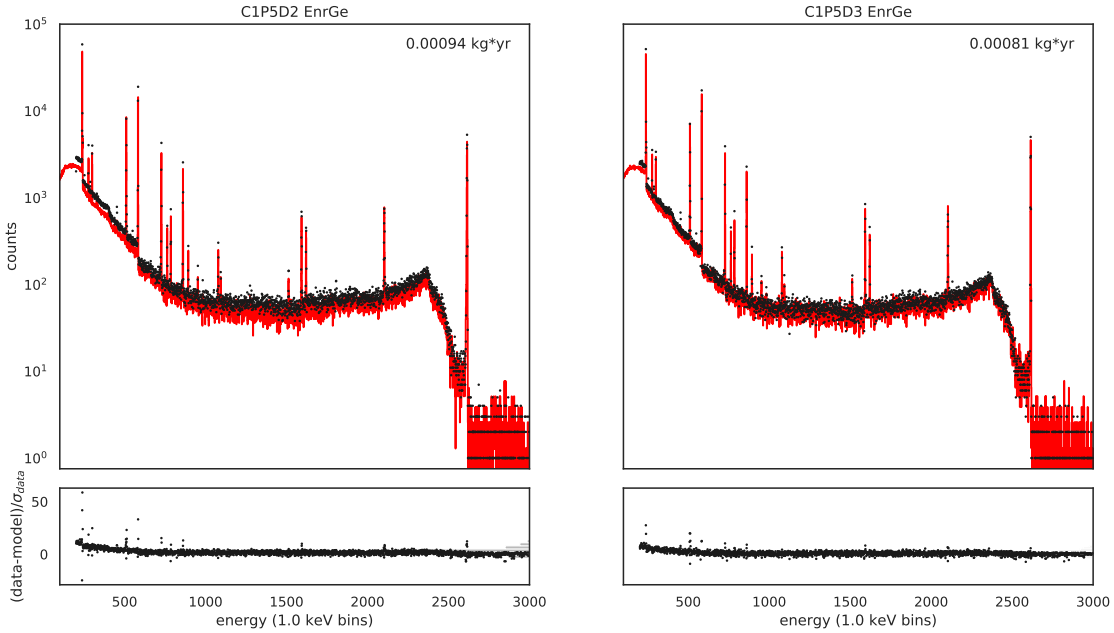
C1P5D2 EnrGe
0.00094 kg*yr
C1P5D3 EnrGe
0.00081 kg*yr
counts
(data-model)/σ_{data}
energy (1.0 keV bins)

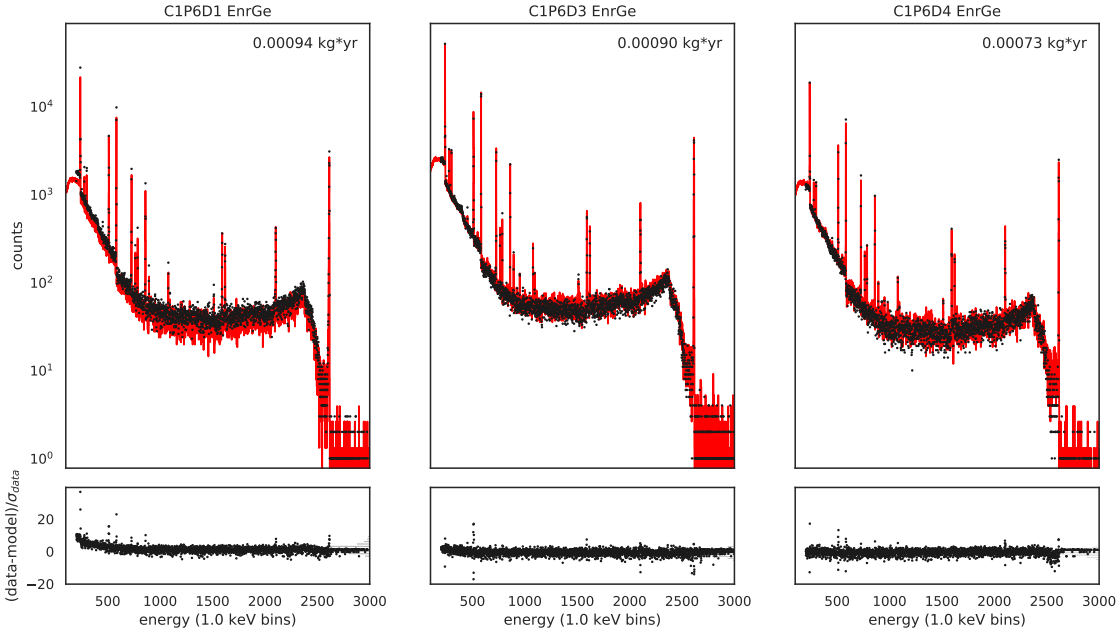
C1P6D1 EnrGe
0.00094 kg*yr
C1P6D3 EnrGe
0.00090 kg*yr
C1P6D4 EnrGe
0.00073 kg*yr
counts
(data-model)/σ_{data}
energy (1.0 keV bins)

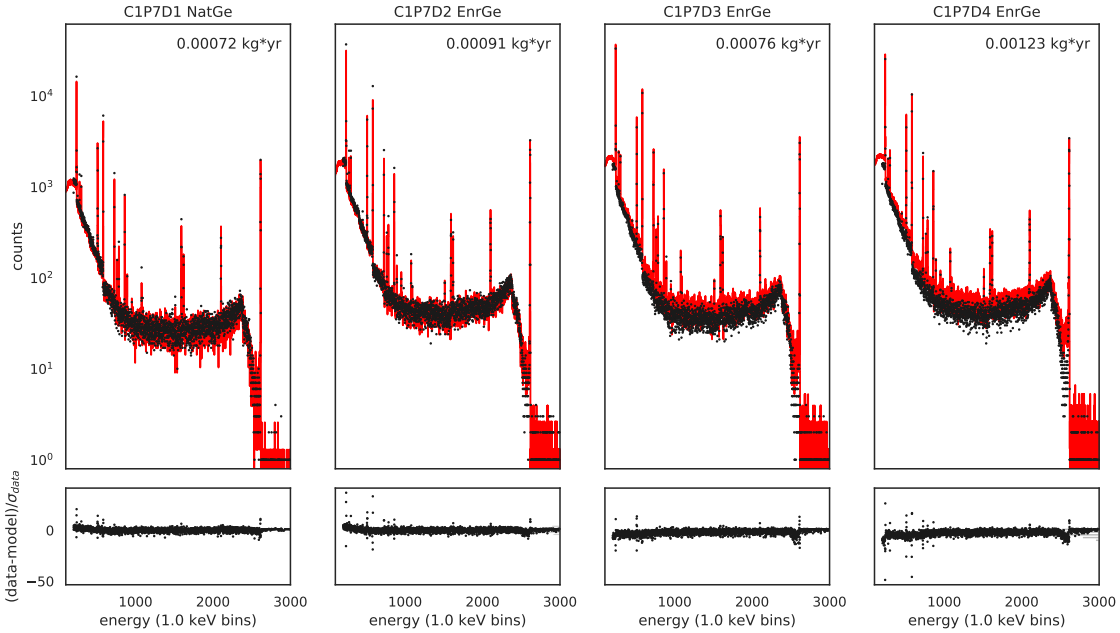
C1P7D1 NatGe
0.00072 kg*yr
C1P7D2 EnrGe
0.00091 kg*yr
C1P7D3 EnrGe
0.00076 kg*yr
C1P7D4 EnrGe
0.00123 kg*yr
counts
(data-model)/σ_{data}
energy (1.0 keV bins)

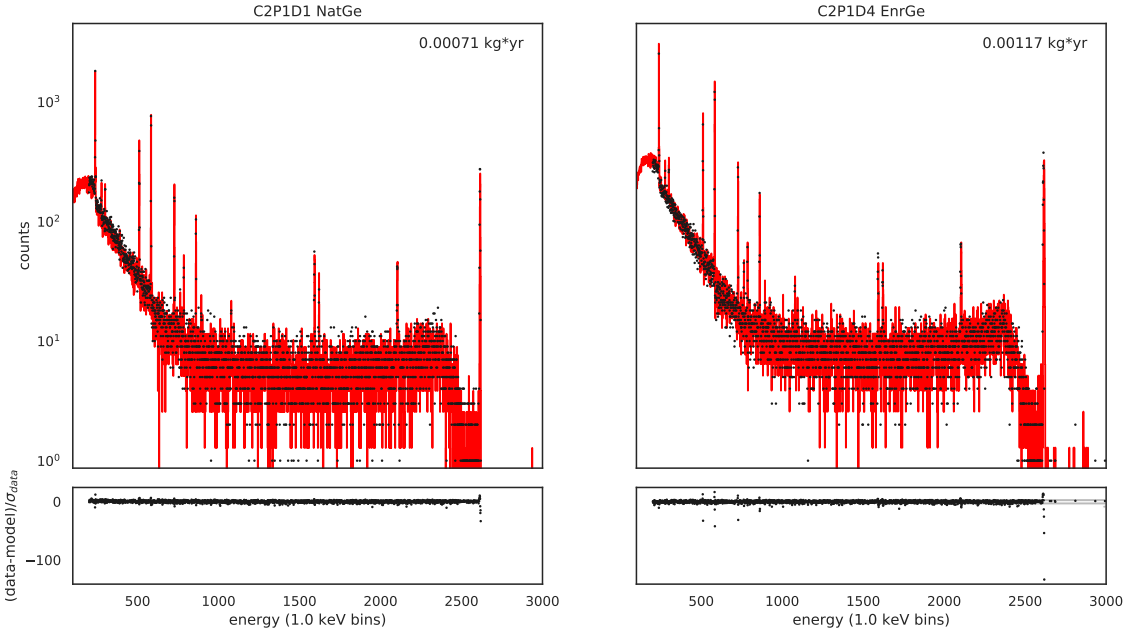
C2P1D1 NatGe
0.00071 kg*yr
C2P1D4 EnrGe
0.00117 kg*yr
counts
(data-model)/σ_{data}
energy (1.0 keV bins)

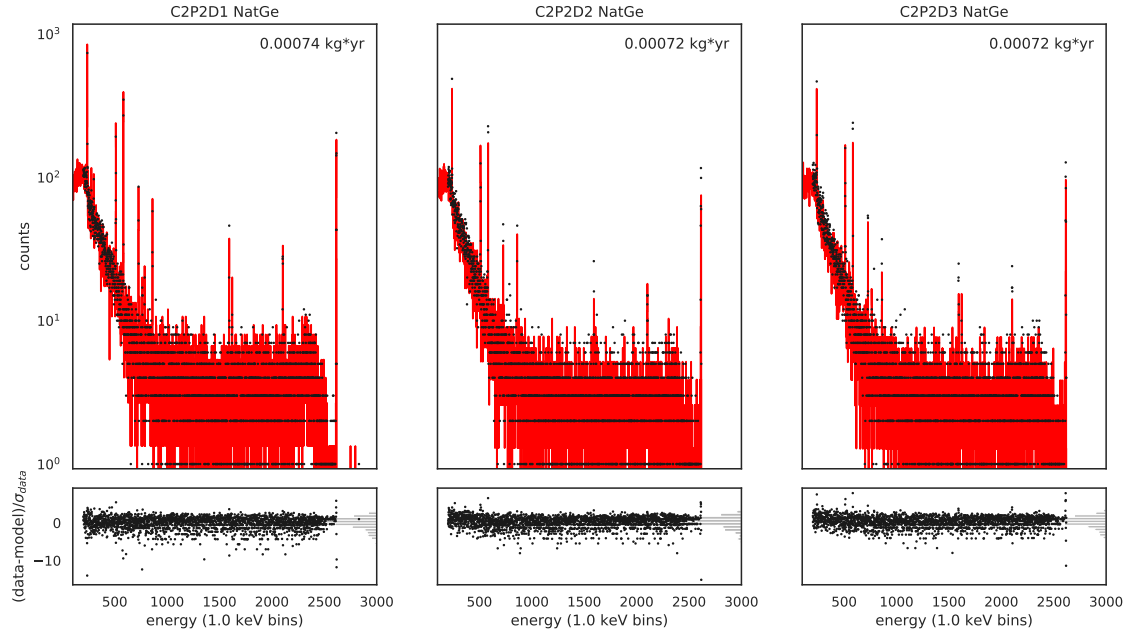
C2P2D1 NatGe
0.00074 kg*yr
C2P2D2 NatGe
0.00072 kg*yr
C2P2D3 NatGe
0.00072 kg*yr
counts
(data-model)/σ_{data}
energy (1.0 keV bins)

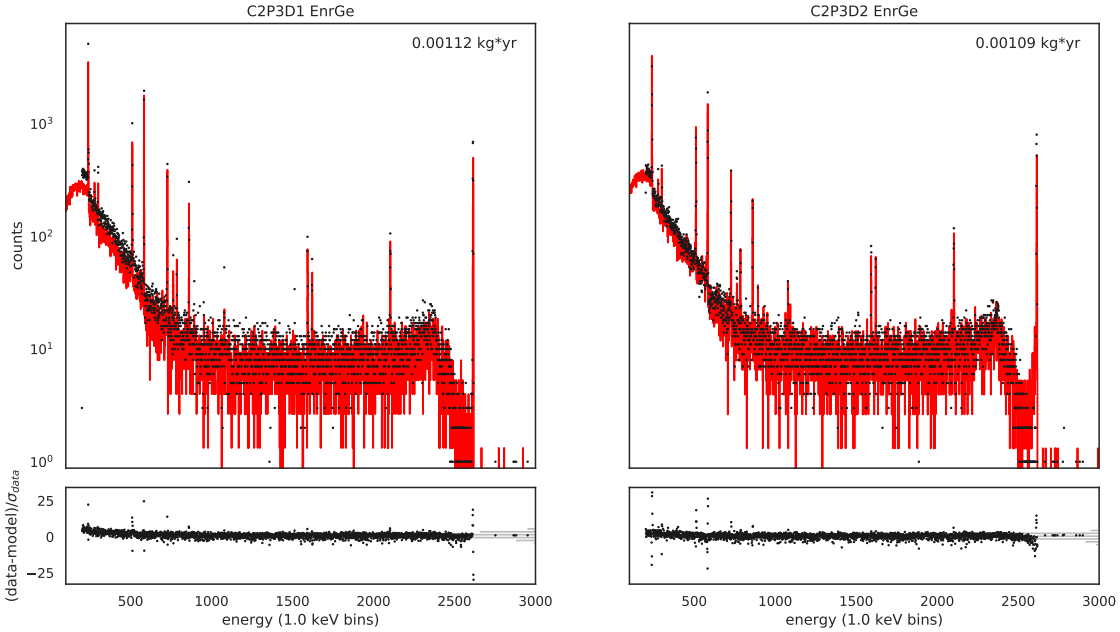
C2P3D1 EnrGe
0.00112 kg*yr
C2P3D2 EnrGe
0.00109 kg*yr
counts
(data-model)/σ_{data}
energy (1.0 keV bins)

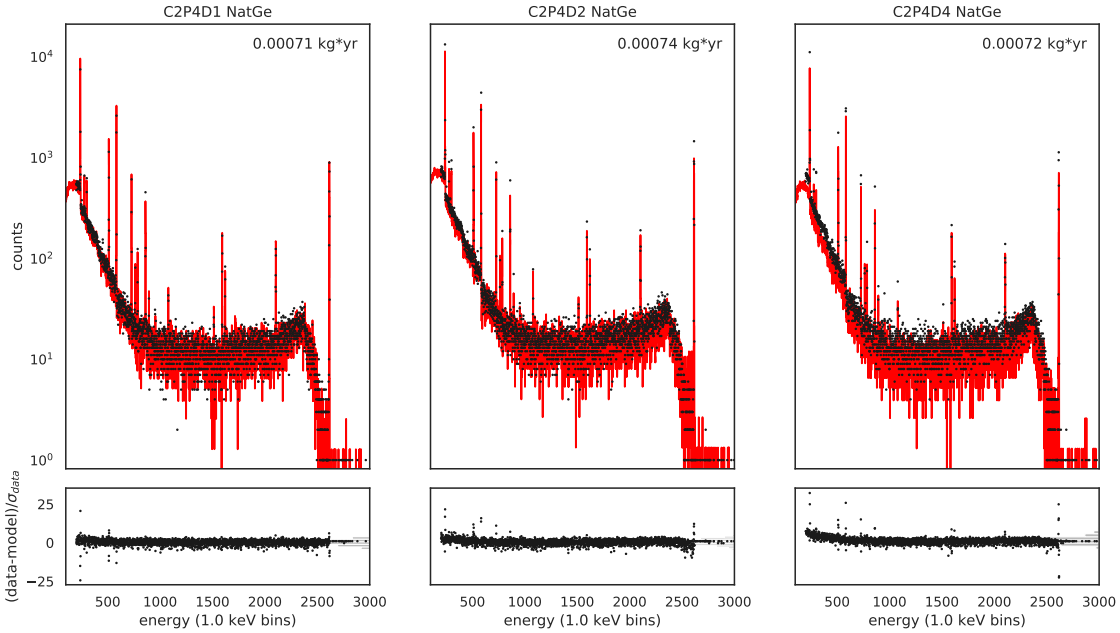
C2P4D1 NatGe
0.00071 kg*yr
C2P4D2 NatGe
0.00074 kg*yr
C2P4D4 NatGe
0.00072 kg*yr
counts
(data-model)/σ_{data}
energy (1.0 keV bins)

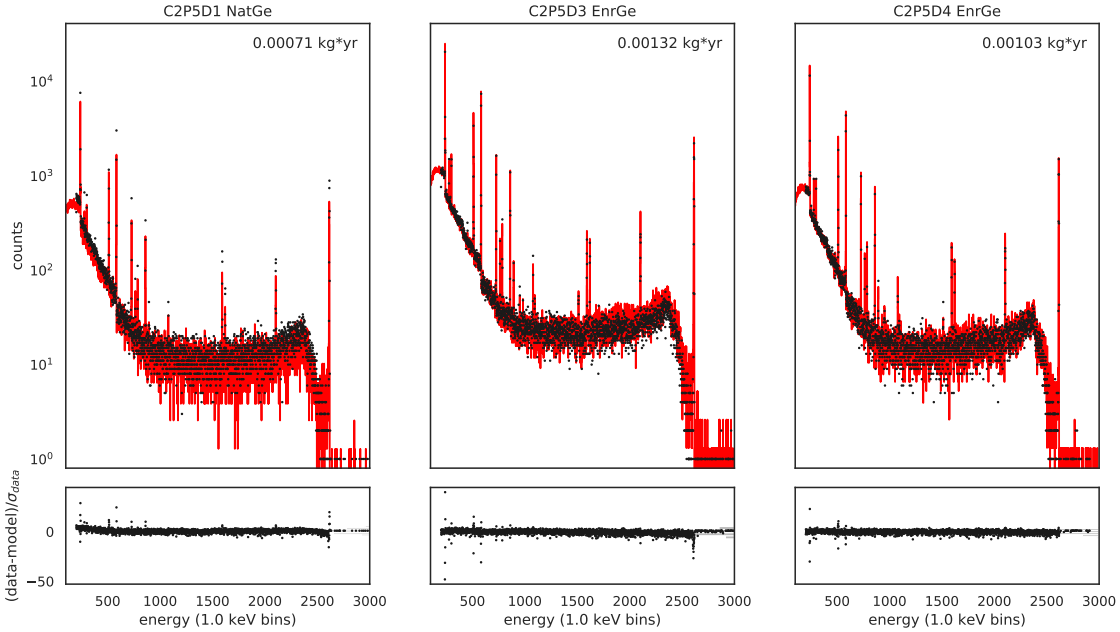
C2P5D1 NatGe
0.00071 kg*yr
C2P5D3 EnrGe
0.00132 kg*yr
C2P5D4 EnrGe
0.00103 kg*yr
counts
(data-model)/σ_{data}
energy (1.0 keV bins)

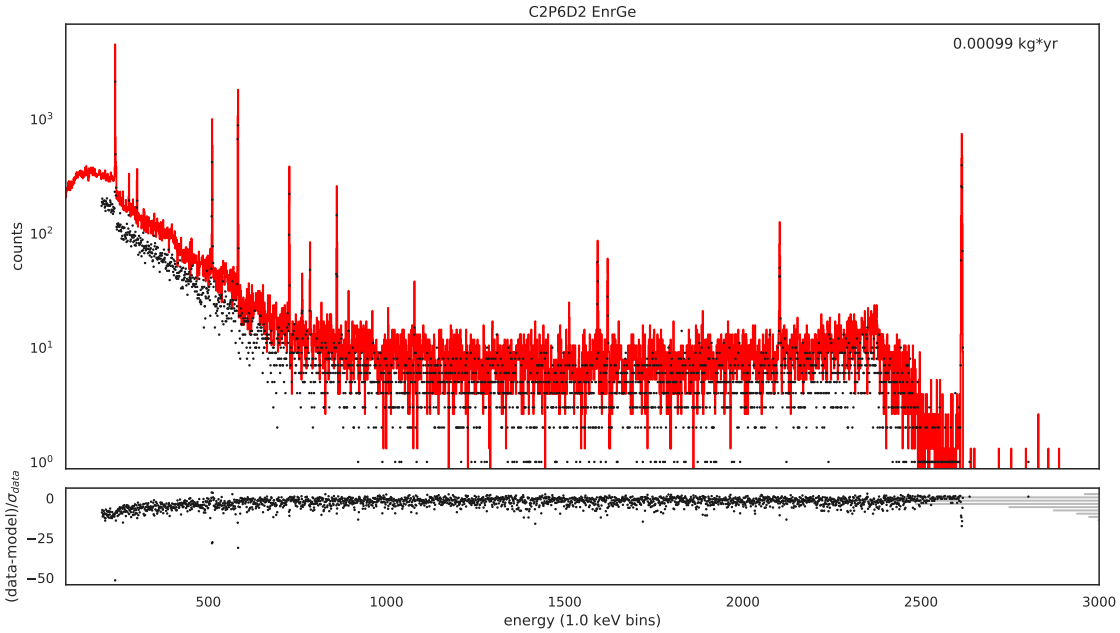
C2P6D2 EnrGe
0.00099 kg*yr
counts
(data-model)/σ_{data}
energy (1.0 keV bins)

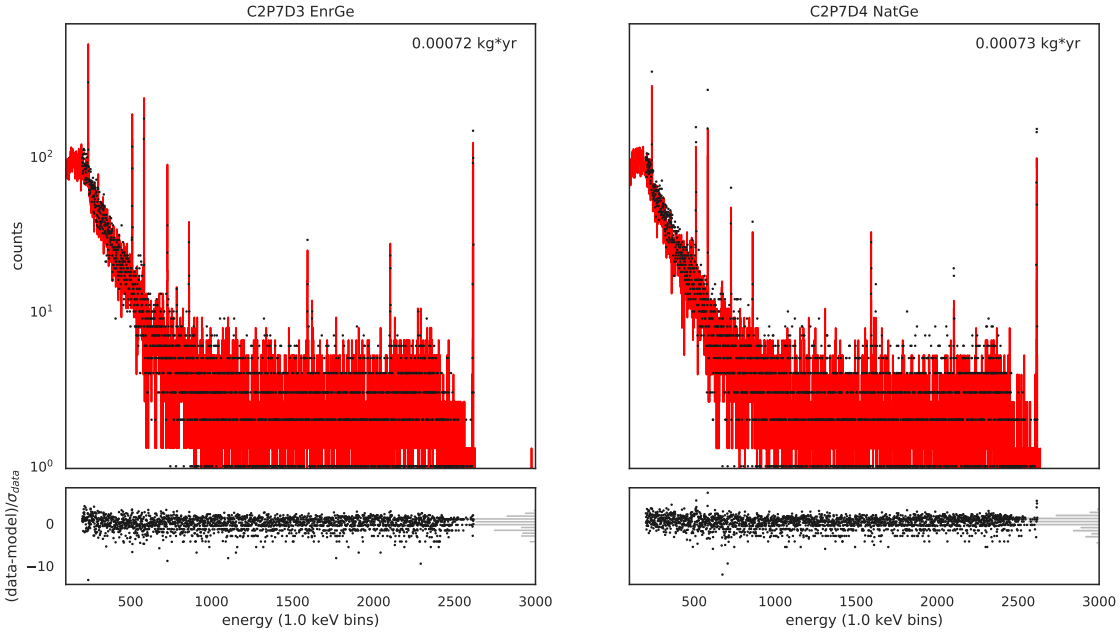
C2P7D3 EnrGe
0.00072 kg*yr
C2P7D4 NatGe
0.00073 kg*yr
counts
10^2
10^1
10^0
(data-model)/σ_{data}
0
−10
500
1000
1500
2000
2500
3000
energy (1.0 keV bins)

C-2 M2 Calibration Source

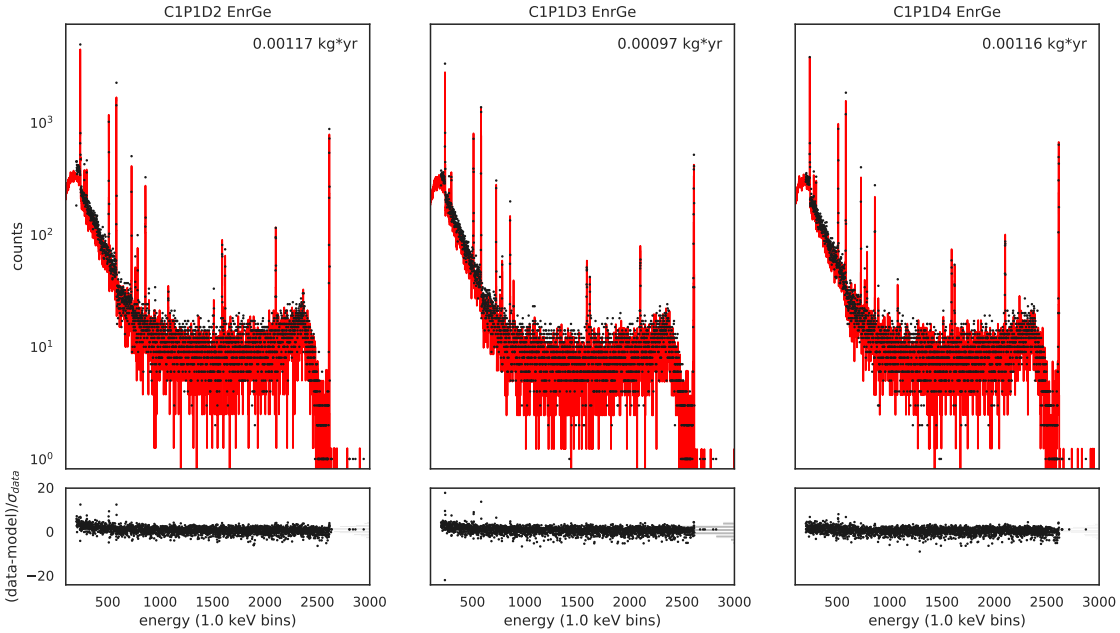

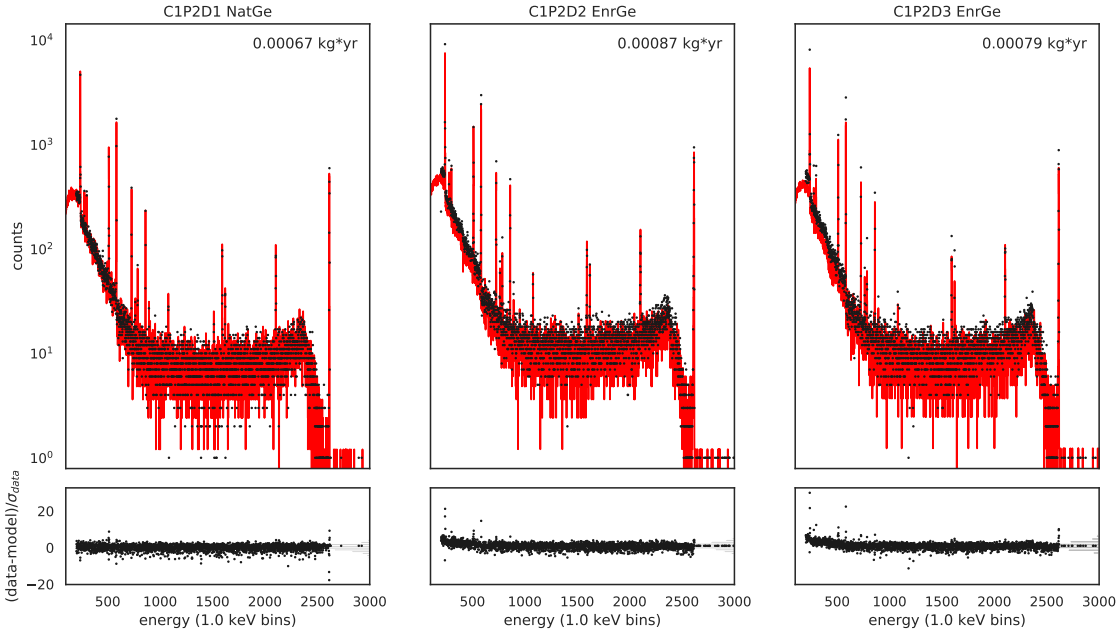

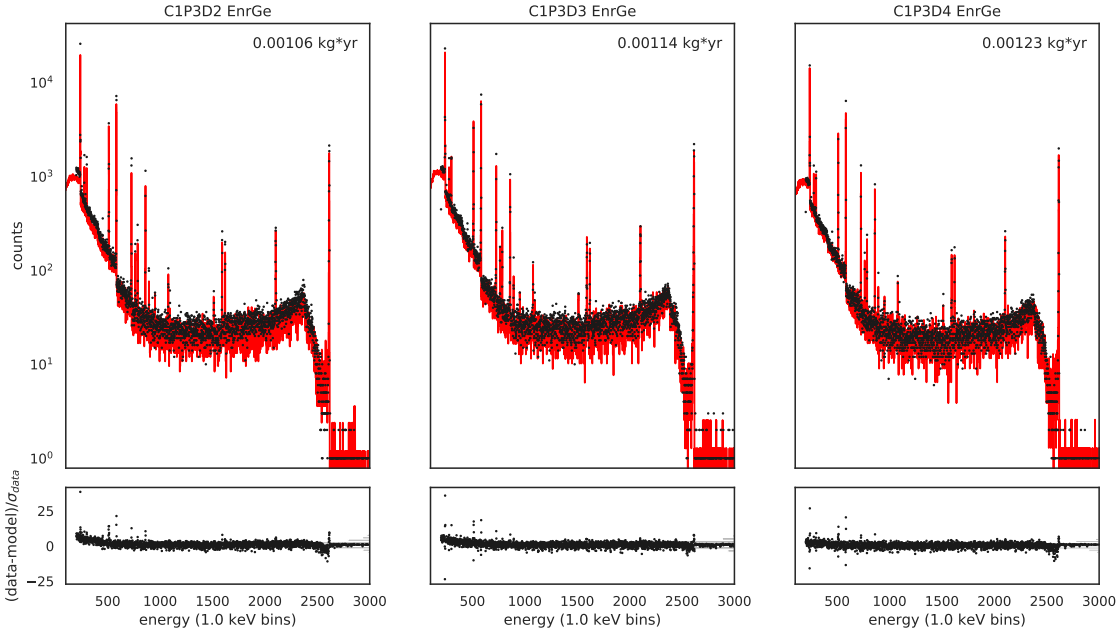
C1P3D2 EnrGe
0.00106 kg*yr
C1P3D3 EnrGe
0.00114 kg*yr
C1P3D4 EnrGe
0.00123 kg*yr
counts
(data-model)/σ_{data}
energy (1.0 keV bins)

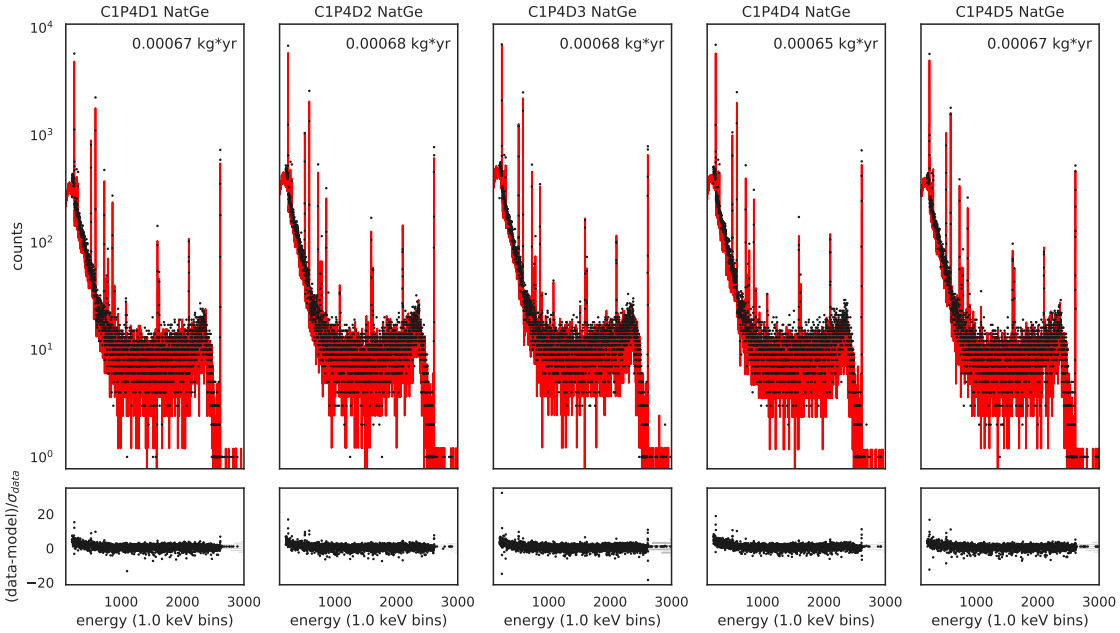
C1P4D1 NatGe
0.00067 kg*yr
C1P4D2 NatGe
0.00068 kg*yr
C1P4D3 NatGe
0.00068 kg*yr
C1P4D4 NatGe
0.00065 kg*yr
C1P4D5 NatGe
0.00067 kg*yr
counts
(data-model)/σ_{data}
energy (1.0 keV bins)

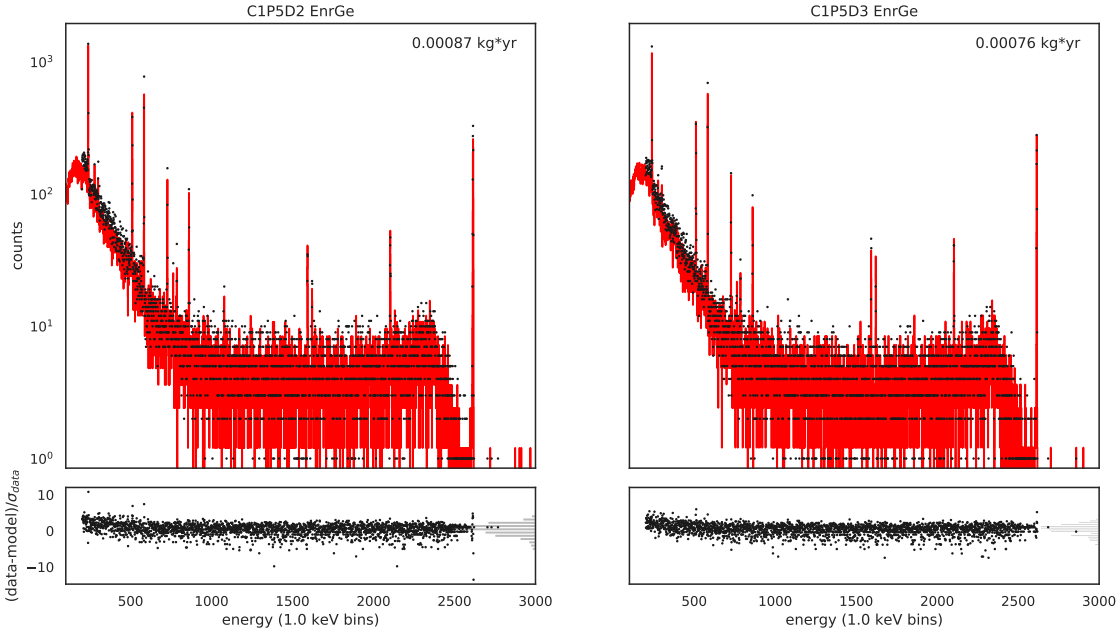
C1P5D2 EnrGe
0.00087 kg*yr
C1P5D3 EnrGe
0.00076 kg*yr
counts
(data-model)/σ_{data}
energy (1.0 keV bins)

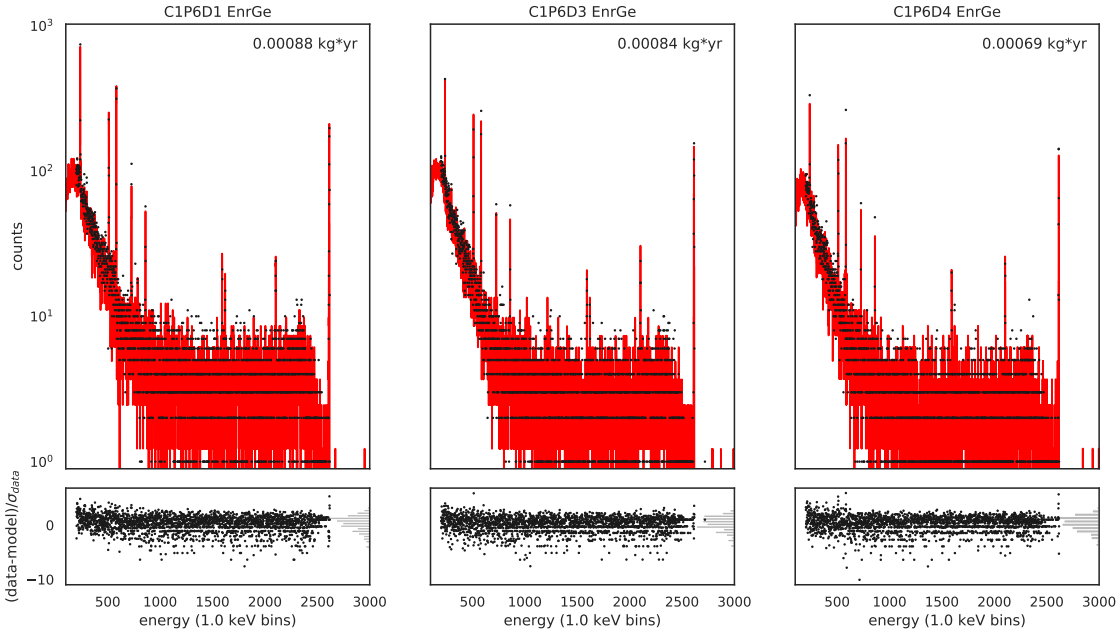
C1P6D1 EnrGe
0.00088 kg*yr
C1P6D3 EnrGe
0.00084 kg*yr
C1P6D4 EnrGe
0.00069 kg*yr
counts
(data-model)/σ_{data}
energy (1.0 keV bins)

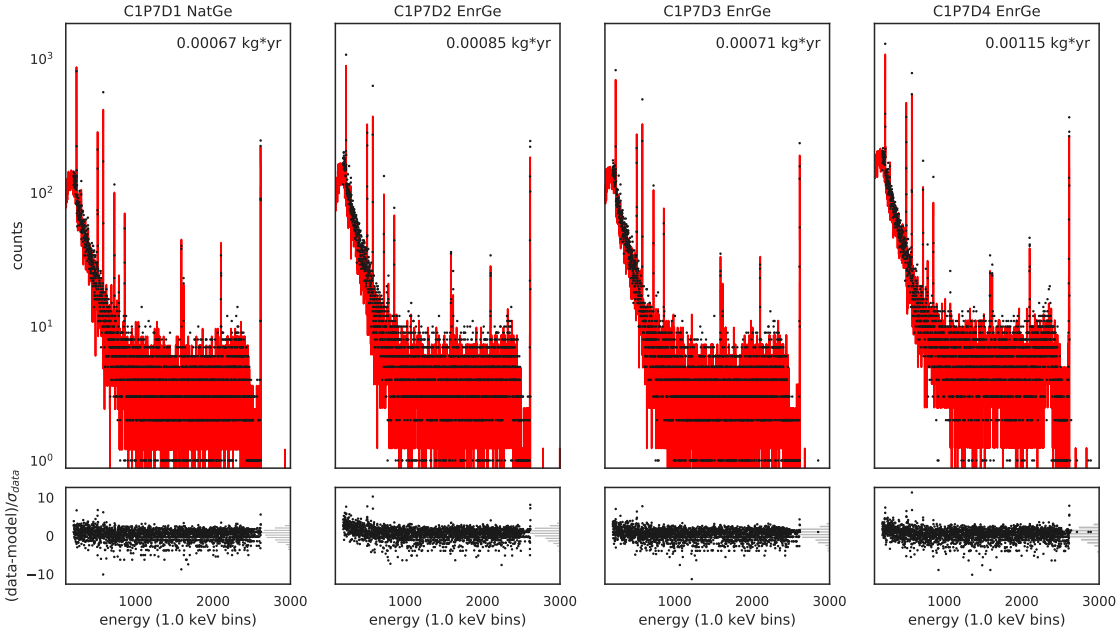
C1P7D1 NatGe
0.00067 kg*yr
C1P7D2 EnrGe
0.00085 kg*yr
C1P7D3 EnrGe
0.00071 kg*yr
C1P7D4 EnrGe
0.00115 kg*yr
counts
(data-model)/σ_{data}
energy (1.0 keV bins)

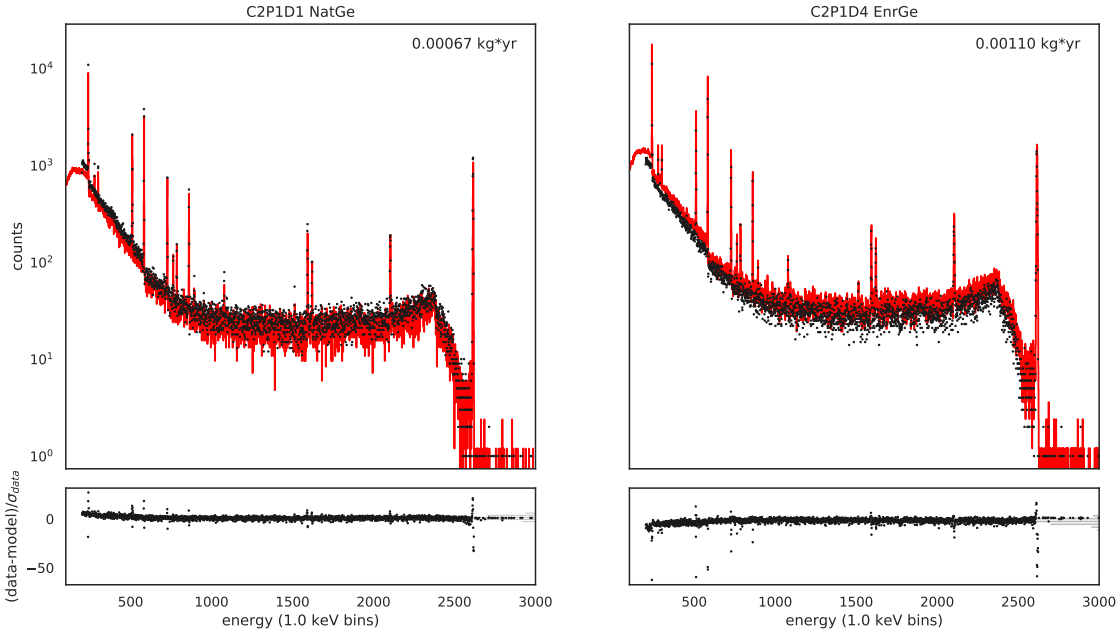
C2P1D1 NatGe
0.00067 kg*yr
C2P1D4 EnrGe
0.00110 kg*yr
counts
(data-model)/σ_{data}
energy (1.0 keV bins)

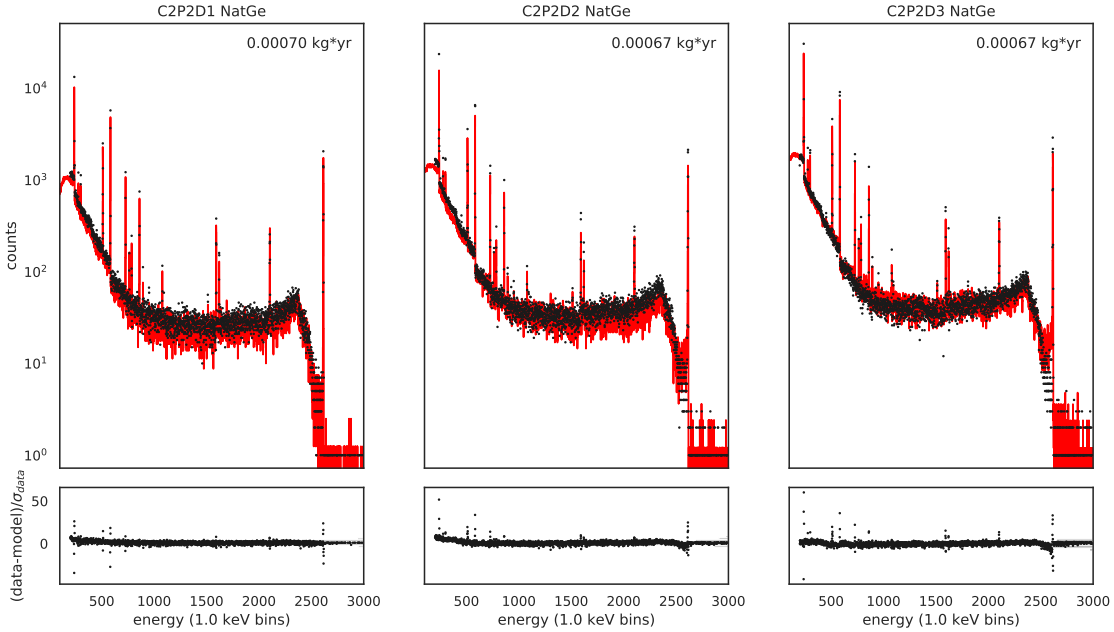
C2P2D1 NatGe
0.00070 kg*yr
C2P2D2 NatGe
0.00067 kg*yr
C2P2D3 NatGe
0.00067 kg*yr
counts
(data-model)/σ_{data}
energy (1.0 keV bins)

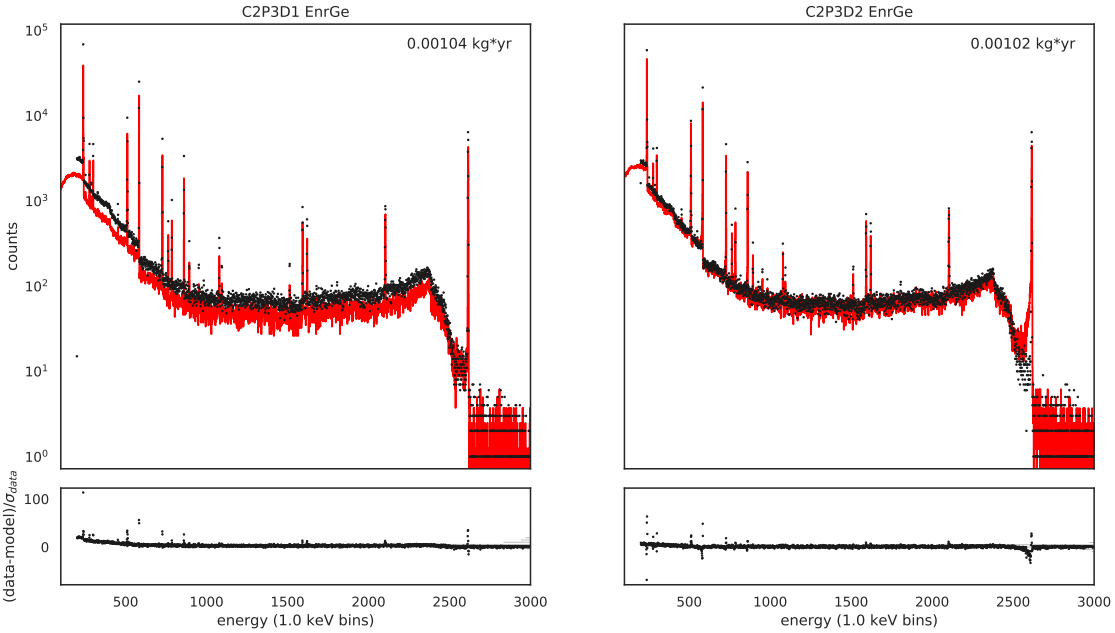
C2P3D1 EnrGe
0.00104 kg*yr
C2P3D2 EnrGe
0.00102 kg*yr
counts
(data-model)/σ_{data}
energy (1.0 keV bins)

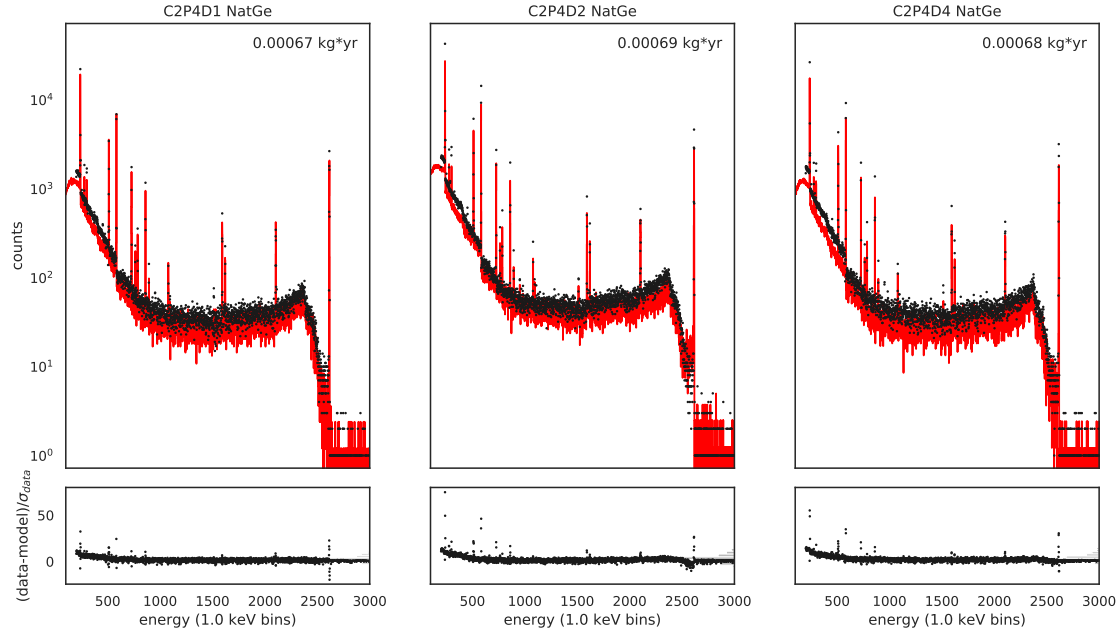
C2P4D1 NatGe
0.00067 kg*yr
C2P4D2 NatGe
0.00069 kg*yr
C2P4D4 NatGe
0.00068 kg*yr
counts
(data-model)/σ_{data}
energy (1.0 keV bins)

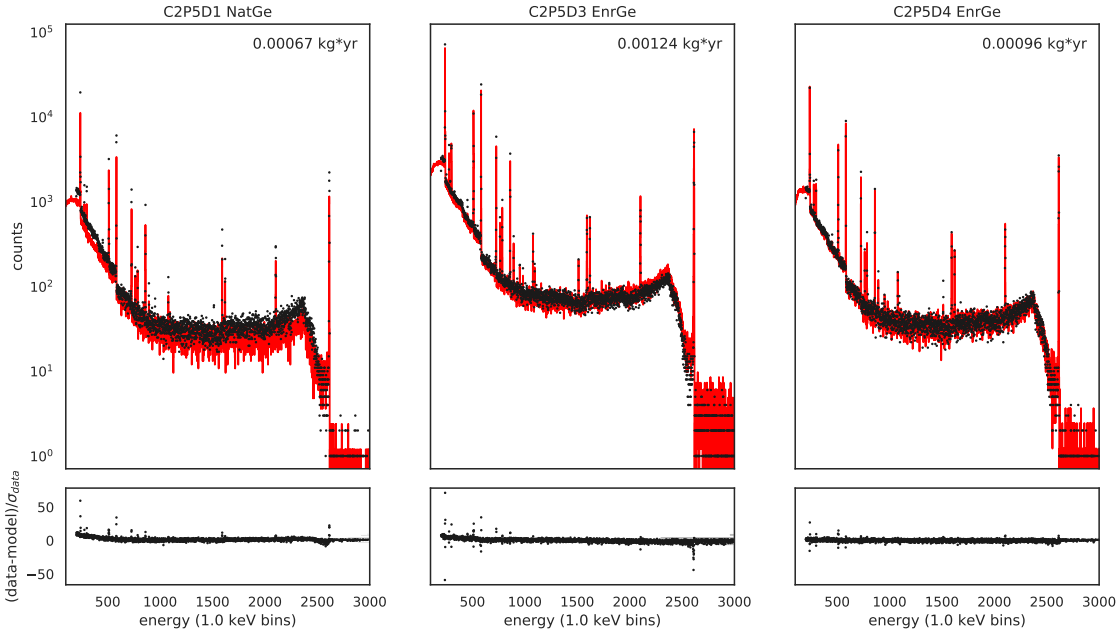
C2P5D1 NatGe
0.00067 kg*yr
C2P5D3 EnrGe
0.00124 kg*yr
C2P5D4 EnrGe
0.00096 kg*yr
counts
(data-model)/σ_{data}
energy (1.0 keV bins)

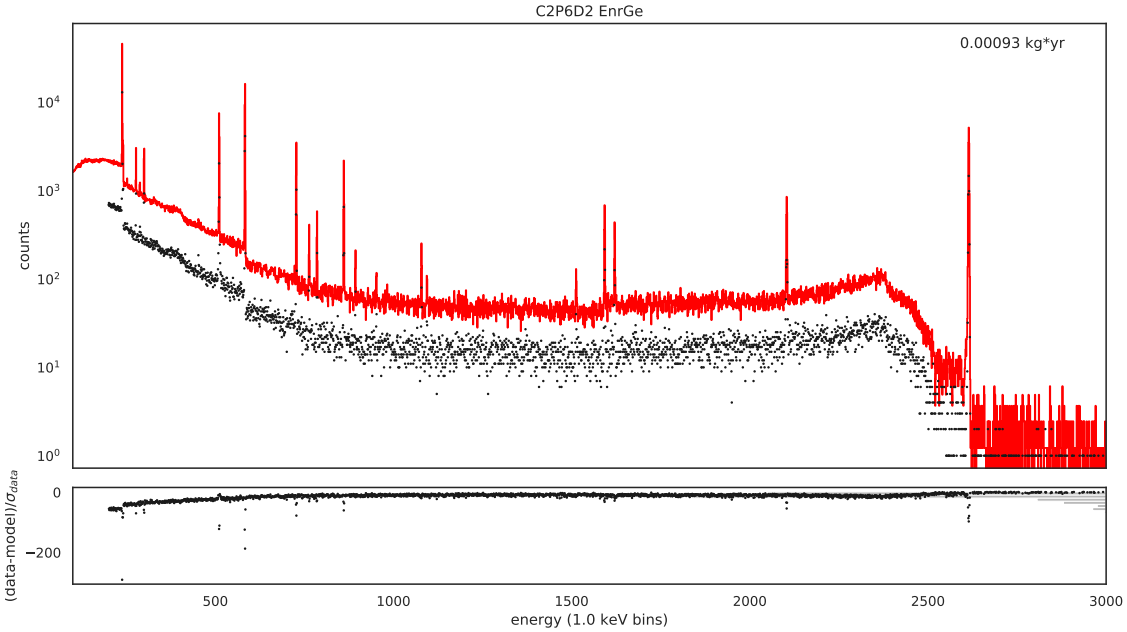
C2P6D2 EnrGe
0.00093 kg*yr
counts
(data-model)/σ_{data}
energy (1.0 keV bins)

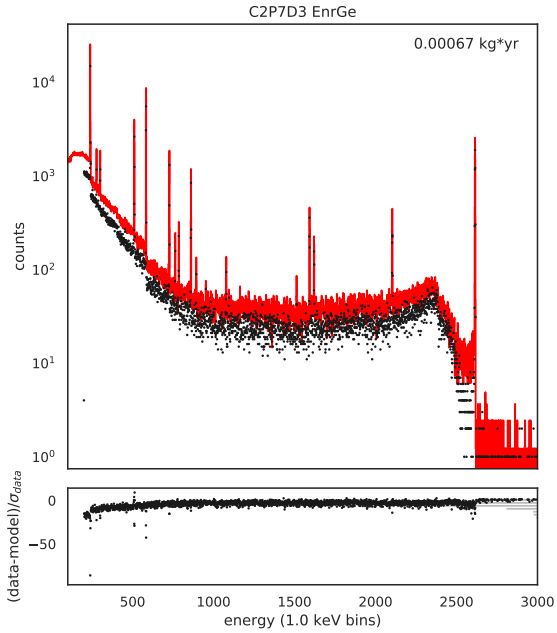
C2P7D3 EnrGe
0.00067 kg*yr
counts
(data-model)/σ_{data}
energy (1.0 keV bins)

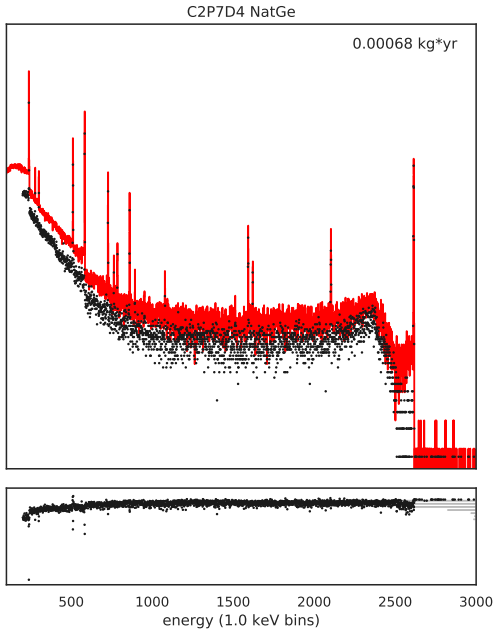
C2P7D4 NatGe
0.00068 kg*yr
energy (1.0 keV bins)

APPENDIX D
DETAILED EXPECTED CONTRIBUTIONS

Tables D.1 and D.2 provide an ordered list of components expected based on prior distributions to contribute to DS1-6a under two sets of cuts: data cleaning and DCR; and data cleaning, multiplicity, and DCR.

Table D.1: The second and third columns present the counts attributed to each component and the percentage of the total fitted counts. The subsequent columns summarize each component's prior distribution.

Parameter	Counts	%	Prior Mean μBq kg^{-1}	Prior Std. Dev. μBq kg^{-1}
2v_bulk_EnrGe	87,390.63	61.64	79.94	79.94
Pb210_pbbrem_RadShieldAssembly_001_RadShieldPb_001	13,714.45	9.67	555549.64	24997.74
Co60_bulk_RadShieldAssembly_001_RadShieldCuOuter_001	4,797.07	3.38	21.79	10.89
K40_bulk_RadShieldAssembly_001_RadShieldPb	4,407.63	3.11	418.88	173.45
Co60_bulk_DUCopperSpringClipCo60	3,733.89	2.63	703.79	351.90
2v_bulk_NatGe	3,276.80	2.31	7.04	7.04
U238_bulk_RadShieldAssembly_001_RadShieldPb	3,088.85	2.18	36.07	24.87
Rn222_surf_N2	1,708.17	1.20	89.20	44.60
U238_bulk_LMFEs	1,483.55	1.05	10571.45	263.83
K40_bulk_RadShieldAssembly_001_RadShieldCuInner_001	1,341.98	0.95	12.41	2.48
Th232_bulk_LMFEs	1,319.76	0.93	7566.31	136.08
U238_bulk_M1CPHVCables	1,301.80	0.92	1405.38	800.36
Co60_bulk_NatGe	988.64	0.70	2.39	1.19
U238_bulk_M2CPHVCables	939.95	0.66	1405.38	800.36
K40_bulk_M1CPHVCables	887.16	0.63	12411.36	12411.36
K40_bulk_M2CPHVCables	860.15	0.61	12411.36	12411.36
Th232_bulk_RadShieldAssembly_001_RadShieldPb	726.00	0.51	5.27	5.27
K40_bulk_Connectors	723.92	0.51	29011.55	29011.55
Th232_bulk_M1CPHVCables	678.55	0.48	585.97	356.95
K40_bulk_VesselCopper	579.98	0.41	12.41	2.48
Th232_bulk_M2CPHVCables	491.67	0.35	585.97	356.95
U238_bulk_M1StringHVCables	380.69	0.27	1405.38	800.36
Rn222_bulk_N2	376.70	0.27	1165.00	233.00
Co60_bulk_VesselWeldedCopperCo60	365.33	0.26	2.53	1.26
U238_bulk_M1StringSigCables	314.15	0.22	1405.38	800.36
K40_bulk_M1StringHVCables	274.34	0.19	12411.36	12411.36
U238_bulk_M2StringHVCables	253.03	0.18	1405.38	800.36
K40_bulk_M1StringSigCables	229.04	0.16	12411.36	12411.36
U238_bulk_M2StringSigCables	200.98	0.14	1405.38	800.36
U238_bulk_M1CPSigCables	199.51	0.14	1405.38	800.36
Th232_bulk_RadShieldAssembly_001_RadShieldCuOuter_001	190.57	0.13	1.10	0.20
U238_bulk_RadShieldAssembly_001_RadShieldCuOuter_001	189.44	0.13	1.49	0.25
Th232_bulk_RadShieldAssembly_001_RadShieldCuInner_001	187.22	0.13	0.12	0.12
Th232_bulk_M1StringHVCables	186.39	0.13	585.97	356.95
K40_bulk_RadShieldAssembly_001_RadShieldCuOuter_001	184.33	0.13	12.41	2.48
U238_bulk_Connectors	182.90	0.13	539.77	409.18
K40_bulk_M2StringHVCables	181.07	0.13	12411.36	12411.36
Th232_bulk_Connectors	164.77	0.12	390.28	361.48
Th232_bulk_M1StringSigCables	153.64	0.11	585.97	356.95
U238_bulk_M2CPSigCables	144.06	0.10	1405.38	800.36
K40_bulk_M2StringSigCables	143.11	0.10	12411.36	12411.36
Co60_bulk_EnrGe	140.73	0.10	0.15	0.07
K40_bulk_ThermosyphonAndShieldCopper	139.78	0.10	12.41	2.48
K40_bulk_M1CPSigCables	135.97	0.10	12411.36	12411.36
U238_bulk_RadShieldAssembly_001_RadShieldCuInner_001	133.08	0.09	0.11	0.11
K40_bulk_M2CPSigCables	131.83	0.09	12411.36	12411.36
Th232_bulk_M2StringHVCables	123.98	0.09	585.97	356.95
K40_bulk_ColdPlateCopper	112.80	0.08	12.41	2.48
Th232_bulk_M1CPSigCables	103.99	0.07	585.97	356.95
Th232_bulk_VesselCopper	100.92	0.07	0.12	0.12
Th232_bulk_M2StringSigCables	98.52	0.07	585.97	356.95
Th232_bulk_M2CPSigCables	75.35	0.05	585.97	356.95
U238_bulk_VesselCopper	72.49	0.05	0.11	0.11
K40_bulk_M1DUCopper	68.63	0.05	12.41	2.48
U238_bulk_EnrGe	61.39	0.04	0.01	0.01
U238_bulk_ThermosyphonAndShieldVespel	57.95	0.04	1049.68	1049.68
U238_bulk_M1CrossarmHVCables	57.06	0.04	1405.38	800.36
K40_bulk_ThermosyphonAndShieldVespel	47.43	0.03	10859.94	9308.52
Co60_bulk_ThermosyphonAndShieldWeldedCopperCo60	47.40	0.03	2.53	1.26
U238_bulk_DUCoatedCopper	47.02	0.03	3109.25	746.22
U238_surf_M1DUCopper	46.28	0.03	2.80	0.56
U238_bulk_DUPTFE	44.13	0.03	4.97	4.97
K40_bulk_LMFEs	42.89	0.03	4717.18	4717.18
K40_bulk_M1CrossarmHVCables	40.47	0.03	12411.36	12411.36
Th232_bulk_EnrGe	39.62	0.03	0.01	0.01
Th232_bulk_DUCoatedCopper	39.42	0.03	2150.21	121.71
K40_bulk_M2DUCopper	36.92	0.03	12.41	2.48
Th232_surf_M1DUCopper	33.14	0.02	1.80	0.36
U238_bulk_M2CrossarmHVCables	32.09	0.02	1405.38	800.36
U238_bulk_M1CrossarmSigCables	30.43	0.02	1405.38	800.36
K40_bulk_DUCoatedCopper	30.22	0.02	28547.00	2661.73
Th232_bulk_M1CrossarmHVCables	29.92	0.02	585.97	356.95
U238_bulk_NatGe	27.25	0.02	0.01	0.01

Table D.2: The second and third columns present the counts attributed to each component and the percentage of the total fitted counts. The subsequent columns summarize each component's prior distribution.

Parameter	Counts	%	Prior Mean μBq kg^{-1}	Prior Std. Dev. μBq kg^{-1}
K40_bulk_M1StringCopper	26.21	0.02	12.41	2.48
U238_surf_M2DUCopper	24.39	0.02	2.80	0.56
Th232_bulk_ThermosyphonAndShieldCopper	23.63	0.02	0.12	0.12
U238_bulk_M2BottomSeal	23.60	0.02	116.91	116.91
U238_bulk_M2TopSeal	23.59	0.02	116.91	116.91
K40_bulk_M2CrossarmHVCables	22.49	0.02	12411.36	12411.36
K40_bulk_M1CrossarmSigCables	21.58	0.02	12411.36	12411.36
Ge68_bulk_EnrGe	20.51	0.01	0.02	0.01
Th232_bulk_ColdPlateCopper	19.32	0.01	0.12	0.12
K40_bulk_M2StringCopper	18.04	0.01	12.41	2.48
Th232_surf_M2DUCopper	17.88	0.01	1.80	0.36
Th232_bulk_NatGe	17.72	0.01	0.01	0.01
Th232_bulk_M2CrossarmHVCables	17.50	0.01	585.97	356.95
U238_bulk_M2CrossarmSigCables	17.12	0.01	1405.38	800.36
U238_bulk_ThermosyphonAndShieldCopper	17.05	0.01	0.11	0.11
Th232_bulk_M2BottomSeal	16.60	0.01	65.32	10.52
Th232_bulk_M2TopSeal	16.58	0.01	65.32	10.52
Th232_bulk_M1CrossarmSigCables	15.96	0.01	585.97	356.95
U238_bulk_StringCoatedCopper	14.46	0.01	3109.25	746.22
U238_bulk_ColdPlateCopper	13.91	0.01	0.11	0.11
K40_bulk_SpringWashers	13.54	0.01	2047.87	2047.87
U238_bulk_SpringWashers	13.40	0.01	134.32	3.73
Th232_bulk_StringCoatedCopper	12.35	0.01	2150.21	121.71
K40_bulk_M2CrossarmSigCables	11.99	0.01	12411.36	12411.36
Th232_bulk_M1DUCopper	10.87	0.01	0.12	0.12
U238_surf_M1StringCopper	10.57	0.01	2.80	0.56
Th232_bulk_M2CrossarmSigCables	9.34	0.01	585.97	356.95
K40_bulk_StringCoatedCopper	8.92	0.01	28547.00	2661.73
Th232_surf_M1StringCopper	8.18	0.01	1.80	0.36
U238_bulk_M1DUCopper	8.04	0.01	0.11	0.11
U238_surf_M2StringCopper	7.37	0.01	2.80	0.56
U238_bulk_ThermosyphonAndShieldCoatedCopper	6.68	0.00	3109.25	746.22
Th232_bulk_M2DUCopper	6.01	0.00	0.12	0.12
Th232_bulk_ThermosyphonAndShieldCoatedCopper	5.73	0.00	2150.21	121.71
Th232_surf_M2StringCopper	5.72	0.00	1.80	0.36
K40_bulk_ThermosyphonAndShieldCoatedCopper	4.67	0.00	28547.00	2661.73
Th232_bulk_M1StringCopper	4.54	0.00	0.12	0.12
U238_bulk_M2DUCopper	4.42	0.00	0.11	0.11
U238_bulk_M1BottomSeal	4.29	0.00	94.52	94.52
Co60_bulk_DUCoatedCopperCo60	4.11	0.00	1.10	0.55
U238_bulk_DUVespel	3.96	0.00	1049.68	1049.68
Ge68_bulk_NatGe	3.48	0.00	0.01	0.00
U238_bulk_M1StringCopper	3.30	0.00	0.11	0.11
Th232_bulk_M2StringCopper	3.18	0.00	0.12	0.12
Th232_bulk_SpringWashers	3.03	0.00	24.67	2.76
U238_bulk_VesselCoatedCopper	3.00	0.00	3109.25	746.22
K40_bulk_DUPTFE	2.85	0.00	4.65	0.62
K40_bulk_DUVespel	2.80	0.00	10859.94	9308.52
Th232_bulk_VesselCoatedCopper	2.57	0.00	2150.21	121.71
Th232_bulk_Bellows	2.39	0.00	12000.00	12000.00
U238_bulk_M2StringCopper	2.29	0.00	0.11	0.11
K40_bulk_VesselCoatedCopper	2.02	0.00	28547.00	2661.73
Co60_bulk_StringCoatedCopperCo60	1.96	0.00	1.10	0.55
Co60_bulk_ThermosyphonAndShieldCoatedCopperCo60	1.69	0.00	1.10	0.55
Co57_bulk_NatGe	1.32	0.00	0.00	0.00
K40_bulk_M2BottomSeal	1.20	0.00	93.09	93.09
K40_bulk_M2TopSeal	1.19	0.00	93.09	93.09
Th232_bulk_M1BottomSeal	1.18	0.00	20.69	20.69
Th232_bulk_DUPTFE	1.10	0.00	0.10	0.01
Th232_bulk_ThermosyphonAndShieldVespel	0.81	0.00	11.77	11.77
U238_bulk_M1TopSeal	0.79	0.00	94.52	94.52
Co60_bulk_VesselCoatedCopperCo60	0.58	0.00	1.10	0.55
Th232_bulk_M1TopSeal	0.22	0.00	20.69	20.69
U238_bulk_Bellows	0.19	0.00	3000.00	3000.00
K40_bulk_Bellows	0.11	0.00	4000.00	4000.00
Th232_bulk_DUVespel	0.05	0.00	11.77	11.77
K40_bulk_M1BottomSeal	0.01	0.00	4.65	0.62
K40_bulk_M1TopSeal	0.00	0.00	4.65	0.62
U238_bulk_SSCFVacHW	0.00	0.00	3000.00	3000.00
Co57_bulk_EnrGe	0.00	0.00	0.01	0.00
K40_bulk_GlassBreak	0.00	0.00	5523055.20	248227.20
K40_bulk_SSCFVacHW	0.00	0.00	4000.00	4000.00
Th232_bulk_GlassBreak	0.00	0.00	48684.00	8114.00
Th232_bulk_SSCFVacHW	0.00	0.00	12000.00	12000.00
U238_bulk_GlassBreak	0.00	0.00	161681.00	74622.00

APPENDIX E
DETAILED REGRESSION RESULTS

Tables E.1 and E.2 provide an ordered list of components resulting from regression of simulations to open and blind DS1-6a data under two sets of cuts: data cleaning and DCR; and data cleaning, multiplicity, and DCR.

Figures E.1-E.9 display the posterior distributions for all fitted parameters representing a unique combination of decay chain and hardware component. Each plot displays all hardware components for a given decay chain. The posteriors are plotted alongside their prior distributions, which are shown in grey. Points represent the distribution means and lines cover 68% credible intervals.

Table E.1: The second and third columns present the counts attributed to each component and the percentage of the total fitted counts. The subsequent columns summarize each component's prior distribution and marginal posterior distribution.

Parameter	Counts	%	Prior Mean μBq kg^{-1}	Prior Std. Dev. μBq kg^{-1}	Posterior Mean μBq kg^{-1}	Posterior Std. Dev. μBq kg^{-1}
2v_bulk_EnrGe	78,581.26	40.69	79.94	79.94	71.93	1.02
Co60_bulk_RadShieldAssembly_001_RadShieldCuOuter_001	18,377.60	9.52	21.79	10.89	83.12	6.50
Pb210_pbbrem_RadShieldAssembly_001_RadShieldPb_001	14,407.69	7.46	555549.64	24997.74	583917.52	21744.97
U238_bulk_RadShieldAssembly_001_RadShieldPb	14,248.53	7.38	36.07	24.87	166.22	15.51
2v_bulk_NatGe	14,199.52	7.35	7.04	7.04	30.44	2.29
K40_bulk_RadShieldAssembly_001_RadShieldPb	11,103.21	5.75	418.88	173.45	1053.51	136.33
Th232_bulk_RadShieldAssembly_001_RadShieldPb	8,453.90	4.38	5.27	5.27	61.37	3.64
Co60_bulk_NatGe	4,663.25	2.41	2.39	1.19	11.18	0.94
Rn222_surf_N2	4,133.76	2.14	89.20	44.60	213.97	36.68
Th232_bulk_M1CPHVCables	3,186.00	1.65	585.97	356.95	2743.26	322.49
U238_bulk_M2CPHVCables	2,182.65	1.13	1405.38	800.36	3266.27	679.07
Th232_bulk_M2CPHVCables	1,757.36	0.91	585.97	356.95	2091.66	328.37
U238_bulk_M1CPHVCables	1,547.67	0.80	1405.38	800.36	1675.11	672.97
U238_bulk_LMFEs	1,484.57	0.77	10571.45	263.83	10580.03	263.97
K40_bulk_RadShieldAssembly_001_RadShieldCuInner_001	1,388.55	0.72	12.41	2.48	12.86	2.43
Th232_bulk_LMFEs	1,330.73	0.69	7566.31	136.08	7628.21	137.49
Co60_bulk_DUCopperSpringClipCo60	965.42	0.50	703.79	351.90	180.93	63.87
Th232_bulk_RadShieldAssembly_001_RadShieldCuInner_001	731.65	0.38	0.12	0.12	0.46	0.12
U238_bulk_M1StringHVCables	611.55	0.32	1405.38	800.36	2257.37	768.03
K40_bulk_VesselCopper	534.72	0.28	12.41	2.48	11.41	2.42
Th232_bulk_Connectors	531.02	0.27	390.28	361.48	1233.39	352.54
Th232_bulk_M1StringHVCables	472.21	0.24	585.97	356.95	1475.86	351.67
U238_bulk_M1StringSigCables	469.72	0.24	1405.38	800.36	2070.00	769.97
K40_bulk_M1StringHVCables	437.62	0.23	12411.36	12411.36	20879.59	10401.41
U238_bulk_M2StringHVCables	413.41	0.21	1405.38	800.36	2253.84	770.17
Rn222_bulk_N2	398.09	0.21	1165.00	233.00	1241.06	233.36
K40_bulk_M1StringSigCables	365.43	0.19	12411.36	12411.36	19991.56	10355.05
Th232_bulk_M1StringSigCables	349.13	0.18	585.97	356.95	1326.50	346.66
Co60_bulk_VesselWeldedCopperCo60	326.36	0.17	2.53	1.26	2.32	1.14
U238_bulk_M2StringSigCables	303.27	0.16	1405.38	800.36	2105.67	770.73
Th232_bulk_VesselCopper	283.90	0.15	0.12	0.12	0.34	0.12
U238_bulk_Connectors	250.90	0.13	539.77	409.18	754.02	375.08
K40_bulk_Connectors	242.76	0.13	29011.55	29011.55	20540.98	14489.37
Th232_bulk_M2StringHVCables	232.64	0.12	585.97	356.95	1074.98	353.87
K40_bulk_M2StringHVCables	231.49	0.12	12411.36	12411.36	17612.62	10002.07
Co60_bulk_EnrGe	213.61	0.11	0.15	0.07	0.22	0.07
U238_bulk_M1CPSigCables	212.76	0.11	1405.38	800.36	1509.27	730.45
Th232_bulk_RadShieldAssembly_001_RadShieldCuOuter_001	209.32	0.11	1.10	0.20	1.19	0.20
U238_bulk_RadShieldAssembly_001_RadShieldCuInner_001	204.94	0.11	0.11	0.11	0.18	0.09
U238_bulk_RadShieldAssembly_001_RadShieldCuOuter_001	192.73	0.10	1.49	0.25	1.51	0.25
K40_bulk_RadShieldAssembly_001_RadShieldCuOuter_001	187.19	0.10	12.41	2.48	12.58	2.46
K40_bulk_M2StringSigCables	180.02	0.09	12411.36	12411.36	17520.97	10144.93
U238_bulk_M2CPSigCables	172.72	0.09	1405.38	800.36	1725.91	757.88
Th232_bulk_M2StringSigCables	165.64	0.09	585.97	356.95	992.99	342.86
Th232_bulk_M1CPSigCables	165.47	0.09	585.97	356.95	924.09	346.93
K40_bulk_ThermosyphonAndShieldCopper	137.25	0.07	12.41	2.48	12.22	2.47
K40_bulk_ColdPlateCopper	113.29	0.06	12.41	2.48	12.40	2.46
Th232_bulk_M2CPSigCables	105.19	0.05	585.97	356.95	826.96	345.36
U238_bulk_EnrGe	105.09	0.05	0.01	0.01	0.03	0.01
U238_bulk_VesselCopper	86.14	0.04	0.11	0.11	0.15	0.09
K40_bulk_M1CPSigCables	75.64	0.04	12411.36	12411.36	12247.09	8478.31
K40_bulk_M1DUCopper	68.92	0.04	12.41	2.48	12.36	2.49
U238_bulk_M1CrossarmHVCables	53.82	0.03	1405.38	800.36	1388.37	712.00
U238_bulk_DUCoatedCopper	47.86	0.02	3109.25	746.22	3132.96	749.09
U238_surf_M1DUCopper	47.45	0.02	2.80	0.56	2.83	0.56
U238_bulk_DUPTFE	46.30	0.02	4.97	4.97	6.62	4.01
Co60_bulk_ThermosyphonAndShieldWeldedCopperCo60	44.15	0.02	2.53	1.26	2.42	1.17
Th232_bulk_EnrGe	41.31	0.02	0.01	0.01	0.02	0.01
U238_bulk_ThermosyphonAndShieldVespel	41.02	0.02	1049.68	1049.68	1191.88	783.65
Th232_bulk_DUCoatedCopper	39.55	0.02	2150.21	121.71	2155.90	121.00
U238_bulk_NatGe	38.30	0.02	0.01	0.01	0.02	0.01
K40_bulk_LMFEs	38.00	0.02	4717.18	4717.18	5821.22	3662.96
K40_bulk_M2DUCopper	37.03	0.02	12.41	2.48	12.54	2.46
Th232_bulk_ThermosyphonAndShieldCopper	34.07	0.02	0.12	0.12	0.19	0.10
Th232_surf_M1DUCopper	33.98	0.02	1.80	0.36	1.86	0.36
K40_bulk_ThermosyphonAndShieldVespel	33.05	0.02	10859.94	9308.52	10804.84	7026.91
Th232_bulk_M1CrossarmHVCables	32.33	0.02	585.97	356.95	687.18	325.37
U238_bulk_M2TopSeal	30.92	0.02	116.91	116.91	171.88	98.37
U238_bulk_M2BottomSeal	30.63	0.02	116.91	116.91	172.19	98.11
U238_bulk_M2CrossarmHVCables	30.50	0.02	1405.38	800.36	1458.64	728.43
K40_bulk_DUCoatedCopper	30.23	0.02	28547.00	2661.73	28546.52	2664.41
U238_bulk_M1CrossarmSigCables	28.20	0.01	1405.38	800.36	1435.94	726.91
Th232_bulk_ColdPlateCopper	26.29	0.01	0.12	0.12	0.18	0.10
K40_bulk_M1StringCopper	26.02	0.01	12.41	2.48	12.40	2.47
K40_bulk_M1CrossarmHVCables	25.48	0.01	12411.36	12411.36	13652.66	9141.23
U238_surf_M2DUCopper	24.92	0.01	2.80	0.56	2.82	0.56
K40_bulk_M2CrossarmHVCables	24.51	0.01	12411.36	12411.36	15773.32	9724.75
Ge68_bulk_EnrGe	22.62	0.01	0.02	0.01	0.02	0.01
K40_bulk_M1CrossarmSigCables	19.91	0.01	12411.36	12411.36	14741.49	9392.21

Table E.2: The second and third columns present the counts attributed to each component and the percentage of the total fitted counts. The subsequent columns summarize each component's prior distribution and marginal posterior distribution.

Parameter	Counts	%	Prior Mean μBq kg^{-1}	Prior Std. Dev. μBq kg^{-1}	Posterior Mean μBq kg^{-1}	Posterior Std. Dev. μBq kg^{-1}
Th232_bulk_M2CrossarmHVCables	18.78	0.01	585.97	356.95	657.00	322.03
K40_bulk_M2StringCopper	18.15	0.01	12.41	2.48	12.47	2.51
Th232_bulk_NatGe	18.14	0.01	0.01	0.01	0.02	0.01
Th232_surf_M2DUCopper	18.01	0.01	1.80	0.36	1.82	0.36
Th232_bulk_M2TopSeal	16.91	0.01	65.32	10.52	65.96	10.60
Th232_bulk_M2BottomSeal	16.84	0.01	65.32	10.52	65.88	10.57
U238_bulk_ThermosyphonAndShieldCopper	16.63	0.01	0.11	0.11	0.14	0.08
U238_bulk_M2CrossarmSigCables	16.56	0.01	1405.38	800.36	1467.81	737.77
Th232_bulk_M1CrossarmSigCables	16.14	0.01	585.97	356.95	653.36	327.26
U238_bulk_StringCoatedCopper	14.63	0.01	3109.25	746.22	3120.46	748.31
U238_bulk_ColdPlateCopper	14.37	0.01	0.11	0.11	0.14	0.09
Th232_bulk_M1DUCopper	13.79	0.01	0.12	0.12	0.17	0.10
K40_bulk_M2CrossarmSigCables	13.52	0.01	12411.36	12411.36	15923.53	9826.37
U238_bulk_SpringWashers	13.41	0.01	134.32	3.73	134.34	3.71
K40_bulk_SpringWashers	13.35	0.01	2047.87	2047.87	2673.18	1620.46
Th232_bulk_StringCoatedCopper	12.37	0.01	2150.21	121.71	2152.52	121.19
U238_surf_M1StringCopper	10.71	0.01	2.80	0.56	2.80	0.56
Th232_bulk_M2CrossarmSigCables	9.79	0.01	585.97	356.95	642.58	324.49
K40_bulk_StringCoatedCopper	8.97	0.00	28547.00	2661.73	28516.53	2676.38
Th232_surf_M1StringCopper	8.37	0.00	1.80	0.36	1.82	0.36
U238_surf_M2StringCopper	7.42	0.00	2.80	0.56	2.81	0.56
U238_bulk_M1DUCopper	7.40	0.00	0.11	0.11	0.14	0.08
U238_bulk_ThermosyphonAndShieldCoatedCopper	6.79	0.00	3109.25	746.22	3109.53	748.83
Th232_bulk_M2DUCopper	6.29	0.00	0.12	0.12	0.16	0.10
Th232_surf_M2StringCopper	5.82	0.00	1.80	0.36	1.81	0.36
Th232_bulk_ThermosyphonAndShieldCoatedCopper	5.73	0.00	2150.21	121.71	2151.50	121.98
Th232_bulk_M1StringCopper	5.18	0.00	0.12	0.12	0.16	0.10
K40_bulk_ThermosyphonAndShieldCoatedCopper	4.69	0.00	28547.00	2661.73	28552.77	2689.23
U238_bulk_M1BottomSeal	4.64	0.00	94.52	94.52	122.75	74.93
U238_bulk_M2DUCopper	4.38	0.00	0.11	0.11	0.14	0.08
U238_bulk_DUVespel	4.27	0.00	1049.68	1049.68	1364.21	835.30
Co60_bulk_DUCoatedCopperCo60	3.94	0.00	1.10	0.55	1.12	0.52
Th232_bulk_M2StringCopper	3.55	0.00	0.12	0.12	0.16	0.10
U238_bulk_M1StringCopper	3.51	0.00	0.11	0.11	0.14	0.08
Ge68_bulk_NatGe	3.45	0.00	0.01	0.00	0.01	0.00
U238_bulk_VesselCoatedCopper	3.07	0.00	3109.25	746.22	3114.55	750.51
Th232_bulk_SpringWashers	3.04	0.00	24.67	2.76	24.68	2.77
K40_bulk_DUVespel	2.91	0.00	10859.94	9308.52	13025.65	7725.28
K40_bulk_DUPTFE	2.85	0.00	4.65	0.62	4.65	0.63
U238_bulk_M2StringCopper	2.59	0.00	0.11	0.11	0.14	0.08
Th232_bulk_VesselCoatedCopper	2.57	0.00	2150.21	121.71	2149.89	123.66
K40_bulk_M2CPSigCables	2.45	0.00	12411.36	12411.36	7361.81	5767.92
Th232_bulk_Bellows	2.22	0.00	12000.00	12000.00	15144.60	9396.18
K40_bulk_VesselCoatedCopper	2.02	0.00	28547.00	2661.73	28560.57	2652.50
Co60_bulk_StringCoatedCopperCo60	1.94	0.00	1.10	0.55	1.13	0.52
Co60_bulk_ThermosyphonAndShieldCoatedCopperCo60	1.71	0.00	1.10	0.55	1.13	0.52
Co57_bulk_NatGe	1.38	0.00	0.00	0.00	0.00	0.00
Th232_bulk_M1BottomSeal	1.25	0.00	20.69	20.69	27.06	16.57
K40_bulk_M2TopSeal	1.21	0.00	93.09	93.09	120.26	73.72
K40_bulk_M2BottomSeal	1.14	0.00	93.09	93.09	120.68	74.20
Th232_bulk_DUPTFE	1.10	0.00	0.10	0.01	0.10	0.01
U238_bulk_M1TopSeal	0.80	0.00	94.52	94.52	122.64	74.87
Th232_bulk_ThermosyphonAndShieldVespel	0.79	0.00	11.77	11.77	15.31	9.35
Co60_bulk_VesselCoatedCopperCo60	0.58	0.00	1.10	0.55	1.13	0.52
Th232_bulk_M1TopSeal	0.20	0.00	20.69	20.69	26.70	16.44
U238_bulk_Bellows	0.18	0.00	3000.00	3000.00	3855.38	2374.60
K40_bulk_Bellows	0.10	0.00	4000.00	4000.00	5130.03	3176.88
Th232_bulk_DUVespel	0.06	0.00	11.77	11.77	15.19	9.40
K40_bulk_M1CPHVCables	0.02	0.00	12411.36	12411.36	3649.15	3179.27
K40_bulk_M1BottomSeal	0.01	0.00	4.65	0.62	4.65	0.62
K40_bulk_M2CPHVCables	0.00	0.00	12411.36	12411.36	1150.83	1018.91
K40_bulk_M1TopSeal	0.00	0.00	4.65	0.62	4.66	0.62
U238_bulk_SSCFVacHW	0.00	0.00	3000.00	3000.00	3873.77	2384.23
Co57_bulk_EnrGe	0.00	0.00	0.01	0.00	0.01	0.00
K40_bulk_GlassBreak	0.00	0.00	5523055.20	248227.20	5523361.47	247424.98
K40_bulk_SSCFVacHW	0.00	0.00	4000.00	4000.00	5128.67	3175.29
Th232_bulk_GlassBreak	0.00	0.00	48684.00	8114.00	48731.66	8117.21
Th232_bulk_SSCFVacHW	0.00	0.00	12000.00	12000.00	15491.61	9469.04
U238_bulk_GlassBreak	0.00	0.00	161681.00	74622.00	163949.82	71573.30

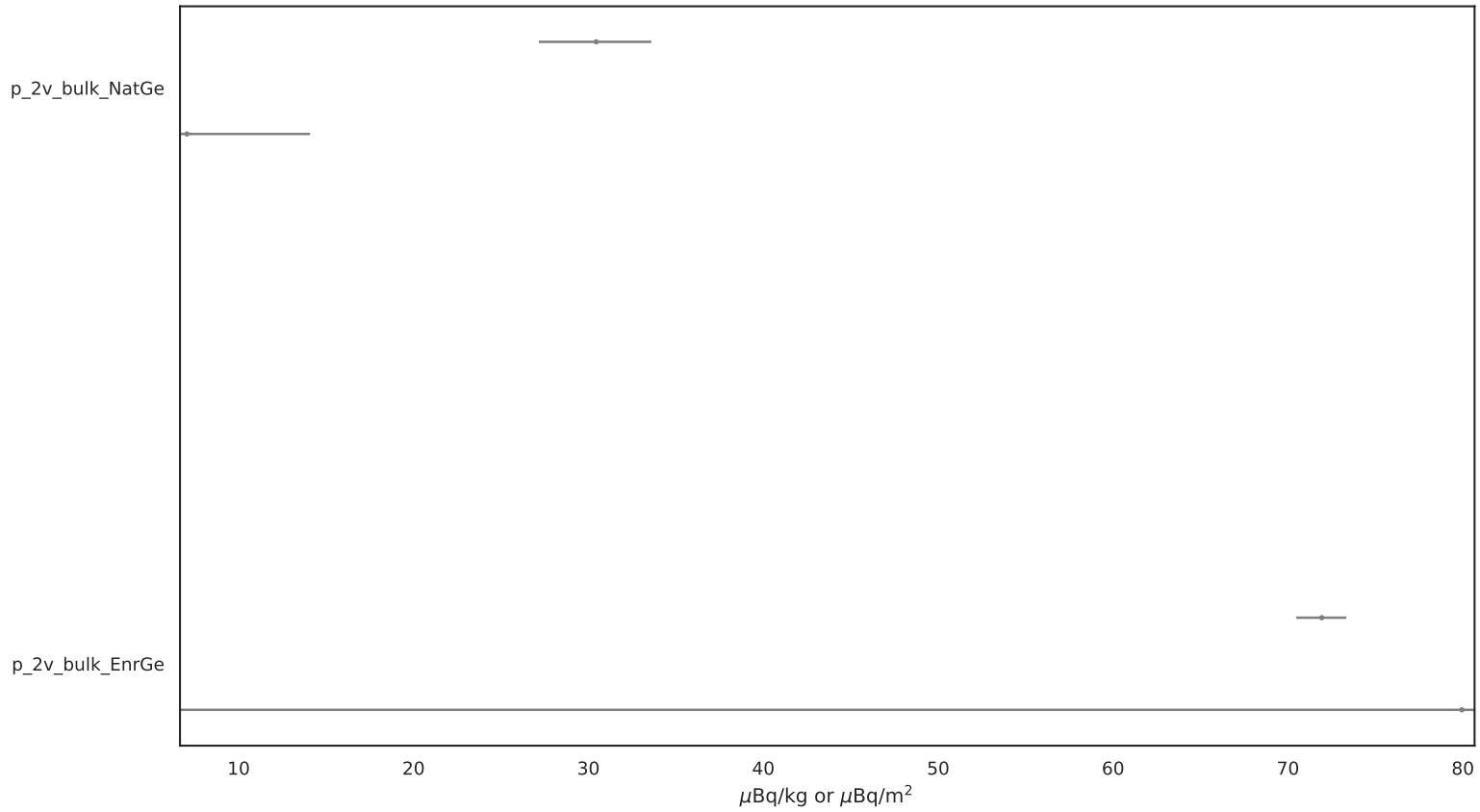

Figure E.1: $2\nu\beta\beta$

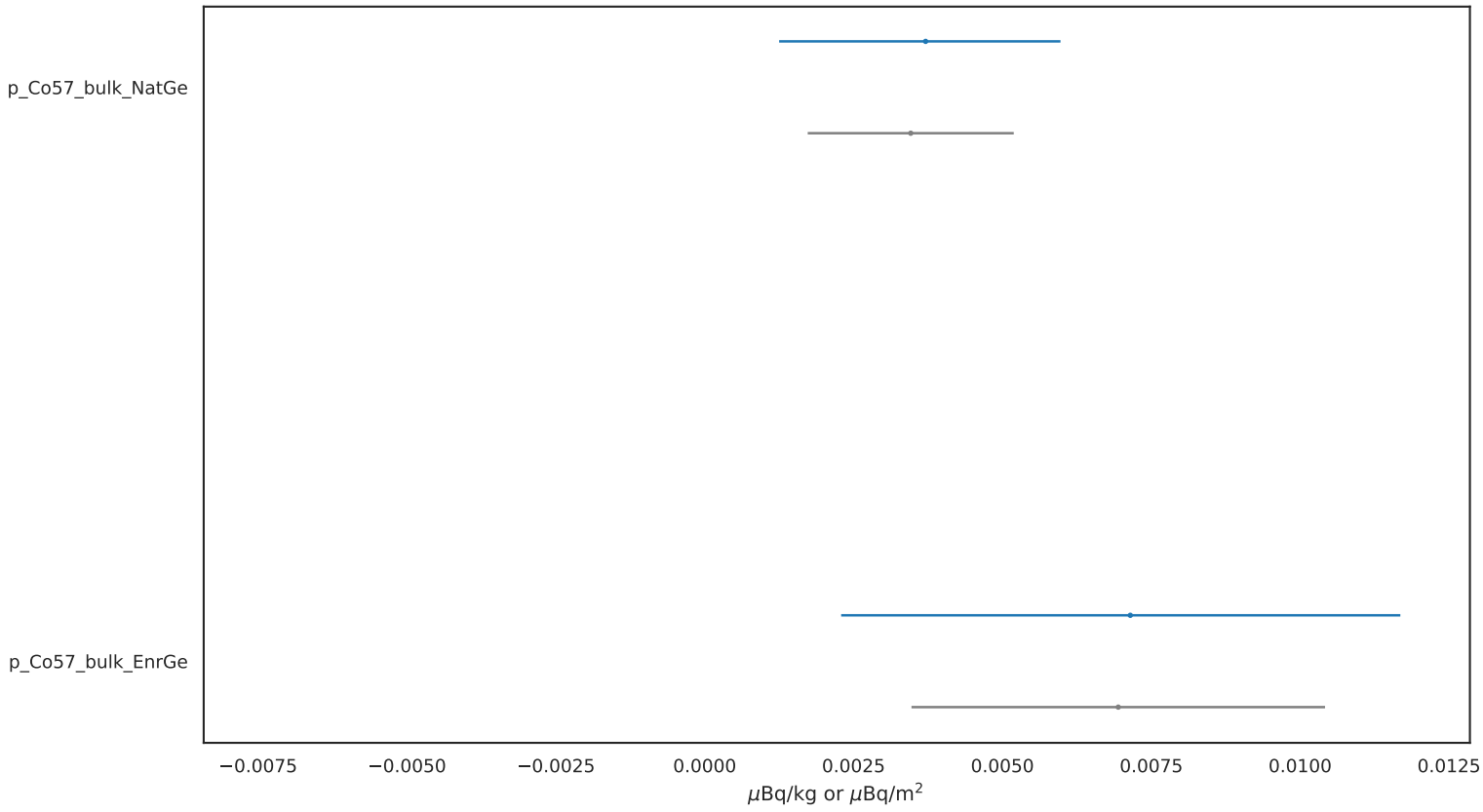

Figure E.2: ^{57}Co

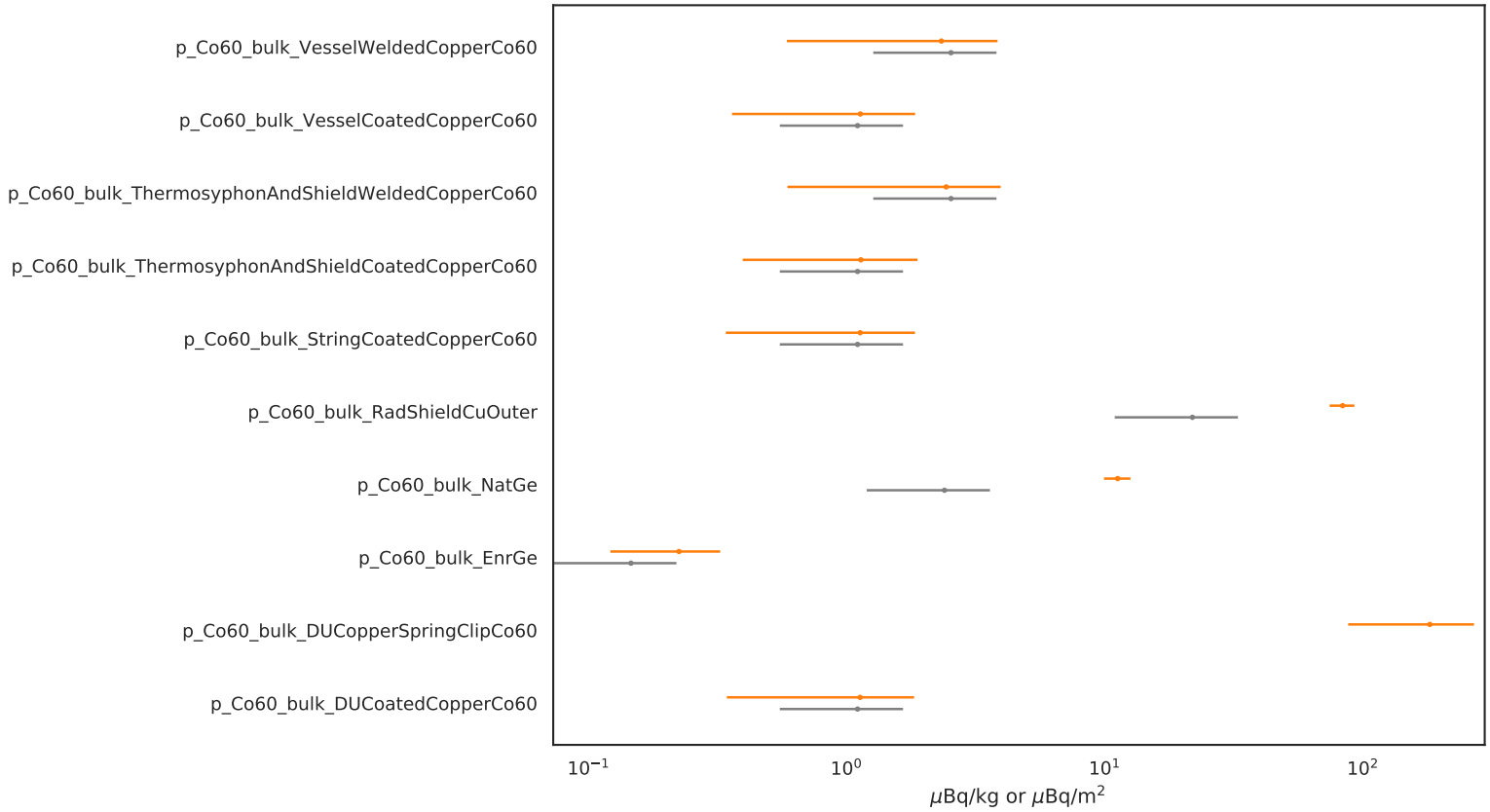

Figure E.3: ^{60}Co

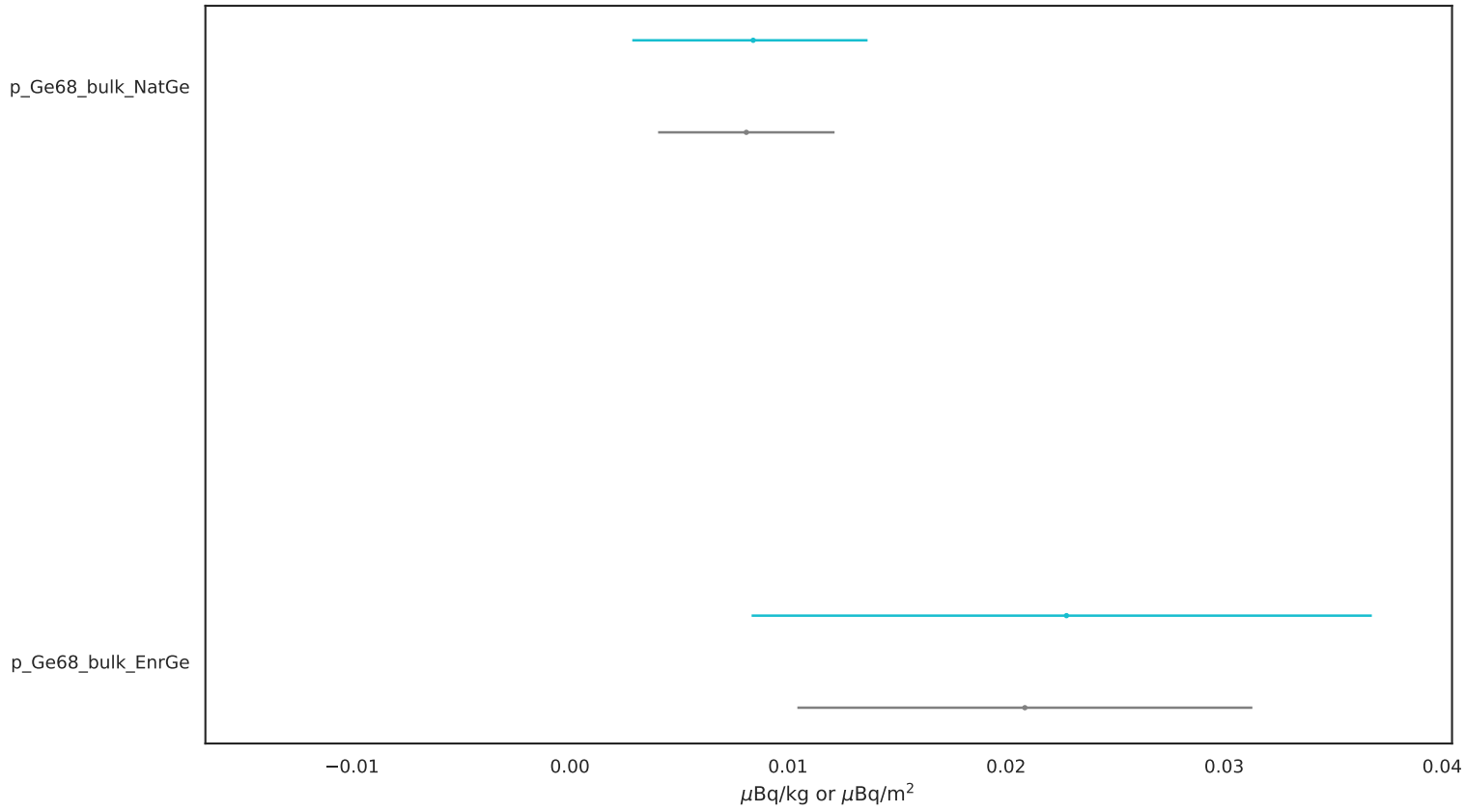

Figure E.4: ^{68}Ge

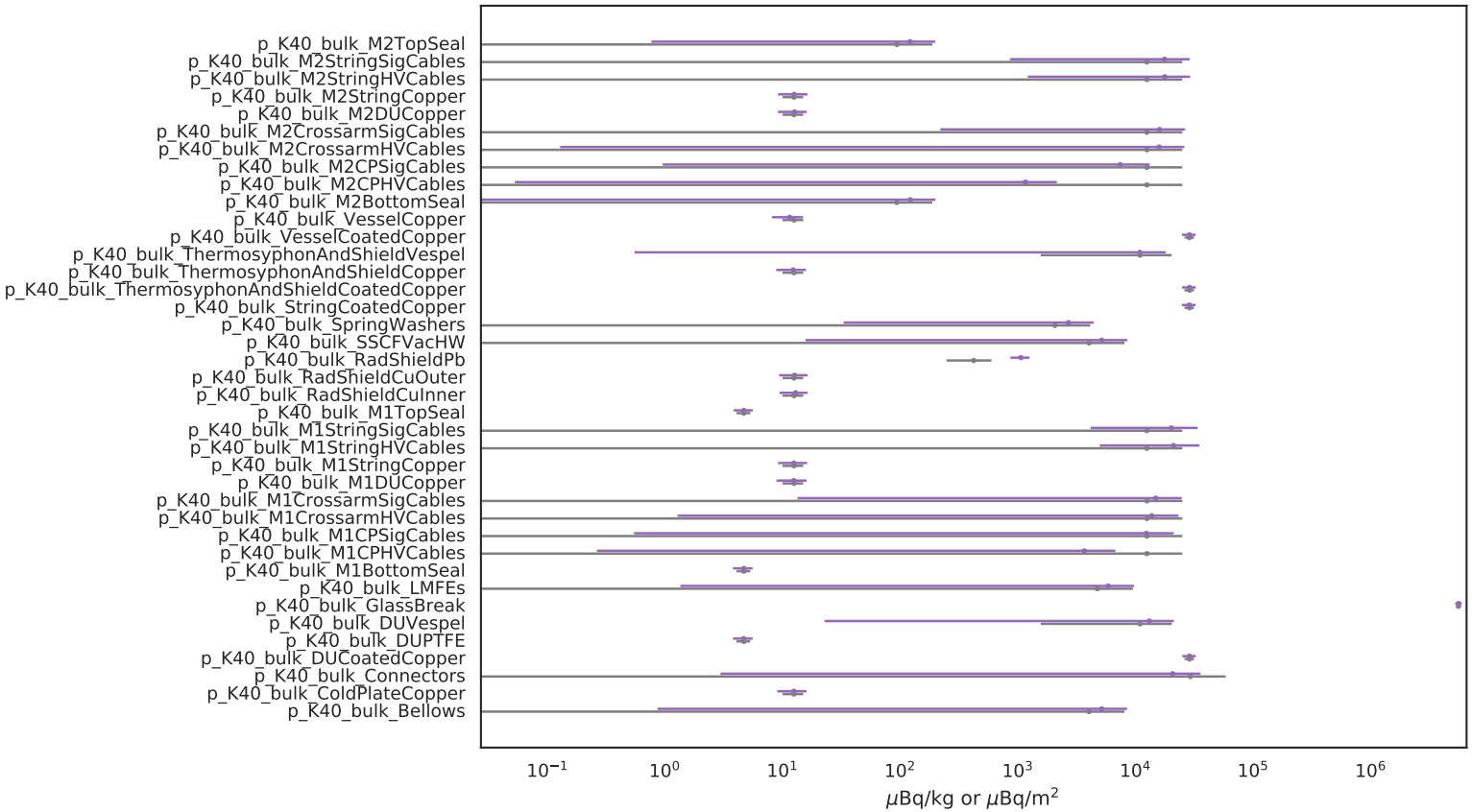

Figure E.5: ^{40}K

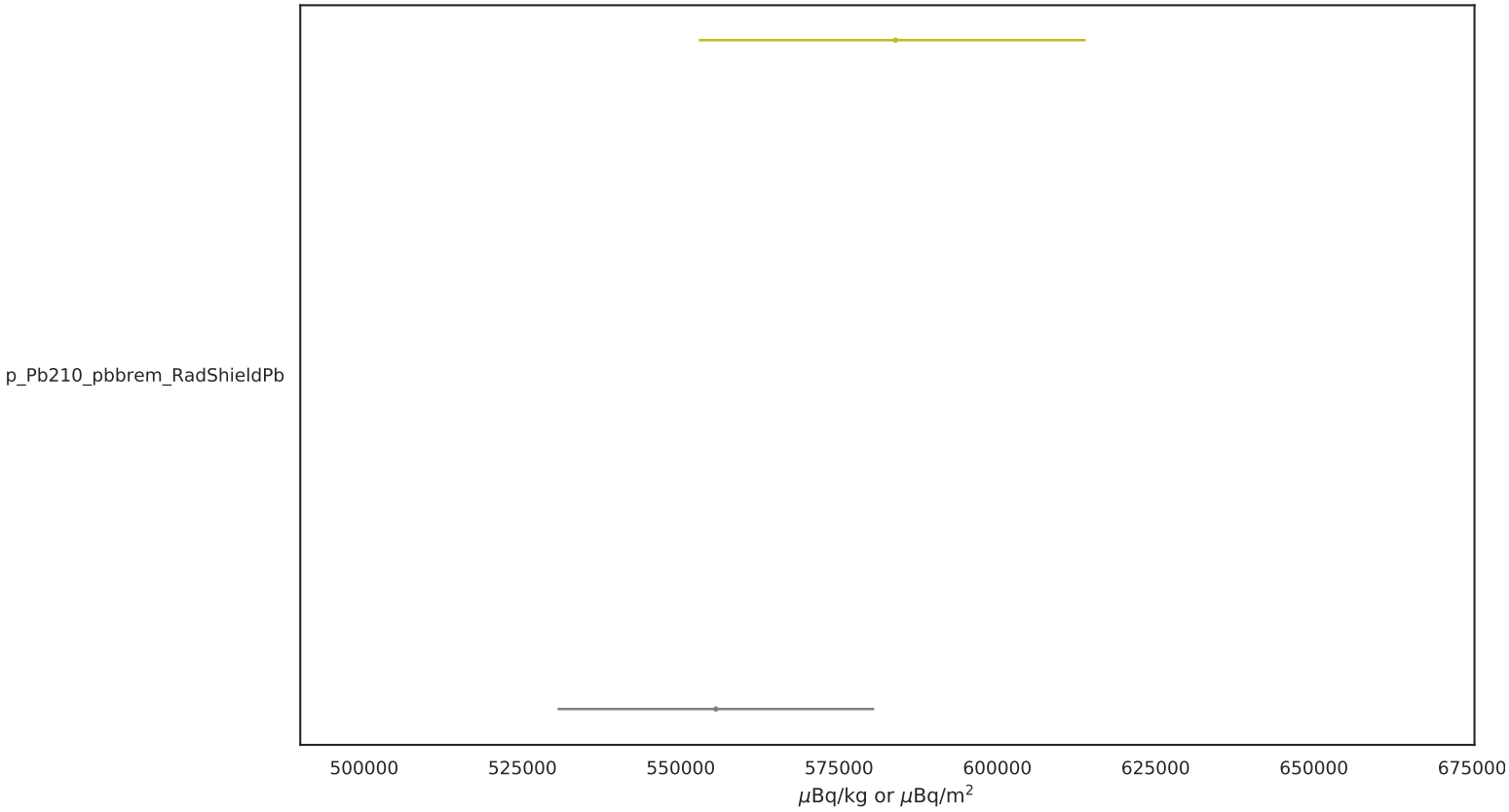

Figure E.6: ^{210}Pb

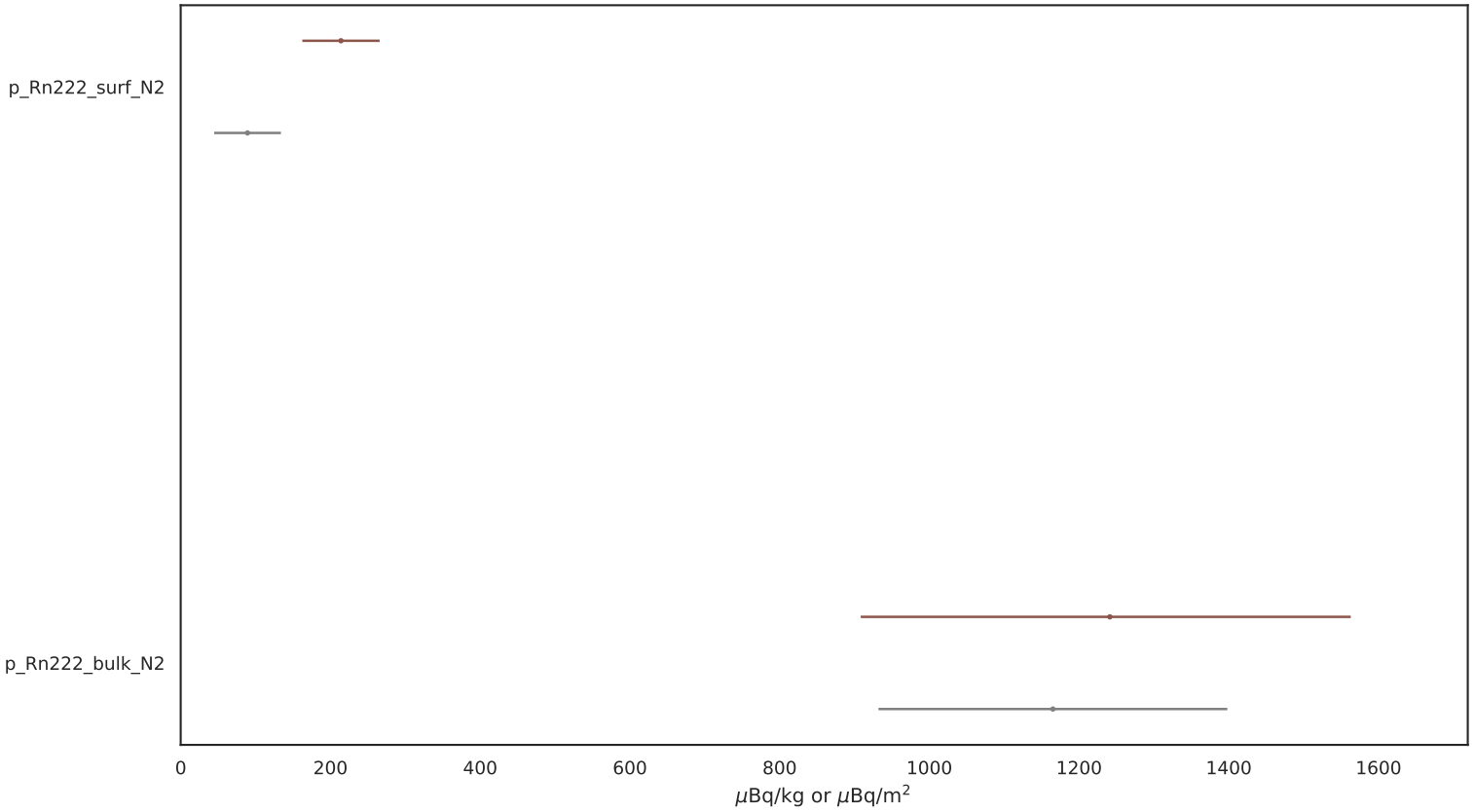

Figure E.7: ^{222}Rn

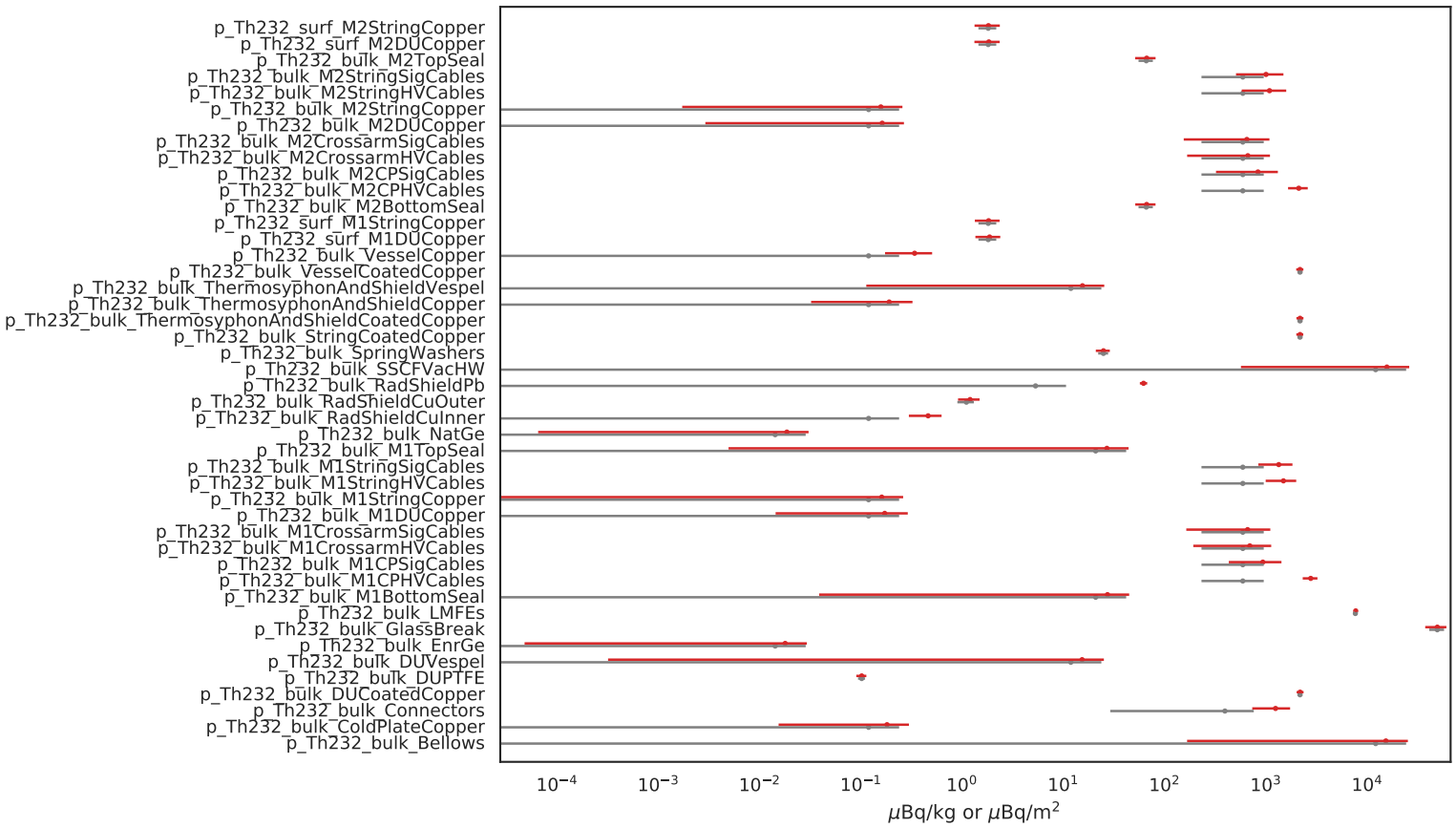

Figure E.8: ^{232}Th

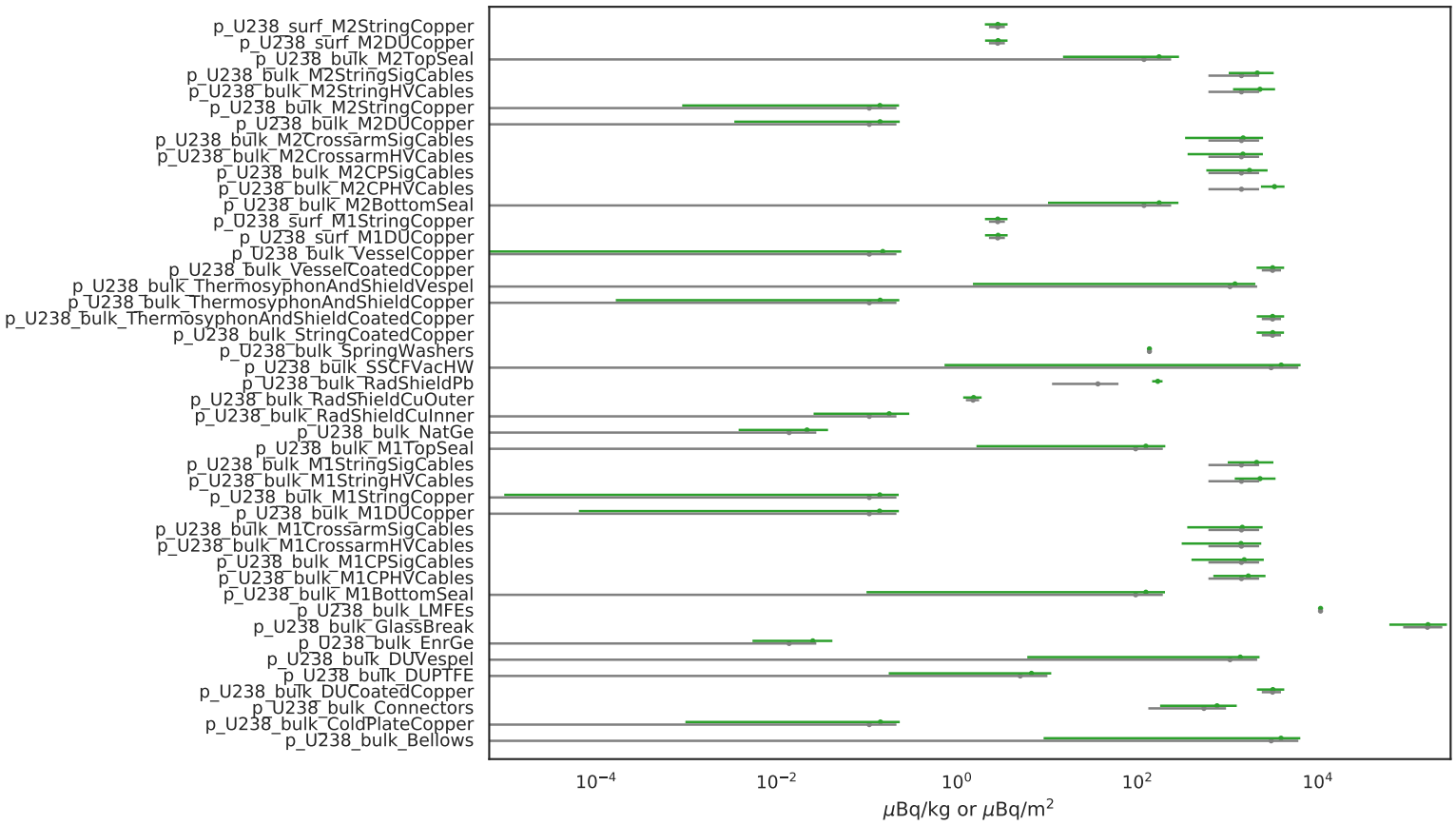

Figure E.9: ^{238}U

BIBLIOGRAPHY

[1] L. M. Brown. The idea of the neutrino. *Physics Today*, 31:23, 1978.

[2] C. L. Cowan et al. Detection of the free neutrino: a confirmation. *Science*, 124:103–104, 1956.

[3] S. Fukuda et al. Evidence for oscillation of atmospheric neutrinos. *Phys. Rev. Lett.*, 81:1562, 1998.

[4] Q. R. Ahmad et al. Direct evidence for neutrino flavor transformation from neutral-current interactions in the Sudbury Neutrino Observatory. *Phys. Rev. Lett.*, 89:011301, 2001.

[5] B. Pontecorvo. Mesonium and anti-mesonium. *Sov. Phys. JETP*, 6:429, 1957.

[6] Z. Maki et al. Remarks on the unified model of elementary particles. *Prog. Theor. Phys.*, 28: 870–880, 1962.

[7] B. Kayser. Introduction to massive neutrinos. *4th Moriond Workshop: Massive Neutrinos in Particle Astrophysics C84-01-15*, 1984.

[8] Ch. Kraus et al. Final results from Phase II of the Mainz neutrino mass search in tritium β-decay. *Eur. Phys. J. C*, 40:447–468, 2005.

[9] V. N. Aseev et al. Upper limit on the electron antineutrino mass from the Troitsk experiment. *Phys. Rev. D*, 84:112003, 2011.

[10] Planck Collaboration. Planck 2018 results. VI. cosmological parameters. *arXiv:1807.06205 [astro-ph.CO]*, 2018.

[11] S. Dell'Oro et al. Neutrinoless double beta decay: 2015 review. *Adv. High Energy Phys.*, 2016: 2162659, 2016.

[12] M. Tanabashi et al. 2018 review of particle physics. *Phys. Rev. D*, 98:030001, 2011.

[13] M. Goldhaber et al. Helicity of neutrinos. *Phys. Rev.*, 109:1015, 1958.

[14] G. Backenstoss et al. Helicity of μ^- mesons from π-meson decay. *Phys. Rev. Lett.*, 6:415, 1961.

[15] M. Robinson. *Symmetry and the Standard Model: Mathematics and Particle Physics*. Springer, Verlag, NY, 2011.

[16] T. Yanagida. Horizontal symmetry and masses of neutrinos. *Prog. Theo. Phys.*, 64:1103–1105, 1980.

[17] S. Pirro et al. Prospects in double beta decay searches. *Eur. Phys. J. A*, 27:25–34, 2006.

[18] J. Engel F. T. Avignone, S. R. Elliott. Double beta decay, Majorana neutrinos, and neutrino mass. *Rev. Mod. Phys.*, 80:481–516, 2008.

[19] D. Perkins. *Particle Astrophysics, 2E*. Oxford University Press, Oxford OX2 6DP, 2009.

[20] R. Saakyan. Two-neutrino double-beta decay. *Annu. Rev. Nucl. Part. Sci.*, 63:503–529, 2013.

[21] J. Engel and J. Menendez. Status and future of nuclear matrix elements for neutrinoless double-beta decay: a review. *Rep. Prog. Phys.*, 60:046301, 2017.

[22] J. Schechter and J. W. F. Valle. Neutrinoless double-β decay in SU(2) $\times$ U(1) theories. *Phys. Rev. D*, 25:2951–2954, 1982.

[23] S. R. Elliott and P. Vogel. Double beta decay. *Annu. Rev. Nucl. Part. Sci.*, 52:115–151, 2002.

[24] G. J. Feldman and R. D. Cousins. Unified approach to the classical statistical analysis of small signals. *Phys. Rev. D*, 57:3873, 1998.

[25] G. Punzi. Sensitivity of searches for new signals and its optimization. *Conf. Proc. PHYSTAT SLAC eConf*, C030908:79, 2003.

[26] J. A. Detwiler. MAJORANA DEMONSTRATOR $0\nu\beta\beta$ decay sensitivity calculations. *Internal Document https://mjdoc.npl.washington.edu/record/1458*, 2011.

[27] G. Heusser. Low-radioactivity background techniques. *Annu. Rev. Nucl. Part. Sci.*, 45:543–590, 1995.

[28] J. A. Formaggio and C. J. Martoff. Backgrounds to sensitive experiments underground. *Annu. Rev. Nucl. Part. Sci.*, 54:361–412, 2004.

[29] J. J. Gomez-Cadenas and J. Martin-Albo. Phenomenology of neutrinoless double beta decay. *Gran Sasso Summer Institute 2014 Hands-On Experimental Underground Physics at LNGS - GSSI14*, 2014.

[30] W. Rodejohann M. J. Dolinski, A. W. P. Poon. Neutrinoless double-beta decay: status and prospects. *Annu. Rev. Nucl. Part. Sci.*, 2019.

[31] N. Abgrall et al. The MAJORANA DEMONSTRATOR neutrinoless double-beta decay experiment. *Adv. High Energy Phys.*, 2014:365432, 2014.

[32] N. Abgrall et al. New limits on bosonic dark matter, solar axions, Pauli exclusion principle violation, and electron decay from the MAJORANA DEMONSTRATOR. *Phys. Rev. Lett.*, 118: 161801, 2017.

[33] S. I. Alvis et al. First limit on the direct detection of lightly ionizing particles for electric charge as low as e/1000 with the MAJORANA DEMONSTRATOR. *Phys. Rev. Lett.*, 120:211804, 2018.

[34] S. I. Alvis et al. Search for trinucleon decay in the MAJORANA DEMONSTRATOR. *Phys. Rev. D*, 99:072004, 2019.

[35] J. Heise. The Sanford Underground Research Facility at Homestake. *J. Phys.: Conf. Ser*, 606: 012015, 2015.

[36] S. Zimmermann et al. Implementation and performance of the electronics and computing system of the gamma ray energy tracking in-beam nuclear array (GRETINA). *IEEE Trans. Nucl. Sci.*, 59:2494–2500, 2012.

[37] M. A. Howe et al. Sudbury Neutrino Observatory neutral current detector acquisition software overview. *IEEE Trans. Nucl. Sci.*, 51:878–883, 2004.

[38] N. Abgrall et al. The MAJORANA DEMONSTRATOR calibration system. *Nucl. Instrum. Meth. A*, 872:16–22, 2017.

[39] P. N. Luke et al. Low capacitance large volume shaped-field germanium detector. *IEEE Trans. Nucl. Sci.*, 36:926–930, 1989.

[40] W. Shockley. Currents to conductors induced by a moving point charge. *J. Appl. Phys.*, 9: 635–636, 1938.

[41] N. Abgrall et al. The MAJORANA DEMONSTRATOR radioassay program. *Nucl. Instrum. Meth. A*, 828:22–36, 2016.

[42] I. Guinn et al. Low background signal readout electronics for the MAJORANA DEMONSTRATOR. *AIP Conf. Proc.*, 2015.

[43] N. Abgrall et al. The MAJORANA parts tracking database. *Nucl. Instrum. Meth. A*, 779:52–62, 2015.

[44] H. S. Miley et al. New techniques and results in ^{76}Ge double-beta decay. *Nucl. Phys. B (Proc. Suppl.)*, 28A:212–215, 1992.

[45] D.-M. Mei et al. Cosmogenic production as a background in searching for rare physics processes. *Astropart. Phys.*, 31:417–420, 2009.

[46] S. R. Elliott et al. Fast-neutron activation of long-lived isotopes in enriched Ge. *Phys. Rev. C*, 82:054610, 2010.

[47] N. Abgrall et al. The processing of enriched germanium for the MAJORANA DEMONSTRATOR and R&D for a next generation double-beta decay experiment. *Nucl. Instrum. Meth. A*, 877: 314–322, 2018.

[48] M. Laubenstein and G. Heusser. Cosmogenic radionuclides in metals as indicator for sea level exposure history. *Appl. Radiat. Isot.*, 67:750–754, 2009.

[49] G. Heusser et al. Low-level germanium gamma-ray spectrometry at the μBq kg^{-1} level and future developments towards higher sensitivity. *J Radiat. Env.*, 8:495–510, 2006.

[50] G. F. Knoll. *Radiation Detection and Measurement, 4E.* John Wiley & Sons, Hoboken, NJ, 2010.

[51] S. I. Alvis et al. Multi-site event discrimination for the MAJORANA DEMONSTRATOR. *arXiv:1901.05388 [physics.ins-det]*, 2019.

[52] J. Gruszko et al. Delayed charge recovery discrimination of passivated surface alpha events in p-type point-contact detectors. *J. Phys.: Conf. Series*, 888:012079, 2017.

[53] J. Gruszko. Surface alpha interactions in p-type point-contact HPGe detectors: Maximizing sensitivity of 76Ge neutrinoless double-beta decay searches. *PhD Thesis University of Washington*, 2017.

[54] W. H. Press et al. *Numerical Recipes: The Art of Scientific Computing, 3E.* Cambridge University Press, Cambridge, United Kingdom, 2007.

[55] G. Gilmore. *Practical Gamma-ray Spectrometry, 2E.* John Wiley & Sons, Hoboken, NJ, 2008.

[56] S. I. Alvis et al. A search for neutrinoless double-beta decay in ^{76}Ge with 26 kg-yr of exposure from the MAJORANA DEMONSTRATOR. *arXiv:1902.02299 [nucl-ex]*, 2019.

[57] M. Agostini et al. Discovery probability of next-generation neutrinoless double-β decay experiments. *Phys. Rev. D*, 96:053001, 2017.

[58] M. Agostini et al. Background free search for neutrinoless double beta decay with GERDA Phase II. *Nature*, 544:5–132, 2017.

[59] L. Hehn et al. Spectral analysis for the MAJORANA DEMONSTRATOR experiment. *arXiv:1711.03177 [physics.ins-det]*, 2017.

[60] S. Agostinelli et al. Geant4—a simulation toolkit. *Nucl. Instrum. Meth. A*, 506:250–303, 2003.

[61] M. Boswell et al. MaGe—a Geant4-based Monte Carlo application framework for low-background germanium experiments. *IEEE Trans. Nucl. Sci.*, 58:1212–1220, 2011.

[62] The MAJORANA Collaboration. MAJORANA DEMONSTRATOR final design report. *Internal Document https://mjdoc.npl.washington.edu/record/1616*, 2012.

[63] G. Giovanetti. P-type point contact germanium detectors and their application in rare-event searches. *PhD Thesis University of North Carolina at Chapel Hill*, 2015.

[64] R. J. Cooper and D. C. Radford. A PSA heuristic code. *Internal Document https://mjdoc.npl.washington.edu/record/1060*, 2009.

[65] J. A. Detwiler. Backgrounds from bulk U and Th in Ge detectors. *Internal Document https://mjdoc.npl.washington.edu/record/446*, 2008.

[66] Private correspondence between M. Busch and I. J. Arnquist. New assay data for 2018 run of signal cable. 2018.

[67] M. Kidd. Updated radiopurity requirements for components of the thermosiphon. *Internal Document https://mjdoc.npl.washington.edu/record/1368*, 2010.

[68] J. Detwiler et al. The MAJORANA DEMONSTRATOR background criteria for Critical Decision 4. *Internal Document https://mjdoc.npl.washington.edu/record/1591*, 2012.

[69] Private correspondence between T. Gilliss and B. Bos. Bulk and surface ^{222}Rn activities in the nitrogen purge volume. 2019.

[70] C. E. Aalseth et al. Search for neutrinoless double-beta decay in ^{76}Ge with the MAJORANA DEMONSTRATOR. *Phys. Rev. C*, 120:132502, 2018.

[71] J. Detwiler et al. DEMONSTRATOR background calculations spreadsheet. *Internal Document https://mjdoc.npl.washington.edu/record/1259*, 2010.

[72] D.-M. Mei et al. Muon-induced background study for underground laboratories. *Phys. Rev. D*, 73:053004, 2006.

[73] E. Aguayo et al. Depth requirements for a tonne-scale ^{76}Ge neutrinoless double-beta decay experiment. *arXiv:1109.4154 [nucl-ex]*, 2011.

[74] W. R. Gilks, S. Richardson, and D. J. Spiegelhalter. *Markov Chain Monte Carlo in Practice*. Chapman & Hall, London, England, 1996.

[75] P. D. Hoff. *A First Course in Bayesian Statistics*. Springer Science+Business Media, New York, New York, 2009.

[76] S. Duane et al. Hybrid Monte Carlo. *Phys. Lett. B*, 195:216–222, 1987.

[77] S. Brooks et al. *Handbook of Markov chain Monte Carlo*. CRC Press, Boca Raton, FL, 2011.

[78] M. Betancourt. A conceptual introduction to Hamiltonian Monte Carlo. *arXiv:1701.02434v2 [stat.ME]*, 2018.

[79] M. D. Hoffman and A. Gelman. The No-U-Turn Sampler: Adaptively setting path lengths in Hamiltonian Monte Carlo. *J. Mach. Learn. Res.*, 15:1593–1623, 2014.

[80] C. Bishop. Model-based machine learning. *Philos. Trans. Royal Soc. A*, 371:20120222, 2013.

[81] J. Salvatier. Probabilistic programming in Python using PyMC3. *PeerJ Comput. Sci.*, 2016.

[82] A. Gelman. Multilevel (hierarchical) modeling: What it can and cannot do. *Technometrics*, 48: 432–435, 2012.

[83] The GERDA Collaboration. Results on $\beta\beta$ decay with emission of two neutrinos or majorons in ^{76}Ge from GERDA Phase I. *Eur. Phys. J. C*, 75:416, 2015.

[84] R. Barlow and C. Beeston. Fitting using finite Monte Carlo samples. *Comput. Phys. Commun.*, 77:219–228, 1993.

[85] C. Goldbach et al. ILIAS Edelweiss stainless steel. *https://www.radiopurity.org*, 2016.

[86] D. S. Leonard et al. Systematic study of trace radioactive impurities in candidate construction materials for EXO-200. *Nucl. Instrum. Meth. A*, 591:490–509, 2008.

[87] I. J. Arnquist et al. ICP-MS assay of etchant solutions and copper parts for uranium & thorium. *Internal Document https://mjdoc.npl.washington.edu/record/1814*, 2016.

[88] K. J. Thomas et al. MJD glass break, bellows. *Internal Document https://mjdoc.npl.washington.edu/record/1938*, 2016.

[89] Private correspondence between M. Green and S. Lassell. NAA of the PTFE o-ring. 2016.

[90] J. Strain. Radioactivity analysis of Sullivan lead bricks. *Internal Document https://mjdoc.npl.washington.edu/record/1280*, 2010.